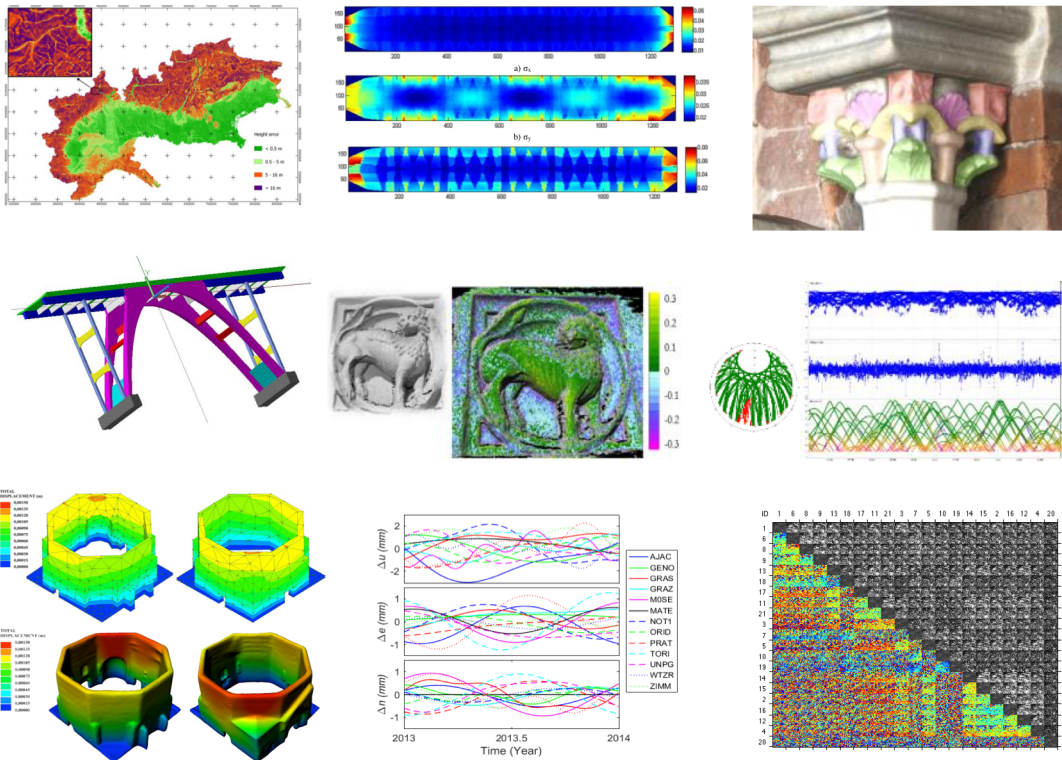


Antonio Vettore editor

RICERCHE DI GEOMATICA 2016



GEOMATICS RESEARCH 2016



**STUDI PRESENTATI ALLA DODICESIMA EDIZIONE DEL PREMIO AUTeC
STUDIES PRESENTED TO THE TWELFTH EDITION OF THE AUTeC AWARD**

Associazione **U**niversitari di **T**opografia e **C**artografia



RICERCHE DI GEOMATICA 2016

*

GEOMATICS RESEARCH 2016

*STUDI PRESENTATI ALLA DODICESIMA EDIZIONE DEL PREMIO AUTEc
STUDIES PRESENTED TO THE TWELFTH EDITION OF AUTEc AWARD*

Questo volume raccoglie gli articoli che hanno partecipato al **Premio AUTEc 2016**. Il premio è stato istituito nel 2005 e, fino al 2015, veniva conferito ogni anno ad una tesi di Dottorato giudicata particolarmente significativa sui temi di pertinenza del SSD ICAR/06 (Topografia e Cartografia) nei diversi Dottorati di Ricerca attivi in Italia.

A partire dal 2016 si è deciso di differenziare la competizione sulla base dell'affinità tra gli argomenti sviluppati e di attribuire fino a tre premi uno per ciascuna delle tre sezioni tematiche proprie del settore:

1. Geodesia, GNSS, Navigazione
2. Fotogrammetria e Laser Scanner
3. GIS, Remote Sensing

Ciascun candidato riassume in un articolo i punti salienti della propria tesi. Gli articoli vengono sottoposti al giudizio di una Commissione giudicatrice costituita dai membri della Giunta AUTEc vigente nell'anno in cui si conferisce il premio. Nell'anno 2016 la Commissione è risultata composta dai professori Ludovico Biagi del Politecnico di Milano, Ambrogio Manzino del Politecnico di Torino, Fabio Radicioni dell'Università di Perugia, Salvatore Troisi dell'Università di Napoli Parthenope, Grazia Tucci dell'Università di Firenze.

Il premio AUTEc 2016 è stato così assegnato:

- per la sezione tematica **Fotogrammetria e Laser Scanner** alla Dott.ssa Marina Santise, che ha conseguito il Dottorato di Ricerca presso l'Università di Parma, per la sua tesi dal titolo "UAS PHOTOGRAMMETRIC BLOCKS: ACCURACY, GEOREFERENCING AND CONTROL";
- per la sezione tematica **GIS, Remote Sensing** alla Dott.ssa Martina Porfiri, che ha conseguito il Dottorato di Ricerca presso l'Università La Sapienza di Roma con la sua tesi dal titolo "DIGITAL SURFACE MODEL GENERATION OVER URBAN AREAS USING HIGH RESOLUTION SATELLITE SAR IMAGERY: TOMOGRAPHIC TECHNIQUES AND APPLICATION TO 3-D CHANGE MONITORING".

Per la sezione Geodesia, GNSS, Navigazione, il premio non è stato assegnato.

Il premio e la pubblicazione degli articoli in un volume e-book vogliono essere un riconoscimento degli Universitari del SSD ICAR/06 per il lavoro di questi giovani ricercatori e una motivazione per continuare le loro ricerche.

Prof. Antonio Vettore
Coordinatore AUTEc 2016-2017



*The volume contains the papers submitted for applying to the **AUTEc Award 2016**. The award was established in 2005 and until 2015 it has been assigned annually to the most scientifically-sound Ph.D. thesis realized in one of the Italian Doctoral Courses pertaining to the scientific sector ICAR/06 (Surveying and Mapping). Since 2016, up to three awards have been established, each one related to one of the following thematic sections:*

- *Geodesy, GNSS, Navigation*
- *Photogrammetry and Laser Scanner*
- *GIS, Remote Sensing*

Candidates are invited to summarize the main outcomes of their research in a paper. Then, articles are examined by a Commission composed by current members of the AUTEc Executive Board. In 2016, the Commission was composed by Professors Ludovico Biagi from the Polytechnic of Milan, Ambrogio Manzino from the Polytechnic of Turin, Fabio Radicioni from the University of Perugia, Salvatore Troisi from the University of Naples Parthenope, Grazia Tucci from the University of Florence.

The winners of the AUTEc Award 2016 are:

- *Section “Photogrammetry and Laser Scanner”:* Dr. Marina Santise, who followed the Doctoral Course at the University of Parma, for her thesis entitled “Uas photogrammetric blocks: accuracy, georeferencing and control”;
- *Section “GIS, Remote Sensing”:* Dr. Martina Porfiri, who followed the Doctoral Course at the University of Roma La Sapienza, for her thesis entitled “Digital surface model generation over urban areas using high resolution satellite sar imagery: tomographic techniques and application to 3-D change monitoring”.
- *Section “Geodesy, GNSS, Navigation”:* not assigned.

AUTEc Awards and “Ricerche di Geomatica” e-book, which are both promoted by ICAR/06 academics and AUTEc associates, aim at rewarding young researchers for their efforts in challenging studies and stimulating their future works.

*Prof. Antonio Vettore
AUTEc Coordinator 2016-2017*



Associazione Universitari di Topografia e Cartografia

AUTEc (Associazione Universitari di Topografia e Cartografia) si è costituita a Bologna il 9 febbraio 1998. Possono iscriversi a questa Associazione i docenti universitari inquadrati nel Settore Scientifico Disciplinare ICAR/06 - Topografia e Cartografia (Settore Concorsuale 08/A4 - Geomatica).

L' **AUTEc** si propone i seguenti obiettivi:

- creare un luogo di incontro per discutere problemi di sviluppo della ricerca, di allocazione delle risorse e di promozione di iniziative didattiche di formazione;
- coordinare le iniziative nei riguardi di Enti ed Organismi nazionali ed internazionali, comunitari e non, con i quali intercorrono rapporti, per sviluppare e promuovere una politica di richieste e di scelte coordinata;
- promuovere quanto necessario per migliorare la qualità dell'insegnamento delle discipline del settore e il loro impatto sulla realtà produttiva del Paese;
- diffondere in maniera sistematica le informazioni che riguardano il settore.

AUTEc è retta da un Coordinatore nazionale coadiuvato dalla Giunta. Le cariche si rinnovano ogni biennio. Hanno rivestito la carica di Coordinatore AUTEc i professori:

Riccardo Galetto, ordinario dell'Università degli Studi di Pavia, nel biennio 1998-1999;
Giorgio Bezoari, ordinario del Politecnico di Milano, nel biennio 2000-2001;
Bruno Astori, ordinario del Politecnico di Torino, nel biennio 2002-2003;
Anna Spalla, ordinario dell'Università degli Studi di Pavia, nei bienni 2004-2005 e 2006-2007;
Benedetto Villa, ordinario dell'Università degli Studi di Palermo, nei bienni 2008-2009 e 2010-2011;
Gabriele Bitelli, ordinario dell'Università degli Studi di Bologna, nei bienni 2012-2013 e 2014-2015.

Dal 2016 riveste la carica di Coordinatore il prof. Antonio Vettore, ordinario dell'Università degli Studi di Padova.

AUTEc is the Italian Association of the academics (University Professors and Researchers) belonging to the Scientific Sector ICAR/06 - Surveying and Mapping. It was founded in Bologna, February 9, 1998.

AUTEc has the following objectives:

- *to create a meeting place to discuss issues related to research development, resource allocation and promotion of educational training in the scientific sector;*
- *to co-ordinate actions and to promote a common policy towards national and international entities and organizations;*
- *to promote what is necessary to improve both the quality of teaching of the disciplines of the scientific sector and their impact on the national productive reality;*
- *to disseminate information related to the scientific sector in a systematic manner.*

AUTEc is governed by a National Coordinator assisted by an Executive Board. The positions are renewed every two years.

The position of AUTEc Coordinator was covered by:

Riccardo Galetto, Full Professor at the University of Pavia, in the period 1998-1999;
Giorgio Bezoari, Full Professor at the Polytechnic of Milan in 2000-2001;
Bruno Astori, Full Professor at the Polytechnic of Turin in 2002-2003;
Anna Spalla, Full Professor at the University of Pavia, in the two-year periods 2004-2005 and 2006-2007;
Benedetto Villa, Full Professor at the University of Palermo, in the two-year periods 2008-2009 and 2010-2011;
Gabriele Bitelli, Full Professor at the University of Bologna, in the two-year periods 2012-2013 and 2014-2015;

Since 2016 holds the position of Coordinator Antonio Vettore, Full Professor at the University of Padova.



Indice

*

Index

	Sezione Tematica 1 Geodesia, GNSS, Navigazione * <i>Thematic Section 1</i> <i>Geodesy, GNSS, Navigation</i>	p. 7
POLUZZI Luca	CONTINUOUS MONITORING OF STRUCTURES USING GNSS TECHNOLOGY	p. 9
TAVASCI Luca	THE USE OF GEODETIC REFERENCE FRAMES FOR MODERN GNSS SURVEYS	p. 19
	Sezione Tematica 2 Fotogrammetria e Laser Scanner * <i>Thematic Section 2</i> <i>Photogrammetry and Laser Scanner</i>	p. 29
ARTESE Serena	SURVEY, DIAGNOSIS AND MONITORING OF STRUCTURES AND LAND USING GEOMATICS TECHNIQUES: THEORETICAL AND EXPERIMENTAL ASPECTS	p. 31
DALL'ASTA Elisa	SEMI-GLOBAL TECHNIQUES IN IMAGE MATCHING AND CHANGE DETECTION WITH APPLICATIONS TO CIVIL AND ENVIRONMENTAL ENGINEERING	p. 43
SANTISE Marina	UAS PHOTOGRAMMETRIC BLOCKS: ACCURACY, GEOREFERENCING AND CONTROL	p. 55
SPANGHER Anna	CONTRIBUTION OF GEOMATIC MODELS TO STRUCTURAL ENGINEERING	p. 67
	Sezione Tematica 3 GIS e Remote Sensing * <i>Thematic Section 3</i> <i>GIS and Remote Sensing</i>	p. 79
FISSORE Vanina	SPATIAL DATA UNCERTAINTY SOURCES IN THE FOREST RESEARCH CONTEXT	p. 81
NOARDO Francesca	SPATIAL ONTOLOGIES FOR ARCHITECTURAL HERITAGE	p. 93
PORFIRI Martina	DIGITAL SURFACE MODEL GENERATION OVER URBAN AREAS USING HIGH RESOLUTION SATELLITE SAR IMAGERY: TOMOGRAPHIC TECHNIQUES AND APPLICATION TO 3-D CHANGE MONITORING	p.105



AUTEc

Associazione **U**niversitari di **T**opografia **e** **C**artografia

Sezione Tematica 1 Geodesia, GNSS, Navigazione

*

*Thematic Section 1
Geodesy, GNSS, Navigation*

CONTINUOUS MONITORING OF STRUCTURES USING GNSS TECHNOLOGY

L. Poluzzi

DICAM – Geomatic Division – University of Bologna, Italy
 luca.poluzzi5@unibo.it

KEY WORDS: GNSS, Monitoring, Garisenda Tower, Reference System, Time Series, Sequential Filter

ABSTRACT:

Nowadays, GNSS technology can be a useful tool, not only for navigation and location aspects, but also for precise positioning applications, such as monitoring of structures. The traditional approach of GNSS monitoring is based on a relative positioning between a reference station, assumed as stable, and a rover one. The continuous monitoring based on a daily position estimation produces a time series that can be useful for studying structure stability, whereas if the goal is a “early warning” systems then 1Hz GNSS data should be used.

In the first part of this work, aspects related to GNSS monitoring have been investigated using a GNSS receiver located on the top of the Garisenda tower (Bologna, Italy) since October 2013. The acquired data, amounting to a couple of years, have been processed starting from four GNSS reference stations located in the area surrounding the tower. A single base data processing has been performed, assuming each reference stations as stable, and four time series have been obtained. A comparison of the estimated mean velocities shows significant differences, probably due to some instabilities of reference stations. Therefore, a model for each reference station has been defined using Precise Point Positioning approach; these models have been considered for a new data processing. The new time series have a higher level of accuracy respect the previous ones. The residual velocity obtained by removing the weighted average of velocity, derived from all the Reference Station, from the velocity of the Monitored Station, can be considered as close to the real structural movements and, in our case, the results indicate that this velocity is not significant.

The second part of this work aims to evaluate a strategy for filtering a daily kinematic GNSS solution using a running smoothing model based on the observations of previous days, in order to obtain a less scattered solution. A test has been conducted with a permanent GNSS station located on Garisenda tower. Because of the presence of the adjacent Asinelli tower, which is taller than the Garisenda, sky visibility is not optimal; for this reason, a sequential filtering can be adopted in order to obtain more accurate solutions. The test was performed using RTKLIB software to calculate 1 Hz baselines between the test station and a master one located on a stable area, about 1 km away from the tower. In order to obtain reliable results, several variables have been considered both in the data processing phase and in defining the filter. All results are reported and discussed in detail in the work. The test results reveal a reduction in scatter of about 20% in the filtered kinematic time series.

The results shown in this paper have been published in FIG conference proceeding (Barbarella et al., 2016; Gandolfi et al., 2015a).

1. INTRODUCTION

The monitoring of structures, land, cultural heritage and so forth has great importance today and thanks to advanced technologies, “early warning systems” have increasingly become a focus of interest (Blewitt et al., 2009). Many different sensors are available for this purpose and each one has its strengths and weaknesses. For instance, the classical topographic techniques are very precise, but they are expensive and too complicated to implement for continuous monitoring, whereas alternative topographical techniques are usually affected by time drifts and unable to detect slow movements. Integrating technologies of a different nature is always advantageous, especially if the monitored object may have either rapid or slow movements.

GNSS (Global Navigation Satellite System) allows an all-weather continuous remote control, as well as a quite low cost both for instrumentations and for monumentation aspects.

In this work, some studies have been conducted concerning both the stability of the tower, by means of observations at 24 hours, both concerning methods for real-time monitoring to early warning issues.

The traditional approach to GNSS monitoring is based on relative positioning between a Reference Station (RS) and one, or more, Monitoring Stations (MS); repeatability and accuracy of a GNSS relative positioning depend on the distance between RS and MS. A RS should be materialized as near as possible to MS, in order to obtain high precision using L1 receivers in cases such as structural monitoring, when the expected movements are usually very small and slow.

For data processing, several software packages are available, both by GNSS manufacturers and by scientific institutions. Recent free and open source software packages, such as RTKLIB (Takasu, 2011) and GoGPS (Realini and Reguzzoni, 2013), are particularly interesting. They allow a much higher level of customization of the data processing and post-processing phases and, for short distances, they offer performances comparable with those of more consolidated software packages, such as Bernese (Dach et al., 2015), Gamit (Herring et al., 2006).

The continuous monitoring based on a daily position estimation produces a time series that can be useful both for structure stability studies. The time series of MS position is obtained by single base positioning, starting from a RS of known position is known and assumed as stable. This hypothesis means that any movements of a RS would be entirely attributed to the MS; therefore, the time series of MS position may potentially represent not only movements of the monitored structure, but also any possible movements of the RS.

In order to investigate how the choice of the RS and the initial hypothesis of its stability affect the MS results, a case study with one MS and more than one RS can be considered. The time series of MS positions can be calculated from each RS, performing single base data processing. The monitoring results should be independent from the RS and the different MS time series are expected to be consistent with each other, regardless of the RS considered in data processing.

In this work, the monitoring of a historical tower, the Garisenda tower in Bologna (Italy) (Figure 1), has been considered as the case study. A GNSS permanent station was installed on top of the

tower in October 2013, and has been considered as the MS. A particularity of this case study is the presence of four existing GNSS permanent stations located in an area of about 2 km from the tower; data acquired from the four stations were available and they have been considered as RS. Furthermore, the four permanent stations were installed years earlier than the MS, between 2004 and 2012, and the prolonged GNSS data series have been used to estimate models of RS positions, by means of Precise Point Positioning (PPP) approach (Bisnath and Gao, 2009) and GIPSY OASIS II software (Webb and Zumberge, 1993). The models of RS have been useful to investigate how behaviours of RS affect the monitoring results.

The second part of this work is instead related to the kinematic processing of GNSS data in order to create methods for real-time monitoring.

The ultimate accuracy of a kinematic GNSS solution also depends on the visibility conditions of the sky, which should be as open as possible. When the boundary conditions are less than optimal, the final solution can be characterized by biases that are localized in particular time windows and due mainly to the constellation geometry or multipath effects (Wübbena et al., 2001). With the aim of reducing these effects, many studies have investigated the possibility of modelling the effects themselves based on the solutions of previous days and have proposed methods to this end. Several authors have defined different techniques for mitigating the multipath effect from calculated coordinates (Bock et al., 2000; Forward et al., 2003; Ragheb et al., 2007). Starting from the background art, this work proposes a method to reduce scatter in the GNSS data relying on a model generated considering previous data acquired over several days. All of the results refer to the aforementioned case of study, the Garisenda tower.

2. THE CASE OF STUDY

2.1 The Garisenda tower in Bologna (Italy)

In this work, the data acquired by a GNSS station located on the top of the Garisenda tower of Bologna (Italy) have been used. The Garisenda tower is one of the most important features of Bologna's cultural heritage, but it is notoriously affected by problems of stability and has already been monitored using different techniques (Baraccani et al., 2014). Moreover, the adjacent Asinelli tower constitutes an example of an unavoidable obstacle to satellite signals, which may affect GNSS solutions and should be considered a habitual problem in these applications. As shown in Figure 1, the Asinelli tower is about 50 meters taller than the Garisenda tower and stands very close to it, on the south side. The Garisenda tower can be dated to around the last two decades of the eleventh century and during construction the foundation soil underwent subsidence phenomena (Giordano, 2000). This caused the tower, originally about 60 m tall, to tilt markedly. Today it stands at a height of 48 m and has a slope of 3.22 m towards the northeast. Therefore, several projects have been undertaken to reinforce the structure over the last decade and after completion of the work, at the beginning of the year 2011, a monitoring system was installed on the tower in order to monitor its structural behaviour by means of a long-base deformometer, deformometer, extensimeter, laser displacement sensor and inclinometers. In 2013, the Department of Civil, Environmental and Materials Engineering of Bologna University installed a permanent GNSS station on the roof of the Garisenda for the double purpose of monitoring the building and testing the satellite technology for this type of application. The station acquires 1 Hz GNSS data and send them via mobile phone technology to a computer server that stores all the received raw data.



Figure 1 – Two Tower of Bologna (the Garisenda tower is the left one)

3. STRUCTURAL MONITORING FOR STABILITY ANALYSIS

As mentioned in the introduction, the traditional approach to GNSS monitoring is based on relative positioning between a reference station (RS) and one or more monitoring stations (MS), materialized at different locations of a monitored object. Positions of MS are measured from RS, assumed as stable. It is also known that repeatability and accuracy of a GNSS relative positioning, in differential data processing approach, depend on the distance between RS and MS. For that reason, in such cases as structural monitoring when the expected movements are usually very small and slow, a RS has to be materialized as near as possible to MS.

In this case study, data acquired by four existing dual frequency geodetic GNSS permanent stations located in the area surrounding the Garisenda tower were available.

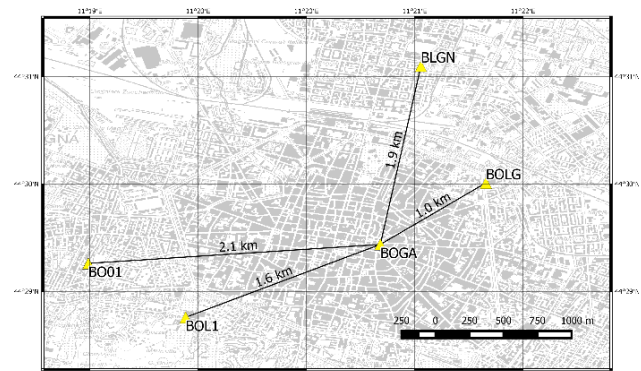


Figure 2 - Map showing the positions of the Garisenda tower MS (BOGA) and the four RS (BOLA, BOLG, BLGN, BOO1)

Those four permanent stations, established at different times and for various applications and purposes, are considered as the RS.

BOLA: Dual frequency geodetic GNSS Permanent station installed on the roof of the School of Engineering and Architecture by the Department of Civil, Environmental and Materials Engineering (DICAM) of the University of Bologna in 2004, for real-time positioning applications.

BOLG: Dual frequency geodetic GNSS Permanent station installed by the Department of Physics and Astronomy (DIFA) of the University of Bologna in 2005 and part of EUREF Permanent Network (EPN).

BLGN: Dual frequency geodetic GNSS Permanent station installed by the Italian National Institute of Geophysics and Volcanology (INGV) in 2008, primarily for geodynamics studies.

BO01: Dual frequency geodetic GNSS Permanent station installed in 2012 by a private company for precise positioning applications in Emilia Romagna (Italy).

The four RS (Figure 2) are located within about 2 km from the MS on the Garisenda tower, their characteristics are listed in Table 1.

GNSS Reference Station	Receiver Type	Antenna Type and Radome	Distance from BOGA (km)
BOL1	Leica GX1230GG	LEIAX1202GG NONE	1.6
BOLG	LeicaSR9500	LEIAT302+GP	1.0
BO01	Trimble 5700	TRM41249.00 TZGD	2.1
BLGN	Leica SR520	LEIAX1202 NONE	1.9

Table 1 - Characteristics of each GNSS RS and their distances from the MS.

The receiver on the Garisenda tower (Rec. Type: Leica GX1230GG, Ant. Type: LEIAX 1202GG, Radome: NONE) has been acquiring data since October 2013, therefore a period of about 2 years (from 2013.7 to 2015.7) is available.

3.1 Data processing and results assuming each reference station as stable

GNSS data acquired by the Garisenda station (BOGA) during the 2 years period have been processed with data acquired by each RS, using RTKLIB and performing a single-base positioning. RTKLIB is an open source software package, which features several calculation modes. The RS have been assumed as stable and have been assigned fixed ITRF2008 coordinates; the main calculation parameters adopted for the data processing are listed below:

- Constellation: GPS+GLONASS
- Observables: Carrier Phase
- Frequencies: L1+L2
- Positioning Mode: Static
- Filter Type: Forward
- Ionosphere Correction: Broadcast
- Tropospheric Correction: Saastamoinen
- Satellite Ephemeris/Clock: Broadcast
- Data sampling: 30 seconds
- A Perl script has been implemented to automate the data processing phases. The results of data processing are four time series of MS positions, each referred to one of the RS.
- In order to separate the plane components and the height, all results and graphs have been represented in local geodetic reference frame.

To make the reading of this work easier, we define $BOGA_{BOL1}$ the time series of the MS BOGA obtained from the reference station BOL1; time series of BOGA obtained from the other RS are named accordingly.

3.2 First results and discussion

The four time series of the MS have been represented into the same graph (Figure 3), in order to compare the results obtained from the different RS. For each time series, mean velocities of the MS have been estimated. Since the main purpose of this work is not to discuss the position determination of an unknown point

but the monitoring of a point, the time series displayed in Figure 3 have been shifted of a fixed value in y-axis. This allows a better view of results and, in particular, it highlights differences between the mean velocity values, as well as the presence of signals and the scattering of each solution. The gaps in time series, evident in the graphs, have been caused by problems of the MS and interruptions of data transmission. The two vertical lines, after epoch 2014.5, mark an interval of time when the MS receiver have been substituted with another of the same type, to allow a firmware update.

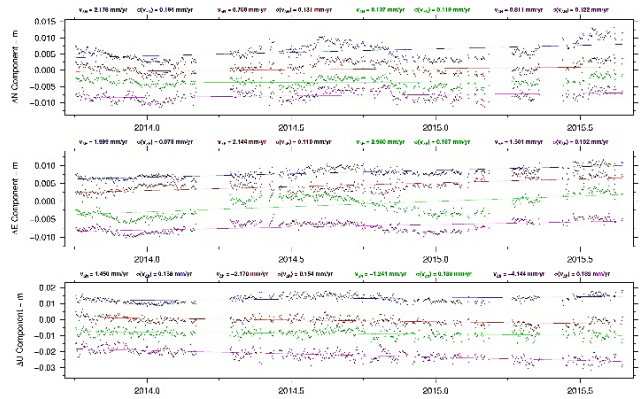


Figure 3 – Time series of BOGA, in local geodetic components, derived from RS assumed as stable. The time series are represented in different colours: $BOGA_{BOL1}$ in blue, $BOGA_{BO01}$ in red, $BOGA_{BOLG}$ in green and $BOGA_{BLGN}$ in magenta.

As Figure 3 illustrates, the four time series of BOGA show some differences, both in terms of estimated mean velocities of the MS and of signal presence.

For a better comparison of results, the estimated mean velocities of BOGA and root mean squares values are listed in Table 2; for each local geodetic component a weighted average of velocities have been calculated and they are also shown in Table 2. The inverse of the square of RMS has been assumed as weight.

Time Series	\bar{V}_N (mm/y)	$\sigma_{\bar{V}_N}$ (mm/y)	\bar{V}_E (mm/y)	$\sigma_{\bar{V}_E}$ (mm/y)	\bar{V}_U (mm/y)	$\sigma_{\bar{V}_U}$ (mm/y)
$BOGA_{BLGN}$	0.82	0.12	1.50	0.10	-4.14	0.19
$BOGA_{BO01}$	0.77	0.13	2.14	0.11	-2.17	0.15
$BOGA_{BOL1}$	2.18	0.19	1.99	0.07	1.45	0.16
$BOGA_{BOLG}$	0.14	0.12	2.96	0.19	-1.24	0.18
Weighted Average	0.75		1.97		-1.34	
RMS	0.90		0.60		2.33	

Table 2 - BOGA mean velocities, estimated for the time series obtained assuming the RS as stable, and weighted averages of velocities in each local geodetic component.

The MS position should be independent from the RS considered in the single base data processing and the four resulting BOGA time series should provide results that are consistent with each other. To evaluate the level of agreement between the time series of solutions, Pearson's correlation coefficients (Pearson, 1895) have been calculated, assuming the $BOGA_{BOL1}$ solution as reference (Table 3). Figure 3 and Table 2 show some significant differences between the mean velocities of the MS, estimated for the four time series.

Time Series	ρ_N	ρ_E	ρ_U
<i>BOGA_{BOLG}</i>	0.62	0.70	0.03
<i>BOGA_{BO01}</i>	0.90	0.65	0.29
<i>BOGA_{BLGN}</i>	0.59	0.64	-0.28
Average	0.70	0.66	0.02

Table 3 - Pearson's coefficients, calculated assuming *BOGA_{BOL1}* as reference, for the time series obtained with stable RS.

In Figure 3, the East components appear to be one characterized by more scattered solutions and more differences between time series signals, particularly the *BOGA_{BOLG}* solution (green dots in Figure 3). The y-axis scale of the height component is different from the one of North and East, therefore some characteristics and differences may not be visible in Figure 3.

Table 2 shows that the height components have the highest value of RMS of the weighted average of estimated velocities. The correlation coefficients in Table 3 indicate that the results obtained from the four RS, assumed as stable and located close to the MS, have only a partial agreement, with the lowest values of correlation in the height component.

Most likely, those differences are partly due to the initial hypothesis of stability of the RS. With the single base data processing used, any movements of a RS would be attributed entirely to the MS, thus inducing potentially erroneous interpretations of results.

In order to take local movements and signals of RS into account and to investigate the possibility of improving the solutions' agreement, the entire dataset has been processed considering the local movements of each RS, by means of time series models of RS positions, obtained by a Precise Point Positioning (PPP) approach.

3.3 Data processing and results considering a local time series model for each reference station

In a second data processing, four time series of MS positions have been calculated applying a synthetic model to each RS; as mentioned above, the RS models have been defined employing a PPP approach and Gipsy OASIS II. The RS have been installed earlier than the MS and the GNSS series of RS are all longer than the 2 years period used to calculate the BOGA solutions. For each RS, the model has been defined using all data available. For prolonged geodetic time series, PPP approach provides results comparable with those of other scientific software packages, but referred to the global reference frame (Gandolfi et al., 2015b).

3.3.1 Model generation using PPP and Gipsy-OASIS II software package

In order to obtain a synthetic model for each RS without introducing any direct cross-correlation between stations, a data-processing based on PPP approach represents a possible solution, as well as quite fast and accurate. Over the last few years, PPP has achieved performance levels comparable to those obtainable through the differencing approach (Griffiths and Ray 2009; Bisnath and Gao 2009), especially for GNSS permanent stations. It is known that PPP provides solutions referred to the reference frame of the orbits, which constitute the only constraint to a reference frame. Using this approach, each RS can be processed separately from the others and the result is a time series referred to the reference frame of the orbits (now IGB08 or ITRF2008). In this reference frame, a point located on the Eurasian plate moves with an average velocity of about 2.5 cm/year in North-East direction. This average motion can be removed using a Helmert transformation (Boucher and Altamimi, 2011), which moves the

solution from the ITRS to ETRS. In this Reference System, realized through the ETRF2000, a point in Italy is characterized by a residual velocity of a few mm/year (Barbarella et al., 2013).

GNSS Reference Station	\bar{V}_N (mm/y)	σ_{V_N} (mm/y)	\bar{V}_E (mm/y)	σ_{V_E} (mm/y)	\bar{V}_U (mm/y)	σ_{V_U} (mm/y)
BLGN	2.18	0.04	1.91	0.03	2.46	0.15
BO01	2.83	0.05	1.14	0.05	3.74	0.17
BOL1	2.54	0.06	1.49	0.03	-0.48	0.11
BOLG	3.20	0.06	0.77	0.07	1.41	0.17
Weighted Average	2.60		1.51		1.29	
RMS	0.44		0.53		1.87	

Table 4 - Average velocities of RS, derived from PPP modeling, and weighted averages of velocities in each local component.

Using GIPSY OASIS II software package, the data processing of the four RS has been performed and each solution was transformed in ETRF2000.

Average velocities of each RS have been estimated with the method described; the values are shown in Table 4 and are useful for some later analyses.

3.3.2 Results

The complete models of RS, described in 3.3.1, have been applied to the time series obtained by the first data processing performed assuming the RS as stable.

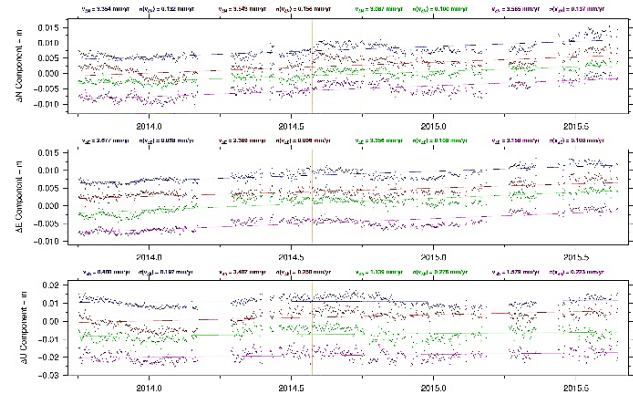


Figure 4 – Time series of BOGA, in local geodetic components, derived from the four RS and considering the RS models. The time series are represented in different colours: *BOGA_{BOL1}* in blue, *BOGA_{BO01}* in red, *BOGA_{BOLG}* in green and *BOGA_{BLGN}* in magenta.

The results of this second processing are four new time series, where local movements and signals of RS are considered. In order to assess the influence of the RS models on MS results, the new time series of BOGA have been represented in local geodetic frame and analyzed like the previous time series, computing mean velocities and correlation coefficients. The new time series have been represented into the same graph (Figure 4).

Estimated mean velocities of the MS and their respective root mean square values are listed in Table 5, weighted averages of velocity values in each local component are also reported.

Table 6 shows the Pearson's correlation coefficients, calculated assuming the *BOGA_{BOL1}* solution as a reference.

Time Series	\bar{V}_N (mm/y)	$\sigma_{\bar{V}_N}$ (mm/y)	\bar{V}_E (mm/y)	$\sigma_{\bar{V}_E}$ (mm/y)	\bar{V}_U (mm/y)	$\sigma_{\bar{V}_U}$ (mm/y)
<i>BOGA_{BOLI}</i>	3.35	0.13	2.68	0.09	0.49	0.20
<i>BOGA_{BLGN}</i>	3.56	0.14	3.16	0.10	1.58	0.22
<i>BOGA_{BOOI}</i>	3.54	0.16	2.37	0.10	3.41	0.26
<i>BOGA_{BOLG}</i>	3.09	0.10	3.36	0.11	1.14	0.28
Weighted Average	3.32	/	2.85	/	1.49	/
RMS	0.23	/	0.45	/	1.27	/

Table 5 - BOGA mean velocities, estimated for the time series obtained considering the RS models, and weighted averages of velocities in each local geodetic component.

Time Series	ρ_N	ρ_E	ρ_U
<i>BOGA_{BOLG}</i>	0.82	0.81	0.39
<i>BOGA_{BOOI}</i>	0.88	0.90	0.68
<i>BOGA_{BLGN}</i>	0.81	0.88	0.37
Average	0.84	0.86	0.48

Table 6 - Pearson’s correlation coefficients, calculated assuming *BOGA_{BOLI}* solution as reference, for time series obtained with RS models

Mean velocities of BOGA (Table 5) have been estimated for time series calculated considering synthetic RS models referred to the ETRF2000 reference systems; for this reason, the values of mean velocities in local components amount to a few mm/year.

Compared to the mean velocities in Table 2, the values shown in Table 5 are more similar and, in each local component, the root mean squares values of weighted average velocity are lower, especially for North and height component.

As mentioned before, MS solutions should be independent from the RS considered in data processing and each time series should give the same results for the BOGA station.

Table 6 shows correlation coefficient values that are overall higher than those of the previous results (Table 3), particularly in height component. Such increase suggests that considering the RS models, and thus considering movements and signals of RS, results in an improvement in the level of agreement between the four solutions.

Time Series	\bar{V}_N (mm/y)	$\sigma_{\bar{V}_N}$ (mm/y)	\bar{V}_E (mm/y)	$\sigma_{\bar{V}_E}$ (mm/y)	\bar{V}_U (mm/y)	$\sigma_{\bar{V}_U}$ (mm/y)
<i>BOGA_{BOLI}</i>	0.76	0.46	1.16	0.54	-0.81	1.88
<i>BOGA_{BLGN}</i>	0.97	0.47	1.64	0.54	0.28	1.89
<i>BOGA_{BOOI}</i>	0.95	0.47	0.86	0.54	2.11	1.89
<i>BOGA_{BOLG}</i>	0.49	0.46	1.84	0.54	-0.16	1.89
Weighted Average	0.78	/	1.37	/	0.36	/
RMS	0.22	/	0.45	/	1.25	/

Table 7 - Quasi residual velocities of the Garisenda tower

Obviously, these results (Table 5) don’t represent movements of the structure where the MS is located, but they represent movements of the structure together with the residual velocity of the ETRF2000 in the area of study. A rigorous procedure to remove residual velocity of the ETRF2000 cannot be defined. However, considering the respective locations of RS and MS, a weighted average velocity based on the mean velocities of each

RS can be computed (Table 4); these RS velocity values can be subtracted from the velocities of MS in Table 5 and a quasi-residual velocity of the structure can be estimated (Table 7).

4. STRUCTURAL MONITORING FOR EARLY WARNING APPLICATIONS

In this paragraph, a possible technique for early warning application by using kinematic mode was described. With this aim, a monitoring system that provides real-time positions and the critical threshold of detectable displacement is required. If the boundary conditions (visibility satellites, SNR, PDO parameters, presence of obstacles in the nearness) are optimal, the solutions have to represent the “best description” of the studied phenomenon. Unfortunately, in most real cases, we don’t have such favorable conditions, so the solutions are often affected by bias localized at particular times or period of the day. Therefore, some parameters used for the data processing can play an important role in the final solutions. For that reason, some tests were performed by using different values of the cutoff angles and changing other parameters with the aim to find the best boundary condition for the applied context.

4.1 Data processing

Also for GNSS kinematic data processing, there are several software packages available. For that reason, different tests have been performed using some of these softwares, but in this paper only the results processed with RTKLIB will be shown. Kinematic differential post processing was used to calculate baselines between the Garisenda station (BOGA) and a reference one (BOLI) about 1.6 km away from the tower (Figure 5).



Figure 5 – Map of BOGA and BOLI location

Both stations provide 1 Hz data. For this work, 15 days of data were processed. Despite the short length of the baseline between the GNSS stations, some parameters may have an impact on the data processing, the carrier phase (or a combination of different carrier phases) and the cut-off angle in particular.

With regard to the carrier phase, a test was performed to compare the L1 solution with L1+L2. Because of the short baseline length, other combinations were not considered. This test showed that the use of only one frequency (L1) makes it possible to have a higher number of fixed solutions (+10%), but at the same time results in a higher RMS (+22% on average). Thus, it was decided to use the carrier frequencies L1 + L2.

The elevation mask is a parameter that can significantly impact both the accuracy and scattering of solutions. In particular, when obstacles are present, they limit sky visibility and produce multipath effects. Figure 6 shows the cycle slip map area located in the southern part of the skyplot and the multipath graph, which reveals a high correlation between multipath effects and SNR quality.

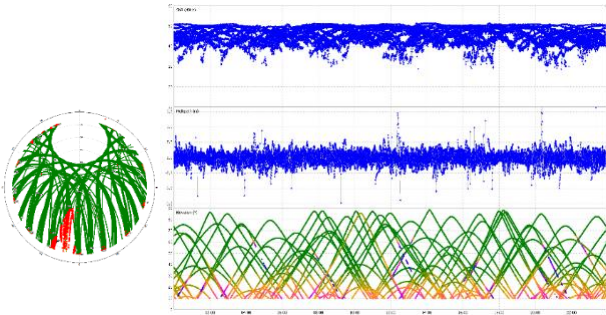


Figure 6 – Cycle slip skyplot (left) and SNR/Multipath/Elevation graphs (right) of BOGA site (DOY: 355 year: 2013).

In light of these considerations, as a preliminary test, four different calculations were performed using different elevation masks (10°,13°,15°,25°). The test was performed on the whole dataset and has evidenced how the best results, in terms of scattering of the solutions, were obtained for a 10° elevation mask (Table 8).

Elevation mask	σ_N (mm)	σ_E (mm)	σ_U (mm)
10°	5.7	4.1	8.9
13°	6.4	8.0	9.4
15°	7.2	6.4	13.0
25°	120.7	59.9	199.9

Table 8 - Repeatability of the kinematic solution in terms of standard deviation considering different elevation mask angles for data processing.

The main calculation parameters adopted for the data processing are listed below.

- Constellation: GPS+GLONASS
- Observables: Carrier Phase
- Frequencies: L1+L2
- Position Mode: kinematic
- Filter Type: Forward
- Ionosphere Correction: Broadcast
- Tropospheric Correction: Saastamoinen
- Satellite Ephemeris/Clock: IGS Precise
- Data sampling: 1Hz

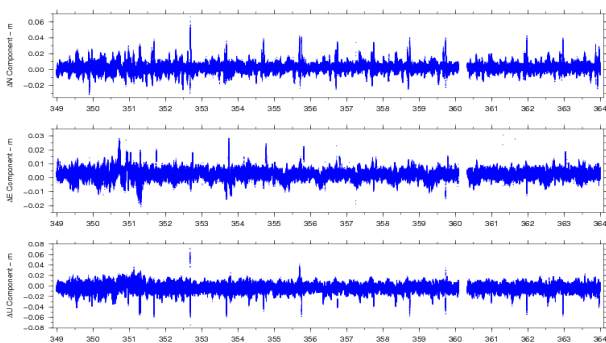


Figure 7 – Kinematic time series of 15 days in the Local Geodetic components (N, E, U), cleaned of outliers. The X-axis is expressed in DOY of the year 2013.

All calculations, results and graphs have been represented in a geodetic local reference frame where the origin was defined

using 15 days of static data processing. The reason for this choice was the need to separate the plane components from the height one. The first results revealed a higher scattering of solutions for the North component compared to the East one, which is quite unusual for the GNSS technique, but could be explained by considering the obstacle in the southern sky represented by the Asinelli tower. The time series of the three geodetic components shown in Figure 7 provide evidence of some recursive systematic effects. It is unlikely that they represent the movement of the structure. We investigated the solutions in detail and evaluated the possibility that the difficulties in estimating the coordinates could be due to the satellite constellation.

In particular, the presence of some regular spikes over the complete time series was examined in depth. The autocorrelation function (Cliff and Ord, 1973) was applied to the solutions; the results obtained are shown in Figure 8. The highest peak was located at 86164 seconds, which represents the sidereal day (Radovanovic, 2000), indicating the recursive GNSS constellations. As the systematic effects are constant, it is conceivable to create a daily empirical model with the aim of smoothing the original solution and obtaining more stable results. Below we describe the strategies adopted to create the daily models and the results obtained for the dataset considered.

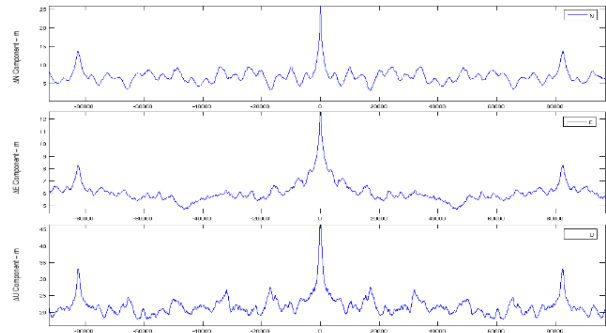


Figure 8 – Autocorrelation function in the three Local Geodetic components (N, E, U). The x-axis represents the time delay expressed in seconds.

4.2 Definition of the smoothing model

The results obtained using the autocorrelation function provide evidence of a recursive effect with the amplitude of a sidereal day. This effect is not due to movements of the structure and can be reduced by creating a model from the solution of previous days. The model has to have the length of a sidereal day.

In order to create such a model, several steps have to be performed. The first step consists in the rejection of outliers. This was achieved by means of an iterative process based on the hypothesis of linear motion of the solution for very short time windows. The main reason for splitting the time series into short blocks is to preserve the predominant pattern of the time series and remove just single spikes or outliers. For this purpose, every day was divided into 30 periods of 2880 seconds each and then a linear regression for each component was computed using a traditional weighted least squares approach. The weight assumed for the computation was the inverse of the formal variance derived from the data processing. With i defined as the component (North, East and Up), the slope m^i and the y-axis intercept q^i of the linear regression were obtained for each period, thus enabling a calculation of the residuals $v^i(t)$:

$$v^i(t) = S^i(t) - [q^i + m^i * t] \tag{1}$$

where $S^i(t)$ represents the solution of the i -th component at the epoch t .

An iterative loop was used to seek and remove the furthest outlier by comparison of the maximum residuals with the standard deviation σ , calculated as:

$$\sigma^i = \sqrt{\frac{\sum_n v^i(t)^2}{n}} \quad (2)$$

where n is the number of solutions for each block ($\max\{n\}=2880$). We assumed a solution to be an outlier when one of the three associated residuals was more than 3 times larger than the associated standard deviations. If a solution was considered as an outlier, it was removed from the time series and all the sequences resulting from the calculation of the linear regression and rejection of outliers were re-processed.

The time series without outliers ($C^i(t)$) were subsequently used to generate the sidereal filter. From the cleaned daily time series, we generated files containing *sidereal daily* time series (with a length of one sidereal day – 86164 seconds). From these files a sidereal daily model was calculated by means of a weighted running average of $2r + 1$ seconds (for the first and last r epochs of each sidereal day; data were taken from the previous or subsequent sidereal days).

For each block of $2r+1$ data, the average value was calculated using the following equation:

$$m^i(t^*) = \frac{\sum_{\tau=i-r}^{i+r} \frac{C^i(\tau)}{(\sigma^i(\tau))^2}}{\sum_{\tau=i-r}^{i+r} \frac{1}{(\sigma^i(\tau))^2}} \quad (4)$$

with

$$t^* = \frac{\sum_{\tau=i-r}^{i+r} \tau}{2r+1} \quad (5)$$

Where $\sigma^i(\tau)$ represents the formal error associated with the $C^i(\tau)$ solution, $d^i(t^*)$ represents the value of the model for the i -th at time t^* and t^* represents the mean time of the values considered. The reason for this definition, as regards both the model and associated time, is to compensate for any possible lack of data. Where data are lacking, the value of the running average should be located at the mean time relative to the considered data. The model created was not equally spaced in time and in order to remedy this aspect, the last step was to resample the model, thereby generating the final model of 86164 values (sidereal seconds).

We assumed m^{ik} as the final resampled model for the k -th day and i -th component. It is important to underline that when this method is used, the sidereal models are always full of data and a model can be estimated for each sidereal day. The smoothing model for the kinematic solution of the generic k -th day could be built using an average of several (d) models based on previous days. We defined this smoothing model M^{ik} as:

$$M^{ikd} = \frac{m^{i(k-1)} + \dots + m^{i(k-d)}}{d} \quad (6)$$

And the filtered solution was calculated as:

$$F^{ikd}(t) = C^{ik}(t) - [M^{ikd}(t) - \bar{M}] \quad (7)$$

with \bar{M} average of $M^{ikd}(t)$

Considering the absence of movements during the test campaign, the standard deviation of the time series C^{ik} and F^{ikd} were considered to evaluate the repeatability of the solutions.

The next section is dedicated to evaluating the improvement achieved by changing the dimension of d , considering a reasonable value of the parameter r .

4.3 Test results obtained from the Garisenda tower GNSS station

The value r of the seconds to be used for the moving average was first determined by carrying out several tests. Considering that an excessively high value of r does not enable rapid movements to be picked up, but on the other hand an r value that is too low does not remove the white noise, we chose $r = 100$ seconds for all the tests.

d	i	Day (K)							Average	
		9	10	11	12	13	14	15		
0	N	5.7	6.2	7.0	7.3	6.2	5.8	6.3	6.4	6.13
	E	2.9	3.5	4.7	3.7	2.6	3.0	3.4	3.4	
	h	6.9	8.6	10.5	10.5	7.6	7.7	8.5	8.6	
1	N	4.0	4.4	6.8	6.9	6.7	4.5	4.8	5.4	5.83
	E	2.6	3.3	4.5	5.2	3.7	2.5	3.4	3.6	
	h	6.1	7.5	10.6	11.7	9.1	6.4	7.7	8.5	
2	N	3.4	4.3	6.2	5.8	5.0	4.6	4.2	4.8	5.15
	E	2.2	3.2	4.0	4.2	2.8	2.5	3.1	3.2	
	h	5.4	7.0	9.6	9.6	7.5	6.1	7.1	7.5	
3	N	3.3	4.2	6.0	5.5	4.7	4.3	4.4	4.6	4.96
	E	2.2	3.1	4.0	3.8	2.6	2.5	3.3	3.1	
	h	5.1	6.9	9.2	9.1	6.8	5.9	7.3	7.2	
4	N	3.2	4.2	5.9	5.2	4.5	4.1	4.4	4.5	4.84
	E	2.2	3.0	3.9	3.6	2.4	2.4	3.0	2.9	
	h	5.1	6.9	9.1	8.8	6.5	6.0	7.2	7.1	
5	N	3.3	4.2	5.8	5.1	4.3	4.0	4.3	4.4	4.79
	E	2.2	3.0	3.9	3.5	2.3	2.3	3.0	2.9	
	h	5.1	6.9	9.1	8.6	6.3	5.9	7.3	7.0	
6	N	3.3	4.2	5.9	5.1	4.2	4.0	4.3	4.4	4.76
	E	2.2	3.0	3.9	3.5	2.2	2.3	3.0	2.9	
	h	5.1	6.9	9.2	8.5	6.1	5.8	7.2	7.0	
7	N	3.3	4.3	5.8	5.1	4.2	4.0	4.3	4.4	4.74
	E	2.2	3.0	3.9	3.5	2.2	2.3	3.0	2.9	
	h	5.1	6.9	9.2	8.5	6.1	5.8	7.1	6.9	
8	N	3.3	4.3	5.9	5.1	4.2	4.0	4.3	4.4	4.75
	E	2.3	3.0	3.9	3.4	2.3	2.3	3.0	2.9	
	h	5.1	6.9	9.1	8.5	6.1	5.8	7.1	6.9	

Table 9 – Standard deviation (mm) of the daily kinematic solution filtered by models calculated using an increasing number of preceding days (d). $d = 0$ represent unfiltered solution.

Particular attention was given when selecting the value of d . We assessed the improvement in terms of scatter of the solutions by considering models that were generated varying d from 1 to 8 days and testing them for seven days starting from the ninth. The results in terms of scattering and the improvements obtained with the F^k time series compared to the C^k time series are shown in Table 9 and Table 10, respectively.

It may be observed from Table 9 that North is the least precise plane component, though the Easting component is usually the weaker one in GNSS. This is probably due to the specific location of the station, as the Asinelli tower is south of the Garisenda

tower and thus occludes the sky in the direction that mainly influences the North determination.

d	i	Day (K)							Average	
		9	10	11	12	13	14	15		
1	N	31	29	3	5	-9	22	25	15	3.90
	E	11	6	4	-40	-41	17	1	-6	
	U	12	13	-1	-11	-20	17	9	3	
2	N	40	30	11	20	18	21	33	25	15.33
	E	23	10	13	-13	-7	16	11	8	
	U	22	19	8	8	1	20	16	14	
3	N	42	32	15	25	24	26	30	28	18.39
	E	25	14	15	-2	3	16	3	10	
	U	26	20	12	13	10	23	14	17	
4	N	43	32	16	29	28	29	31	30	20.68
	E	24	15	16	4	10	20	11	14	
	U	26	20	13	17	15	22	14	18	
5	N	42	32	17	30	30	32	32	31	21.65
	E	24	16	16	5	12	22	12	15	
	U	26	20	13	18	17	23	14	19	
6	N	42	32	16	30	32	31	32	31	22.21
	E	23	16	16	7	14	24	13	16	
	U	27	20	13	19	19	24	15	20	
7	N	42	31	17	30	33	31	33	31	22.41
	E	22	16	16	7	15	25	13	16	
	U	26	20	13	19	20	25	16	20	
8	N	42	31	17	29	32	32	33	31	22.29
	E	21	16	15	7	14	25	14	16	
	U	26	20	13	19	20	25	17	20	

Table 10 – Reduction (%) in the standard deviation of the daily kinematic solutions filtered by models calculated using an increasing number of preceding days (d) compared to the original cleaned solution.

As shown in Table 10, the highest scatter reduction was achieved precisely in the Northern component, and especially where $d=7$. Also, considering the overall improvement, $d=7$ appears to be the best choice for this context.

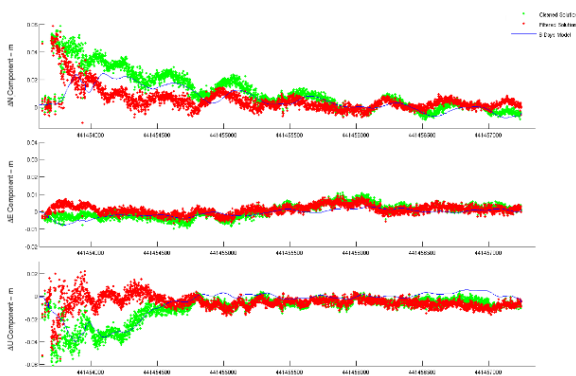


Figure 9 – Comparison between the Cleaned Solution (green), Filtered Solution (red) and 7-Day Model Applied (blue)

Figure 9 shows an example of how the filter works over a time span of about one hour. The original cleaned solution C^k is

represented by green dots, the 7-day M^k model by a blue line and the filtered F^k solution by red dots. As is evident, the filter reduces the original systematic effect, rapidly correcting the solution and bringing the values close to zero.

5. CONCLUSIONS

Some aspects concerning the stability of reference frame, in particular when dealing with structural monitoring, have been investigated in this work. The monitoring of an historical tower, the Garisenda tower located in Bologna (Italy), has been selected as a case study. Four GNSS dual frequency permanent stations are available in an area of about a 2 km from the tower. The four stations have been considered as RS in single base data processing, to obtain four time series of the MS; the four solutions are expected to be consistent and independent from the RS. Under the hypothesis of stable RS, the results show significant differences, both in terms of mean velocity and in terms of internal variability; the differences are also shown by low values of Pearson's correlation coefficient, calculated between each solution and the solutions obtained by BOLI RS. These results seem to indicate that the initial hypothesis of stability of the RS affects the solutions, which may represent not only any possible displacements of the monitored structure but also possible movements of the RS. In order to consider this aspect, each RS has been processed using PPP approach and synthetic models of each RS movements have been performed. Each model has been applied to the time series of the MS obtained by the first data processing. The new time series show improvements in terms of mean velocity and signals, additionally, the improvements are supported by an overall increase in Pearson correlation coefficients. Obviously, since the models have been generated from a PPP solution of each RS, the synthetic models are referred to an ITRS reference frame and have been subsequently aligned to the ETRS89 reference frame, applying transformation parameters. In the ETRF2000, the coordinates are not characterized by a zero-velocity but by an average velocity that represents the residual intraplate velocity of the area. Therefore, the MS is characterized by a velocity that can be intended as vectorial sum of two components: the structural movement vector and the intraplate residual velocity vector. In this case, the velocity of the MS is about 3.3, 2.8, 1.4 mm/y in North, East and Up component respectively and it is consistent with the intraplate residual velocity. Removing the weighted average velocity derived by all the RS from the velocity of the MS, the resulting velocity can be regarded as close to the real structural movements and, in our case, the results seem to indicate that this velocity is not significant.

The adopted approach can be particularly important for the investigation of very small and slow movements; when the entity of movements is very high, in studies of movements of a structure or a part of territory, such as landslides, these considerations represent a second order problem.

Concerning structural monitoring for early warning applications, boundary conditions are known to influence the quality of a GNSS solution. In particular, multipath effects or reduced sky visibility can generate daily biases in the kinematic solutions. In this work, a strategy for improving the repeatability of a GNSS solution for monitoring purposes has been evaluated. The strategy is based on subtracting an empirical model from the kinematic solution. The model can be estimated on the basis of the 7 preceding daily solutions. In order to evaluate the improvements achieved by this approach, a test has been performed using a GNSS receiver located on top of the Garisenda tower, which is overlooked by the adjacent Asinelli tower. The obtained results showed that it is possible to improve the solutions by about 20% in terms of scatter. The standard

deviations of the residual time series were 4.4, 2.9, 6.9 mm in the North, East and Up components, respectively, as opposed to 6.4, 3.4, 8.6 mm when the data were unfiltered. This improvement increases the sensitivity of the monitoring system in defining a minimum threshold of significant movement, thus improving its accuracy.

In particular, the system is able to detect movements of about 1 cm in planimetry and 2 cm in height. In fact, considering the mean square errors and an alternative hypothesis of the movement significance to 3σ takes around threshold values of 13.2, 8.7, 20.7 mm for ΔN components, ΔE and Δh .

The proposed method can be easily implemented also for real-time solutions, useful in early warning systems. Moreover, this approach can improve the solution in the presence of non-optimal boundary conditions. The number of days used to generate the models and the number of epochs considered in the running average have to be determined on a case-by-case basis.

REFERENCES

- Baraccani, S., Gasparini, G., Palermo, M., Silvestri, S., Trombetti, T. (2014). A Possible Interpretation of Data acquired from Monitoring Systems. In B.H.V. Topping and P. Iványi (Ed.), Twelfth International Conference on Computational Structures Technology (pp. 1–12). Stirlingshire, Scotland: Civil-Comp Press.
- Barbarella, M., Gandolfi, S., Poluzzi, L., Tavasci, L. (2013). Il monitoraggio della rete Rete Dinamica Nazionale dal 2009 al 2013. In Conferenza Nazionale ASITA (pp. 95–102). Centro Congressi – Riva del Garda, Italy.
- Barbarella, M., Gandolfi, S., Cacciamani, L., Poluzzi, L. (2016). Stability of the reference frame for structural monitoring applications using GNSS. In FIG Working Week 2016. Christchurch (NZ).
- Bisnath, S., Gao, Y. (2009). Current state of precise point positioning and future prospects and limitations. *Observing Our Changing Earth*. Gandolfi, S., Poluzzi, L., Tavasci, L. (2015). Structural Monitoring Using GNSS Technology and Sequential Filtering. (May 2015), 17–21.
- Blewitt, G., Hammond, W. C., Kreemer, C., Plag, H.-P., Stein, S., Okal, E. (2009). GPS for real-time earthquake source determination and tsunami warning systems. *Journal of Geodesy*, 83(3–4), 335–343. <http://doi.org/10.1007/s00190-008-0262-5>
- Bock, Y., Nikolaidis, R. M., de Jonge, P. J., Bevis, M. (2000). Instantaneous geodetic positioning at medium distances with the Global Positioning System. *Journal of Geophysical Research*, 105(B12), 28223. <http://doi.org/10.1029/2000JB900268>
- Boucher, C., Altamimi, Z. (2011). Memo: Specifications for reference frame fixing in the analysis of a EUREF GPS campaign.
- Cliff, A., Ord, J. (1973). Spatial autocorrelation.
- Dach, R., Lutz, S., Walser, P., Fridez, P. (2015). Bernese GNSS Software Version 5.2.
- Forward, T., Stewart, M. P., Tsakiri, M. (2003). Gps Data Stacking for Small Scale Gps Deformation Monitoring Applications.
- Gandolfi, S., Poluzzi, L., Tavasci, L. (2015a). Structural Monitoring Using GNSS Technology and Sequential Filtering. In FIG Working Week 2015. Sofia (BG).
- Gandolfi, S., Tavasci, L., Poluzzi, L. (2015b). Improved PPP performance in regional networks. *GPS Solutions*, 1–13.
- Giordano, F. (2000). La torre Garisenda. (Costa, Ed.). Bologna: Fondazione del Monte di Bologna e Ravenna.
- Griffiths, J., Ray, J. R. (2009). On the precision and accuracy of IGS orbits. *Journal of Geodesy*, 83(3–4), 277–287.
- Herring, T., King, R., McClusky, S. (2006). GAMIT reference manual. GPS Analysis at MIT, Release.
- Pearson, K. (1895). Note on regression and inheritance in the case of two parents. *Proceedings of the Royal Society of London*.
- Radovanovic, R. (2000). High accuracy deformation monitoring via multipath mitigation by day-to-day correlation analysis. 13th International Technical Meeting.
- Ragheb, A. E., Clarke, P. J., Edwards, S. J. (2007). GPS sidereal filtering: coordinate- and carrier-phase-level strategies. *Journal of Geodesy*, 81(5), 325–335. <http://doi.org/10.1007/s00190-006-0113-1>
- Realini, E., Reguzzoni, M. (2013). goGPS: open source software for enhancing the accuracy of low-cost receivers by single-frequency relative kinematic positioning. *Measurement Science and Technology*.
- Takasu, T. (2011). RTKLIB: An open source program package for GNSS positioning. 2011-06 11). [2011-07-20]. <http://www.rtklib.com/prog/>
- Webb, F. H., Zumberge, J. F. (1993). An introduction to GIPSY. OASIS-II, JPL Publ., D-11088.
- Wübbena, G., Bagge, A., Boettcher, G., Schmitz, M., Garbsen, D., Andree, P. (2001). Permanent Object Monitoring with GPS with 1 Millimeter Accuracy. *Millimeter*, 1000–1008.

THE USE OF GEODETIC REFERENCE FRAMES FOR MODERN GNSS SURVEYS

L. Tavasci

University of Bologna, School of Architecture and Engineering, Department of Civil, Chemical, Environmental and Materials Engineering - DICAM
Viale del Risorgimento 2, Bologna, Italy
luca.tavasci2@unibo.it

KEY WORDS: PPP, Geodetic Network, GPS-7, NRTK, Reference Frame, RDN, ETRF2000

ABSTRACT:

In the last decades many new surveying techniques have become available, each characterized by a specific accuracy and field of application. At the same time new complex databases have been developed with the aim to overlay different representations of the territory, in many cases derived from different kinds of survey. Consequently, it grew the need to use for the higher number of applications the same common reference system in order to “speak the same language”. In particular in Italy there is a ministerial decree that states that is mandatory for all the public administrations to use an official reference frame, being it the ETRF2000 at the epoch 2008.0. Therefore, is of the major importance for every surveyor to have methods and infrastructures allowing him to properly refer its coordinates to the official reference frame. In this paper it has been analyzed the way to provide a reliable access to the official reference frame for all those applications where the sub-centimeter accuracy is not requested, whilst one of the most important aspects is the reduction of the time needed for the survey. The PPP technique has been considered, being it one of the most important innovations of the last decades in geodesy, but it has been done under the light of a future use for technical applications, thus considering observing-sessions of few hours (24, 12, 6, 3, 1, 1/2). Being PPP solutions natively aligned to the global reference frame, which is properly linked to the other intra-plate reference frames. Therefore, this technique allows a direct access to all the well defined reference systems for which are known the transformation parameters with respect to the others. Furthermore, despite the longer observation time needed to reach the centimeter level accuracy, PPP may have some advantage in particular in certain remote areas or in particular catastrophic scenarios. Looking at the more classic GNSS applications, have been evaluated the actual precisions that one could reach by using the NRTK technique, and some possible critical issues. After several tests this technique has demonstrated to be a powerful tool that allows to reach few-centimeter accuracy after less than ten minutes of measuring in good working conditions. Nevertheless, NRTK has shown some critical aspects that force not to rely completely on this technique. The passive geodetic reference networks materialized on the ground have been considered as a complement of the NRTK infrastructures to support every kind of GNSS survey, being it done with NRTK or with a classical static post-processing or RTK techniques.

1. INTRODUCTION

In the earlier decades of the past century the geodetic reference frames were constituted by a set of points materialized on the ground. These points were specifically designed and included in different networks depending on the specific purpose: the definition of planimetric coordinates or the height. All these networks were passive, with the needs to be measured repeatedly over time by means of terrestrial surveys. This aspect has restricted the spatial extension of these geodetic networks that covered local areas only, of different extensions and relevance.

With the advent of the GNSS technique a new kind of reference networks has become necessary and possible at the same time. GNSS provide three-dimensional coordinates at once, thus the new reference networks are realized for both planimetric and height purposes. It must be said that GNSS coordinates relates to a geometric shape (the ellipsoid) rather than to the gravity field. For this reason the ellipsoidal height measured using satellite technology is a geometric dimension unusable for most applications for that is necessary to convert the orthometric height through a model of the undulation of the geoid.

The reference networks measured through GNSS observations do not have any limitations in their spatial extension and could be of two different types: the ones that we hereafter call “passive frames” and the one that we will call “active frames”. As “passive” we refer to such networks made of points materialized on the ground in places where is possible to put a GNSS receiver and acquire good observations. These points are left without instrumentations after their measurement and it is

possible for everyone to re-occupy the point with own instruments for survey purposes. The managing institute of a passive reference network must calculate the coordinates of the frame and provide the users of the monograph for each point also reporting the coordinates and the reference system to that are referred. The managing institute of a passive reference network must calculate the coordinates of the frame and provide monographs to the users. Each of these should at least indicate the coordinates and the reference system to that are referred, together with all the information useful to find the point on the ground. As “active network” we will refer to those frames constituted by permanent GNSS stations continuously acquiring satellite data. The points of these networks are not available for the users to set up their own instruments, but data collected by the permanent stations are made available in a standard format as RINEX (Receiver Independent Exchange Format) files.

The most important reference frame available is actually the ITRF (International Terrestrial Reference Frame) that realize the global reference system ITRS (International Terrestrial Reference System) which is ideally linked to the earth center of mass and its rotation axis. ITRF is monitored through the IGS tracking network which is constituted by hundreds of GNSS permanent stations worldwide distributed, together with other spatial techniques (VLBI, SLR, Doris). The global reference frames, of which ITRF is the most accurate one, are fundamental for the defining of the satellite orbits and clocks (ephemerids), but are also very important as common reference to represent coherently the whole world and compare coordinates between different continents.

Is important to be noticed that all the modern reference frames monitored through permanent stations are defined not only as clusters of coordinates but also as clusters of mean velocities referred to each site. This allows to correctly represent over the time the positions of the monitored points, that are following the crustal deformations. Such deformations often have magnitude up to several centimeters that if not considered leads to obsolescence the coordinate of a reference frame after very few years.

On the one hand the reference coordinates must change over time in order to represent the real state, on the other hand changing coordinates are not suitable for many local applications such as cartography. For this reason ITRF is not the only frame defined and officially adopted as reference by national geographic services; in spite of it were defined other dynamic reference systems that are linked to one specific tectonic plate. For instance, the ETRS89 is a reference system linked to the Eurasian tectonic plate (coincident to ITRS at epoch 1989.0) and defined through the ETRF2000 (European Terrestrial Reference Frame). By using ETRF instead of ITRF the coordinates remain more stable (even less than a mm/year of change rate) over time, but are no longer comparable directly to coordinates of points that lie on other continents. This causes no matters until is known the relation between the global and the regional reference system, defined through proper transformation parameters that can be easily applied to the coordinates.

Have available a reliable and accurate reference frame is crucial in order to share geographic information with a “common language”. This became truer because of a number of new surveying techniques, spatial or terrestrial, that allow to acquire a great amount of geometric data in few time and with different accuracies and space extensions. Moreover, the regional services managing the topographic representation of the territory are increasingly interested in having advanced databases that include all the surveys available and acquired in different epochs.

The modern GNSS surveys may be divided in two types: the ones that require to the surveyors to know the coordinates of at least one point to be measured together with the others, and the ones for which a surveyor gets directly the coordinates of the new measured points expressed in a known reference system. Into the first type there are the “classic” surveys based on the calculation of the carrier phase differences in post-processing or the RTK (Real Time Kinematic) surveys. For the first ones the reference coordinates of one or more points are needed in order to align the network (or the baseline) to the reference frame, whereas for the RTK technique the master station must be installed onto a point of known coordinates which permits access to the reference frame. In the second category there are survey techniques such as NRTK (Network RTK) or the PPP (Precise Point Positioning). The NRTK technique allows the surveyor to operate with just one GNSS receiver, obtaining accurate coordinates thanks to the spatial corrections forwarded by a real time service based on a network of permanent stations located in the area. The coordinates obtained in the survey are expressed in the same reference frame to which are aligned the permanent stations of the network.

All the above mentioned GNSS techniques are based on a relative approach: the position of the receivers are calculated as tridimensional differences with respect to other receivers on the ground. The PPP technique is based on the mathematical modeling of the main spatial-correlated errors affecting the GNSS observations and the use of both carrier phases and code signals. The peculiarity of PPP is to provide accurate coordinates of a single stand-alone receiver expressed in the same reference system used to define the satellite ephemerids. To do this, precise orbits and clock products are necessary.

Nevertheless, the obtained coordinates have the same accuracy than the ones obtainable using relative approaches, or even better. This is surely true if considering data acquired for 24 hours as ones provided by permanent stations and, together with the capability to overlook the relative distances between the stations, this made PPP a widely used tool for the monitoring of permanent tracking networks.

Finally, as to be noticed that for the GNSS techniques of the first type there are clear and reliable information in literature concerning the accuracy that can be obtained depending on the time of the observing session and the relative distance between the receivers. Instead, for NRTK and for PPP are not so clear the actual precisions that one can obtain through these techniques, and this has been one of the main aspect addressed in this work. In the first section it has been analyzed the PPP as a possible survey tool for more technical applications that ones related to permanent stations, in particular evaluating the performances at the change of the observing-session time span. Particular attention has been paid on the detection of the outlier solutions, which is critical aspect of a technique where every solution is quite independent from the others and any adjustment is possible. In the second section the geodetic networks nowadays present on the territory have been analyzed. The actual performances of the NRTK were evaluated and the possible integration of such services with the passive networks available on the territory has been analyzed.

2. PRECISE POINT POSITIONING FOR SURVEYS

PPP has demonstrated to provide a repeatability of the measures of less than one centimeter (Gandolfi et al. 2016) if considering the daily RINEX files provided by permanent stations. Otherwise, technical surveys require for observing sessions as short as possible in order to contain the costs and improve the productivity. Compared to the other GNSS techniques the PPP have the advantages to require less instrumentations (only one GNSS geodetic class receiver) and to be completely independent from any geodetic infrastructure on the ground: passive reference networks, NRTK networks, internet or radio connectivity etc. On the other hand PPP require for post processed products (ephemerids and modeling parameters) available only after few days from the survey, but above all are not clear the performances that PPP can provide for few hours of observing-sessions. The idea has been to split a 24 hour RINEX file into several ones of shorter time spans, in particular: 12, 6, 3 hours, 1 hour and ½ hour. This was done using the TEQC free software package (Estey and Meertens 1999) and each of the obtained RINEX file simulates an independent survey of the same point.

2.1 Dataset and PPP processing

In order to have a good consistency of the dataset and perform reliable statistical analysis it has been considered one year (2013) of daily RINEX files provided by 14 permanent stations located in and around Italy (Figure 1). All these stations belong to the EPN (European Permanent Network) (Bruyninx et al. 2001) and have available reference solutions expressed in the IGB08 (EPN_A_IGB08.SNX) that we used to verify if the PPP solutions are biased with respect to the reference frame. Table 1 reports the number of RINEX files obtained for each considered time span.

The about 445000 file composing the whole dataset were processed using the PPP approach by means of the GIPSY OASIS II software package developed by the JPL (Jet Propulsion Laboratory – NASA) version 6.3 (Webb and

Zumberge 1997). This software allows obtain ambiguity fixed solutions through the WLPB algorithm (Bertiger et al. 2010) and the use of proper products made available by JPL.

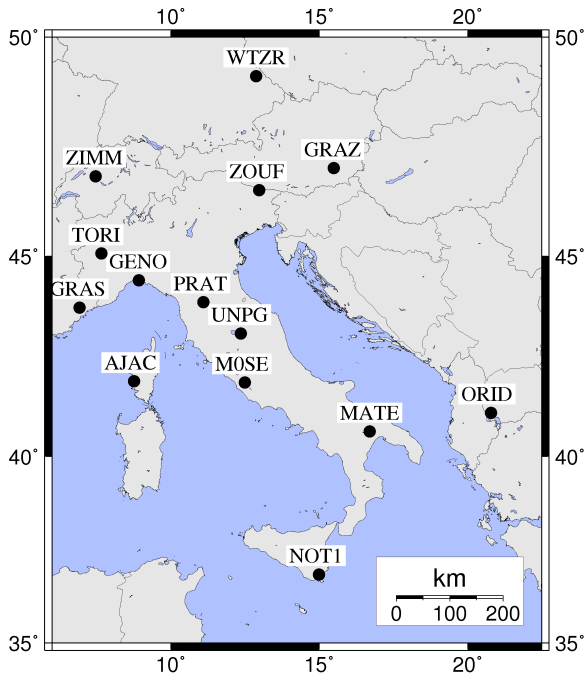


Figure 1 – Location of the 14 EPN permanent stations that provided the analyzed dataset.

For this calculation standard parameters for static processing were selected together with the WMF-1 (Kouba 2008) troposphere model. Post processed orbits linked to the IGB08 were used, thus all the PPP solutions are aligned to this reference frame.

For each station	
RINEX time span	no. of RINEX files
24 hours	365
12 hours	730
6 hours	1460
3 hours	2920
1 hour	8760
½ hour	17520

Table 1 – Number of RINEX files produced and calculated for each of the considered time spans.

2.2 First results and outliers detection

The coordinates of the PPP solutions were firstly compared to the official reference IGB08 positions and in Tab. 2 are reported the mean of the differences between each solution and the reference ant the corresponding epoch. Mean biases reach the centimeter level only for the solutions related to ½ hour time span, that are also the more scattered. In the other cases the PPP solutions can be considered substantially not biased with respect

to the reference frame, it's true especially if considering that IGB08 was not exactly up to date for the year 2013.

Obs. time	Mean of the differences S_{kj} with respect to the IGB08 reference solutions (mm)		
	n	e	u
½ h	2.7	13.0	6.7
1 h	2.4	3.7	5.6
3 h	2.5	1.0	4.8
6 h	2.5	0.8	4.9
12 h	2.7	0.9	4.7
24 h	2.8	0.9	4.6

Table 2 – Mean biases of the PPP solutions with respect to the formal IGB08 SINEX solutions. The values are reported separately for each of the considered observing-session time spans.

The aim of the work was to verify the actual precision of the PPP in terms of repeatability of the measures. For this purpose a reference position of each site was needed. Such reference must not be influenced by seasonal movements or biases, thus a model of the position for each site has been estimated based on the more precise solutions, that are the ones obtained for the 24 hours files. These models were estimated through the expression:

$$mod(t) = q + t * m + \sum_{i=1}^5 [A_i \sin(2\pi f_i * t) + B_i \cos(2\pi f_i * t)]$$

where q and m are the intercept and the slope of a the regression line, whereas f_i are the 5 most powerful frequencies estimated through the Lomb-Scargle periodogram (Lomb 1976; Scargle 1982). Coefficients A_i and B_i represent the amplitude of the sine waves related to each of the 5 frequencies found out. Figure 2 show the wave part of the calculated models divided for each topocentric component.

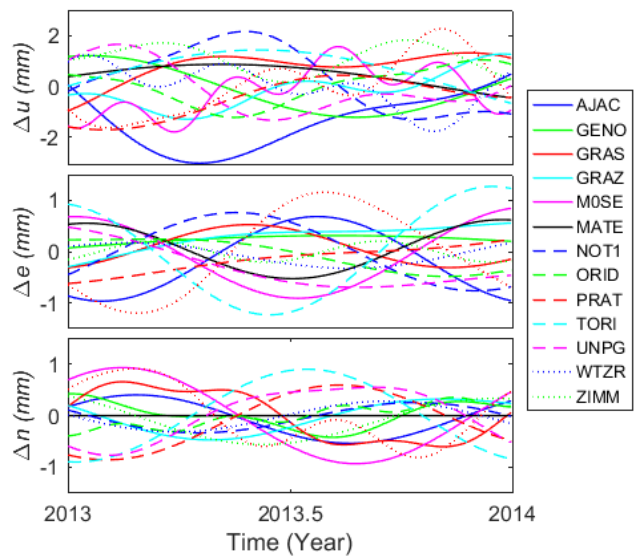


Figure 2 – Representation of the seasonal part of the reference models for each time series of coordinates of the 14 considered sites.

For each PPP solution was calculated the residual value v of the coordinates with respect to the related position model at the corresponding time. These residuals represent best estimation of the “real error” of the obtained coordinates. Note that v can be calculated only having a consistent time series and this information is not available in the case of technical survey. Nevertheless, the GIPSY software provides an estimated formal error for each solution, which is the only available tool that a surveyor can have for judge the quality of its measure. The first point addressed has been to evaluate the percentage of cases where the PPP solutions are completely wrong by looking at the formal error provided by GIPSY. This can be done only setting a threshold value that defines what is “wrong”. Clearly this threshold depends on the specific application of each survey that is impossible to define a priori. In an arbitrary way it has been considered as “wrong” each solution that may have an error higher than 30 cm. Thus it was estimated the percentage of

solutions having a formal error minor than 10 cm, meaning the statistical probability of 99,7% to have the error within three time this threshold supposing a normal distribution of the errors. Table 3 reports the percentages of wrong solutions that are very small with the exception of the ½ hour solutions. The NOT1 station is the only one showing a behavior different respect to the others. All the “wrong” solutions were removed from the dataset.

A critical case that may occur is that a solution with a residual v higher than 30 cm, thus “wrong”, is not recognizable through the formal error. The percentage of solutions with a formal error minor than 10 cm but having a real error higher than 30 cm is null for all the time spans higher than 1 hour, and still remain within 0.5% even for the shorter observing-sessions. Also these solutions were rejected from the dataset for the further analysis.

Obs. time	AJAC	GENO	GRAS	GRAZ	MOSE	MATE	NOT1	ORID	PRAT	TORI	UNPG	WTZR	ZIMM	ZOUF	Mean Value
24 h	0.0	0.0	0.0	0.0	0.0	0.0	0.0	0.0	0.0	0.0	0.0	0.0	0.0	0.0	0.0
12 h	0.0	0.0	0.0	0.0	0.0	0.0	0.5	0.0	0.0	0.0	0.0	0.1	0.0	0.0	0.0
6 h	0.0	0.0	0.0	0.0	0.0	0.0	1.0	0.0	0.0	0.0	0.1	0.1	0.0	0.0	0.1
3 h	0.0	0.0	0.0	0.0	0.0	0.0	2.1	0.0	0.0	0.0	0.1	0.1	0.0	0.0	0.2
1 h	0.0	2.3	0.0	0.1	0.2	1.0	13.5	0.0	0.1	0.9	0.1	0.1	0.0	0.1	1.3
½ h	41.3	86.0	45.3	33.8	39.0	73.0	88.7	43.7	65.6	76.4	55.8	28.7	44.5	55.8	55.5

Table 3 – Percentages of the solutions having a formal error higher than 10 centimeters and thus considered outliers.

2.3 Precision of the PPP for short observing-sessions

After having rejected the outlier solutions, the RMS of each time series of the residuals v has been calculated. These values were averaged on the 14 considered stations and Figure 3 shows the mean RMS of the residuals divided for each observing-session time span and for the three topocentric components.

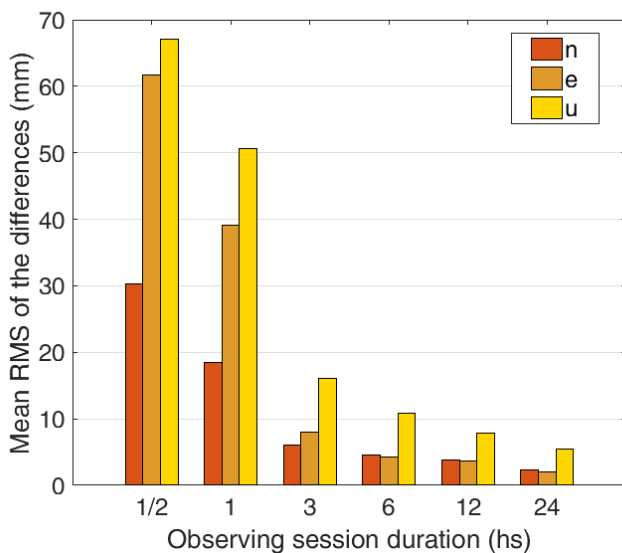


Figure 3 – Precision of the PPP solutions for the observing-session time spans considered in the test. Values are referred to the RMS of the residuals with respect to reference values and are averaged on the 14 considered stations.

The PPP confirms a very high precision, which is under one centimeter in for the plan if considering observing-sessions at least 3 hours long. Precision is worsening for the shorter observing-sessions, but still remain under the 5 centimeters for one hour of observations and 10 centimeters for ½ hour.

As shown in the above section the formal error given by the software is a quite efficient tool for the detection of the wrong solutions, but had to be evaluated the actual reliability of this parameter for the estimation of the real precision of a PPP solution. In Table 4 are reported the percentages of the solutions having a residual higher than three time the GIPSY formal error. The formal error seems to underrate the real error in a very high percentage of cases, especially for observing-sessions longer than three hours. For the shorter time spans, the lower number of observations reduces the redundancy of the equations and the software takes into account this fact increasing the formal error that is thus more reliable for the less precise solutions.

Obs. time	Solution with a residual $v_{kj} >$ than $3\sigma_{ppp}$		
	N	E	U
0.5	1%	1%	1%
1	22%	24%	19%
3	31%	28%	24%
6	41%	35%	28%
12	51%	40%	31%
24	47%	44%	36%

Table 4 – Percentages of the solutions having errors underrated by the formal error given by the software.

The precision of the PPP for very short observing-sessions is not yet at the same level of what can be achieved using relative GNSS positioning. Nevertheless, with at least three hours of

observations is possible to reach accuracies at the centimeter level that can be suitable for many technical applications. An example of scenario where the PPP may have a major advantage with respect to other techniques is after a catastrophic natural event that compromises the geodetic networks present on the ground. If the signs of a passive network are removed or the reference stations of a permanent network change their coordinates as for certain earthquakes, then it can be possible to define new reference points with an actual accuracy of few centimeters by doing 3 hours of observing-sessions and a PPP processing. This is even more truth for remote areas where GNSS infrastructures are not present and in case of disasters it become important to monitoring the territory in fewer time as possible after the event.

3. A SYNERGY BETWEEN CLASSIC AND NRTK GEODETIC NETWORKS

During the last decade the development of topographic databases that allow the integration of many different geographic data has contributed to increase the need of a common reference for all the surveys. In Italy, a ministerial decree states that since 2012 all the public administrations must use the ETRF89 as reference system, and in particular the reference frame ETRF2000 at epoch 2008.0, for all the geographic applications. Moreover, looking for instance at the case of Regione Emilia-Romagna (RER), is rising the need to update the technic cartography through small local surveys on the changing areas instead of using the more expensive extensive techniques such as the aerial photogrammetry (MUDE project - <http://www.mude.piemonte.it>). This means that a technician that makes a survey on a newly constructed building must have the possibility to access easily to the same reference frame used to define the cartography that has to be updated with the new data. The geodetic infrastructures nowadays existent onto the RER territory have been considered in order to understand how these

could work together. Two passive GNSS networks are present: the IGM95 and its densification called GPS-7. The first one has been materialized and measured in the nineties and has constituted the fundamental infrastructure in the following years. IGM95 has been measured through a classic GPS post-processing approach and a proper adjustment of the baselines. The distances between its points of about 20 km is not easily suitable for technical surveys, thus a densification of the IGM95 have been conceived and realized during the early 2000s. This network was designed to have a maximum distance between the points of about 7 km and thus called GPS-7. Since the ETRF2000 has been chosen to be the official reference, it was necessary to have a dynamic GNSS permanent network able to monitoring its position with a sub-centimeter level of accuracy. 99 permanent stations already existing in Italy were selected to become the new dynamic reference network RDN (Rete Dinamica Nazionale) and were aligned to the ETRF2000 becoming officially an EPN densification of class B (Citaizone). Four of these stations lie in the RER territory. Both IGM95 and GPS-7 have been linked to RDN and their coordinates were transformed into the new official reference frame. Also a number of unofficial GNSS permanent stations are present in RER, some property of research institutes and some others owned by private companies for commercial purposes. In particular two private networks for real time services are existing: the ItalPOS by Leica Geosystem and the NRTK service of the FoGER foundation. In Figure 4 is shown the overview of the above-cited infrastructures for the case of RER.

3.1 NRTK services: performances and critical aspects

The NRTK technique seems to be the best one to get access to a common reference frame: all the users can measure with a nominal precision of few centimeters coordinates expressed in the reference frame used to align the permanent stations of the network. Surveys can be performed in real time with a single GNSS receiver thus reducing the costs.

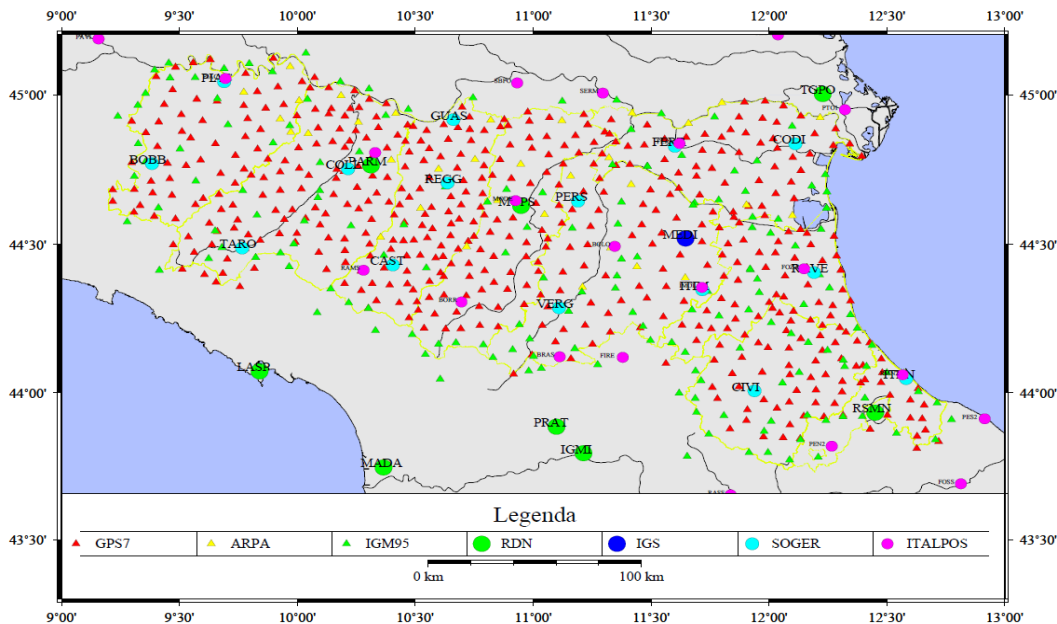


Figure 4 – Overview of the GNSS networks present on the RER territory.

Nevertheless, there are several reasons not to rely on the NRTK technique as the unique tool for accessing a defined reference frame. First of all, a stable internet connection is fundamental

for maintaining fixed the phase ambiguities and reach a reliable positioning. This is not ever possible at the time, especially in some mountainous areas. Furthermore, there is no way for the

surveyor to verify the accuracy of the obtained coordinates and the rightness of the reference frame provided by the NRTK service, because none official protocol obligates the supervisors of the networks to certify these metadata. Moreover, the existing NRTK services are not publics nor legally obligate to keep functioning. This means that these services might cease to exist whenever the owners decide that they are no longer profitable.

In addition to these reasons, very few tests on the actual performances of the NRTK have been performed in the last decades and there are few information concerning the possible malfunctioning of the system and the real obtainable precisions. Therefore, several tests have been performed in order to assess the performances of the NRTK by using the service of the FoGER foundation.

The tests were based on the idea to acquire for hours coordinates estimated through NRTK every 5 seconds on static positions. A single NRTK measure of, as instance, 10 minutes of observations has been assumed that produces the same coordinates of the mean of the coordinates acquired every 5 seconds for the same 10 minutes. Then, by means of moving averages of different time spans, it has been analyzed the impact of a different time of observation on the NRTK solutions.

About 30 hours of observations were acquired in different sessions on three different sites, Bologna, Cesena and Imola, on ad hoc static supports for the antenna. Only the coordinates recorded with a fixed phase ambiguity have been considered. For each site an estimation of the reference position of the measured point was done averaging all the coordinates acquired in all the sessions. The difference of each measure with respect to the reference, representing the error of the solution, was calculated and becomes the object of the further analysis. In the Figures 5-10 are reported the values of these differences: in blue dots refer to single epochs acquired every 5 seconds, whilst the red, green, black, yellow and blue lines represent the moving averages having time spans of respectively 1, 5, 10, 15 and 20 minutes. The Figures here reported are just an example of the whole analysis and are representative of the different behaviors that characterize the whole dataset.

Figure 5 shows a case of stable functioning of the NRTK service. The single epoch solutions have a maximum variation of coordinates of about 4-5 cm. Solutions obtained for one minute of observing-session have similar errors, while for 5 minutes the precision is slightly better.

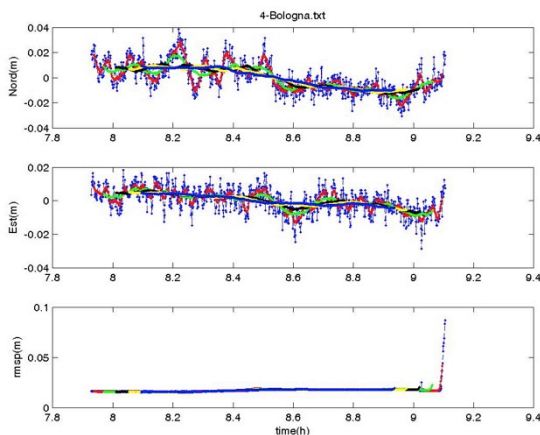


Figure 5 – Time series of the residuals with respect to the reference position for the plan topocentric components of the Bologna test-site. Blue dots represent the single-epoch measures whilst the red, green, black, yellow and blue lines represent respectively the solutions for observing-sessions of 1, 5, 10, 15,

and 20 minutes. The bottom graph represents the plan formal error.

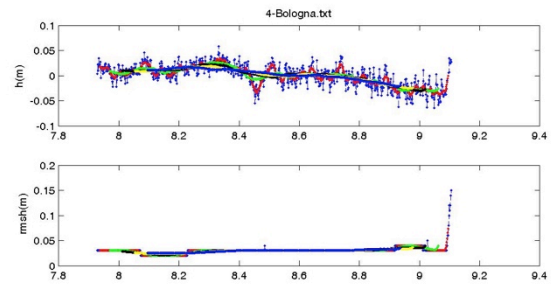


Figure 6 – Time series of the residuals with respect to the reference position for the height component of the Bologna test-site. Blue dots represent the single-epoch measures whilst the red, green, black, yellow and blue lines represent respectively the solutions for observing-sessions of 1, 5, 10, 15, and 20 minutes. The bottom graph represents the plan formal error.

Looking at the black lines is evident how for 10 minutes of observing-session, the coordinate variation is reduced to less than 2 cm, that is quite the same of what obtainable for the time spans of 15 and 20 minutes.

In the Figure 7 is reported a case where the NRTK solutions are less stable: the variability of the coordinates obtained for a single epoch is about 10 centimeters and, again, is evident how ten minutes of observing-session are strongly improving the stability of the obtained coordinates. In this case, also if using 20 minutes observations the coordinates have a maximum variation of about 5 cm during the 2 hours concerning this test session. The bottom image represents the formal error given by the instrument, that in this case shows to be a quite good estimation of the real error.

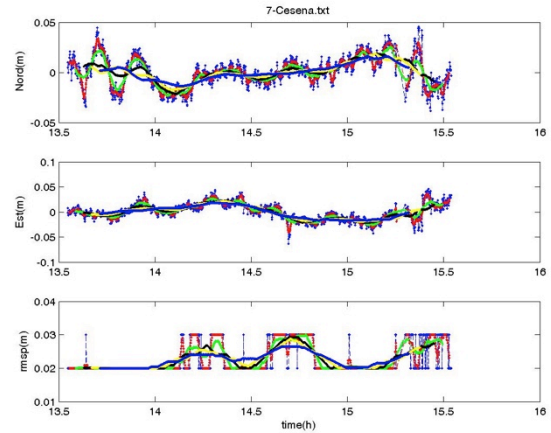


Figure 7 – Time series of the residuals with respect to the reference position for the plan topocentric components of the Cesena test-site. Blue dots represent the single-epoch measures whilst the red, green, black, yellow and blue lines represent respectively the solutions for observing-sessions of 1, 5, 10, 15, and 20 minutes. The bottom graph represents the plan formal error.

The Figure 9 is showing an example of critical functioning of the NRTK. Keeping in mind that only solutions having fixed ambiguities are considered, is evident that some of these have errors of about one meter. Also for solutions relating to observing-session of one minute and 5 minutes the errors reach such value. Using 10 minutes of observations, the criticality is

strongly reduced and reaches errors within 10 centimeters. In this case the formal error is not at all representative of the wrong functioning of the service, and this is a critical aspect because a surveyor cannot have any warning on the field that allows him to decide to repeat the measurement.

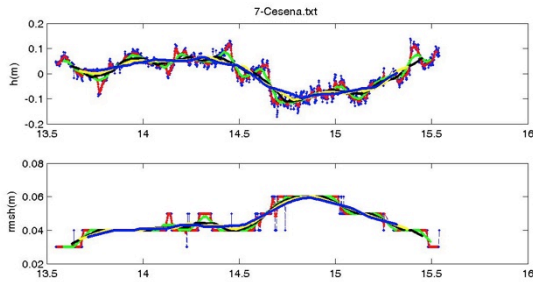


Figure 8 – Time series of the residuals with respect to the reference position for the height component of the Cesena test-site. Blue dots represent the single-epoch measures whilst the red, green, black, yellow and blue lines represent respectively the solutions for observing-sessions of 1, 5, 10, 15, and 20 minutes. The bottom graph represents the plan formal error.

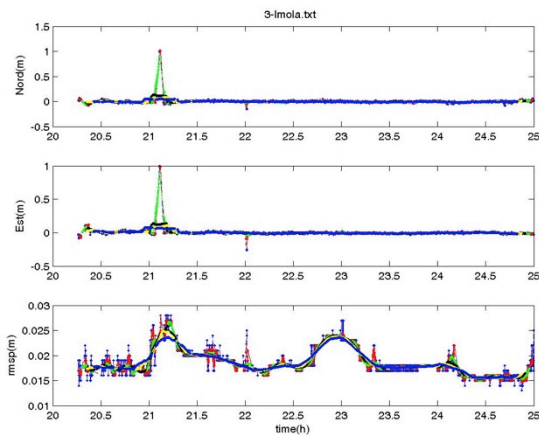


Figure 9 – Time series of the residuals with respect to the reference position for the plan topocentric components of the Imola test-site. Blue dots represent the single-epoch measures whilst the red, green, black, yellow and blue lines represent respectively the solutions for observing-sessions of 1, 5, 10, 15, and 20 minutes. The bottom graph represents the plan formal error.

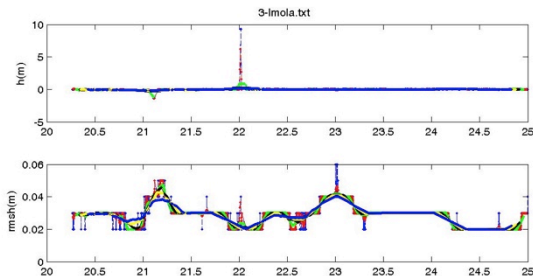


Figure 10 – Time series of the residuals with respect to the reference position for the height component of the Imola test-site. Blue dots represent the single-epoch measures whilst the red, green, black, yellow and blue lines represent respectively the solutions for observing-sessions of 1, 5, 10, 15, and 20 minutes. The bottom graph represents the plan formal error.

The results concerning the height component are reported in Figures 6, 8, 10 and show very similar behaviors of the solutions. As usual for GNSS this component is less precise than the plan ones and, even in good conditions, the estimation of the ellipsoidal height by means of NRTK cannot be trusted with an uncertainty of less than 10-15 cm.

These test results are confirming on the one hand the strength of the NRTK technique that allows a positioning with few centimeters of error by doing just about ten minutes of measuring sessions. On the other hand the tests have evidenced some cases where the use of the NRTK without any other method to check the quality of the positioning may lead to gross errors.

3.2 The use of passive GNSS reference networks as complement of NRTK networks

The passive GNSS networks such as IGM95 or GPS-7 have some strengths with respect to the NRTK networks that have to be considered. First of all, a passive network once that has been measured and calculated has the same accuracy level in every condition. The coordinates loose accuracy after some years because of the crustal movements with respect to the reference system. If using the ETRS89 these deformations are within 5 mm/year (Cenni et Al. 2016) in Italy despite its territory lies at the borders of the Eurasian plate. This means that after some years the coordinates into the monographs must be updated in dependence of the actually requested accuracy. Nevertheless, this should not be a major problem and reliable coordinates with an accuracy of few centimeters can be provided to the users for each point of the network.

Moreover, the passive networks are necessary for the use of the RTK technique, which could be a better choice than NRTK in some cases. For instance, in the areas where Internet connection is not provided or is not stable, RTK allows the precise positioning by using radio transmitters. In the cases where the reference point is close to the survey area the RTK probably achieve better precisions than NRTK, or the same precisions in fewer time. Having available a reference network such as GPS-7, the baseline length could probably be lower than 2 km and for so short distances the two receivers have more probability to see the same set of satellites, reducing the risk to have false fixing of the ambiguities.

Finally, the passive networks nowadays present on the RER territory are owned by the same public administrations that must use the official reference frame for every kind of geographic or cartographic application. This means that a network such as GPS-7 cannot be abandoned for commercial reasons or private interests, and the reference frame to which the coordinates refer cannot be changed without the knowing/permits of the official authority. Therefore, a surveyor who has to certify that its coordinates are referred to the official reference frame, needs only to show the monograph and the coordinates assigned at the master station.

All these aspects are quite complementary to the advantages of the NRTK technique, and the passive networks could be together with the active ones in order to provide the users an easy and reliable access to the reference frame that must be used. The NRTK measurements could be certified to be referred to the correct frame if the surveyor set up its instrument on a GPS-7 point before to move on the survey area. Doing it he can compare the obtained coordinates to the official ones, and if the discards are lower than a certain value it means that the NRTK service is working well and into the correct reference system. The results of the previous section can help defining modalities of this operation and the limiting value to accept or not the measure. A proposal can be to measure the reference point with

a session of 10 minutes and accept a maximum difference between the obtained coordinates and the reference ones of 7-10 centimeters.

The case of rejection could be due to the use of a different reference system for the NRTK service or be due to a malfunctioning of the system or a false fixing of the phase ambiguities. The measure should be repeated after an instrumental restart in order to ensure if the matter concerns the reference system. In such case the two measures must agree within 3-4 centimeters and in absence of alternatives the surveyor can move on two other nearby GPS-7 points and measuring them. Having available a double set of coordinates for the same points is possible to estimate the transformation parameters linking the correct reference system to the one used by the NRTK service.

Once on the survey area, a good practice can be to install a local reference point and measure it twice, checking the difference between the coordinate that should be within 3-4 centimeters, and then measure again this point every time the system is restarted. In such way there is no possibility to perform the survey in presence of strong malfunctioning or false ambiguity fixing.

For all these reasons the passive networks materialized on the ground still have a purpose, but on the other hand is necessary to maintain these infrastructures with proper investments. The points markers can be accidentally removed during road works if not properly signalized, therefore is fundamental to replace the marker as soon as possible because the users must be confident to find the reference points. Another focus could be to provide the users of free digital monographs, well updated and easy to find on the web. Another issue is the need to re measure the point located in the areas that had a strong earthquake event having caused significant displacements. In that case have to be selected carefully the subset of points to be re measured.

In return for this kind of investments there is the possibility to have a reliable tool that provide the base for an homogeneous and coherent use of the most common GNSS techniques as RTK, NRTK and static post-processing.

4. DISCUSSION ON THE USE OF THE GEODETIC REFERENCE FRAMES FOR TECHNICAL SURVEYS

On the one hand a modern reference frame have to be defined with the best accuracy possible at the date in order to better support the most advanced techniques and to be coherent with the shape of the earth crust and its evolutions. Nevertheless, for the technical surveys where sub-centimeter level of accuracy is not a real need, the most important aspect concerning a reference frame is the possibility to refer easily every kind of survey to it.

Many survey concerning buildings and structures still have to be performed through the use of classical terrestrial instrumentation to reach certain details. These instruments are very powerful on restricted areas, but it is not easy to link a survey to a reference frame in absence of a network of points fine enough. The only network actually present in Italy having a number of points high enough is the cadastral one, which is completely biased or deformed with respect to reality.

The best way to get access to the correct reference frame is certainly to materializing one or more local reference points close enough to the survey area. GNSS is surely the most performing technique nowadays available for the measuring of point with relative distances of kilometers. Therefore, is fundamental to provide infrastructures and methods suitable for every type of GNSS positioning.

From a certain point of view, the PPP should be the best technique in order to access a properly defined reference frame as the ETRF: coordinates are directly referred to the global reference frame, which is linked to the ETRS89 through known parameters (Boucher and Altamimi 2011) easily applicable referring to the correct epoch. Nevertheless, the PPP technique is not a common technique and cannot be considered an alternative to the others, at least for the next decade. Moreover, there is a gap in terms of time of observing-session necessary to perform a measure precise enough by means of PPP with respect to other techniques.

The NRTK technique seems to be the best choice at the date: is only necessary to align carefully the permanent stations to the correct reference frame. All the users can measure coordinates expressed into the correct reference using a single receiver, and the working time required is very low. Nevertheless, this approach have some critical aspects discussed in the section 3.1 that suggest that is not a wise choice rely entirely on the NRTK networks for the surveys that must agree with the official reference frame.

The passive reference networks, such as the GPS-7, can still be the basic infrastructure that allows both to perform relative positioning by means of RTK or static post-processing and to control the NRTK surveys. This kind of infrastructures needs for a careful maintenance, but may bring considerable advantages to the community if properly used.

Finally, a mention must be done to the particular and complex case of the Italian territory: on the one hand Italy lies at the borders of the Eurasian plate, thus having non-negligible changes of coordinates even with respect to the ETRS89, while, on the other hand, the official reference frame is actually a static realization of the ETRF2000, being it fixed to the epoch 2008.0. This means that after a certain periods the reference-coordinates become unavoidably incoherent with the reality, both for crustal deformations and for displacements due to earthquakes. After a limited number of years from the definition of the reference-coordinates this is not a real problem for the technical/cartographic applications, but with the improvement of the surveying methods and the available accuracies this will be one of the main issue for the Italian geodesy.

REFERENCES

- Bertiger W, Desai SD, Haines B, Harvey M, Moore AW, Owen S, Weiss JO (2010) Single receiver phase ambiguity resolution with GPS data. *J Geod* 84(5):327–337
- Boucher C, Altamimi Z (2011) Memo: specifications for reference frame fixing in the analysis of a EUREF GPS campaign. [http:// etrs89.ensg.ign.fr/memo-V8.pdf](http://etrs89.ensg.ign.fr/memo-V8.pdf)
- Bruyninx C, Becker M, Stangl G (2001) Regional densification of the IGS in Europe using the EUREF permanent GPS network (EPN). *Phys Chem Earth, Part A* 26(6):531–538
- Cenni N., Belardinelli M.E., Baldi P., Loddo F., Gandolfi S., Poluzzi L., Tavasci L., Mantovani E., Babbucci D., Viti M. 2016. The present Italian kinematic pattern from GNSS data. *Atti del 35° Convegno Nazionale del Gruppo Nazionale di Geofisica della Terra Solida.*
- Estey LH, Meertens CM (1999) TEQC: the multi-purpose toolkit for GPS/GLONASS data. *GPS Solut* 3(1):42–49

Gandolfi S, Tavasci L, Poluzzi L (2016) Improved PPP performance in regional networks. *GPS Solut* 20:485. doi:10.1007/s10291-015-0459-z

Kouba J (2008) Implementation and testing of the gridded Vienna mapping function 1 (VMF1). *J Geod* 82(4–5):193–205

Lomb NR (1976) Least-squares frequency analysis of unequally spaced data. *Astrophys Space Sci* 39(2):447–462

Scargle JD (1982) Studies in astronomical time series analysis. II- Statistical aspects of spectral analysis of unevenly spaced data. *Astrophys J* 263:835–853

Webb FH, Zumberge JF (1997) An introduction to GIPSY/OASIS II. JPL Publication. D-11088, Jet Propulsion Lab, Pasadena



Associazione **U**niversitari di **T**opografia **e** **C**artografia

Sezione Tematica 2 Fotogrammetria e Laser Scanner

*

*Thematic Section 2
Photogrammetry and Laser Scanner*

SURVEY, DIAGNOSIS AND MONITORING OF STRUCTURES AND LAND USING GEOMATICS TECHNIQUES: THEORETICAL AND EXPERIMENTAL ASPECTS

S. Artese

Dept. of Informatics, Modeling, Electronics and System (DIMES), University of Calabria, Cubo 39/C, Via Ponte Pietro Bucci, 87036 Rende (CS), Italy - serena.artese@gmail.com

KEY WORDS: Photogrammetry, Laser Scanner, Structures, Landslides

ABSTRACT:

The Geomatics techniques for the detection and representation of the land and objects have seen an exceptional development in recent years. The applications are innumerable and range from land planning to geophysics, from mitigation of landslide risk to monitoring of artefacts, from cultural heritage to medicine.

With particular regard to the structures and to the land, the technologies used can be divided into three categories: techniques based on the acquisition and processing of images, techniques based on the measurement of angles and distances, and combinations of the foregoing. In the present paper, a series of applications of Geomatics techniques, carried out during the PhD studies of the author, are shown. Finally two new applications for deflection measurement of bridges under dynamic load are presented.

1. INTRODUCTION

The continuing evolution of surveying techniques and 3D modeling, and, more generally, of Geomatics techniques based on sensors and the development of ever more efficient systems for the display of digital data, highlights the added value of the use of these methods in the field of evaluation, diagnosis and monitoring of structures and land.

In particular, there is a growing awareness about the active contribution that these technologies can provide in interpretation, storage, and data archiving and enhancement of detected objects.

The growing role of survey methods and digital three-dimensional modeling, in structural and territorial fields, is confirmed by the growth in demand, and their increasing use at different levels of scale and resolution. Obviously the use of these instruments fits within the coding of a cognitive process, in which particular attention is paid to the integration of both traditional and innovative methods.

In the dissertation, after an overview of Geomatics techniques and their basic theoretical concepts, a series of applications have been shown. In the following, three applications (to Cultural Heritage, structures and land) are described. Finally two new methods (patent pending) for deflection measurement of bridges under dynamic load are presented.

2. INTEGRATION OF 3D SURVEYING TECHNIQUES: THE ESCUELAS PIAS CHURCH IN VALENCIA

In the following example, the operations carried out for the 3D modeling of the Escuelas Pias Church and the results will be described. The surveying was carried out in the framework of activities of the Universitat Politècnica De València (Upv), coordinated by prof. José Luis Lerma García.

2.1 Escuelas Pías Church

The "Escuelas Pías" is a clerical religious order founded in the 17th century by St. José de Calasanz (1557-1648), dedicated to the apostolate and to the education of children and young people, especially the poor (Verdú, 1996). It is the first free public school in Europe. To this order belongs the parish

Church of St. Joaquin, also known as Escuelas Pías Church (Figures 2.1, 2.2), located in the heart of the old town of Valencia (Spain).

Characterized by a central and decagonal plan, the Church was built between 1767 and 1772 under the patronage of the Archbishop of Valencia Andrés Mayoral Alonso de Mella (1738-1769). The project supervisor was the architect Antonio Gilabert (1716-1792). Joseph Puchol started to design the first level between 1767 and 1768. Antonio Gilabert modified the original plans of Puchol, and the ornament turned from Gothic to Baroque style with neoclassical insertions.



Figure 2.1. Iglesia de las Escuelas Pías (Valencia)

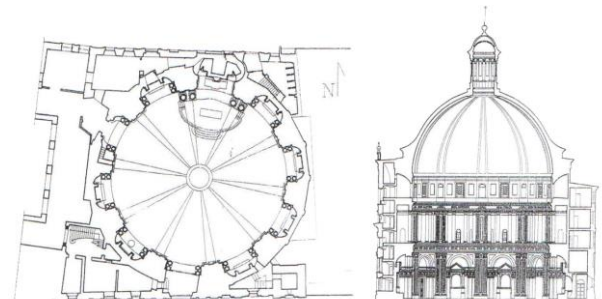


Figure 2.2. Plan and elevation of the Escuelas Pías Church

The Church, with its imposing height of 48 m, is dominated by a large hemispherical dome of about 24 m in diameter surmounted by a lantern with fairing. The dome rests on ten large trapezoid section pillars and ten subsidiary spaces

occupied by several radial chapels. This Church represents a superb example where it is possible to appreciate the Classical turning point dictated by the creation in 1768 of the Real Academia de Bellas Artes de San Carlos, which through its architecture, encouraged the flowering of the Classical Baroque style prevalent from the mid-18th century in the city of Valencia (Cruilles and Monserrat, 1876; Gómez, 1987).

2.2 Surveying operations

For the survey of the Escuelas Pías Church, the FARO Focus3D S 120 was used, one of the present smallest and lightweight 3D laser scanners.

To measure accurately the Church, 40 scans were acquired, with a 0.07°/point resolution at a rate of 120,000 points/s. Spherical targets with a diameter of 14 cm were distributed across the church and at various heights in order to facilitate the alignment of scans in post processing.

In addition to the laser scanner acquisitions, several photos were acquired, in order to obtain a textured 3D model. External survey was carried out using a Leica Scan Station. A survey with a thermal camera was also carried out (Figure 2.3).

The IR shots were used to detect hidden cracks, above all in the dome.



Figure 2.3. The survey with laser scanner and thermal camera

2.3 The Registration: comparison among different software

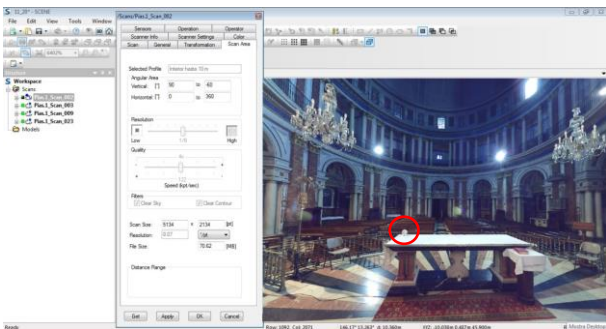


Figure 2.4. Screenshot of FARO Scene®; a spherical target is circled.

Several control points obtained through spherical targets were used inside the church. Global coordinates were not requested; therefore, no geodetic survey was performed.

FARO Scene® software is able to recognize automatically the spherical shape and extract its center as the point of binding (Figure 2.4).

The procedure to register can be summarized in the following

steps: (1) identification of the position of the targets in the various scans; (2) identification of at least 3 common targets between 2 scans; (3) assignment to targets of the same nomenclature for each scan; (4) union of scans that have at least 3 common target with the same nomenclature; (5) creation of a group of aligned scans.

In this case study, four scans were aligned using the four visible spherical targets. The same coordinates were used in three different software packages in order to compare the results. The coordinates of the targets were obtained with FARO Scene.

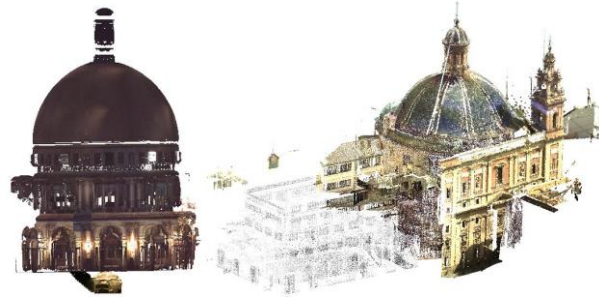


Figure 2.5: Aligned scans.

FARO Scene®: In FARO Scene it is possible to use different types of reference objects to register. Spherical targets were extracted manually by selecting the points corresponding to each target scan and performing an optimization. In this way the coordinates of the targets in different scans were found.

A group of aligned scans with a standard deviation of 0.002 m was achieved.

Leica Cyclone®: Leica Cyclone Register is based on the transformation of a rigid body, in which the estimation of parameters is performed by least squares, following closed form. The calculation of the matrix is carried out through quaternions and their multiplication to define axis and rotation angles as proposed by Horn (Horn, 1987). A standard deviation of 0.0022 m was achieved for the aligned scans.

3DVEM – Register®: 3DVEM – Register is a low-cost and user-friendly software developed for registration of LiDAR datasets by GIFLE at the Polytechnic University of Valencia. The indirect registration method among point clouds and/or 3D models is based on a 3D rigid transformation that is adjusted globally through a virtual reference network. The registration can be solved either by least-squares adjustment or by robust estimators (both Danish Method and Minimum Sum) (Fabado et al., 2013). A standard deviation of 0.0023 m was obtained for the aligned scans. It is worth noticing that 3DVEM – Register reports on the precision estimates of the exterior orientation parameters for each scan. Therefore, it is very easy to confirm the quality of the final registration.

Registration evaluation on the dome: To evaluate the registration performance, meshes were obtained from the registered point clouds. 3DReshaper® software was used for meshing. For each mesh, only the point cloud obtained from the union of registered scans was used, without filling holes and without noise reduction. All this was done in order to have a reference reflecting the point cloud, without arbitrary filters. The comparison between the model and the point cloud, for all three clouds aligned with the three different software packages was made in Geomagic Studio® software (Figure 2.6). The regular intrados dome of the church was used as testing area. The different points-deviations model results are presented below.

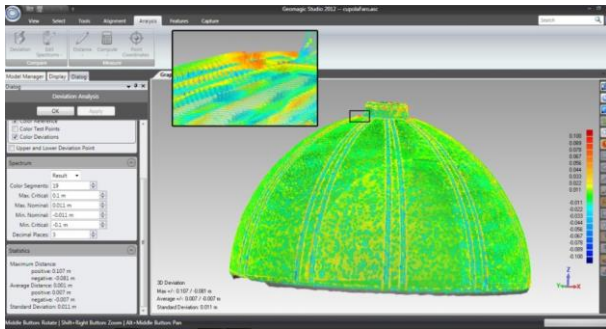


Figure 2.6. Comparison between model and point cloud after FARO Scene

	+ d_{Mean}	- d_{Mean}	d_{Mean}	+ $d_{Max.}$	- $d_{Max.}$	σ_d
Faro Scene	0.007	-0.007	0.001	0.107	-0.081	0.011
Leica Cyclone	0.006	-0.007	0.001	0.092	-0.075	0.011
3DVEM Register	0.006	-0.007	0.001	0.089	-0.079	0.010

Table 2.1. Distance deviations between point clouds and meshes (in m).

The overall comparison can be summarized in the following Table 2.1. Quite similar distance differences are obtained with the three registration software. Only the maximum positive distance achieved with FARO Scene deviates more than both Leica Cyclone and 3DVEM – Register. It is worth noticing that the values are quite comparable, with slightly better results for the 3DVEM – Register software.

Table 2.2 reports on the differences achieved among meshes. The closeness in the output meshes after registration with Leica Cyclone and 3DVEM – Register is evident. In fact, the values are very similar. However, mesh obtained after registration with FARO Scene shows a greater deviation, not only with Leica Cyclone but also with 3DVEM – Register. The values are, in any case, thoroughly acceptable, given the accuracy of the instrument used and the size of the Church.

	+ d_{Mean}	- d_{Mean}	d_{Mean}	+ $d_{Max.}$	- $d_{Max.}$	σ_d
Scene - Cyclone	0.005	-0.004	0.000	0.085	-0.100	0.007
3DVEM – Scene	0.004	-0.005	0.000	0.072	-0.086	0.007
3DVEM – Cyclone	0.001	-0.001	0.000	0.048	-0.053	0.002

Table 2.2. Comparison between the different results of the deviations mesh-mesh.

In conclusion of the registration step, obtained indirectly by using only spherical targets, we can make the following remarks (Artese et al., 2014):

- The results show a substantial agreement between the three solutions. Noteworthy is the fact that the software 3DVEM®-Register gives the error estimates for each station;
- To have more meaningful results, additional studies should be undertaken with larger datasets regarding both scan positions and different numbers of targets.

2.4 3D model and detection of structural problems

The survey executed by laser scanner highlights some aspects, not yet solved, regarding the form and the building history of the church: first of all, the shape of the dome.

The masonry dome, built by using bricks, was often described erroneously as a hemisphere, similar to the Pantheon. Actually, the dome presents a radial symmetry, but the vertical section is obtained through two circular arches, with a radius of 28.50 m. The building of the dome was very troublesome, due to its large dimensions. In correspondence to several dome slices, some cracks can be observed. Furthermore, the floor presents a slope: it is not clear if the slope is the same as in the original project, or if other problems occurred during construction.

2.4.1 Comparison between actual and ideal shape of the dome – Thermal camera surveying – Cracks on the dome

The results of the laser scanner survey allowed us to obtain the deviations of the dome surface with respect to a likely design surface. It is highly interesting that the deviation between the real surface (best fitting ideal surface) and a bohemian vault (slice of dome), that is the more likely design surface, is at a maximum near the cracks, where these are present.

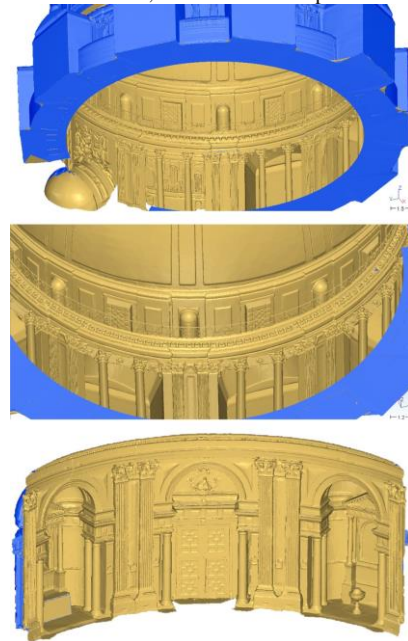


Figure 2.7. Level of detail of the mesh

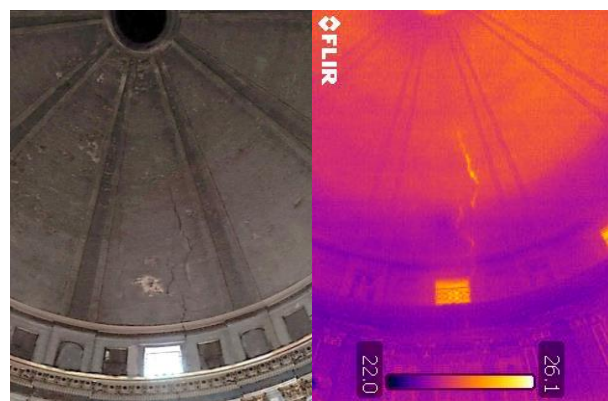


Figure 2.8. The crack on a dome slice and the corresponding thermal image



Figure 2.9. A view of the 3D model textured with the thermal image

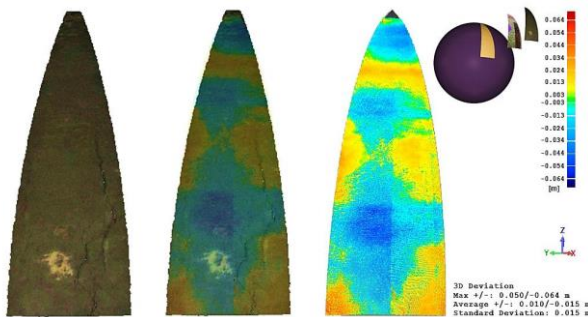


Figure 2.10. The deviations between ideal and actual surface

In the above figures, we can observe: (1) some details of the 3D mesh of the church (Figure 2.7); (2) the crack on a dome slice and the corresponding thermal image (Figure 2.8); (3) the 3D model textured with the thermal image (Figure 2.9); (4) the deviations between ideal and actual surface (Figure 2.10).

2.4.2 The deviations of the symmetry axis

Another question regards the floor and the axis of drum, dome and lantern.

The low slope, present in the floor, is not directed towards the main altar, but has an orthogonal direction, so it is unlikely that it was foreseen in the original project. The axis of the church should give some information useful for hypothesizing the causes of the floor slope.

To find the axis of the church, horizontal sections were obtained on the 3D model every meter; the centroids of the sections, were then found. The most likely axis should be the line that interpolates all centroids. The axis found with the above described procedure shows a deviation of about 0.44 degrees with respect to the vertical (from the floor to the top of the dome). The centroids move in the direction of the transept to the left for an observer looking at the principal altar. The floor of the church has a slope of about 0.137 degrees in the same direction. Since the biaxial compensator of both laser scanners used for the survey has a precision of 0.015 degrees, the slope of the floor is real. Given that the deviation of the axis is to some degree greater than the slope of the floor we could make the following hypotheses: (a) the whole church suffered a subsidence after its realization, (b) due to small errors during

the building, the central axis was not vertical also at the end of its realization.

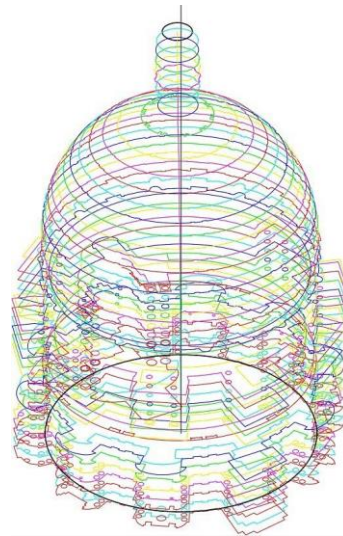


Figure 2.11: Nadiral view and zoom.

Figure 2.11 is an axonometric view (the thin black line is the vertical in the bottom center). The envelope of the horizontal sections centroids is highlighted (Cyan: lower church and drum - Pink: Dome - Yellow: lantern).

It should be noted that the direction of the axis of the lantern is quite different from the one of the church. This is evidenced by the position of the projection of the centroids on a horizontal plane. At this point we can consider as valid both hypotheses about subsidence and small aligning errors. In any event, the data collected and the results of the processing offer useful information to historians of art and to structural engineers for reconstructing the building history and better understanding the origin of the structural problems of the church.

3. THE SURVEY, THE REPRESENTATION AND THE STRUCTURAL MODELING OF ANCIENT AND MODERN BRIDGES

In the last few years, at the SmartLab laboratory at the University of Calabria, activities were developed in the field of surveying, monitoring and representation of structures. In the framework of these activities, Geomatics techniques have been used widely for the surveying of bridges since 2014.

The authorities in charge of maintenance of the road structures (ANAS, Regions, Provinces) have to face different problems for both new and dated structures. In the first case, you have the working plans and the design drawings, so the goal of the surveys is to get the *as built*, to be compared with the project, for testing activities and accounting of work performed, as well as for documentation purposes (Fuchs et al., 2004, Zogg and Ingensand, 2008). In the case of dated structures, very often it is very often not possible to obtain the design documents, so then the survey is also used to reconstruct the manner of execution and disassemble the organism into the structural elements that were considered and dimensioned during the design phase (Lubowiecka et al., 2009). The results of the measurements are used for documentation and representation purposes, as well as for the reconstruction of the constructive procedures. The finite element modeling of the structures was obtained to simulate their behavior in case of earthquake. The analysis of the calculation results allows us to identify the critical parts of the

structures, possibly to be reinforced, and which present the maximum stress. The surveys and representations are used also for the identification of degraded areas or which have detachments of bar coverage, on which we must intervene with actions of recovery and restoration.

An accurate finite element model is used, finally, for the identification of the vibration modes of the structure independently from external stresses, necessary for predicting its behavior under dynamic loads.

The following describes the operations performed for surveying and modeling of a bridge located on a road managed by the Province of Cosenza. It dates back to the 50s of the last century: it is an arch bridge made of reinforced concrete. The survey in this case is aimed at the exact reconstruction of its geometry, the identification of foundation settlement and finite element modeling, to simulate the behavior of the structure under seismic conditions.

3.1 Instruments and methodology

It was decided to use laser scanner technology, with an integrated camera, and a GPS for the georeferencing, in order to acquire large amounts of geometric and photographic data in a short period.

The choice of the laser scanner to perform a survey in a satisfactory manner, with adequate precision and completeness of representation, must take into account, in addition to the mandatory considerations about the accuracy and the flow rate, some other practical-operational features.

Fundamental to this is the evaluation of the number of scans necessary for the complete visibility of all parts of the object to be surveyed, and the conditions in which it must operate to perform the survey. The laser scanner RIEGL VZ 1000 was used, with the following characteristics:

- Accuracy of single point: $\pm 8\text{mm}$.
- Range: from 1m to 1400 m.
- Sampling frequency: until 122.000 points/sec.
- Field of view: 100° (Vertical) - 360° (Horizontal).
- Leveler and magnetometer.
- GPS receiver.
- Nikon D610 Camera with a 20 mm calibrated lens.
- Acquisition of pulse waveform return.

This last characteristic allows us to discriminate the terrain or a object from the vegetation that covers it. The processing of data from the laser scanner was performed with the RiscanPro[®] and Geomagic[®] software.

It must be noted that the laser scanner is equipped with a GNSS receiver which allows just an approximate positioning of the station (single point positioning) with the use of the code and the method of pseudorange, whereby, to obtain an accurate geo-referencing, we used a Leica Viva dual-frequency receiver, capable of receiving the signals from GPS and GLONASS constellation. For the data processing of satellite measurements in differential mode, we made use of data acquired by the permanent station GNSS positioned at the Laboratory of Geomatics, Department of Civil Engineering - University of Calabria, which captures data at a sampling rate of one second. The processing of the acquired data, performed with the Leica Geo Office[®] software, provided the coordinates of the station points with centimeter accuracy.

3.2 The Caprovìdi bridge

The Caprovìdi bridge, in place at S. Angelo, at the town of Cetraro (CS), is located at km 1+900 of Provincial Road number 26. Is a reinforced concrete arch bridge, cast in place,

with two frame piers convergent with the plinths of the supporting arch (Figure 3.1).



Figure 3.1 The Caprovìdi bridge.

Three scans were used (Figure 3.2). Due to the topographic situation, in fact, it was not possible to obtain access to the area on the hydraulic right side of the river, for which some parts were not visible; the thick vegetation was also an obstacle which prevented scanning of some parts of the bridge abutments. Lastly, the support bases of the arch and of the Y piers are covered by backfill terrain. For each scan a partial spatial overlap with the adjacent ones was planned.

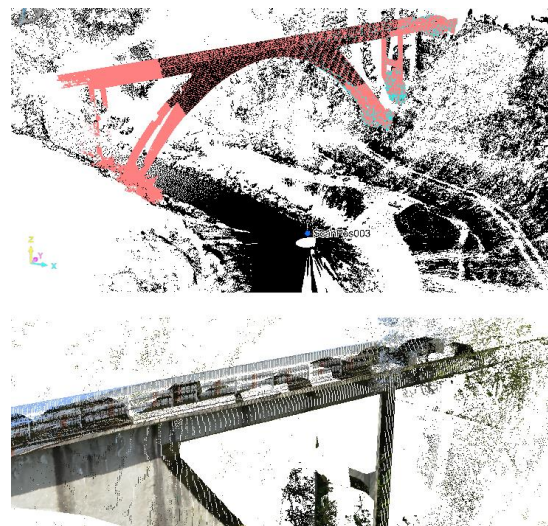


Figure 3.2 Union of scans and detail of a colored point cloud.

Two scans were performed from the two sides of the bridge; for the third acquisition, performed under the deck, the instrument was positioned with an inclination of 90° . Also in this case, some details of the bridge were scanned with more definition. Cylindrical targets were positioned, having a diameter of 14 cm, to facilitate the alignment of the scans in the data processing. The reference system of the first station was used also for the subsequent ones. The targets, having reflecting surface, were positioned in such a way as to be easily and clearly visible in the scans. For accurate georeferencing, acquisitions were used performed by the dual-frequency GNSS receiver, post-processed along with the data collected from the fixed permanent station. The filtering and the reduction of the point clouds was particularly delicate. While having the possibility of discriminating the return pulses, a thorough job on the part of the operator was necessary, since the automatic procedures were influenced by the vegetation and the geometry of the work. In the absence of the project drawings, the survey was aimed at the reconstruction of the structure, but also at obtaining the initial

design (reverse engineering). For this reason, two 3D models were created: the first was obtained directly from the mesh generated after the steps of registration, filtering and decimation; the second one is the geometrically regular model, which should constitute the project work. The first model can be used for documentation, while the second is used as a basis for structural modeling. Recent applications aim at obtaining the finite element model directly from the point cloud (Castellazzi et al., 2015; Vosselman et al., 2004). In figure 3.3, the mesh obtained after the elimination of the vegetation is observed. There is an evident lack of information, especially in the areas of the foundations.

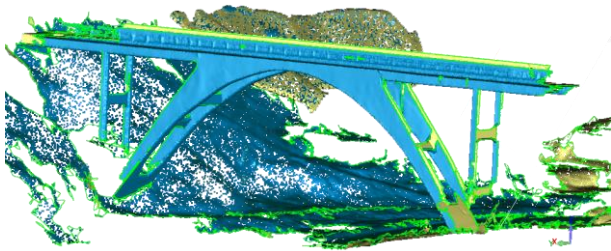


Figure 3.3 Mesh without vegetation.

The on-site investigation and detailed measurements allowed us to integrate the results of the laser scanner survey and to develop the likely geometric model of the project, shown in Figure 3.4 with the main structural elements highlighted in different colors.

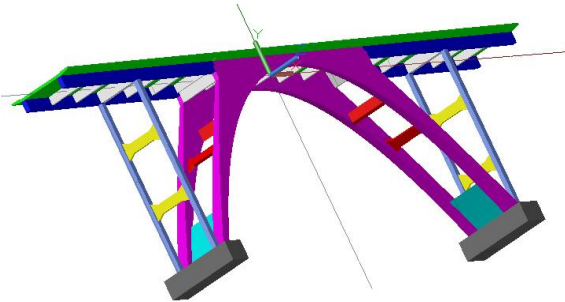


Figure 3.4 The geometric model.

Figure 3.5 shows the deviations between the ideal geometric model and the point cloud. It can be observed that the deviations are typically of centimetric order, within the manufacturing tolerances for this kind of structure (cast on site).



Figure 3.5 Deviations points-model in correspondence to deteriorated areas and vegetation.

The red and blue areas identify irregularities generally due to detachment of material. The very high values of the maximum and minimum deviations are due to the presence of some unfiltered points, automatically assigned by the software to a wrong surface.

During vectorization, we proceeded to eliminate eventual interference between the various simple solids that form the overall volume. The model so obtained, in this case, was used for the dynamic identification, a very useful procedure also for detecting possible damage to the structure.

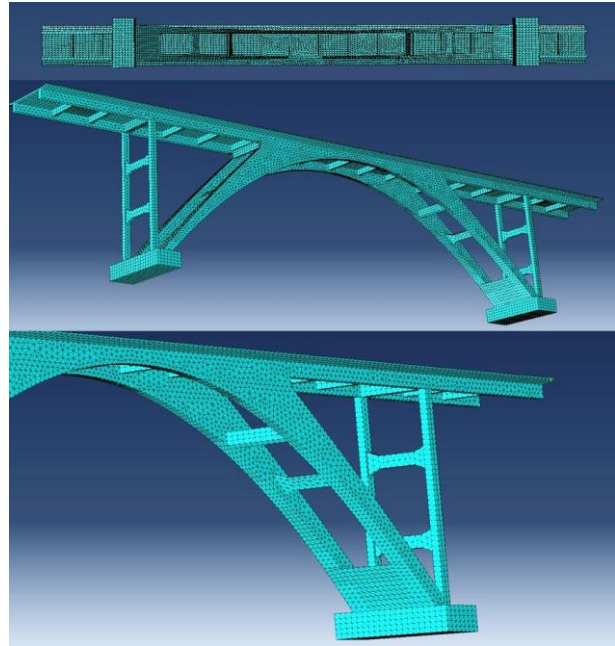
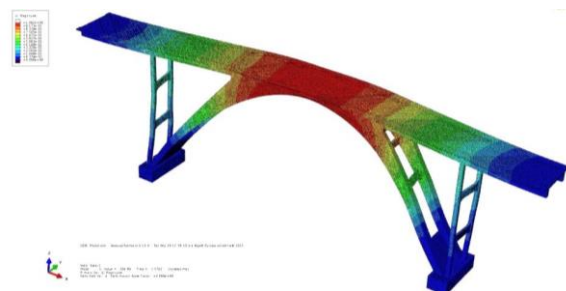


Figure 3.6 Views of the FEM model.

The initial model was transformed into the finite element model (FEM) and analyzed using the Abaqus® (ABAQUS, 2014), structural analysis software which through automatic procedures imports the vectorized graphic model and converts it into a finite element mesh, in this case 4-node tetrahedral elements with only 3 degrees of freedom per node (U_x , U_y , U_z). This type of element was used to generate the mainly structured and anyway quite regular mesh, without losing accuracy, even in zones with variable thickness (Figure 3.6).

The outputs of the structural calculations performed on the finite element model, were compared with those obtained through *in situ* measurements obtained by positioning some unidirectional acceleration transducers on the bridge, arranged in an appropriate manner, of piezo-electric type, with a sensitivity equal to 10 V/g. These sensors identified the real vibration modes of the structure subjected to ambient noise and uncontrolled stress, FDD (Figure 3.7).



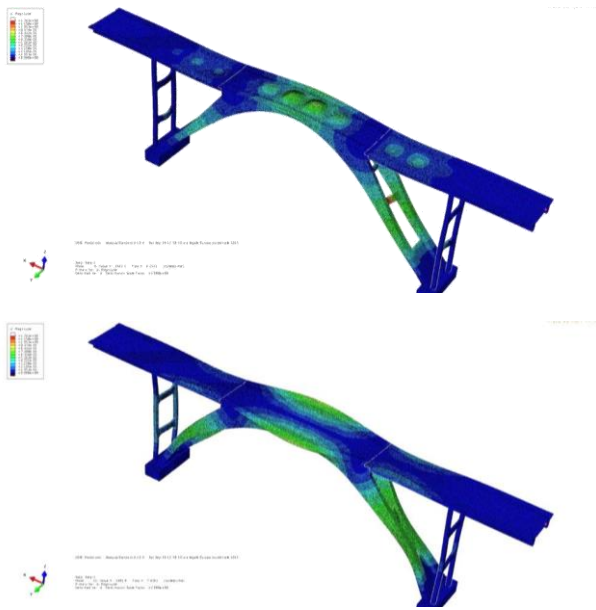


Figure 3.7 vibration modes.

The analysis results are in perfect agreement with the measurements *in situ* and specific procedures were not necessary for updating the identification of the mechanical characteristics of the structure, which were in agreement with the design values or measured on site (Artese et al., 2015).

4. LANDSLIDE MONITORING

The survey and the representation of the land have been part of the main objectives of Geomatics disciplines since their origins. The methods of modern Geomatics, composed of a combination of different sensors and devices for the storage, transmission and processing of data of environmental type, allow us to obtain very detailed representations of the earth's surface, from which it is possible to derive much information useful to geological investigation (Fabris et al., 2011; Achilli et al., 2015).

It is possible to distinguish two main fields of geological investigation: (a) the geomorphological characterization, i.e. the study of the developmental aspects of a territory and the group of transformations due to the effect of various physical agents through their morphological representation; and (b) the continuous and/or discontinuous monitoring, covering the systematic control of changes in the spatial configuration of an area with respect to a predetermined time interval.

The monitoring is generally extended to the structures sited near the crown and the ridges of the landslide. In the case of great phenomena, a large number of activities (geological, geotechnical, etc) are performed, and the need to coordinate all of the studies is felt. For monitoring landslides, the measurements are performed by using total stations (Stiros and al. 2004), photogrammetry (Scaioni and al. 2014), conventional laser scanner (De Agostino and al. 2012; Artese and al., 2013), and recent models capable of giving full waveform (Mallet and Bretar 2009; Pirotti and al. 2013). Global Navigation Satellite System (GNSS) receivers are used since several years, and recent applications use also low-cost instruments (Glabsch and al. 2009). SAR interferometry is used both from satellite (Kimura and Yamaguchi 2000; Bratus, 2015) and ground based (Tarchia and al. 2003).

The tools and methods of Geomatics allow us to identify and classify the main structural components of an area, and to

interpret their spatial correlations and dynamics, with a quantitative description of the earth's surface (Pike and al., 2009). It is possible to derive, from the Digital Terrain Model, deterministic and probabilistic models, used to evaluate the dynamic and evolutionary mechanisms present in an area, to predict possible scenarios of transformation and for risk assessment. The typologies of information can be only metric, or concern quality aspects related to specific geological features (Pavlopoulos and to. 2009). The extraction of this information is usually done at the end of a process of processing data that allows us to obtain 3D models endowed with a high level of detail. The representation of an area, through modeling of the natural elements that compose it, is a fundamental tool for analyzing and controlling the mechanisms of instability that often characterize terrain slopes and rock faces (Scaioni and Alba, 2010), to assess the levels of risk (Ferrero and al, 2011), and to simulate the possible paths of falling rocks and stone material according to analytical models of investigation (Slob et al, 2004).

All geomatics activities should be integrated with geotechnical surveys, in order to better understand the collapse mechanism of the landslide and to set up a model, also useful for early warning (Artese and al., 2015). The parameters to be measured, during monitoring, can be: direct parameters i.e. quantities that describe directly the behavior of the landslide (vertical and horizontal movements, deformations, rotations); indirect parameters i.e. data representing the boundary conditions of the landslide (pore pressure, groundwater levels, meteorological parameters, hydrology, seismicity). The frequency of surveys, during monitoring, depends on: the scope of the monitoring; the evolution of the phenomena; the observation periods. The data collection can be manual (executed by operators), automatic (managed by remote centers) and mixed. Generally monitoring is activated for safety purposes to population centers, infrastructure and engineering installations, or for study aims.

4.1 The Vermicelli Landslide

In March 2010, after a winter animated by prolonged heavy rains, on the north-west of the University of Calabria, on the slope of Contrada Vermicelli, some landslides were activated, two of which, the most significant, are next to each other but clearly distinguished (Figure 4.1).



Figure 4.1: The University of Calabria Landslide. Orthophoto and Cartography.

The landslide system in question was classified on the basis of direct observations and consists of two major landslides (Magarò et al., 2012): a Rotational slide (Slide A) and a Translational slide (Slide B), with probable sliding surface arranged in correspondence with a level clay.

The survey was executed using the terrestrial laser scanner RIEGL VZ-1000 with full waveform technology, and involved

the whole landslide. The survey was aimed at creating a 3D model (Figure 4.2) with high resolution, usable for geomorphological investigations and geotechnical analysis. At the same time a 3D model (Figure 4.3) was made starting from the 1K map of the area of the University of Calabria (flight 2006).

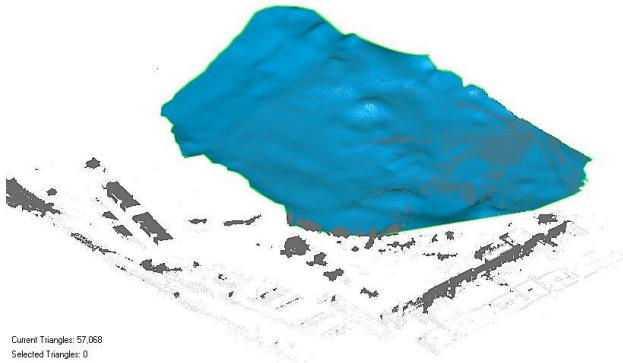


Figure 4.2: Model from the survey.

The survey was carried out in one day, performing two scans from two stations, with a resolution of 10 cm at a distance of 100 m. Georeferencing of the survey, in the UTM-ETRF2000 system, was performed using the GNSS receiver and the magnetometer the laser scanner is equipped with, high precision not being necessary.

For the processing of point clouds the software Riegl Riscan Pro® was used; for modeling and analyzing the difference between the surfaces of the two models the Geomagic Studio® Software was used.

The stored scans are aligned through tie-points, i.e. the vertices of the university “cubes” and the dormitories. At first, all scans, each with its own reference system, were referred to a coordinate system of the project corresponding to the one internal to the instrument in the first scanning position. The interactive tool multi-station adjustment was then applied to minimize the alignment errors by calculating the best geometry of overlap between the two scans. The optimized alignment allowed us to obtain a standard deviation less than 2 cm.

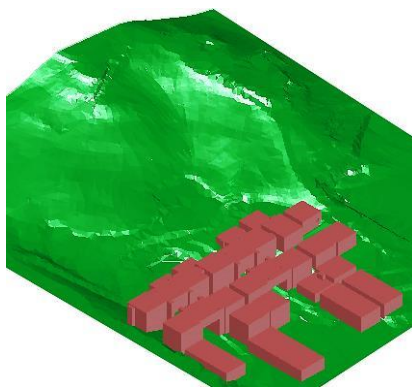


Figure 4.3 Model from 1K map.

After the alignment, we proceeded with the filtering and the consequent removal of those points that cannot be used for the reconstruction. Initially the points not lying in the study area were simply removed manually; after that a selection was conducted and the automatic deletion of the irrelevant points by the multi-target classification from the full waveform analysis. The mere differentiation of echoes was not enough to correctly

identify land points. It was decided, therefore, to resort to a procedure called terrain filter, by means of which it is possible, in an entirely automatic manner, to extract and eliminate, with high accuracy, the additional points belonging to the vegetation and to extraneous elements. The tool is based on an iterative procedure capable of generating a series of surfaces, equidistant from the surface of interest, with respect to which an automatic selection is made of the points too external or excessively far away from the surface to reconstruct. Although much of the points belonging to the vegetation and to foreign elements were removed automatically, we encountered some problems in those areas with the presence of compact vegetation. For the filtering of these areas, we resorted to additional localized operations of filtering and to manual removal. Finally the clouds were resampled using a octree procedure. From resampled data a mesh was created with a resolution of 2 cm using the Geomagic Studio software, in order to preserve as much detail as possible. The most obvious problem during the reconstruction was the impossibility of obtaining closed and perfectly continuous surfaces, especially in the part where the vegetation was too dense. Due to the lack of information about the real shape of the land in these areas, it was decided to close the holes with approximate planes or geometric surfaces, respecting the morphology of the visible parts.

Once the model is created, it is overlapped to the one obtained from maps, using as tie points the vertices of the university “cubes” and the dormitories.

From the comparison of the two models, it was possible to make some observations. In figure 4.4, the two landslides are recognizable, their real limits and the depletion and accumulation zones. The precision of the results depends fundamentally on that of Cartography. We can evaluate an accuracy of the final result of about 25 cm.

The survey can also be used for studies and analysis of the evolution of the area or to monitor additional collapse events: through the data acquired at different times it is possible to examine the evolution of the phenomenon.

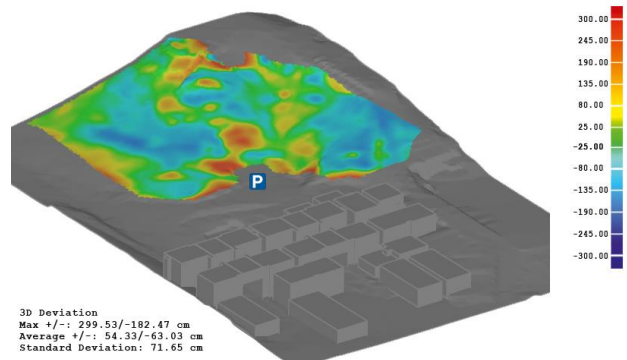


Figure 4.4: Comparison of the two models.

From the 3D model derived from the scans, it is possible to derive a set of geometric entities such as polylines and contour lines, which can be exported and reused in a CAD program and allow the evaluation of distances, volumes, trajectories and the interaction between various elements (Hoffmeister et al., 2012).

5. DYNAMIC MEASUREMENTS: THE USE OF A LASER POINTER FOR MONITORING BRIDGE DEFLECTIONS

The possibility to perform fast and accurate image processing, thanks to the power of the most recent computers, allows us to make use of new exciting applications of this technology in

several fields and, in particular, for the monitoring of large structures.

The bridges, due to their dimensions and great loads, are often monitored. To control the state of health of a bridge, static loads are applied to the structure, materialized by a convoy of heavy trucks parked on the deck in known positions. The deflections of the beams are then measured by using levels or total stations. Dynamic measurements have been recently proposed, by using Micro Electro-Mechanical Systems (Yu et al., 2013) or Digital Image Correlation (Yoneyama and Ueda, 2012).

In the test described in the following, a very cheap instrumentation was used. The variation of the tangent to the elastic line was captured by using a laser pointer. A video of the oscillations of the laser footprint during the test was acquired. By analyzing the single frames, the variable position of the footprint centroid gives information about the inclination changes and, consequently, about the dynamic deflections. The geometry of the test was set up in order to amplify the movements of the laser footprint and, consequently, to get a high precision. In the following, the last test executed using this method is described.

5.1 The test layout

The University of Calabria is characterized by a South-North axis, along which the buildings of the Departments are sited. The axis is materialized by a sequence of double-deck bridges: the upper deck can be used for vehicular traffic, while the lower one is reserved for pedestrians (Figure 5.1). The layout of the test is shown in figure 5.2. The laser pointer is fixed to a tubular element of the truss beam of the bridge (figure 5.3).



Figure 5.1: The double-deck bridges.

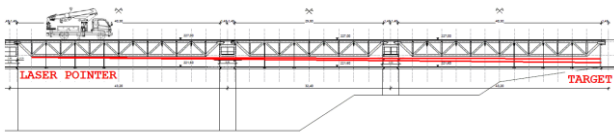


Figure 5.2: The layout of the test.



Figure 5.3: The laser pointer and the holder (left); The pedestrian deck (right): the target is on the front wall.

The laser beam is projected onto a flat target fixed to a vertical wall of the north terminal abutment. To point exactly at the

target, the pointer is mounted on a holder, usually used on optical tables, which allows precise horizontal and vertical movements. The holder is equipped with a strong magnetic base. The camera used to obtain the video was positioned on a robust tripod, slightly lateral with respect to the laser beam path.

5.2 The instruments used and the expected precision

The main characteristics of the laser pointer used are as follows:

- Wavelength 532 nm (Green)
- Beam diameter 2.0 mm
- Beam divergence 0.8 mrad
- Power 100 mW (Gaussian Beam)
- Pointing stability < 0.05 mrad

The video was shot using a NIKON D610 camera with a 55 mm NIKKOR (previously calibrated) lens. The distance to the target was chosen so that the medium scale of the frames was 1 pixel=0.2 mm. Taking into account the maximum pointing stability of the laser pointer, a more detailed scale of the frame would be useless. Given that the distance from the laser pointer to the target was 115.7 m, we obtained a beam footprint of 95 mm and a maximum pointing instability of 5.8 mm (23 pixels).

The correlation techniques allowed us to determine the centroid of the footprint with an accuracy of one pixel, so almost the total expected error in the measurements of the beam inclination was due to the laser pointer instability and can be evaluated as 0.05 mrad.

5.3 The Test and the Results

The test was carried out during the movements of a truck elevator, having a weight of about 260 kN, used for work on the façade of a building alongside the bridge. The video was shot when the truck left the bridge. Due to the limited space, the truck performed some forward and backward movements to reach the optimal alignment before the final reverse run.

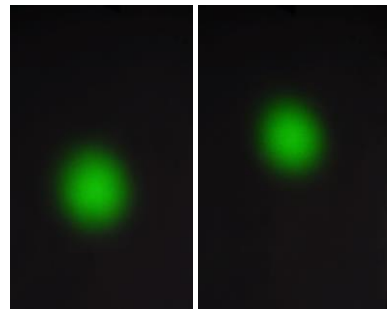


Figure 5.4: two frames acquired at the beginning and at the end of the test: after the truck left the bridge, the footprint is higher.

In Figure 5.4, we can observe two frames obtained during the test. The ISO sensitivity and the aperture were chosen in order to execute automatically a radiometric cut off, thus achieving two goals: a better defined shape of the laser beam footprint was obtained and the saturation of the image in the center zone of the footprint avoided. This allows a more accurate determination of the centroid.

The frames were processed by using a code in Matlab® expressly realized. The position of the centroids (rows, columns) is given in pixels.

Figure 5.5 shows the position of the centroid during the test.

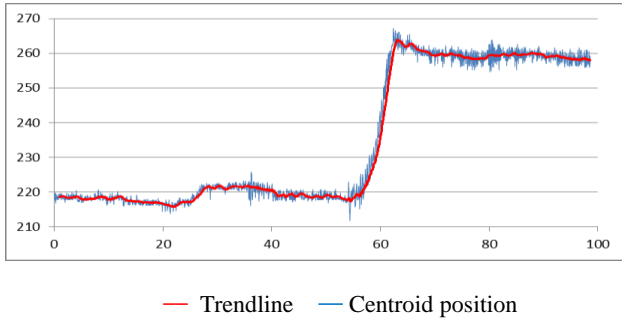


Figure 5.5: The vertical position of the centroid of the footprint during the test.

The origin of ordinates is at the bottom of the frame. The values have been transformed in mm. The scale of the frames was obtained by measuring a known length on a rectified frame. Abscissae are in seconds.

A sudden variation is evident, equal to about 40 mm, corresponding to an inclination change of 0.346 mrad. A rough estimation of the deflection can be made by considering the laser positioned in correspondence to a bearing and a constant section of the truss beam. In this case the above inclination variation implies a deflection variation of the laser beam of about 6.9 mm at a distance of 20 m (middle of the span). Thus, it is possible to evaluate the variation of the truss beam deflection in 4.6 mm.

It is also possible to observe that the pointing stability was less than 0.05 mrad.

From a qualitative point of view, we can observe that the forward-backward movements of the truck are clearly reflected in the movements of the laser beam. Furthermore, some oscillations are recognizable after the truck left the bridge.

In conclusion, this method seems to be promising for bridge monitoring. A camera with a high frame rate could allow the study of the frequencies, but the problem of pointing stability needs to be considered.

A further refining should be made if a 3D model were available, in order to execute a FEM study and to compare theoretical and experimental results.

6. DINAMIC MEASUREMENTS: THE USE OF TLS AND GNSS FOR MONITORING THE ELASTIC LINE OF A BRIDGE

For the surveying of the bridges, laser scanning is by now a consolidated technique. The comparison of several scans acquired at different times, allows us to obtain, for example, the deviations between corresponding points of the bridge surface under different conditions. The laser scanner can thus be used for monitoring purposes.

The very high acquisition rate of this instrument is exploited to perform mobile mapping (Schwarz et al., 1993; Tao and Li, 2007). For this aim, the laser scanner is mounted on a vehicle: a mobile instrument is used to map a static object (land).

One can think, however, of using this instrument in a reverse way: a fixed instrument can be used to survey a mobile object. In particular, the deflections of the superstructure of a bridge could be dynamically measured in near real time.

In the following, a method is described for the dynamic surveying of the elastic line of a bridge, along with the first experimental tests.

6.1 The method

The method consists of placing a laser scanner, set up as line-scanner, under the superstructure of a bridge and acquiring continuously a line parallel to the axis of the deck.

The displacements with respect to the line surveyed under static conditions and without loads, allow us to obtain the elastic line.

It is possible, in this way, to extract an elastic line for each scanned line; that is, up to several dozens of lines per second.

The accuracy achievable depends on the instrument used. At present, several laser scanners reach precisions of about 1 mm for distances up to 200 m; if the required range is higher, then more powerful models could be used, at the cost, however, of lesser accuracy.

The operating mode is also important for the precision of the result. The best performances are obtained when the sampling rate is low: this lowers some effects, like, for example, the vibrations of the rotating mirror axis.

Furthermore, we must consider that the goal is to reconstruct a line, obtained starting from a series of points. The best fitting line has in general an accuracy rather better than each single point, so the final result could reach a precision higher than that declared for the instrument used.

6.2 First Tests: The Cannavino Bridge at Celico and the double-deck bridges at University of Calabria

The Cannavino bridge (Figure 6.1) is characterized by a cantilever prestressed concrete structure. A cantilever collapse occurred during its realization in 1972, and it was subject of several studies (Wittfoht, 1983).

In recent years, the end of the cantilevers have showed noticeable deflections; for this reason, a periodic monitoring with total station is performed by the technicians of ANAS, the Italian National Autonomous Roads Corporation.

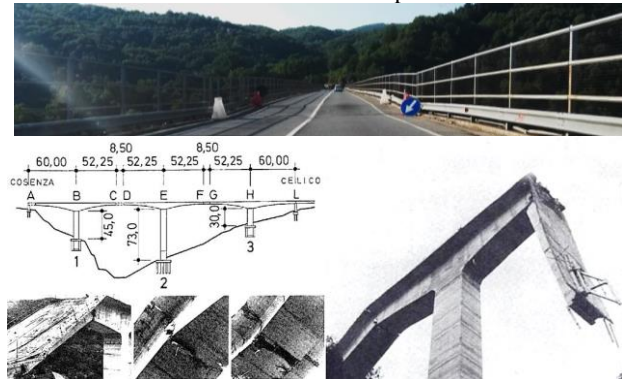


Figure 6.1: The Cannavino bridge. The present situation, a quoted elevation and photo of collapse (1972)

The instrument used for the test is a Riegl VZ1000 Laser Scanner, as described above. In this case, the laser scanner was used in the line scan configuration. The function timestamp was used, so that for each measured point the instant of acquisition was recorded; to this aim, the GPS receiver integrated in the laser scanner was used.

The instrument was placed under the deck, near a pile, and a longitudinal path continuously acquired along the sidewalk. The scans were performed during a normal traffic period.

A scan rate of 110,000 points per second was selected.

The data acquired were processed with the RiSCAN PRO® software. A text file was obtained, containing the coordinates of the measured points, along with the timestamp. This file was

processed with a Matlab® code realized on purpose and the single lines were extracted. The evaluation of the displacements was obtained using a spreadsheet and a cad program.

The following remarks can be made:

The row data generate very close lines that can be grouped in three curves groups. This can be caused by vibrations of the axis of the scanning mirror. To obviate this problem, the convergence of all lines at a point at the beginning of the cantilever was imposed.

Figure 6.2 shows the layout of the test and some results. The trendlines obtained diverge going to the end of the cantilever (each color refers to a different instant); the distance reaches a value of about 6 mm. This result is reasonable for normal traffic loads. The coordinates, referred to the intrinsic instrument reference system, are in meters.

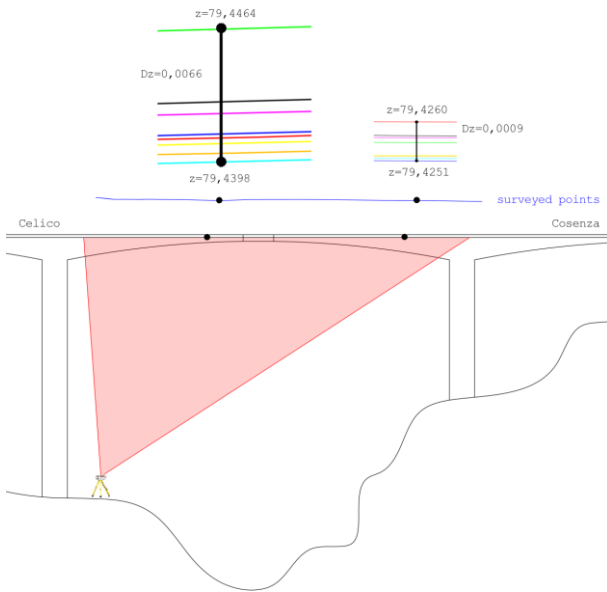


Figure 6.2: The layout and some results of the test.

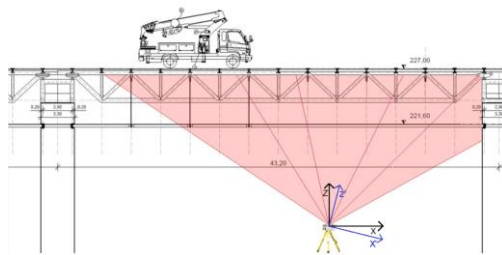


Figure 6.3: The layout of the test on the Bridge of University of Calabria.

For the second test, the University of Calabria bridges have been chosen. The laser scanner has been positioned on a tripod under the bridge. The path followed for the scans corresponds to a generatrix of the highest tubular element of the truss beam (Figure 6.3).

The acquisition rate was set to 70,000 points per second, which implies a slow rotation of the scan mirror.

During the test, a video was acquired from the last floor, and the truck movements were recorded. The video was synchronized to the scan acquisitions.

The data acquired were processed with the software RiSCAN PRO® and the same procedure of the test on Cannavino bridge was followed.

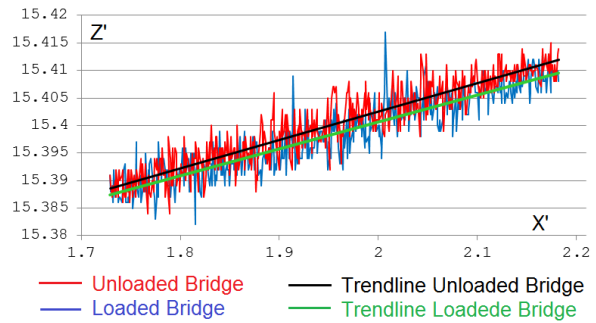


Figure 6.4: The profiles of the tubular beam at the south zone of the span.

The results are shown in the figure 6.4. The coordinates, referred to the intrinsic instrument reference system (X',Z'), are in meters. It is possible to observe that the lines obtained at the beginning and at the end of the test have a height difference of about 2 mm in the middle zone of the span. This value is in full agreement with the results obtained using the laser pointer.

6.3 Conclusions and Ideas for future developments

Several critical issues must be faced for the development of a methodology suitable for effectively monitoring the dynamic behavior of a bridge.

First of all, the obtained elastic lines should be exactly related to the moving loads at the moment of the single scan (load intensity, position, speed). To reach this goal, the synchronization of the laser scanner and of the instruments used to detect the position of the moving loads should be guaranteed. Timestamp should be very useful for this aim.

If the laser pointer is used, a problem to face could be the positioning on the bridge, along with the synchronization of the camera.

Other problems are due to the powering of the instruments if a continuous monitoring should be performed.

These aspects will be dealt with during the next experimental tests.

REFERENCES

ABAQUS 6.14 Analysis User's Manual.

Achilli, V., Carrubba, P., Fabris, M., Menin, A., & Pavanello, P. (2015). An archival geomatics approach in the study of a landslide. *Applied Geomatics*, 1-11.

Artese, G., Perrelli, M., Artese, S., Manieri, F., & Principato, F. (2013, February). The contribute of geomatics for monitoring the great landslide of Maierato, Italy. In International Workshop "The Role of Geomatics in Hydrogeological Risk (pp. 27-28).

Artese, G., Perrelli, M., Artese, S., Meduri, S., & Brogno, N. (2015). POIS, a Low Cost Tilt and Position Sensor: Design and First Tests. *Sensors*, 15(5), 10806-10824.

Artese, S., Altomare, C., Lerma, J., L., Zinno, R. (2014). Terrestrial laser scanning registration analysis and its effects on a masterpiece dome. In: *EUROMED 2014 Proceedings*. Cyprus, 3-8 novembre 2014

Artese, S., Miceli, A., Talarico, P., Venneri, A., Zagari, G., Zinno, R. (2015). Ponti antichi e moderni: utilizzo di tecniche geomatiche per il rilievo, la rappresentazione e la modellazione strutturale. *Atti 19a Conferenza Nazionale ASITA*, 29-30

- Settembre - 1 ottobre 2015, Lecco - Polo di Lecco del Politecnico di Milano - ISBN 978-88-941232-2-7
- Bratus, A. (2015). Monitoraggio di dissesti franosi con metodologia integrata basata sull'uso di sistema radar interferometrico terrestre (GBSAR). Tesi di Dottorato.
- Castellazzi G., D'Altri A.M., Bitelli G., Selvaggi I. and Lambertini A. (2015), From laser scanning to finite element analysis of complex buildings by using a semi-automatic procedure, *Sensors*, 15(8), 18360-18380.
- Cruilles, V. S., & Monserrat, M. D. (1876). *Guía urbana de Valencia: antigua y moderna*.
- De Agostino, M., Lingua, A., & Piras, M. (2012). Rock face surveys using a LiDAR MMS. *Ital. J. Remote Sens*, 44, 141-151.
- Fabado, S., Seguí, A. E., Cabrelles, M., Navarro, S., García-De-San-Miguel, D., & Lerma, J. L. (2013). 3DVEM Software Modules for Efficient Management of Point Clouds and Photorealistic 3d Models. *ISPRS-International Archives of the Photogrammetry, Remote Sensing and Spatial Information Sciences*, 1(2), 255-260.
- Fabris, M., Menin, A., & Achilli, V. (2011). Landslide displacement estimation by archival digital photogrammetry. *Italian Journal of Remote Sensing*, 43(2), 23-30.
- Ferrero A. M., Migliazza M., Roncella R., Rabbi E. (2011). Rock slopes risk assessment based on advanced geo structural survey techniques. *Landslides*, 8: 221-231.
- Fuchs, P.A., Washer, G.A., Chase, S.B., and Moore, M. (2004), Applications of Laser-Based Instrumentation for Highway Bridges, *Journal of Bridge Engineering*, ASCE, November/December, pp. 541-549.
- Glabsch, J., Heunecke, O., & Schuhbäck, S. (2009). Monitoring the Hornbergl landslide using a recently developed low cost GNSS sensor network. *Journal of Applied Geodesy*, 3(3), 179-192.
- Gómez, J. B. (1987). *Los comienzos de la arquitectura académica en Valencia: Antonio Gilabert*.
- Hoffmeister, D., Tilly, N., Curdt, C., Aasen, H., Ntageretzi, K., Hadler, H., ... & Bareth, G. (2012). Terrestrial laser scanning for coastal geomorphologic research in Western Greece. *Int Arch Photogramm Remote Sens Spat Inf Sci*, 39(B5), 511-516.
- Horn, B. K. (1987). Closed-form solution of absolute orientation using unit quaternions. *JOSA A*, 4(4), 629-642.
- Kimura, H., & Yamaguchi, Y. (2000). Detection of landslide areas using satellite radar interferometry. *Photogrammetric Engineering and Remote Sensing*, 66(3), 337-344.
- Lubowiecka, I.; Armesto, J.; Arias, P.; Lorenzo, H. (2009) Historic bridge modelling using laser scanning, ground penetrating radar and finite element methods in the context of structural dynamics. *Engineering Structures*, 31, 2667-2676.
- Magarò, F., Ietto, F., Ponte, M. (2012), Studio di un versante in frana in località "Vermicelli" di Rende (CS). Tesi di laurea Università della Calabria A.A. 2011-2012
- Mallet, C., & Bretar, F. (2009). Full-waveform topographic lidar: State-of-the-art. *ISPRS Journal of photogrammetry and remote sensing*, 64(1), 1-16.
- Pavlopoulos K., Evelpidou N., Vassilopoulos A. (2009), *Mapping geomorphological environments*. Springer, Berlino. ISBN 978-3-642-01950-0.
- Pike R. J., Evans I. S., Hengl T. (2009), Geomorphometry: a brief guide, in Hengl T., Reuter H. I. (a cura di), *Geomorphometry: concepts, software, applications*, Elsevier, Amsterdam: 3-30. ISBN 0123743451, 780123743459.
- Pirotti, F., Guarnieri, A., & Vettore, A. (2013). Vegetation filtering of waveform terrestrial laser scanner data for DTM production. *Applied Geomatics*, 5(4), 311-322.
- Scaioni M., Alba M. (2010), Understanding changes and deformations on multi temporal rock face point clouds. *International Archives of Photogrammetry and Remote Sensing*, 38 (3A): 67-72.
- Scaioni, M., Feng, T., Barazzetti, L., Previtali, M., Lu, P., Qiao, G., ... & Li, R. (2014). Some applications of 2-D and 3-D photogrammetry during laboratory experiments for hydrogeological risk assessment. *Geomatics, Natural Hazards and Risk*, (ahead-of-print), 1-24.
- Schwarz, K. P., Martell, H. E., El-Sheimy, N., Li, R., Chapman, M. A., & Cosandier, D. (1993, October). VIASAT-A mobile highway survey system of high accuracy. In *Vehicle Navigation and Information Systems Conference*, 1993., Proceedings of the IEEE-IEE (pp. 476-481). IEEE.
- Slob S., Hack R., Van Knappen B., Kemeny J. (2004), Automated identification and characterization of discontinuity sets in outcropping rock masses using 3D terrestrial laser scan survey techniques. *EUROCK 2004 & 53rd Geomechanics Colloquium*, 7-9 ottobre, Salisburgo: 439-443.
- Stiros, S. C., Vichas, C., & Skourtis, C. (2004). Landslide monitoring based on geodetically derived distance changes. *Journal of surveying engineering*, 130(4), 156-162.
- Tao, C. V., & Li, J. (Eds.). (2007). *Advances in mobile mapping technology*. CRC Press.
- Tarchia, D., Casagli, N., Fanti, R., Leva, D. D., Luzi, G., Pasuto, A., ... & Silvano, S. (2003). Landslide monitoring by using ground-based SAR interferometry: an example of application to the Tessina landslide in Italy. *Engineering Geology*, 68(1), 15-30.
- Vosselman, G., Gorte, B. G., Sithole, G., & Rabbani, T. (2004). Recognising structure in laser scanner point clouds. *International archives of photogrammetry, remote sensing and spatial information sciences*, 46(8), 33-38.
- Wittfoht, H. (1983). Ursachen für den Teil-Einsturz des "Viadotto Cannavino" bei Agro di Celico. *Beton-und Stahlbetonbau*, 78(2), 29-36.
- Yoneyama, S., & Ueda, H. (2012). Bridge deflection measurement using digital image correlation with camera movement correction. *Materials Transactions*, 53(2), 285-290.
- Yu, Y., Liu, H., Li, D., Mao, X., & Ou, J. (2013). Bridge deflection measurement using wireless mems inclination sensor systems. *International Journal on Smart Sensing & Intelligent Systems*, 6(1).
- Zogg, H.M., and Ingensand, H. (2008), Terrestrial Laser Scanning for Deformation Monitoring –Load Tests on the Felsenau Viaduct (CH). *The International Archives of the Photogrammetry, Remote Sensing and Spatial Information Sciences*, Volume XXXVII, Part B5, pp. 555-562.

ACKNOWLEDGEMENT

I would like to express my thanks and gratitude to my Supervisor, Prof. Raffaele Zinno, and to Prof. Josè Luis Lerma García for their support and assistance.

SEMI-GLOBAL TECHNIQUES IN IMAGE MATCHING AND CHANGE DETECTION WITH APPLICATIONS TO CIVIL AND ENVIRONMENTAL ENGINEERING

Elisa Dall'asta ^{a,*}

^a DICATeA, University of Parma, 43124 Parma (PR), Italy – dallastaelisa@gmail.com

KEY WORDS: Matching, DSM, Accuracy, Reconstruction, Comparison, Algorithms

ABSTRACT:

Encouraged by the growing interest in automatic 3D image-based reconstruction, the development and improvement of robust stereo matching techniques is one of the most investigated research topic of the last years in photogrammetry and computer vision. This work of thesis wants to present a dissertation of the wide range of modern dense matching algorithms, which are spreading in different application and research fields, with a particular attention to the innovative "Semi-Global" matching techniques. A proprietary semi-global numerical code was implemented for getting insight on the variables and strategies that affect the algorithm performances: the dissertation will face, at a first level, the classical stereo matching implementation (i.e. that operate on two frame); after that, the it will deal with the algorithm developments of multi-image approaches and the innovative extension to bi-dimensional research of correspondences (e.g. temporal point tracking). The metrological characterization of the algorithm has allowed evaluating the influence of several matching variables and functions implemented in the process and comparing the accuracy and completeness of different results (digital surface models, disparity maps and 2D displacement fields). The achieved results, using our code and other commercial and open-source matching programs, will be presented in a wide variety of application fields.

1. INTRODUCTION

Image matching, digital image correlation, stereo correspondences problem: all refer to the class of noncontact techniques that utilize two or more digital images depicting (at least partly) the same scene and provide a dense reconstruction of the shape and the spatial position of the analysed object. In other words, given two (or more) views of a scene, correspondence needs to be established among homologous features (Schenk, 1999), which are projections of the same physical identity in space.

It is possible to say that image matching represents a key component of many photogrammetric and computer vision tasks. However, right now, it is quite hard to identify a completely satisfactory taxonomy of the different techniques: encouraged by the growing interest in automatic 3D image-based reconstruction, a large number of image matching algorithms and methods have been developed and refined over the years leading to the complete automation of the entire 3D modelling process in several application areas. A very good overviews on the topic can be found in literature (see for instance Barnard, et. al, 1982, Scharstein, et. al., 2002)

The Semi-Global matching (SGM) is, actually, one of the best matching strategies, offering good results with low runtime. It consider both the image similarity and the disparity continuity; therefore, several considerations about the implemented matching cost functions (used to realize pixels correlation), the aggregation step that combine these costs and, finally, the choice of penalty functions which enforce depth continuity, need to be evaluated. Indeed, the implementation of these methods requires the introduction of many parameters and their optimal combination is fundamental to have good performances and accurate results.

In order to provide an in-depth view of all these aspects, a proprietary image matching code, based on Hirschmuller SGM algorithm (Hirschmuller, 2008) and optimized with Dynamic Programming (DP) (Birchfield, et. al., 1999) method, has been implemented, enabling the evaluation of the best variables

combinations and the optimal formulation of the matching cost function.

Studies from literature shows that SGM approach is mainly applied in stereo-vision problem (e.g. for photogrammetric applications such as the generation of digital surface/terrain models). In such context, the image geometry allows simplifying the problem of homologous points identification between stereo images, reducing the parallax domain to a mono-dimensional space (i.e. along corresponding epipolar lines). However, the mono-dimensional research of correspondences, represents a limit when the correlation analysis must perform a bi-dimensional investigation of image correspondences (for example, point tracking or displacement analysis). Therefore, an extension of the SGM method is proposed and developed in this work, in order to extend the disparity domain to 2D. Further developments have regarded the algorithm extension to a multi-image matching process.

Following, the core of the algorithm will be presented: in the first part, the method workflow, together with all the implemented strategies, will be accurately described; then, a description of the tests performed for the algorithm calibration and optimization will be presented. Finally, some cases of study for the algorithm surface reconstruction analysis and reliability will be discussed.

2. SGM SOFTWARE CODE

Semi-Global Matching is a method developed by Heiko Hirschmuller from the DLR. He first reported his method in 2005 (Hirschmuller, 2005), and then he elaborated and proposed further improvements in (Hirschmuller, 2005 and 2008). Since its original publication, the Semi-Global Matching technique has been implemented by many researchers and companies.

The numerical code developed in this work, written in a .Net environment (using C# language), performs the images correlation, both with stereo and multi-image approach, using a Semi-Global method. It can produce, as final output, the disparity map of the investigated stereo image pairs, the stereo image correspondences for 2D displacement fields or the raster DSM. The core of the algorithm considers pair of stereo images with

* Corresponding author

known interior and exterior parameters: if standard stereo-matching applications are concerned, the software pre-process the images providing their idealization and epipolar rectification. Then, a series of procedures common to all the different operational modes of the software (stereo-matching, multi-image matching, point tracking, etc.), which represent the real core of the matching process are performed.

Further developments, as already said, have regarded the algorithm extension to a multi-image matching process. Similarly, as far as displacement/tracking analysis is concerned, an algorithm extension for the 2D disparity search space investigation has been developed. In this case, due to the increase requirements of the new algorithm in terms of computational and memory cost, optimization strategies were introduced in the algorithm pipeline.

2.1 SGM algorithm workflow

Assuming a general stereo geometry of two or more images with known relative orientation, the general matching process evolves through the steps schematize in Figure 1.

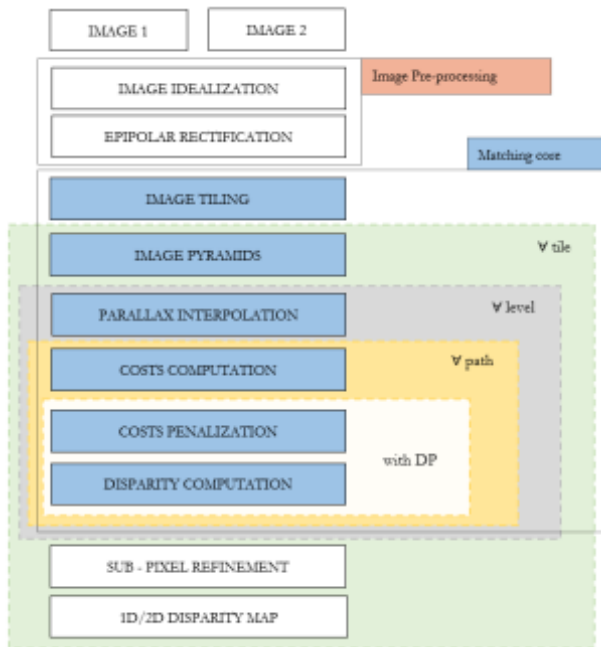


Figure 1. General SGM algorithm workflow (valid for 1D/2D disparity search) for stereo-pairs approach.

At the very beginning of matching processing, the code requires some important variables initialization. If it is not specified, default parameters are internally defined to allow the matching algorithm working; otherwise, the operator can intervene for refining and adjusting the processing variables with regard to the specific problem complexity. The processing parameters that can be set by the operator are: the region of interest (ROI), the disparity search range; the penalization and the similarity cost functions to use; the image window size; the multi-processor option (the algorithm can run on multiple processing cores thanks to parallelization of several computation steps) and finally, it is possible to enable/disable the use of the image tiling and pyramiding strategies.

This step is fundamental since the user can intervene refining the process variables, obtaining more accurate and reliable solution based on the specific analysed problem. In the following paragraphs all these functions and variables are presented.

2.1.1 Image Idealization/rectification

In a first step the images can be idealized and rectified. In the first case, the process consists in removing distortions from the analysed images in order to obtain a new resampled image pair where the effects of the distortions, generally introduced by the camera lens system, are corrected. For each image to resample, the correction to be applied on the image coordinates (i.e. the deformation field) is calculated with the Brown's (Fryer, et. al., 1986) distortion model (other custom distortion models can be specified by the user). In the rectification process, the stereo images are resampled, producing new photograms where corresponding points lie on the same horizontal image line (a deeper description of this procedure can be found in (Hartley, et. al., 2000), where the demonstration of this condition is presented in more details).

2.1.2 Matching by using image tiling

Due to the high memory requirements of SGM, especially if the DSI dimensions are relevant (i.e. using high resolution images and/or wide disparity search range), a tile-based strategy was adopted in order to increase the computational performances. The procedure allows dividing the whole master image into squared areas (partially overlapped) which are individually matched with the slave image (the number of processing cores determines the number of tiles that can be computed concurrently - see Figure 2). Finally, the matching results are merged together, blending the disparity results in the overlapping regions, in order to obtain the full disparity image.

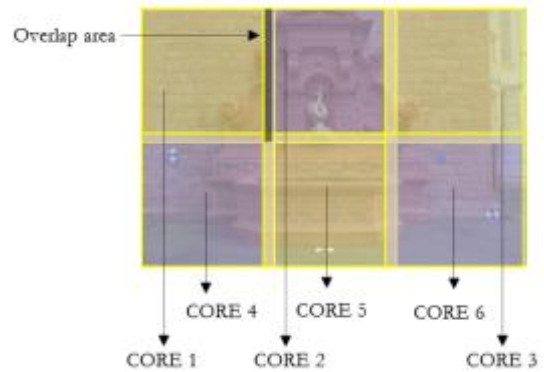


Figure 2. Image tiling concepts: in purple and yellow the image tiles, which are independently processed by a different processor core.

2.1.3 Matching by using image pyramids

In order to perform an efficient stereo matching with high resolution images, the developed software implements also a multi-resolution approach using image pyramids and a coarse-to-fine disparity map evaluation. Every level of the pyramid is down-sampled from the previous level (in particular the resolution is one-half of the previous level scale), resulting in smaller image. As this process proceeds, the result is a set of gradually smoother images, where the spatial sampling density (and, consequently, also the disparity search range) decreases level by level. The idea is that performing image matching on the lower-resolution images allows performing the matching process for fewer pixels (and a smaller disparity search range) and to adaptively compute the matching parameters for the subsequent levels (in particular, the disparity range, except in the first pyramid level, is shrunked w.r.t. the full, user-defined, range).

2.1.4 Variables and implemented functions

The algorithm must consider some parameters that regard the similarity cost functions and others that allow the parallaxes regularity constraint (i.e. penalty functions).

In the developed proprietary SGM algorithm, a generalization of the Hirschmuller semi-global matching has been performed. The cost $L'_r(\mathbf{p}, d)$ of the pixel located in \mathbf{p} at disparity d , along the path direction \mathbf{r} is defined recursively as:

$$L'_r(\mathbf{p}, d) = C(\mathbf{p}, d) + \min_i\{L_r(\mathbf{p} - \mathbf{r}, d + \Delta d_i) + P(\Delta d_i)\} \quad (1)$$

where the first term is the similarity cost associated with a disparity value of d , whereas the second term evaluates the regularity of the disparity field, adding a penalty term P , function of disparity changes (Δd_i) with respect to the previous point ($\mathbf{p} - \mathbf{r}$) in the considered matching path \mathbf{r} . Different cost and penalty functions have been implemented in the Semi-Global matching code, but the abstraction level of the source code allows also the user to provide his own functions.

First, as far as similarity cost computation is concerned (represented by the term $C(\mathbf{p}, d)$ in eq. (1), we have implemented, the most common parametric and non-parametric correlation measures: Sum of Absolute/Squared Differences (SAD/SSD), Normalized Cross Correlation (NCC) and Sum of Humming Distance (SHD):

$$SAD = \sum_{(i,j) \in W} |f(i, j) - g(i + \Delta y, j + \Delta x)| \quad (2)$$

$$SSD = \sum_{(i,j) \in W} (f(i, j) - g(i + \Delta y, j + \Delta x))^2 \quad (3)$$

$$NCC = \frac{\sum_{(i,j) \in W} [f(i, j) \cdot (g(i + \Delta y, j + \Delta x))]}{\sqrt{\sum_{(i,j) \in W} [(f(i, j))^2 \cdot (g(i + \Delta y, j + \Delta x))^2]}} \quad (4)$$

$$SHD = \sum_{(i,j) \in W} f(i, j) \text{ bitwise XOR } g(i + \Delta y, j + \Delta x) \quad (5)$$

$$= f(i, j) \wedge g(i + \Delta y, j + \Delta x)$$

As far as the disparity field regularization terms are concerned, two penalty functions are actually implemented: the one proposed by Hirschmuller, which uses two penalty parameters " P_1, P_2 " (P_1 - for small changes - permits an adaptation to slanted or curved surfaces; P_2 - for larger changes - preserves discontinuities), and a different penalization method, where penalty increases linearly with the disparity difference of neighbour pixels. Furthermore, as reported in (Hirschmuller, 2008), since that big disparity changes are usually indicated by significant intensity variations (as happens near objects borders and discontinuous areas), the penalty P_2 can be set not only as a constant value but it also possible to identify a different definition of the penalization parameter: in this case P_2 is adapted to the intensity gradient between the current and the previous pixel, according to the following equation:

$$P_2 = \begin{cases} \frac{\bar{P}_2}{\Delta I} & \Delta I > t \\ \bar{P}_2 & \Delta I \leq t \end{cases} \quad (6)$$

where $\Delta I = |I_L(\mathbf{p}) - I_L(\mathbf{p} - \mathbf{r})|$ represents the intensity registered difference value between adjacent pixels on the same path \mathbf{r} , ε a constant value and t is an intensity differences threshold.

2.1.5 Matching core and disparity optimization

The minimization problem of the semi-global cost function is solved in our implementation using a DP algorithm combining matching costs along independent one-dimensional paths from all directions through the image (just like in the Hirschmuller implementation). Thus, for each pixel \mathbf{p} and disparity d , the cost is computed by the sum of the matching cost and the minimum path cost of the previous pixel $\mathbf{p} - \mathbf{r}$.

In a DP framework (as the ones implemented in the code and in many SGM software packages (Cox. et. al., 1995), the cost

$L'_r(\mathbf{p}, d)$ is defined recursively for allowing the identification of the $\min_i\{L_r(\mathbf{p} - \mathbf{r}, d + \Delta d_i) + P(\Delta d_i)\}$. In other words, whenever a determinate sub-problem (whose solution contributes together with the other identified optimal sub-problems to the solution of the whole process) is proposed again, it will be not necessary to solve the problem, because its solution has already been calculated (i.e. it is available) and only have to be called back from the memory. The disparity solution of the previous pixels $L_r(\mathbf{p} - \mathbf{r}, d + \Delta d_i)$ are necessary data to obtain the L'_r term but they must not be computed every time such sub-problems arise: the solutions have already been stored.

Two costs penalization strategies have been implemented in the software code: in the initial research stages, a first algorithmic development, which provided more flexibility in terms of penalization paths w.r.t. the first Hirschmuller implementation of SGM, was implemented and tested. Later, on the basis of such results, a different SGM solving approach, algorithmically more similar to the OpenCV Semi Global stereo Block Matching library (OpenCV 2.4.8 StereoSGBM, 2006), has been studied and employed, to improve computational efficiency of the algorithm.

2.1.6 SGM algorithm extension for a bi-directional research of correspondences

Traditional SGM algorithms, which reduce the correlation problem complexity to a sub-set of image points (also called as "scanline"), cannot be used when the displacements tracking of image points is investigated. Furthermore, real data always has imperfections and finding the true disparity should require searching in the Y direction even if an epipolar rectification process is performed. Given these considerations, and in order to create a software able to give a solution to many engineering applications, the proprietary SGM software code was improved, including the possibility to analyse a 2D disparity search domain. The algorithm works within the same pipeline described in paragraph 2.1 but eq. (1) should be extended to consider the 2D search domain:

$$L'_r(\mathbf{p}, d) = C(\mathbf{p}, dx, dy) + \min_{i,j} \left\{ L_r \left(\begin{matrix} \mathbf{p} - \mathbf{r}, \\ dx + \Delta d_i, \\ dy + \Delta d_j \end{matrix} \right) + P(\Delta d_i, \Delta d_j) \right\} \quad (7)$$

where dx and dy , and Δd_i and Δd_j , are respectively the displacement components and the disparity changes along the principal image plane axis.

However, the high amount of memory and calculations required by the original SGM is further increased introducing the 2D disparity search option (for each image pixel, the costs by varying the disparity search range in two direction are stored). Anyway, the use of the multi-resolution strategy has allowed to reduce the disparity search range solving the memory and computation issues.

2.1.7 Sub-pixel refinement

Most dense stereo correspondence algorithms start by establishing discrete pixel matches (integer disparity map) and later refine these matches to sub-pixel precision, estimating a parabola fitting to the cost function. Once the analytical minimum cost is determined, the corresponding fractional offset is used to adjust the initial integer disparities. This process is very simple and yet efficient, but many studies (such as Nehab et. al., 2005, Psarakis et. al., 2005, Stein et. al., 2006) and tests reported that such strategy can lead to a systematic biasing towards integer values of displacements, also known as "pixel-locking (or peak-locking) effect". It produces random or coherent noise in the final reconstruction, introducing erroneous ripples or waves in the reconstruction of the disparity map.

In literature, several methods have been proposed to solve the pixel-locking problem and, since strong pixel locking effects occurred in most of the case studies performed to calibrate the algorithm, (Nehab et. al., 2005) strategy has been studied and later implemented in the proprietary SGM software code. The method proposes a symmetric approach in which both slave and master images are treated equal. The fundamental idea is to find the subpixel refinement by considering a 2-D neighbourhood of the matching cost around each matching pair and finding the optimal cut in the direction of the symmetric lines of the matching cost. Consider two rectified cameras C_1 and C_2 , producing images I_1 and I_2 of an object, such that the scan-lines in each image are corresponding epipolar lines, and defined the metric cost for comparing pixel values as M , we can define

$$F_y(x_1, x_2) = M(I_1(x_1, y), I_2(x_2, y)) \quad (8)$$

so that, instead of work in the disparity space, it is possible to work directly with image coordinates.

With the aim of capture the symmetry of the matching cost function (Figure 3 shows the matching ridge and how the cost functions are symmetric with regard to it), a 2D neighbourhood of matching cost values around (i_1, i_2) is considered, allowing to define a continuous surface $S(x_1, x_2)$ (see Figure 4).

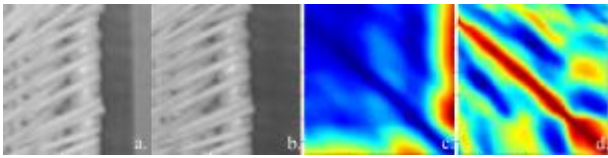


Figure 3. Examples of matching cost functions values and their symmetry w.r.t. the matching ridge. a. Master image; b. Slave image; c. SAD; d. NCC.

The surface can be well-represented by a Gaussian Cylinder (GC) representation (as described in (Nehab et. al., 2005)):

$$S(x_1, x_2) = G(D(x_1, x_2)) \quad (9)$$

$$G(d) = ae^{-d^2} + b \quad (10)$$

$$D(x_1, x_2) = s_1x_1 + s_2x_2 - p \quad (11)$$

since this surface enforces a ridge-like shape for the reconstruction. The parameters a, b, s_1, s_2, p can be determined by a non-linear least squares minimization system (composed by the derivatives of $G(d)$ in a, b, s_1, s_2, p) on the 3×3 neighbourhood around (i_1, i_2) . Once the GC has been estimated the correct coordinate match pair (x_1, x_2) for each pixel can be located directly on the matching ridge.

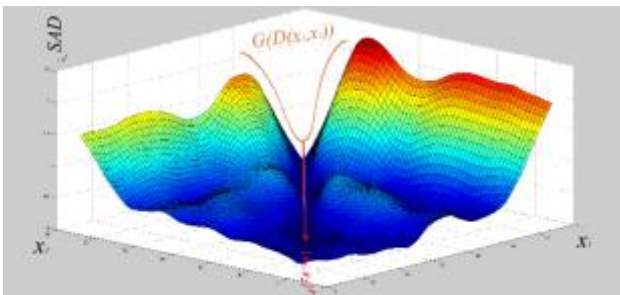


Figure 4. The continuous surface $S(x_1, x_2)$.

2.1.8 Multi-Image SGM extensions

Originally developed for image pairs correlation, the proposed SGM algorithm has been also extended to cope with Multi-Image configurations. The advantages of performing matching across multiple images have been pointed out in different studies where multi-image matching techniques were shown more robust and accurate than pairwise matching algorithm, thanks to the

redundancy of multiple view points. This is true in particular for 3D reconstruction tasks, where the need of the highest robustness/accuracy is more important than the achievement of real-time results.

The term “multi-image” can refer to different matching approach: two methodologies have been implemented and testes in this work of thesis to highlight their performances: a pairwise-based multi-image SGM implementation and an alternative Object Space based approach (OSGM). The first is a multi-baseline stereo method for producing dense depth map by performing pairwise stereo matching on all image pairs: the code initially identifies all the possible pairs of stereo images that build up the photogrammetric sequence and then performs the image correlation of each pair using epipolar rectified images. Considering n pairs of stereo images, the correlation process produces n depth maps that are individually re-projected, in our implementation to a common image plane. This operation is necessary for combining the n depth maps into a unique reference frame. Once the n depth maps have been merged, a median filter is used to filter out the noise: for each pixel of the overlapping depth maps, the depth values are sorted and the median is selected. The latter differs from the original SGM method in two major aspects: firstly, the cost calculation is formulated in object space (instead of in image space) within a dense voxel raster, and uses the radiometric values of all images concurrently, instead of pairwise cost data.

Similarly, the semi-global minimization process is performed into object space as well, since the result of the semi-global optimization directly represents the possible 3D positions of each points (the smoothness constraints have the task to perform the “regularization” of the object Z-coordinates, imposing the continuity of the object surface). Thus, the entire process leads to the generation of height-maps (instead of disparity maps) which indicate the 3D positions of the best matches.

3. ALGORITHM CALIBRATION

In order to get a better understanding of the relationships between all the algorithms variables (penalty functions, similarity cost functions, template size, etc.) a calibration of the algorithm's processing parameters was performed.

Several images datasets were used for studying the algorithm performances: (i) *synthetics images*: image rendering of simple three-dimensional computer generated objects, created in a 3D modelling software and draped with a texture (data are shown in Figure 6 (a–c–d)). For each dataset, images has been taken with different baselines, exposure and perspective effects and the matching performance has been evaluated by comparing the reconstructed parallax map with the original 3D model, considered as “ground-truth”; (ii) *Middlebury Stereo Evaluation Dataset*: high-resolution scientific image dataset (Scharstein et. al., 2014), with highly accurate ground-truth disparities, for stereo and multi-image matching applications, (in particular, the 2014 high-resolution datasets has been used). One case of study are visible in Figure 6 (e); (iii) *CyLab dataset* (Strecha et. al., 2008): high-quality datasets consisting of distortion removed images, known interior orientation parameters and reference laser scanning DSMs. In particular, the Fountain- P11 dataset has been used (see Figure 5 (f)).

The performed calibration tests have regarded in particular the following aspects:

(i) the algorithm accuracy: the SGM algorithm metric accuracy and reliability has been evaluated by comparing, for each case study, the reconstructed parallax map with the provided ground-truth disparities data (i.e. evaluating the algorithm accuracy in finding the corresponding point on image space). Information about the results quality has been acquired through the use of

suitable statistical indicators (such as for example the mean, median and standard deviation values of the differences between the reconstructed and the ground-truth disparity maps). As far as the three-dimensional reconstructed models are concerned, accuracy evaluation has been done by computing the distances between the reconstructed and the ground truth DSMs;

(ii) the results completeness and level of detail: the distribution of the reconstructed parallax values has allowed to evaluate the percentage of pixels whose errors are smaller than an established value: thus highlighting the results reliability in terms of “inlier and outliers percentage”;

(iii) the computational time of the whole matching process: since the computational efficiency of a matching algorithm is becoming a more summarized more influential factor, both SGM implementations (described in paragraph 2.1.5) are tested for analysing the time of the correlation process, in particular the time for computing the matching core step.

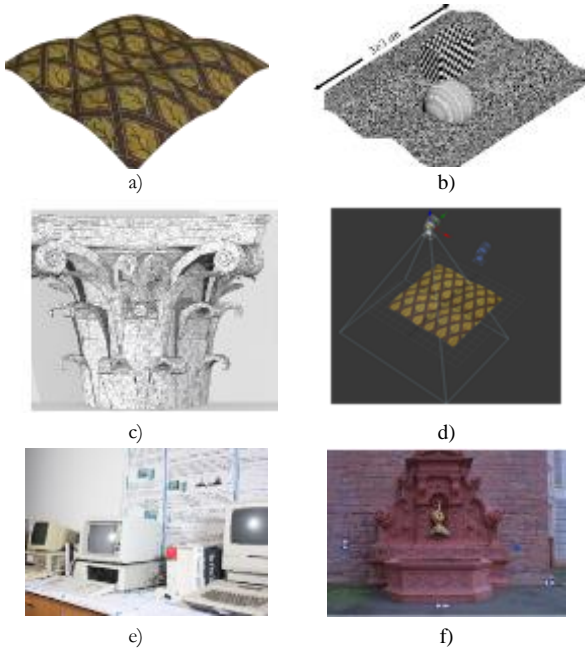


Figure 5. a)-b) Simple computer generated objects used as calibration dataset. c) Synthetic image of a 3D reference model. d) e) Example of Middlebury dataset. Real image of the P11-Fountain dataset.

Many are the SGM processing variables that considerably intervene in the metrological algorithm characterisation; namely, the correlation window size, the regularization and similarity cost functions, the penalty values analysis and identification, the use of multi-resolution and image tiling approaches, etc. Therefore, the following paragraphs will describe how the algorithm performances (in terms of results accuracy, completeness and time of calculation) are influenced by the above parameters. In the following, a summary of the more interesting results is presented

3.1 Algorithm accuracy evaluation

In this first stage, the simple computer generated object, shown in Figure 5 (a), was used as calibration dataset and tests have been computed considering the SAD cost function and full-resolution images (i.e. no image pyramid and tiling processes). First, the calibration of the implemented two penalization methods and their regularization factors (e.g. P_1 and P_2 for Hirschmuller formulation) has been performed.

In order to identify the best penalty values for allowing the correct application of semi global constraints, the accuracy of the method was tested by varying different combinations of penalty values (also with respect to the template size). The results are shown in the diagram in Figure 6, which has allowed the identification of the best values range that produces stable results.

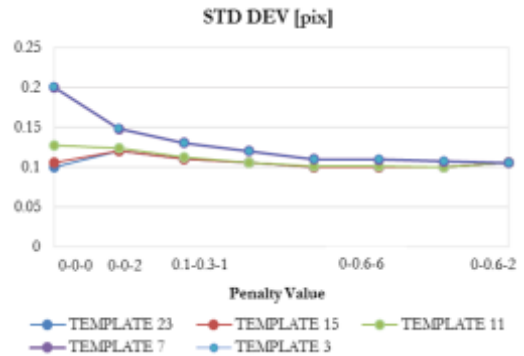


Figure 6. Penalty values calibration.

The diagram shows that the differences on varying the penalty values combination are light: standard deviation values vary in the range of 0.1 pixel. However, if small template size are used (e.g. 3 or 7 pixels window dimension) it is necessary to pay more attention on the penalty values to use in the correlation process. At the same time the results have allowed to assess a penalty value range that has been kept fixed, in the next tests, limiting the number of varying parameters.

A second investigation has regarded the two different penalization function developed in the proprietary software (as described in paragraph 2.1.4): their performances were tested and compared showing practically corresponding accuracies for each examined template size. Thus, in all subsequent algorithm tests, the Hirschmuller defined penalty function was used.

The next testing stage has evaluated the influence of the similarity functions on the final accuracy. For each function also the influence of the template size have been considered. The ideal block size to perform the stereo matching depends on the chosen function: the tests have been conducted using the same synthetic dataset which, not presenting discontinuities, allows to better analyse the influence of the template size on the final parallax accuracy (with bigger template sizes, in fact, object shape discontinuity are likely to produce gross errors). The diagram shown below (Figure 7) allows to observe the variations of the standard deviation w.r.t. the template size.

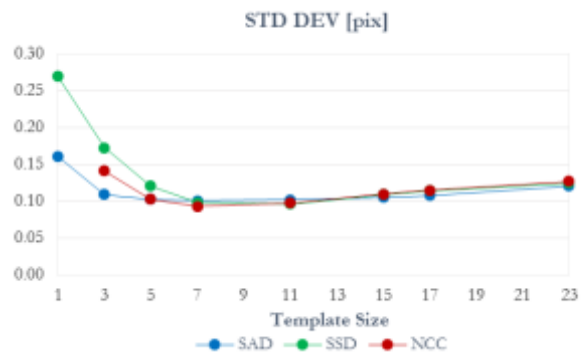


Figure 7. Accuracy of the similarity functions by varying the window template size.

As expected, the enforcement of the disparity continuity allows to obtain comparable results between the evaluated cost functions, showing a light improvements of the accuracy with the increase of the template size. Looking at the diagram, there seems

to be an optimal windows size beyond which the cost functions seems to produce less accurate and reliable results. However, it's worth noting that the maximum differences in the registered standard deviation values are slightly more than one tenth of pixel and the use of NCC with small block size has produced isolate outlier which were removed from the estimation. Finally, the accuracy of the second memory efficient SGM algorithmic implementations (see 2.1.5 paragraph) has been investigated w.r.t. the first implemented method. The following diagram shown in Figure 8 presents an evaluation of each solution accuracy.

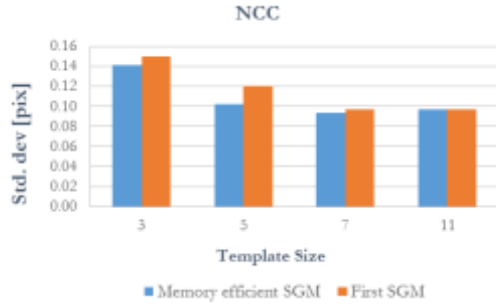


Figure 8. Comparison between the accuracy of the two implementation of SGM: the first implementation and the memory efficient variation.

The results show again the improvement of the accuracy with the increase of the window size: this is evident in the NCC behaviour while the same cannot be said for the SAD cost function, which maintains constant performances for template size greater than 3 x 3 pixels. As regard the accuracies comparison between the two strategies, the novel more efficient implementation seems to be as accurate as the first SGM implementation.

3.2 Algorithm completeness evaluation

A second calibration stage has regarded the study of the algorithm capability of obtaining complete results. The algorithm has been tested, in this context, on the Middlebury datasets, since stereo pairs show characteristics that often generate problems at the matching algorithm in terms of reconstruction abilities. Tests were performed on two dataset ('Playtable' and 'Vintage' cases) using two different similarity functions, no image pyramiding and tiling, and the Hirschmuller penalization method with fixed penalty factors (the optimal set of parameters were previously identified with the tests shown in the previous paragraph). The diagrams shown in Figure 9 present the results of the algorithm completeness of reconstruction capability for the 'Playtable' case ('Vintage' case has shown similar results). The distribution of the parallax errors (evaluated with SAD, NCC, Rank and Census costs functions) has been reconstructed by highlighting the percentage of "inlier" pixels whose errors are lower than 0.5, 1, 2, 4 and 8 pixels respectively. Higher percentage (values) represent thus better results. As far as the two non-parametric Rank and Census transformation are concerned, images have been transformed applying the Rank metric on a 9 x 9 pixels template size and, after that, the correlation has been performed with NCC and SAD cost functions. On the other hand, for Census, the transformation has been performed using a 5 x 5 pixels window size and the matching process has been performed on the Census-transformed images with SHD metric. Both for the SAD and NCC cost functions, the parallax completeness increase with the use of big template size but, the SAD similarity function shows better results since the inlier percentage values, for each considered inlier threshold, are greater than the NCC results. It is interesting to notice that, with

the increase of the window size, NCC data tend more and more towards high accuracies, thus there is a continually improvement of the cost function performances.

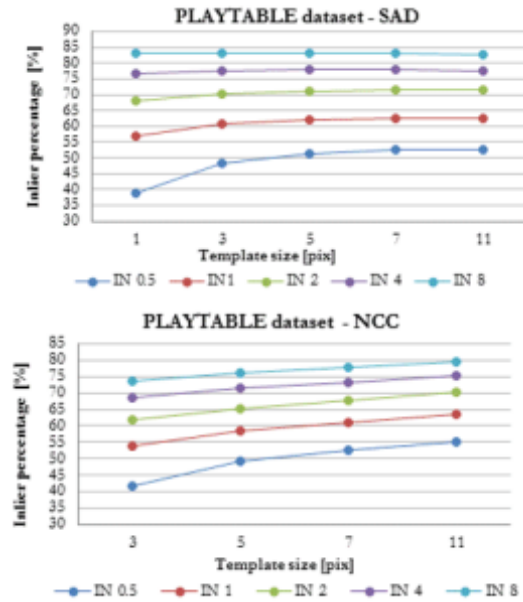


Figure 9. Results of the "Playtable" dataset: Percentage distribution of the inlier parallax values whose errors are lesser than 0.5, 1, 2, 4 and 8 pixels respectively, by using the SAD cost functions.

Differently, SAD completeness levels becomes constant for template greater than 5 pixel. The NCC behaviour can be justified considering the peculiarity of the Middlebury images. In fact, in presence of low contrasted areas, repetitive patterns and constant brightness regions the NCC statistical indicator does not have enough information, with small templates, to produce reliable results. On the contrary, the formulation of the SAD cost function allows performing a better investigation of corresponding luminosity areas (even if low or no-texture are present), while it produces less reliable and accurate results in areas with high contrast and luminosity differences between the images. However, with the use of medium-large template size, the NCC performance can improve significantly thanks to the increase of the radiometric information within the correlation window. A more direct comparison between all the evaluated cost functions results, with regard to the 4 and 0.5 pixels "inlier" percentage (that threshold is considered as a good tolerance ranges for the completeness evaluation with these datasets) is shown in in Figure 10. Looking at the histograms, the worse results are achieved by the Rank cost functions. Anyway, the results trend is similar to the previous SAD and NCC ones, since the completeness levels increase along with the template window size. On the other hand, the Census behaviour shows good results, which are slightly worse than the SAD cost function (that remains the "winner metric") but significantly better than NCC solution with regard to the 4 pixel inliers percentage (Figure 10top). The metric shows thus a good robustness with respect to outliers identification but, at the same time, it proves to be less accurate (see Figure 10bottom) than the other similarity measures. As far as the "Vintage" study case is concerned, a noticeably gap between the cost functions results is shown for each template size under evaluation and, at the same time, the depicted completeness levels are significantly lower. The images "Vintage" dataset has shown thus worsen radiometric characteristic for the matching algorithm capabilities, than those

characterizing the first case. However, comparing the proprietary semi-global algorithm performance with other SGM implementations presented in the Middlebury Stereo Results library, the in-house method shows comparable performance with respect to other strategies.

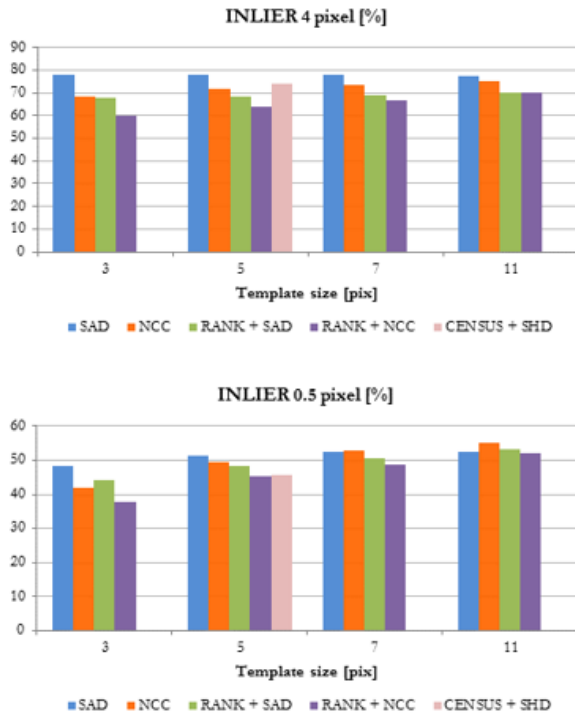


Figure 10. Results of the “Playable” dataset. Comparison between the NCC, SAD, Rank and Census cost functions results, with regard to (top) the 4 pixels “inlier” percentage; (bottom) the 0.5 pixels “inlier” percentage.

3.3 Algorithm computation time evaluation

In this paragraph the process efficiency is considered. In particular, the second SGM implementation, which was developed for obtaining a much faster disparity penalization procedure, has been tested and compared with the first algorithmic implementation. It is important in this analysis to distinguish between the three stages that characterize the matching solving process, namely: the costs computation, the disparity penalization and optimization steps. This proves to be important since the novel more efficient SGM strategy modifies, with significantly lower computational load, the cost data penalization processing stage. Differently, the matching costs analysis and the disparity minima search steps are unchanged between the two SGM approaches.

In the previous diagrams shown in Figure 8, the novel improved SGM algorithm has proved to be as accurate as the previous one. Figure 11 presents instead an evaluation of the novel memory efficient SGM algorithm improvements (in terms of computational time) with respect to the oldest one.

The diagrams show a noteworthy enhancement of the algorithm efficiency: the matching cost stage increase quadratically with the template size both for the two SGM approaches but it is evident the improvement of the novel strategy with respect to the old one in the costs penalization (about 12 seconds instead of the 70 seconds of the oldest method). It is also important noting that, in both cases, the disparities penalization and optimization steps (depicted in orange and grey respectively in the histograms) require the same computational time for each considered template, since the efficiency of these process do not

depend on the size of the correlation window. At the same time, it has been proved that, changing the disparity search range, the total time for performing the penalization step is obviously higher with wider ranges, but the gain w.r.t. the old implementation is basically constant.

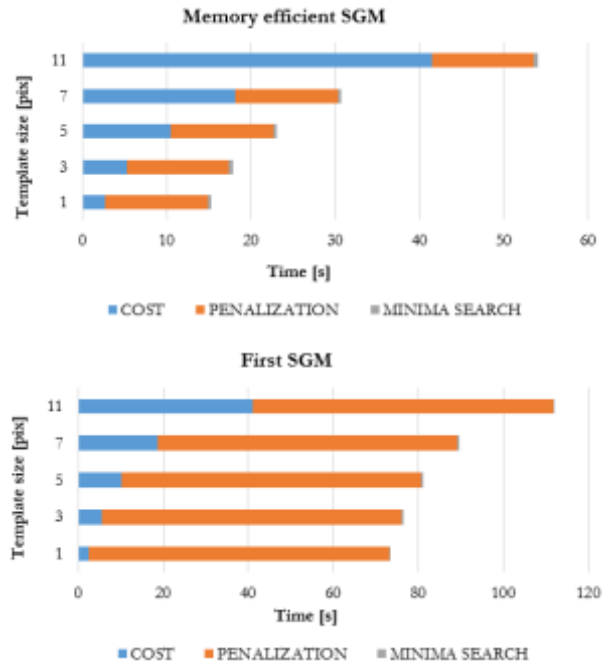


Figure 11. Computational time (in seconds) to process a single image pair, employing SAD similarity functions with different template sizes: a comparison between the novel memory efficient SGM algorithm and the first SGM implementation.

3.4 Evaluation of the sub-pixel refinement accuracy

The simple computer generated object used as calibration dataset, has allowed the clear identification of pixel locking phenomena. Indeed, comparing the “true” disparity map (or ground truth) with those obtained by the method using the three implemented cost functions, a sort of staircase pattern has been observed.

Usually pixel locking is associated to numerical behaviour of the sub-pixel disparity refinement strategy at the end of the matching procedure. For this reason, we have chosen to implement a different refinement strategy where the disparities sub-pixel investigation is performed not with the traditional parabola fitting method (see paragraph 2.1.7 for more details) but with the improved “sub-pixel symmetric refinement”.

The identification of the results biasing towards integer values of displacement can be quantified, as is described in (Overmars et al., 2010), as:

$$C = 1 - \frac{N_{min}}{N_{max}} \quad (12)$$

where N_{min} and N_{max} are the lowest and highest number of counts in the fractional histogram. $C = 0$ indicates complete absence of pixel locking, while $C = 1$ indicates very strong pixel locking. Following, the histogram of the fractional part of the displacement obtained with the novel refinement strategy is shown (Figure 12) compared to that obtained with parabola fitting strategy.

The histogram displays a more irregular distribution of the displacements fractional components, resulting in the improvement of the pixel locking degree index. It is worth nothing that the indicator $C=0.75$ can be quantified, according to (Overmars et al., 2010), as “severe” pixel locking, while a degree

of 0.46 reveals that the result is lightly affected by the locking effect ($C=0.4$ is classified as “mild” degree of pixel locking). Looking at the parallax maps, the new strategy reaches smoother results and, concurrently, the staircase pattern (very evident in the case of the parallax maps obtained with parabola fitting method) is less marked.

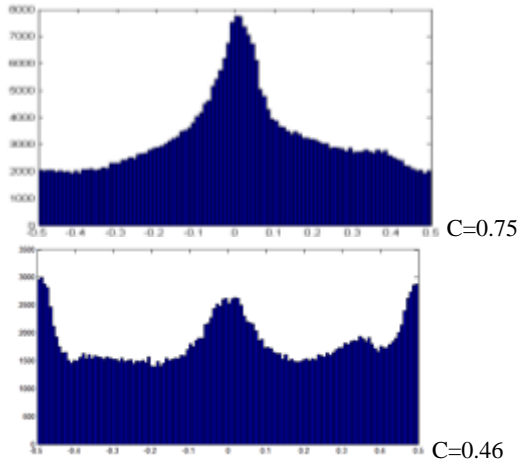


Figure 12. The histogram of the fractional part of the displacements: on the top the results obtained with parabola fitting sub-pixel refinement, on the bottom the results obtained with sub-pixel symmetric refinement method.

3.5 Tiling and Multi-resolution strategies evaluation

A final calibration stage has regarded the evaluation of the accuracy and reliability of the image pyramiding and tiling strategies, employed at the start of the matching workflow for improving the algorithm computational performance.

As far as the tiling performances analysis is concerned, it has been proved that, as expected, even if the tiling process allows reducing the computational efforts of the matching procedure, enabling the simultaneous processing of each tile in parallel, the final quality of the results is a little lower. This is due to the overlap size between adjacent tiles: for well textured scenes an overlap of 20-40 pixels, like the one used for the tests, is sufficient. However, low-textured area or high depth differences in the scene require a higher overlap. The reason of this lies in the fact that the matching solution of the pixels within the overlapped areas can be not well-estimated since the matched points, within these areas, can have not according disparity values in the two different tiles, and the blending procedure can produce inaccurate and noisy results. A good habit to follow may be to use not too small tiles, in order to reduce as much as possible the overlapping areas.

Differently, the performance of the multi-resolution approach has been evaluated considering one-level and three-levels image pyramids in the tests processing. Results, described in Figure 13, show the increase of the standard deviation values of the differences between the ground truth disparities data and obtained final disparity map with the increase of the correlation window size. This is particularly true for medium-large template sizes (bigger than seven pixels).

The use of big template produces the flattening of the images disparities data (the same can be said in terms of depth information), reducing the algorithm capabilities in reconstructing object fine structure and details and increasing the probability of passing wrong information from one level to the next. Furthermore, the image interpolation process intervenes: once the initial low-resolution parallax map has been obtained, a

bilinear interpolation of parallax values between matched conjugate points is computed and utilized as approximate parallax map useful to perform the matching process with the new higher resolution image pairs. Thus, the inaccuracies introduced by the computation of image costs with big template size, together with the image pyramids resampling process, introduce errors that accumulate until the method reaches the original image level, producing lower accurate results.

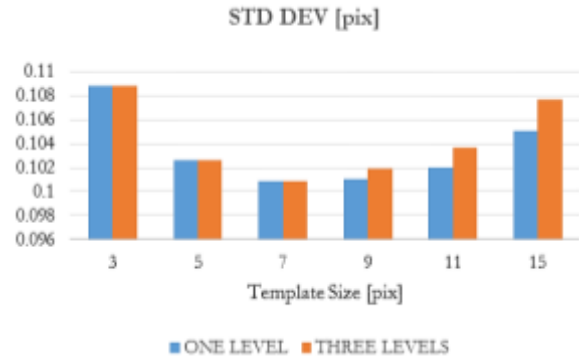


Figure 13. Comparison of the results obtained considering the image matching process with and without the application of the multi-resolution approach: evaluation of the accuracies by varying the window template size.

As regard the computational efficiency improvements as concerned, a significant gain in terms of process time using the multi-resolution approach has been proved.

It is also important considering that the image-pyramids employment offers considerable advantages (in process efficiency) the wider is the disparity search range. In the case of a 250 and 750 pixels disparity ranges, the multi-resolution method is respectively 10 and 20÷25 times faster than the full-resolution approach applied in the same process conditions.

It is possible to say that the use of image pyramids has undoubtedly a key role in correlation processes of high-resolution images (such as, for example, the planetary ones) where high disparity search ranges are needed. Moreover, this strategy has proved to be an essential step of the 2D SGM method workflow because of the quadratic increase of the image points search domain size.

4. TESTS OF SGM SOFTWARE CODE FOR SURFACE RECONSTRUCTION

Tests on real and synthetic images have been performed, evaluating the accuracy of the obtained digital surface models. The comparison has basically two main objectives: first of all, checking the accuracy of the SGM proprietary implementation, and getting insight on the influence of some matching variables in the process. Second, comparing the accuracy and completeness of the digital models obtained using the proprietary code with other commercial and open-source matching programs. The comparisons want also to consider the completeness and the level of detail within fine structures, and the reliability and repeatability of the obtainable data. Where it is not specified, all the used codes/algorithms have considered only stereo pairs in order to identify the correlation performances of each strategy. Following the most interesting case of study are illustrated.

4.1 Comparison of dense matching algorithms

Different algorithms and implementations are considered in the study: freeware software codes (e.g. MicMac (Pierrot Deseilligny et. al., 2011) and OpenCV (OpenCV library, 2016)),

commercial software (e.g. Agisoft PhotoScan - PS (PhotoScan, 2016) and proprietary codes implementing Least Squares matching (LSM) and SGM algorithms.

Tests have been performed on real and synthetic datasets having a 3D reference DSM. In order to obtain comparable solutions, the models were generated using the same known internal and external orientation parameters, making the results as independent as possible from the automatic orientation procedure. Finally, the distances between the reconstructed and the reference DSM have been evaluated to perform the comparison.

The relative accuracy of the reconstructed DSM, with synthetic ('3D Shapes' and 'Capital' cases) and real images ('Fountain' case), is summarized in Table 1 where, for each test case, statistics of the distances between reconstructed and reference DSM are presented. To make the results independent of the total size of the object all the distances standard deviations are normalized with respect to the best value ("Normalized relative accuracy"). At the same time, some methods present, in some areas of the model, very evident gross errors that must be removed from the relative accuracy computation. On the other hand, it's important to highlight which algorithm produces more reliable results (in terms of "inlier percentage"): for each model, tolerance ranges were selected based on some assumption about image matching (and consequent reconstruction) a-priori precision and on the actual performance of the best method. In particular (1 cm for 3D Shape, 3 mm for Capital and 3 cm for the fountain case study ranges) are selected considering that at least one algorithm must produce a 90% in-tolerance 3D model: in this way reconstruction accuracy is related to a sort of quality completeness for each method.

Table 1 shows that, for each test case, the different matching algorithms produce results that are not dramatically different.

	Test cases	LSM	Open CV	PS	SGM	Mic Mac
Normalized relative accuracy	3D Shapes	100	92	91	83	94
	Capital	100	85	83	71	81
	Fountain	90	97	100	89	90
Inlier percentage	3D Shapes	86.9	91.4	88.7	83.2	80.9
	Capital	77.5	92.7	89.27	70.1	66.8
	Fountain	84.6	88.7	97.5	86.5	88.1
Lacks of completeness	3D Shapes	*	NO	***	NO	NO
	Capital	*	NO	*	NO	NO
	Fountain	**	NO	NO	NO	NO
Pixel locking	3D Shapes	***	***	***	***	NO
	Capital	*	**	**	*	*
	Fountain	n/a	n/a	n/a	n/a	n/a

Table 1. Statistics of the reconstructed DSM.

The general trend is similar, though not identical, in particular for computer-generated data. Analysing the first two tests, we can identify that the best solution were obtained by LSM, followed by OpenCV, PhotoScan and SGM. For '3D Shape' case, lack of completeness problems were found, in correspondence to high depth changes, in PhotoScan DSM. Therefore, it is worth noting that low values of discrepancies from the reference model, derived from standard deviation information, cannot be the only indication of the digital model reliability but we have to evaluate the completeness and surface distribution of the points.

Wishing to make a summary of the tests results, it is possible to say that the error maps of LSM (all the maps cannot be presented

in this short thesis summary) usually shows more noisy data, due to its pointwise estimation approach: while semi-global-like methods constrains (with different degree of enforcement) the regularity of the disparity field, every point in LSM methods are considered and evaluated individually. On the other hand, the reconstructed DSM reveals the LSM ability to produce accurate results, as shown not only from standard deviation (see Table 1) but also from spatial distribution of the distance values. However, the disparity regularity constraints (and smoothing filtering procedure – e.g. those implemented in the PS workflow) can generate erroneous systematic surface reconstruction (which must be taken into consideration), if image noise, occlusions, repeated pattern influence a whole matching path.

4.2 Active landslide monitoring in Mont de la Saxe (AO)

The study object is the landslide of Mont de la Saxe in Courmayeur, which is considered one of the most complex landslides in Italy. In (Roncella et al., 2015), authors have been presented a fixed terrestrial stereo photogrammetric system based on a LSM algorithm and developed to monitor shape changes of the scene. However, it has been estimated that the whole process (a service running on a host remote server waits for incoming images from both stations; once a synchronous image pair is available, the DSM generation sequence is activated) taken about 15 minutes on a medium performance server with eight processing cores to produce a DSM with on average 600-700 thousand points. In this regard, the new SGM algorithm was considered a strategic improvement of the processing pipeline since can provide in much less time (ca. 6 minutes) a more dense surface model (the matching can be performed pixel-wise) and is capable of filtering most of the noise connected to low-texture, presence of vegetation or snow, different luminosity conditions (the shoots are not perfectly synchronized) just implementing the regularity constraints.

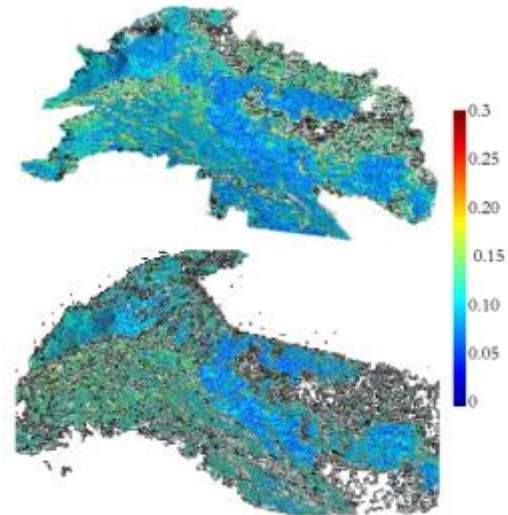


Figure 14. Map of slope displacements (in m) between the 11th and 22nd September. On the top, the results obtained with SGM digital surface models; on the bottom, those obtained with LSM digital surface models.

In order to evaluate the SGM algorithm repeatability, two image pairs of the landslide, taken at a short time distance (the first was shot the 11th September 2014, the second to the 22 September 2014), were analysed, comparing the results obtained with the authors implemented LSM strategy and the novel SGM approach. As far as the quality of the reconstructed DSMs is concerned, it has been demonstrated that the SGM solution

reaches a more accurate and complete surface reconstruction. However, comparing the LSM and SGM solutions a good agreement is shown: most of the surface differences are in the range of ± 5 cm.

After the analysis of the SGM method reliability, the algorithm was tested in the condition required by the monitoring application, i.e. comparing the 11th and 22nd September DSMs for evaluating the landslide displacements during such period (see Figure 14*top*). The same map has been obtained using the two LSM digital surface models for a further visual comparison of the two strategies performances (Figure 14*bottom*). The results confirm the considerations just made: there is a good agreement between the displacements measured by the two methods. Summarizing, during the short considered time period, important slope movements were not observed and just some areas presents medium-high displacements that reach 30 cm. These regions are probably rocks or small stones that collapsed.

Overall, the SGM method appears more accurate and complete, with respect to the LSM: the lower noise level makes the results more complete and detailed. Its employment within the image processing workflow of the photogrammetric monitoring system might allow reaching a higher quality and higher frequency monitoring of the landslide.

4.3 Surface reconstruction of Parma Baptistery zoophorous

An accurate close-range photogrammetric survey was computed to generate high-resolution DSMs of the Benedetto Antelami zoophorous: it is a series of seventy-five sculpted panels in red Verona marble, realized with bas relief technique on the lower level of the external marble façade of the Baptistery of Parma.

A Nikon D3X camera, with 50 mm and 105 mm optics and image resolution of 6048 x 4032 pixels, was used for the photogrammetric investigation. The baptistery zoophorous was firstly surveyed with the 50 mm focal lens reconstruct the whole zoophorus and after, for each panel, sequences of about three-four frames each were taken with the 105 mm optic for having an high-resolution description of the panels details.

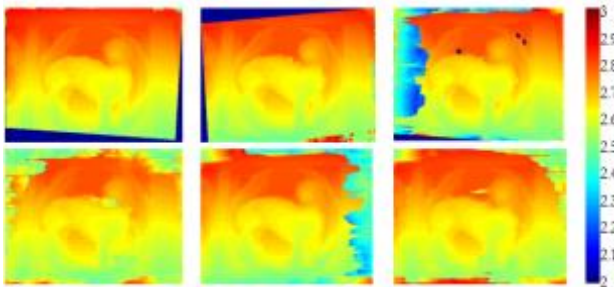


Figure 15. The six depth maps [m] obtained with the pairwise SGM proprietary algorithm.

The attention was focused on the photogrammetric survey of each individual panel performed with the macro optic where only three photographs from different perspective views were acquired. The case of the “Lion” panel is following described. For obtaining the DSM, the proprietary SGM code has been applied in the multi-image pairwise software variation. Being the sequence composed by three images, the method identifies six possible stereo image pairs and, for each one of these, the correlation process with the SGM algorithm is performed, obtaining as output the six depth maps presented in Figure 15. Once the depth maps have been obtained, the method proceeds to the data combination for the achievement of a unique result. Once the final result is produced, the digital surface model can be easily reconstructed (Figure 17 on the left).

In order to have an evaluation of the method accuracy and reliability, the lion mesh has been compared with that obtained from the sequence processing in PS. The comparison result is presented in Figure 16. It is possible to say that the results are almost identical: the lion body is well reconstructed by both the applications and the majority of the differences regards object discontinuity (such as the panel boundaries and small local details) where a discrepancy of about ± 0.1 mm is revealed. Higher differences (that reach up to ± 0.3 mm) characterize the occluded regions where our algorithm, differently from PS, doesn't provide post-processing tasks capable of filling holes and smooth surfaces.

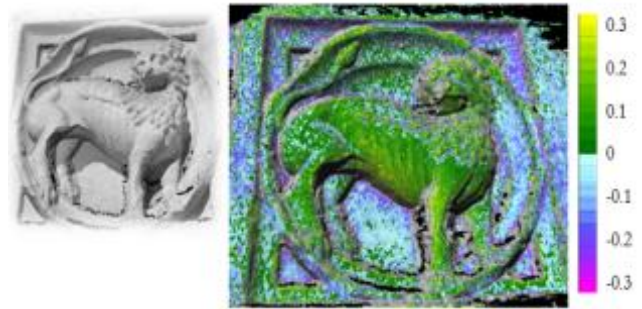


Figure 16. On the left the DSM of the “lion” panel and the comparison (on the right) between the reconstructed DSM obtained using the multi-image SGM and PS software [mm].

A final investigation has regarded the comparison with the LSM method employed using only a one stereo-pair. This test allowed analysing the different behaviour of the algorithms with regard to the robustness of the stereo matching methods in correlating images characterized by high depth and perspective changes and, moreover, to evaluate the lacks and the qualities of both the LSM and SGM methods. As expected, LSM model have presented lack of completeness problems and noisier reconstructed surfaces. On the contrary, the SGM strategy shows its abilities in regularizing object shape and detecting points on high discontinuities and depth changes. However, in this kind of applications where the examined objects present high depth variations and, at the same time, require high completeness level, the multi-image method represents a better strategy than stereo correlation.

5. TESTS OF STEREO SGM SOFTWARE CODE FOR 2D DISPLACEMENTS DOMAINS

The novel algorithmic extension to a bi-dimensional correspondences research through images was applied and verified in different areas of engineering interest, starting from motion tracking of particles within fluids (PIV-Particle Image Velocimetry application), to the mechanical behaviour of materials (DIC-Digital Image Correlation application), up to the 2D displacement field reconstruction of rock glaciers surface. Unfortunately, for brevity needs, one case only will be following presented.

What is common to all these applications is the search and the inspection of the continuous displacement field: in fact, the images points tracking through two or more images can give a complete and accurate description of the variations between different temporal epochs. Therefore, the image correlation with the use of the semi-global algorithm can be an appropriate method since that the hypothesis at the base of the algorithm (i.e. the regularity of the displacement field between adjacent pixels) perfectly fits the physical geometry of these problem. The method variation for performing 2D correspondences search has been applied in the applications above introduces, and its

performance has been always compared with the local LSM method one for evaluate the novel algorithm reliability.

5.1 Rock glacier monitoring system

An evaluation of movements and volumetric changes of an Italian rock glacier, obtained by multi-temporal analysis of UAS images over the period 2012-2015, has been investigated. The study area is located in the western Alps at the head of the Valtournenche Valley (Valle d'Aosta, Italia) on the Italian side of Matterhor. The body of the rock glacier is composed by two lobes, spanning an elevation range between 2600 and 2750 m. It is nearly 400 m long, between 150 and 300 m wide and has an apparent thickness (based on the height of the front) of 20-30 m. The current dataset of observation consists of three UAS flights (October 2012, October 2014 and July 2015) and three GNSS campaigns (mid August 2012, 2013, 2014); mayor information about the case of study can be found in (Dall'Asta et al., 2016). The reconstruction of the rock glacier surface movements is obtained by comparing the orthophotos and the DSM of the three UAS photogrammetric surveys of the investigated area. The photogrammetric workflow has allowed to obtain three raster DSM (with a cell size of 20 cm), and three different sets of orthophotos of the inspected region, with 5 cm pixel size. The orthophotos were analysed to identify the rock glacier displacements using two different methods: (i) a manual identification of well-recognizable points (on the glacier surface) on the orthophotos of three epochs; (ii) an automatic tracking method able to recognize a dense grid of corresponding points between the images (through image correlation analysis).

The automatic procedure can be applied directly to the orthophotos. However, the application of area-based matching algorithms on orthophotos can lead to inaccurate and erroneous matching results since image texture changes, low contrast regions, radiometric transformation problems and, especially, slope illumination variations over the monitored period can worsen the matching algorithms performance. The best way to address the problem would probably be to match the two height maps directly: even if lighting or texture changes occurs in the monitoring period the matching algorithm would not be affected working only on the shape of the glacier surface.

Although the vast majority of commercial or free software expect to work on 8 bit image data, the new SGM algorithm are able to perform the correlation process taking in input also 32-bit floating point rasters, so all the previous limitations are overcome. Following, the results of the automatic tracking of the displacements are presented: data validation has been performed by comparing the achieved displacement vector with those acquired with the manual measurement process (such comparison, being measured on 5 cm orthophotos resolution, can be considered the most suitable and accurate comparison data at the time being).

Tests have regard the following two monitoring periods: a two-years period between October 2012 and October 2014, and a one-year survey between October 2014 and August 2015. The results has been obtained using LSM proprietary algorithm and the novel SGM strategy, with the aim to compare the solutions and thus verify the SGM reliability.

The two-years case results are illustrated in Figure 17, which combined the rock glacier displacements and the relative displacements scatterplot in order to validate the automatic measurements against the manual ones; in Table 2 a summary of the comparison statistics is also presented.

The measurements validation has been performed on 785 points for the LSM solution and 872 points for the SGM one, in the case of two-years monitoring activity and on 881 points (LSM solution) and 996 points (SGM solution), in the one-year

monitoring. The results are very good (Table 2): the R² correlation index indicates a good correlation between the automatic and the manual measurements in both cases, and the Root Mean Squares Error (RMSE) is also good, showing values lower than 12 cm, which approximately corresponds to half pixel of the analysed raster DSM cell size (of 20 cm). In other words, in these two cases, the methods have demonstrated that dense displacement fields, by tracking automatically homologous areas in raster DSMs, can be obtained with accurate and reliable results and sub-pixel precision. At the same time, it is interesting to notice that the SGM strategy achieves, in all the investigated cases, greater inlier percentage: the introduction of the displacements regularization constraint allows to reduce the presence of mismatches and outlier and thus the statistic can be computed considering bigger data samples.

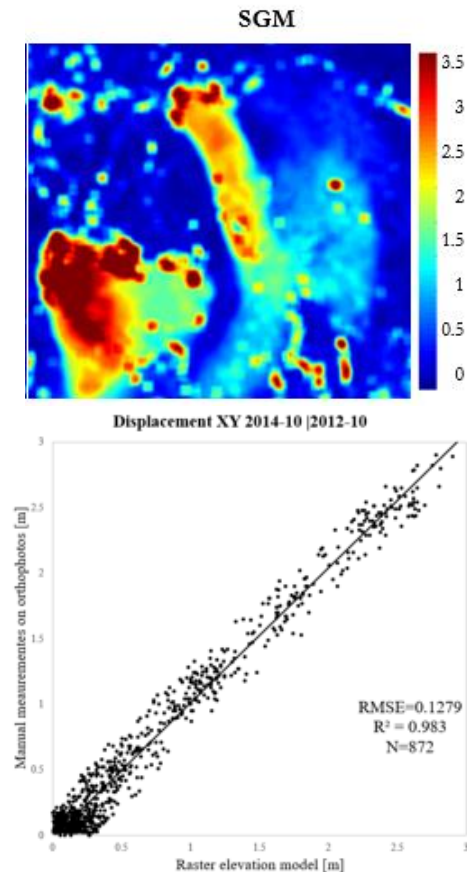


Figure 17. Two-years monitoring activity. *Top*: 2D Displacement [m] coloured map calculated automatically with SGM algorithm; *Bottom*: Scatterplot of displacements obtained from the automatic comparison of DSM and the manual displacement.

		RMSE	R ²	N
Two-years monitoring	LSM	0.122	0.977	785
	SGM	0.127	0.983	872
One-year monitoring	LSM	0.115	0.948	881
	SGM	0.128	0.940	996

Table 2. Summary of the comparison statistics between the automatic DSM comparison technique and the manual identification of the displacements.

With the proposed automatic methodology, a very detailed description of the creep/displacement behaviour of the glacier can be produced.

CONCLUSIONS

This work has been essentially directed to verify the actual capability of a proprietary implemented Semi-Global Matching software code, mainly aimed at three-dimensional surfaces reconstruction. The choice to develop and implement a proprietary algorithm is justified from the desire of maximizing the matching method accuracy and results completeness, paying attention to the process computational efforts as well and the results of the algorithm calibration stage, performed on several image datasets, has allowed to verify all the above described strategy variables.

After the first method calibration and characterization stages, its performance was tested in real applications fields, where problems related to image radiometric content, points visibility, lacks of completeness and the achievement of established metric precisions, significantly intervene. The method achieved not only complete and appealing digital surface/terrain models, showing its higher robustness w.r.t. area-based local method, but also highly accurate reconstructions. This concerns both the developed semi-global implementations for surface reconstruction, i.e. the classical stereo approach, and the SGM variation for the 2D displacement domain analysis. In fact, the algorithm metrological characterization stage and the development of computational optimized strategies has allowed a continuous improvement of the algorithm performances and the possibility to extend the method to the 2D search of image correspondences. Finally, the multi-image algorithmic extensions have also been tested successfully in dense surface reconstruction in different application fields and images acquisition configurations.

Although several image matching open source and commercial applications are available in the photogrammetric images processing panorama, the choice to completely develop the semi-global software code has originated from the need to better acquire competence and knowledge about the several variables and strategies that are involved and influence the image matching process. The use of a proprietary source code has the advantage of allowing the complete control of the process: the problem solutions can be adapted to the user needs, the data input quality, the application field, the precision and accuracy of the results and the required time of process.

REFERENCES

- Barnard, S. T. & Fischler, M. A. (1982). Computational stereo. *ACM Computing Surveys (CSUR)*, 14(4), 553-572.
- Birchfield, S. & Tomasi, C. (1999). Depth discontinuities by pixel-to-pixel stereo. *International Journal of Computer Vision*, 35(3): 269-293.
- Cox, I. J., Roy, S. & Hingorani, S. L. (1995, October). Dynamic histogram warping of image pairs for constant image brightness. In *Image Processing, 1995. Proceedings., International Conference on IEEE*, Vol. 2, pp. 366-369.
- Dall'Asta, E., Forlani, G., Roncella, R., Santise, M., Diotri, F., & di Cella, U. M. (2016). Unmanned Aerial Systems and DSM matching for rock glacier monitoring. *ISPRS Journal of Photogrammetry and Remote Sensing*.
- Fryer, J. G., & Brown, D. C. (1986). Lens distortion for close-range photogrammetry. *Photogrammetric engineering and remote sensing*, 52(1), 51-58.
- Hartley, R.I. & Zisserman, A. (2000). *Multiple View Geometry in Computer Vision*. Cambridge University Press, Cambridge.
- Hirschmuller, H. (2005, June). Accurate and efficient stereo processing by semi-global matching and mutual information. In *Computer Vision and Pattern Recognition, 2005. CVPR 2005. IEEE Computer Society Conference on IEEE*, Vol. 2, pp. 807-814.
- Hirschmuller, H. (2008). Stereo processing by semiglobal matching and mutual information. *Pattern Analysis and Machine Intelligence, IEEE Transactions on*, 30(2), 328-341.
- Nehab, D., Rusinkiewicz, S. & Davis, J. (2005, October). Improved sub-pixel stereo correspondences through symmetric refinement. In *Computer Vision, 2005. ICCV 2005. Tenth IEEE International Conference on IEEE*, Vol. 1, pp. 557-563.
- Open Source Computer Vision Library (last accessed 19.12.2016). StereoSGBM C++ code. <https://github.com/Itseez/opencv>.
- Overmars, E. F. J., et al. (2010). Bias errors in PIV: the pixel locking effect revisited. In: *15th international symposium on applications of laser techniques to fluid mechanics, Lisbon, Portugal*, pp. 5-8.
- OpenCV 2.4.8 StereoSGBM method, single-pass variant. (2006). Reimplementation and modification of H. Hirschmüller's SGM method In *CVPR 2006; PAMI 2008*.
- Pierrot Deseilligny, M. & Clery, I. (2011). *Apero, An Open Source Bundle Adjustment Software For Automatic Calibration And Orientation Of Set Of Images*. In *IAPRS Vol. XXXVIII-5/W16*, Trento.
- PhotoScan. (2016). Algorithms used in Photoscan (last accessed 19.12.16). <http://www.agisoft.ru/forum/index.php?topic=89.0>.
- Psarakis, E. Z. & Evangelidis, G. D. (2005, October). An enhanced correlation-based method for stereo correspondence with subpixel accuracy. In *Computer Vision, 2005. ICCV 2005. Tenth IEEE International Conference on Vol. 1*, pp. 907-912.
- Roncella, R. & Forlani, G. (2015). A fixed terrestrial photogrammetric system for landslide monitoring. In *Modern Technologies for Landslide Monitoring and Prediction*, pp. 43-67. Springer Berlin Heidelberg.
- Scharstein, D. & Szeliski, R. (2002). A taxonomy and Evaluation of Dense Two-Frame Stereo Correspondence Algorithms. *International Journal of Computer Vision*, 47 (1/2/3), pp. 7-42.
- Scharstein, D., Hirschmüller, H., Kitajima, Y., Krathwohl, G., Nešić, N., Wang, X. & Westling, P. (2014). High-resolution stereo datasets with subpixel-accurate ground truth. In *Pattern Recognition*, pp. 31-42. Springer International Publishing.
- Schenk, T. (1999). *Digital Photogrammetry: Volume I*. TerraScience, Laurelville, Ohio, USA. 421 pages.
- Stein, A. N., Huertas, A. & Matthies, L. (2006, May). Attenuating stereo pixel-locking via affine window adaptation. In *Robotics and Automation, 2006. ICRA 2006. Proceedings 2006 IEEE International Conference on IEEE*, pp. 914-921.
- Strecha, C., vonHansen, W., Gool, L. V., Fua, P. & Thoennessen, U. (2008, June). On benchmarking camera calibration and multi-view stereo for high resolution imagery. In *Computer Vision and Pattern Recognition, 2008. CVPR 2008. IEEE Conference on IEEE*, pp. 1-8.

UAS PHOTOGRAMMETRIC BLOCKS: ACCURACY, GEOREFERENCING AND CONTROL

M. Santise^a

^a ¹ DICATeA, University of Parma, 43124 Parma (PR), Italy - marina.santise@studenti.unipr.it

KEY WORDS: UAS, georeferencing, accuracy, control, CV, photogrammetry, MonteCarlo simulations

ABSTRACT:

UAS (Unmanned Aircraft Systems) are today a viable alternative for collecting remote sensing data for a wide range of applications in agriculture, cultural heritage, restoration, environmental monitoring, safety, cadastral management, map updating, etc.. All the above-mentioned applications need a metric validation and reliability of results for the acquired data to be suitable to their purposes. It is in this matter that the photogrammetrists question about the accuracy of the results. In particular, the topic of this work concerns the quality control of both accuracy and reliability of UAS photogrammetric blocks. Investigations has been performed by a series of Monte Carlo (MC) numerical simulation over synthetic blocks in order to study impact of the block control and the camera network design on the block orientation accuracy. In addition, the two most significant empirical investigations on UAS photogrammetry among those investigated by the author are presented.

1. INTRODUCTION

The growing use of UAS (Unmanned Aircraft Systems) platform for aerial photogrammetry comes with a new family of Computer Vision (CV) highly automated processing software expressly built to manage the peculiar characteristics of these blocks of images. It is of interest to photogrammetrists and professionals, therefore, to find out whether the image orientation and Digital Surface Model (DSM) generation methods implemented in such software are reliable and the DSMs and orthophotos are accurate. On a more general basis, it is interesting to figure out whether it is still worth applying the standard rules of aerial photogrammetry to the case of drones, achieving the same inner strength and the same accuracies as well. UAS are today a viable alternative for collecting remote sensing data for a wide range of applications in agriculture (Gini et al., 2013), cultural heritage (Rinaudo et al., 2012), environmental monitoring (Lucieer et al., 2013, d'Oleire-Oltmanns et al., 2012, Laliberte et al., 2010, Dall'Asta et al., 2015a), safety and cadastral management (Baiocchi et al., 2013, Bendea et al. 2008, Wu et al., 2006), map updating (Remondino et al., 2011, Santise et al., 2014), etc... All the above-mentioned applications need a metric validation and reliability of results for the acquired data to be suitable to their purposes. It is in this matter that the photogrammetrists question about the accuracy of the results.

In particular, the topic of this work concerns the quality control, in terms of both accuracy and reliability of UAS photogrammetric blocks. Investigations have been performed by a series of Monte Carlo (MC) numerical simulation over synthetic blocks in order to study impact of the block control and the camera network design on the block orientation accuracy.

In addition, the two most significant empirical investigations on UAS photogrammetry among those investigated by the author are presented. The former case study DSM focuses on the verification of the accuracy of block orientation ad of DSM generation in a test field set up at the Campus of Parma University. The latter describes the first results on the accuracy of a UAS block oriented with GPS-assisted aerial triangulation in the survey of a rock glacier using Real Time Kinematic (RTK) positioning from an on-site ground station.

For a depth analysis of the UAS research, I invite to read the doctoral thesis (Santise, 2015).

2. A SIMULATION STUDY ON GEOREFERENCING UAV BLOCKS

Though embraced also by small surveying and photogrammetric companies, the use of Unmanned Aerial Vehicles (UAV) systems as a photogrammetric data acquisition platform is also fast spreading outside the traditional domain of well-regulated and established aerial photogrammetry: many companies offering UAV surveys are founded by young information technology, telecommunication or computer science engineers, with very little or no background in mapping and a rather strong one in CV. While in aerial photogrammetry the nature of the cartographic products and the prescriptions in tenders where tightly dependent on map scale and therefore well established, UAV photogrammetry is not primarily devoted to map making (though the relative size of this topic on UAV applications might be growing). Constraints on maximum flight altitude above ground means that the image scale range is limited and that relative image scale variation might be larger than in most aerial images, at least in mountain environment or in city centres (provided this would be allowed). This does not amount to any fundamental change with respect to aerial photogrammetry, however focussing on UAV photogrammetry characteristics is worth, to develop or to reengineer methods and techniques for block orientation to improve or ensure survey quality and cost effectiveness. In particular, given the incorporation of SfM techniques in the block orientation pipeline, it is interesting to verify whether the aerial photogrammetry rules for block planning and orientation still apply. This means to investigate the influence of automatic tie point extraction and of the large overlaps between strips used in drone blocks, as to evaluate the accuracies of block adjustment. A second topic is the performance of techniques for block georeferencing, namely Ground Control Points (GCP), on one hand and GPS-Assisted Aerial Triangulation or Direct Georeferencing, exploiting methods and navigation instruments suitable for this purpose, on the other hand.

This section devotes one paragraph to each of the above-mentioned issues that are examined by means of using a series of Monte Carlo (MC) simulations, namely:

- a) Accuracy of different procedures for BBA using GCP;
- b) Accuracy of GPS-Assisted Aerial Triangulation.

- c) Robustness and reliability of UAV blocks with respect to gross errors in on-board GPS positioning.

The simulations are carried out on two basic block shapes: a square block in a) and a rectangular block in b) and c).

2.1 BBA procedure for UAV blocks with GCP

Today every program package for UAV photogrammetry uses algorithms of automatic orientation built around SfM. The flowchart of these programs, either born in CV or in a photogrammetric environment, is essentially identical. However, three main differences can be highlighted:

- the use of self-calibration;
- the solution of the least squares BBA normal equation system that is performed typically with the Gauss-Newton method in photogrammetry and with Levenberg-Marquart method in CV;
- the way block georeferencing and block control are enforced.

Block georeferencing and block control are performed in photogrammetric adjustment programs with the inclusion in the collinearity equation system of the BBA of the GCP information, so that GCP control the extent of the block deformation. To the contrary, CV software typically first executes the BBA in an arbitrary reference system (a sort of Free-Net adjustment (Granshaw, 1980)); then a rigid 3D Helmert transformation between the arbitrary system and the mapping system is computed using the GCP as double points; finally, the Helmert transformation is applied to the coordinates of the tie points (TP) and to the EO parameters. In either cases, photogrammetry or CV, georeferencing is also possible using information from the telemetry data of drone flight, should they have adequate accuracy. In particular, the projection centres can be related to GPS antenna positions and included in the BBA as in GPS-Assisted Aerial Triangulation, or telemetry data referred to projection centres can be used in CV to estimate the Helmert transformation.

Therefore, the CV BBA does not include the information on GCP in the minimization of the bundle. This means that any deformations related to the accumulation of random errors or to the presence of systematic errors are not checked, i.e. maintained within a certain limit. The subsequent similarity transformation certainly will be able to absorb part of deformations but may not be as effective as the photogrammetric procedure. In fact, the magnitude of such deformations, although generally neglected, depends on many parameters and can be ten times or more large than the ground sample distance as reported in (Nocerino et al., 2014). Major deformations could arise with a weak or a ill block geometry design, as for examples elongated objects imaged in a single strip (roads, river banks, walls or dykes), or even in scenes with large planimetric dimensions but a small depth. This weakness can be contrasted by acquiring images at least in three parallel strips in order to constrain the rotation around the mean strip axis, and/or to use high forward and side overlap or to set a well distributed GCP network on the object. In fact, as well documented in (Kraus, 1993), block accuracy and deformation control are a function of the number and distribution of GCP for nadir aerial photogrammetry, as several studies performed with analogue square-format cameras blocks.

With different relative flight height, low quality digital compact cameras with different sensor formats, high forward and side overlaps, algorithms for automatic orientation and different BBA techniques (from CV and from photogrammetry, using GCP or GPS data on board) the world of UAV surveys is quite complex. It is therefore more difficult than it used to be in the past with analogue aerial cameras to optimize design of block parameters. Hence, the main interest is to understand the consequences of the

transition from manual to automatic orientation (i.e. from Von Gruber points to uniformly distributed tie points) and the effect of the overlap percentages actually used with UAV on error propagation from the measures to the tie point ground coordinates in the BBA. Due to the importance of the transition from georeferencing with GCP to georeferencing with GPS on board, also highlighting the differences in accuracy and rigidity of blocks oriented with GPS on board is of interest.

Therefore, error propagation on tie points has been studied employing different georeferencing techniques for UAS photogrammetric blocks: GCP, free-net adjustment and GPS-assisted adjustment. To this aim, rather than a simple covariance propagation, Monte-Carlo simulations were used that consider, however, only the effect of random errors.

Effects of systematic errors have therefore not been taken into consideration in this work, to focus on georeferencing techniques. This does not mean that they can be neglected, in close-range photogrammetric blocks (Dall'Asta et al., 2015b) as well as in UAV photogrammetric blocks. A recent study (James et al., 2014) indicates that the likelihood of systematic DEM error in UAV surveys can be reduced with some operational precautions. If using an accurate pre-calibrated camera, then self-calibration is not required and systematic errors should be negligible; if self-calibration is necessary, systematic error can be significantly reduced through the collection of oblique imagery that could reduce DEM deformation by one to two orders of magnitude.

2.2 Synthetic block generation and Monte-Carlo simulations

A .NET framework was developed in order to create a new or insert data from an existing photogrammetric block, run the MC simulations and perform data analysis. In Figure 2.2.1, the Monte Carlo simulations flowchart is shown.

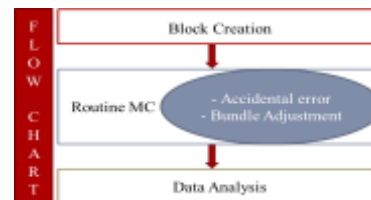


Figure 2.2.1 – Monte Carlo Simulation Flowchart.

In case of generation of a new block, the image block characteristics are specified using a fairly simple and intuitive configuration file where the user can describe the block structure (e.g., a single normal strip, a circular block with all of the images targeting a specific point or an area, a hemispherical distribution of camera stations, an unordered distribution of stations, a combination of above, etc. and the related forward and side overlap). Different object shapes can be defined procedurally or using a discrete set of 3D points: the points are then projected on the image frame and used as tie-points. Using a specified camera model, the pixel coordinates at which each 3D point would be observed in each image are then calculated, with small pseudo random noise added to account for measurement error. Errors in pixel coordinates were generated from a normal distribution with zero mean and a 0.5 pixel standard deviation, a magnitude representative of the precision of commonly achieved by image feature detectors in SfM software (Barazzetti et al., 2010).

Thus, in every simulation sample, the same tie points are used and a new set of errors added.

The user can also specify how the ground control is provided (e.g., using a set of GCP, or using a free net bundle block adjustment (Papo, 1990), or constraining the camera poses and

locations, GPS data, etc.). Various software packages address the reference system definition in different ways: CV-oriented packages use the set of GCP to estimate a seven-parameter transformation; others perform a free-net adjustment with additional constraints. Photogrammetric packages usually implement GCP constraints in the BBA.

A routine performs the inner cycle of the MC simulations adding the errors, executing the bundle adjustment and collecting the orientation solution and the estimated object structure (coordinates of tie points) of each iteration. The MC framework can be interfaced to several BBA routines. In particular, the CALGE BBA module (Forlani, 1986), a widely tested scientific package, was considered the most versatile and efficient for the variety of block configurations in the different case studies. The simulations thus represent synthetic data processed with the same algorithms and the same workflow as real blocks.

At each iteration, the adjusted tie point coordinates are compared to the reference ones (error free) and the statistics are output for the data analysis, in tabular and graphic form.

Though a parametric study according to variables that might describe different forms of block would have been of interest, to limit the computing time it has been decided to study only one block type for each simulation:

- a) a square block, shown in Figure 2.2.2, considered representative of generic UAV blocks, used for the comparison between BBA procedures in photogrammetry and CV, hereafter MC 1;
- b) a rectangular block, shown in Figure 2.2.3, considered representative of a weak geometry for GPS-Assisted Aerial Triangulation, used for the error propagation from the GPS positions to the TP coordinates, hereafter called MC 2;
- c) the same rectangular block MC 2, to study the precision of tie points as a function of on-board GPS precisions as well as the vulnerability to gross errors in the on-board GPS positions.

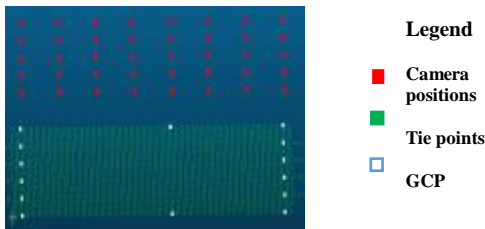


Figure 2.2.2 – Perspective view of the camera positions (in red), tie points (in green) and GCP (in white) for block MC 1.



Figure 2.2.3 – Perspective view of the camera positions (in red) and of the terrain (in white) for block MC 2.

2.3 Simulation MC 1: accuracy of different BBA procedures

The simulation MC 1 aims to estimate the accuracy of the tie points obtained by the photogrammetric method against those obtained with the CV method, i.e. using GCP or using free-net adjustment with and without the 3D Helmert transformation estimation.

Furthermore, to investigate the influence of different levels of overlap between images and the multiplicity of tie points, two different configurations were created for the reference blocks, keeping as common parameters: 100 m relative flight height, a flat terrains area of 420×420 metres and the OI parameters. Also a common camera with a 4000×3000 sensor with $5 \mu\text{m}/\text{pixel}$ size and a 20 mm lens was hypothesized.

To discriminate the influence of overlap and of tie point density, as shown in Figure 2.3.1, forward was fixed to 60% while 1: side overlap of 20% and 2: side overlap of 60% were taken into consideration. Two distributions of tie points were considered: a) 9 points per image as with manual collimations on von Gruber bands in analog-analytical photogrammetry and b) points distributed on a 5×5 m regular grid (as in digital photogrammetry and CV). Combining the variables, four reference blocks were obtained: 1.a, 1.b, 2.a e 2.b.

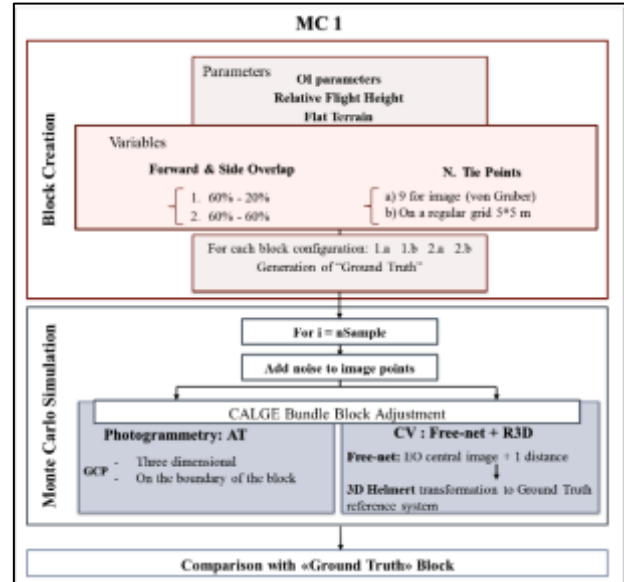


Figure 2.3.1 – Scheme of MC 1 simulation: parameters and variables of “Block creation”, “Monte Carlo Simulation” with noise to image points of each sample and different techniques of BBA and the last “Comparison” step.

Each block was run for 2000 samples, with photogrammetric and CV adjustment. The first type of adjustment uses three-dimensional GCP located on the boundary of the block, according to aerial blocks rules. The second one executes a free-net adjustment constraining the position and the rotations of block central image and the distance between two ground points along a block diagonal, in an arbitrary reference system. Notice that the arbitrary reference is indeed compatible with the reference system (map system), since the EO elements of the central image are fixed to the true values in such system and likewise the scale is fixed 1:1 with the map system. Then a 3D Helmert transformation is estimated between the adjusted (erroneous) GCP coordinates in the arbitrary system and those in the reference (error-free) system (map system).

The features of the reference blocks run in MC 1 are summarized in Table 2.3.1, where for each case of study the number of photos, strips and tie points forming the blocks as well as the overlap and the BBA technique are reported. The 1.b and 2.b cases (60-20% and 60-60% overlap with high density of tie points) were oriented with GCP and with free-net adjustment only (without the 3D Helmert transformation). Indeed, because the high multiplicity of tie-points produces errors comparable with the theoretical precisions, computing the transformation would not add any improvement.

It is interesting to note the variations of tie points number in case of von Gruber or regular grid, more evident in the subsequent Figure 2.3.2. It shows the block geometry of the four reference blocks as a function of number and distribution of tie points (black dots) and of levels of forward and side overlaps. As visible the GCP, green triangles, are located on the block boundary. The number of photos (represented by camera positions in blue squares) increases with increasing side overlap.

Case	N. photos	N. strips	Forward Side Overlap (%)	N. TP	BBA	N. Sample
1.a	40	5	60-20	134	Free-net	2000
				134	Free-net + R3D	2000
				134	GCP	2000
1.b	40	5	60-20	8857	Free-net	2000
				8853	GCP	2000
2.a	72	9	60-60	166	Free-net	2000
				166	Free-net + R3D	2000
				166	GCP	2000
2.b	72	9	60-60	10251	Free-net	2000
				10233	GCP	2000

Table 2.3.1 – Feature of blocks run in MC 1 - Photogrammetry vs CV.

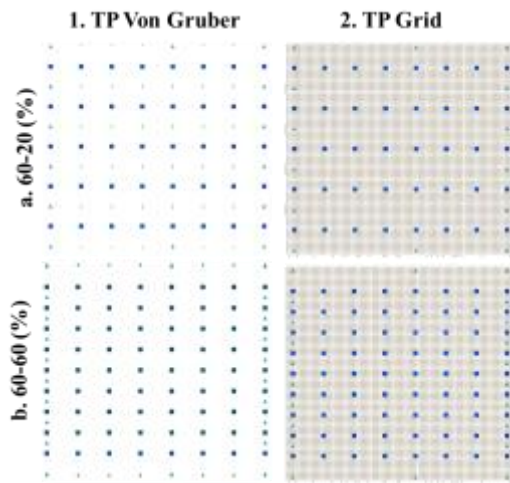


Figure 2.3.2 – Block geometry of reference blocks: 1.a, 1.b, 2.a, 2.b. The camera positions (blue square), tie points (black dots) and GCP (green triangles) are indicated.

2.3.1 Analysis of the results: The MC 1 simulation results are reported in Table 2.3.2 as mean square errors of the ground coordinates. It is immediately clear that photogrammetry behaves the same way with a few or with many tie points; moreover, errors are always smaller than those of CV. In particular, with 60-60% overlap and many tie points, the best result is obtained with 1 cm in planar coordinates and 2 cm in Z.

It is also interesting to look at the distribution of the error over the tie points. Here, however, the graphical representation must be different for case a) and b). Indeed, considering the low number of tie points using only von Gruber bands, plotting the distribution of mean error in a continuous colour map would

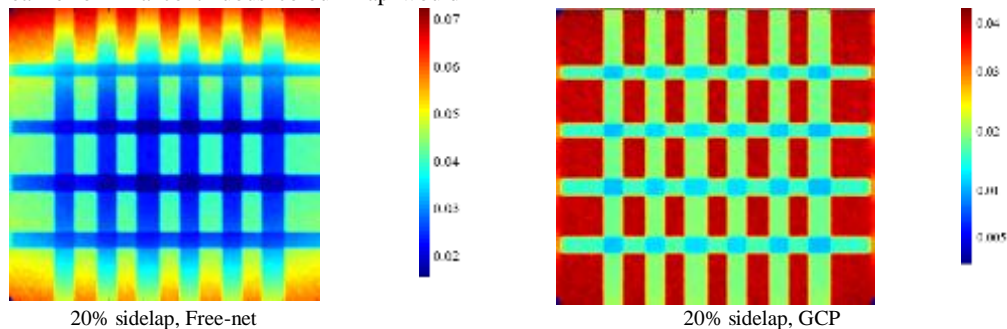


Figure 2.3.3 – Case 1.b: 60-20% overlap, tie point on a regular grid block oriented in free-net adjustment (on the left) and with GCP (on the right). Colour map of the mean error distribution in Z. Note: colour scales are different.

simply depict the chosen interpolation function, not real mean square errors due to excessive spacing of data. Hence, the colour maps of the coordinates mean square error were generated only for the blocks with many tie points. Figure 2.3.3 and Figure 2.3.4 show the distribution of mean errors in Z with tie points distributed on a regular grid. Figure 2.3.3 shows the 1.b case with 60-20% overlap: on the left, the block oriented in free-net adjustment, on the right, the same block oriented with GCP. Instead, Figure 2.3.4 shows case 2.b with 60-60% overlap: on the left, the block oriented in free-net adjustment, on the right, the same block oriented with GCP.

Mean σ_{D_x} , σ_{D_y} , σ_{D_z}	von Gruber TP			TP Grid				
	Case	σ_{D_x}	σ_{D_y}	σ_{D_z}	Case	σ_{D_x}	σ_{D_y}	σ_{D_z}
		(m)	(m)	(m)		(m)	(m)	(m)
GCP	1.a	0.01	0.01	0.03	1.b	0.01	0.01	0.03
	2.a	0.01	0.01	0.03	2.b	0.01	0.01	0.02
FREE NET	1.a	0.09	0.08	0.22	1.b	0.02	0.02	0.04
	2.a	0.04	0.03	0.07	2.b	0.01	0.01	0.03
FREE NET + R3D	1.a	0.03	0.03	0.16				
	2.a	0.02	0.02	0.04				

Table 2.3.2 – Mean square errors (MSE) of the ground coordinates of the MC 1 simulations: in the upper part (blue rows) BBA with GCP, in the lower part (grey rows) results for the CV method before and after Helmert transformation (R3D).

The Figure 2.3.5 a) e b) shows the multiplicity of von Gruber tie points in color maps respectively with 60-20% (left) and 60-60% (right) overlap. As expected, points located on the boundary of the blocks have a lowest multiplicity (2); on the other hand, the multiplicity increases gradually in the center of the block (up to 9 for the 60-60% overlap).

The Figure 2.3.5 c) shows the color map of the multiplicity of tie points distributed on a grid in the 60-60% block. As expected, points located on the upper and lower boundary of the blocks have the lowest multiplicity (2), purple in the legend; on the other hand, the multiplicity increases gradually in the center of the block (with values of 9 for the 60-60% overlap). The identical pattern of this figure compare to the color map of the Z mean error of Figure 2.3.4. Clearly shows that the higher accuracy observed in the high overlap areas is due to higher multiplicity.

In conclusion, higher accuracy are obtained using GCP and forward and side overlap of 60-60%. The higher accuracy on Z is assured using the GCP orientation in whatever block configuration. On the contrary, the accuracy degrades strongly if few points are collimated, the overlaps are low and no GCP are used in the orientation.

Solutions with GCP and with CV methods show comparable values using many tie points, long as they are collimated on all images.

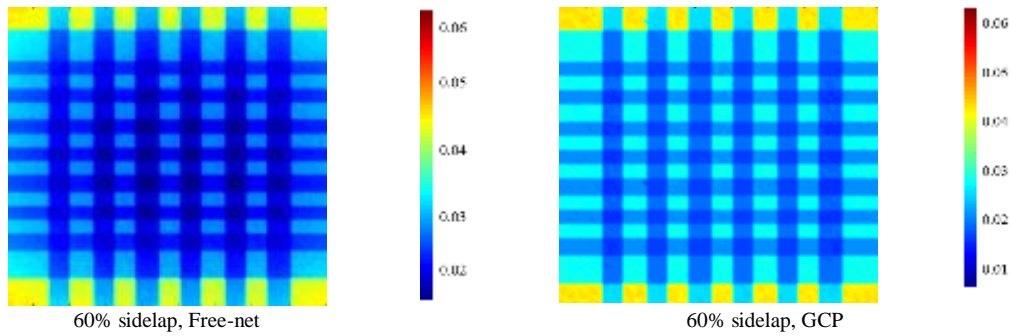


Figure 2.3.4 – Case 2.b: 60-60% overlap, tie point on a regular grid block oriented in free-net adjustment (on the left) and with GCP (on the right). Colour map of the mean error distribution in Z. Note: colour scales are (slightly) different.

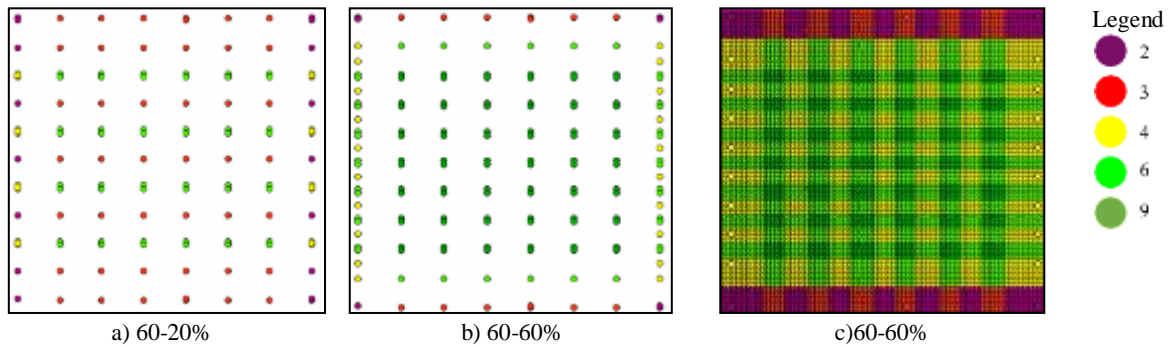


Figure 2.3.5 – Plot of tie point multiplicity on von Gruber bands: a) 60-20% overlap; b) 60-60% overlap. Plot of multiplicity of tie points on a grid: in the case c) of 60-60% overlap. As shown in Legend the lower number is 2, indicated in purple, the higher number is 9, indicated in dark green.

2.4 Georeferencing with GPS on board

The georeferencing with GPS on board, the so-called GPS-assisted aerial triangulation (Cramer et al., 2000, Van Der Vegt, 1989) is another method to define the coordinate datum and control a photogrammetric block.

It is a topical theme for UAS photogrammetry: the capability to use the GPS positions at shooting time of images for georeferencing block is a useful solution from the point of view of time and cost of the survey, especially for periodic control surveys. In fact, georeferencing in a given reference system is normally required in surveys or, as in periodic control surveys, an arbitrary but stable reference system is required. Thus, a surveying campaign for the measurements of GCP with GPS or total stations is usually executed, possibly implying the materialization and maintenance of the GCP or of the reference stations. Manual collimation of the control points on the images is necessary for block adjustment: this is today the only manual operation of the orientation pipeline. However, it is not always possible to place the GCP in the area of interest, especially in the case of remote or inaccessible areas, such as rock glaciers, landslides, etc. Using GPS RTK measurements of on-board navigation instruments pursues the goal of direct georeferencing or at least of GPS-assisted aerial triangulation. Indeed, given the performance of SfM, getting rid of Aerial Triangulation is not really so important in the economy of a photogrammetric project. Therefore, unless a real-time solution is needed, direct orientation as opposed to indirect GPS-assisted AT, as Friess demonstrated already in 1986 (Friess, 1986) does not bring significant advantages in terms of accuracy on ground. Progress in GPS receivers miniaturization and possibly a larger market for L1/L2 that might further reduce costs both mark a steady move towards this georeferencing technique to become a standard.

Operationally, at each shooting, the antenna position is recorded by the receiver. It is not necessary to obtain GPS positions for

each camera station, though this would increase the reliability of GPS and the overall block control. The GPS receiver operates in kinematic mode. If images are acquired in motion, however, as in most UAV, the shooting time must be recorded and the position interpolated over time. In both cases, to use this information in the bundle block adjustment, the mathematical model of the collinearity equations has to be extended to account for the offset between the camera centre and the antenna. The GPS position is referred to the antenna phase centre or to the antenna mount point. Being the camera centre fixed with respect to the antenna, the offset is constant and can be determined by calibration. The GPS data collected by the receiver can be processed according to available instrumentation. RTK mode with respect to a locally set master station or to a network real time kinematic (NRTK) mode allows immediate verification of the quality of positioning. Otherwise, kinematic post processing with respect to a nearby master or to a Virtual Reference Station (VRS) with Virtual Rinx (VRX) data generated within a network of GPS permanent stations can be used. A RTK network allows using just a single GPS receiver (the rover). Moreover, the survey is not bounded by the distance to the master. The VRX files (Gurtner, 1997) can be processed with any GPS software. A calibration is necessary to determine the relative position between camera and antenna to insert the camera positions in the bundle block adjustment (Forlani et al., 2014).

The automation potential of this technique is high, if a specific software pipeline is set up. The bundle block adjustment would then follow GPS data processing and the automatic generation of tie points by SfM algorithms without need for manual collimations.

If GCP are not used, however, the stability of the reference system in periodic surveys depends on the accuracy of GPS measurements and on the spatial distribution of the camera stations. With objects mainly developed in height or in width (i.e. building façades, walls, fronts of landslide), the shooting of two

or more strips at different elevations or at different distances from the object is recommended. As a rule of thumb, an accuracy of kinematic GPS surveys in the 1-2 cm range can be achieved; sub-centimetre accuracies, if necessary, are much harder to guarantee. Georeferencing with GPS on board consists of including in the mathematical model of the collinearity equations, adding the observation equation relating camera centre and antenna phase centre position (Forlani et al., 1994):

$$X_a = X_0 + R_c^G e + S + Dt \quad (1)$$

Where X_a antenna phase centre;

- X_0 camera perspective centre;
- R_c^G image attitude matrix (from camera to object system);
- e eccentricity vector, expressed in the camera system;
- S, D shift and drift parameters;
- t the shooting time of the image.

Drift parameters are supposed to mitigate systematic discrepancies between the GPS and photogrammetric solutions on a block basis or on a strip-by-strip basis.

In this work the shift and drift parameters are not included in the mathematical model when GPS-assisted aerial triangulation accuracy was evaluated.

In the equation (1) the offset vector e is known by calibration while the perspective center and the attitude matrix R_c^G are unknown. The precision of the antenna position is in principle available from the GPS data processing. Individual weights can be assigned to camera stations accounting for the actual PDOP values. However, these estimates are often unrealistically good. In the block adjustment SfM algorithms provide the tie points and their accuracy. On the other hand, the GPS provides the positions of the antenna-camera stations and their accuracy as well as the reference system of the block. Thus, the GPS data substitute for GCP in georeferencing. However, in general, the antenna positions cannot be considered error-free or sometimes even as accurate as photogrammetry. To achieve cm-level accuracy in a GPS kinematic survey it is critical to fix the so-called integer ambiguity (Forlani et al., 2007). In turn, this capability depends on satellite configuration, receiver hardware and software and environment conditions. A poor PDOP, just a few satellites tracked, frequent changes in satellite constellation make it difficult to estimate with enough confidence the integer value. For the above mentioned reasons, therefore, GPS positions must be treated as additional observations and not as ordinary control points.

To investigate the accuracy requirements to the GPS positions and their vulnerability to gross errors, a second series of Monte Carlo simulations, denominated MC 2, was executed. In the following MC 2 simulation will be presented and discussed together with tests on the precisions of tie point coordinates as a function of GPS position errors, including gross errors, for GPS-assisted Aerial Triangulation.

2.5 Simulation MC 2: accuracy of GPS-Assisted Aerial Triangulation

The simulation MC 2 aims to estimate the accuracy of tie points in a block oriented by GPS-assisted aerial triangulation. As previously pointed out, it involves an elongated rectangular block (see Figure 2.2.3), that represents a case with a weak geometry for the adjustment with the GPS data on board. The terrain simulated with a sinusoidal shape with an amplitude of 10% of the relative height flight (100 m) on a regular 5×5 m grid.

The features of the simulation are shown in Figure 2.5.1. In this case, in addition to tie point image coordinates, also GPS positions are affected by noise in each iteration of the MC

routines. Here GPS positions are the only useful information for georeferencing.

A single strip, as is the case of surveys of river beds or map production for road projects, cannot be oriented by GPS on board only. In fact, in this case the rotation of the entire strip around the direction of flight is ill-defined. To avoid this, if measuring GPC is ruled out, the alternative is to enlarge the block by flying two additional parallel strip, one above and one below, with a convenient side overlap. This latter option has been adopted for the simulation, with a 60% sidelap. The area of interest of the simulation is 1.2 km long and 200 m wide. Hence, with a 60% forward overlap, the reference block is composed by 60 images on 3 strips. The inner orientation parameters are the same as the previous simulation MC 1. As for the average errors of the GPS, 3 cm on planimetric coordinates and 5 cm on elevations were assigned. How good RTK position accuracy might be is for obvious reasons difficult to verify in dynamic conditions. Therefore, these conservative values, that are widely obtainable with good satellite configurations in kinematic surveys on the ground, have been selected for random error generation.

As previously, errors are computed by comparison of the estimated tie point coordinates of each iteration with those of the reference block. The MC cycle has been repeated 5000 times.

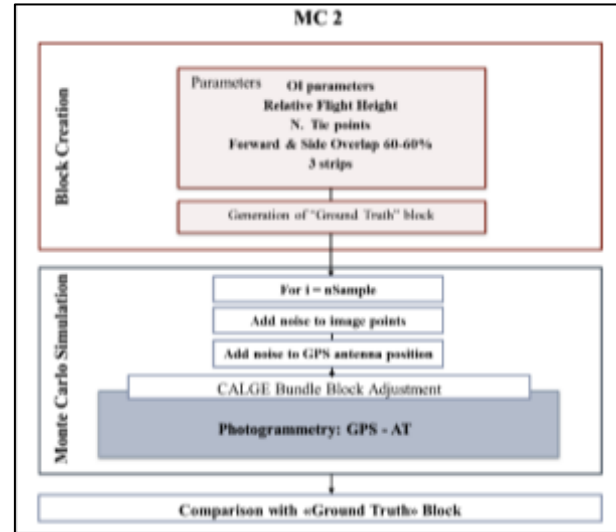


Figure 2.5.1 – Scheme of MC 2 simulation with parameters of “Block creation” step, “Monte Carlo Simulation” with noise added to image points and GPS antenna positions for orientation using GPS-AT and the last “Comparison” step.

2.5.1 Analysis of the results: The MC 2 simulation results are reported in Table 2.5.1 as minimum, maximum and mean square errors of the ground coordinates for the 5000 blocks oriented. It should be noticed that these values account for both the image and the GPS position errors, so they look indeed quite good. Again, it should be stressed that this applies to tie points with a good average multiplicity, at least in the central strip. If we compare the mean square errors of ground coordinates of Table 2.5.2 with the theoretical precision (i.e. the precision from the estimated covariance matrix of the l.s. BBA) of a UAV block adjusted with ground control points we find a good agreement.

	N. of Samples	min	MAX	mean
σ_{D_x} (m)	5000	0.009	0.054	0.014
σ_{D_y} (m)	5000	0.018	0.038	0.025
σ_{D_z} (m)	5000	0.013	0.079	0.030

Table 2.5.1 – Minimum, maximum and mean square errors of the ground coordinates of the MC 2 simulations.

Theoretical precisions	RMS
σ_x (m)	0.014
σ_y (m)	0.010
σ_z (m)	0.029

Table 2.5.2 – Theoretical precisions of ground points in square blocks oriented with GCP.

Table 2.5.2 reports such precisions for the square block of MC 1: the agreement is very good, except for the y coordinate, which is less precise in the three-strip rectangular block. This can be expected, since the Y direction is still affected by the residual ill-

geometry of the block, not completely corrected by the two external strips. However, this means that a UAV block controlled by GPS on board with cm level precision delivers ground coordinates with cm level precision on a par with blocks controlled by GCP.

Figure 2.5.2 shows the colour map of the mean square error distribution for each ground coordinate. It is apparent that the central strip, where point multiplicity reaches 9 has the best precision and is the most uniform; on the contrary, the lateral strips suffer some border effect. Therefore, employing 3 strips delivers more homogeneity to the central strip, the one that actually covers the area of interest.

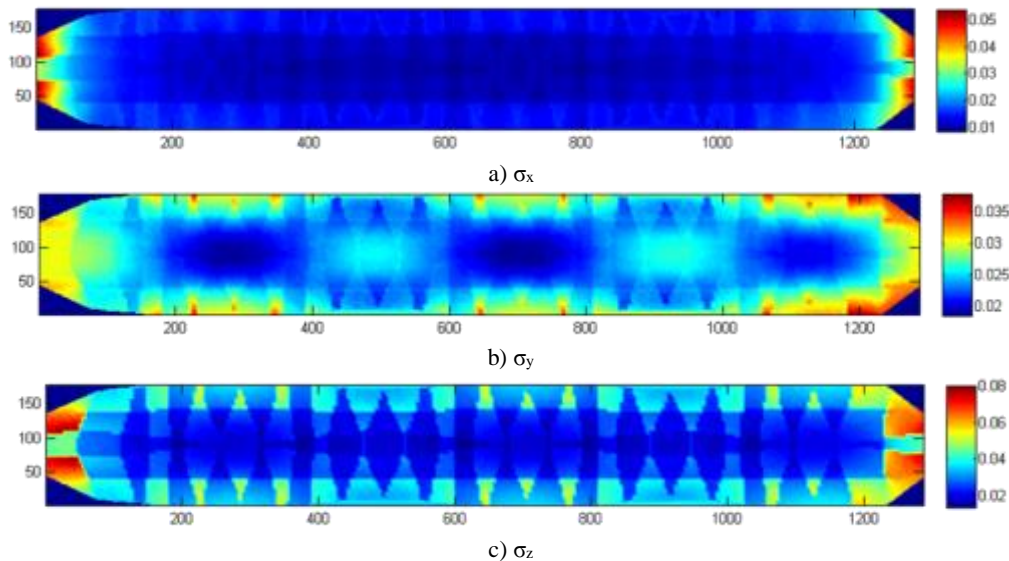


Figure 2.5.2 – Colour map of the mean square error distribution of ground coordinates of the MC 2: a) σ_x , b) σ_y , c) σ_z .

2.6 Required precisions of GPS and sensitivity to gross errors in GPS positions

The Monte Carlo simulations allowed accounting for random errors on block georeferencing with GPS on board. However, two questions are still worth investigating: which category of receiver is required to achieve an assigned precision on the ground coordinates? How much might gross errors (of constant type or of time-variant type) affect the BBA results? How effective is gross error detection in such cases?

To study both issues, one of the three-strips blocks of the previous simulations, containing random errors both on image coordinates and GPS data, was used.

2.6.1 GPS data precision requirements. If soon GPS on board will replace GCP on ground as a mean to georeference UAV blocks, it is worth to find out whether this is going to happen with a loss of precision for ground coordinates (the remarks on Section 2.5.1 hint that this should not be the case). A related question might be what is the ceiling in precision we can get: today improvements can be achieved increasing the GCP density and precision; is this possible with GPS on board as well? To have reference values of precision (computed from the covariance matrix of the BBA), the block of 3 strips has been oriented first with 3 pairs of GCP located in pairs at the strip ends and in the middle of the block. Then a new block orientation, with GPS data only, has been performed using GPS precisions of 3 cm for planimetric and 5 cm for altimetric coordinates (as in the

simulations). Table 2.6.1 and Table 2.6.2 show the average (RMS) theoretical precisions of adjusted ground coordinates, respectively for georeferencing with GCP and with GPS. The mean values are quite similar, i.e. the quality of block control is equivalent. A partial exception is the Y coordinate, which is better in the case of adjustment with ground control because the GCP can compensate for the weakness (asymmetry) of the block geometry in this direction. Thus, the solutions are almost equivalent: the GPS assisted AT works well thanks to high side overlap (60%) and the two lateral strips that join the central one. It should be noticed, however, that the estimated precision for the GCP case have been computed assuming the GCP coordinates error-free. With static GPS measurements (not really the norm with UAV blocks) a GCP accuracy of 1 cm can be assumed. Therefore treating GCP coordinates as error-free might be justified only for GSD larger than 5-6 cm.

Theoretical precisions	RMS	MAX
X (m)	0.014	0.051
Y (m)	0.013	0.027
Z (m)	0.033	0.078

Table 2.6.1 – Orientation with GCP: Theoretical precisions on ground coordinates.

Theoretical precisions	RMS	MAX
X (m)	0.015	0.054
Y (m)	0.025	0.038
Z (m)	0.032	0.079

Table 2.6.2 – GPS assisted aerial triangulation (σ_x, σ_y : 3 cm, σ_z : 5 cm): Theoretical precisions on ground coordinates.

The other question is what is the relationship between the GPS data precision and the ground coordinate precision. As a matter of fact, given the difficulty to reliably estimate GPS precision, this point highlights a potential weakness of GPS-assisted AT, i.e. the dependence of the solution on the weights assigned to GPS observations. To find out, the three-strip block has been adjusted varying GPS precision (see Table 2.6.3 the σ_z GPS and $\sigma_{x,y}$ GPS rows) to reach a comparable Y precision with that of GCP adjustment. Starting with values as 5 cm in Z and 2.5 cm in X and Y, the GPS precisions are improved up to 3 cm in Z and 1.5 cm X and Y.

As it can be seen, even with these last precisions (values that are not so easy to guarantee even with geodetic receivers) a precision comparable to the GCP solution in Y direction cannot be obtained. This implies that if there are asymmetries in the coordinate precision due to block shape, they cannot easily be solved by on board GPS data. Conversely, supposing to use e.g. lower quality L1 only receivers, if lower precisions (from 70 mm up to 150 mm in Z) the precisions on the ground coordinates get obviously worse, though they still remain interesting in absolute terms for many applications. The real limit of the L1 receivers is, however, the time required to fix the integer ambiguity in the case of cycle slips, which can be of several minutes and therefore incompatible with the duration of drones flight, unless the possibility of cycle slip occurring during the flight is ruled out in some way.

6 GCP	σ_z GPS (mm)	Geodetic Receiver			Low-Cost Receiver			
		30	40	50	70	80	100	150
	$\sigma_{x,y}$ GPS (mm)	15	20	25	35	40	50	75
13.99	σ_x (mm)	13.32	13.98	14.68	16.16	16.93	18.51	22.57
13.28	σ_y (mm)	17.99	21.2	24.66	32.01	35.83	43.61	63.54
33.09	σ_z (mm)	29.24	30.4	31.78	35.03	36.84	40.74	51.54

Table 2.6.3 – Precisions on ground coordinates using different precision of GPS data w.r.t. control with GCP: the Geodetic category (σ_z : 30-50 mm) on the left; the Low-Cost category (σ_z from 150mm) on the right.

Another interesting point from Table 2.6.3 is that the estimated precision of ground coordinates changes slowly with varying GPS data precision, though with different paces for the different coordinates. Indeed, in X and Z direction the loss of accuracy is about 70% of the best value; in Y direction the effect is stronger (about 250%) because the weakness in that direction increases with less tight control “from above”.

2.6.2 Vulnerability to gross errors: The incorrect fixing of the integer ambiguity, an event that might well happens in RTK positioning, as well as or the sudden change of constellation in view produce systematic errors in the trajectory. Such errors can be modelled by constant shifts or as time-dependent incremental error (drifts) as in (Eq. 1.), where normally these parameters are applied on a strip-by-strip basis. On one hand, it is important to evaluate the block robustness in such circumstances; on the other hand, it is interesting to know what entity of errors is correctly pinpointed by the data snooping, i.e. the test on normalized residuals.

Several tests were run with the CALGE BBA module in order to estimate the influence of these errors on the block adjustment. Shift and drift errors of different size were applied to the central or to one of the lateral strips of the block (3 strips, 60-60% forward and side overlap, GPS precisions of $\sigma_{x,y}$:3 cm, σ_z :5 cm). No rejection of outliers has been performed: therefore, the corrections to the coordinates represent the effect of the random and gross errors introduced, unless otherwise specified.

Shift errors: Shift errors were increased in size in each coordinate from about 3 times to about 10 times the standard deviation of “correct” GPS observations and varied in sign.

The results of these simulations show the same behaviour. In general, the shift errors imposed on the lateral strip produce more corrections on the ground points in respect of those produced by errors on the central strip. The adjusted block seems to be in most cases just shifted: indeed, the standard deviations of the corrections are the same in both cases. Furthermore, higher input errors produce higher corrections on the ground. In particular, the tie point coordinate most affected is predictably the Z coordinate. A final set of simulations were run with 20 cm shift errors imposed on one coordinate at once on the Lateral strip. The results of the adjustments are shown in Table 2.6.4.

Error value	Shift DX 20 cm		Shift DY 20 cm		Shift DZ 20 cm	
	Mean (m)	σ (m)	Mean (m)	σ (m)	Mean (m)	σ (m)
Case	1		2		3	
DX	0.063	0.021	-0.003	0.022	-0.001	0.021
DY	-0.033	0.043	0.033	0.024	0.219	0.029
DZ	0.001	0.058	-0.004	0.056	0.063	0.137

Table 2.6.4 – Statistics of Ground coordinates corrections for the simulation cases with 20 cm shift error on the Lateral strip of the block.

Large shift errors of 20 cm on coordinates of lateral strip do not seem catastrophic in cases 1 and 2 on X and Y coordinates; even in the Z case, the X coordinate seem unaffected. To highlight the net error effect of GPS shift errors more clearly, differences between the adjusted ground coordinates with 20 cm shift errors in one coordinate at once with the reference block affected by random error only were computed. This is equivalent to run a simulation with image and GPS measurement without random errors and with gross errors only. The results are shown in Table 2.6.5. This comparison with the reference block allows to quantify the only shift errors component because the random error component is removed.

Error value	Shift DX 20 cm		Shift DY 20 cm		Shift DZ 20 cm	
	Mean (m)	σ (m)	Mean (m)	σ (m)	Mean (m)	σ (m)
DX	-0.064	0.007	0.003	0.016	0.001	0.021
DY	0.000	0.033	-0.066	0.004	-0.253	0.024
DZ	-0.003	0.014	0.003	0.012	-0.064	0.124

Table 2.6.5 – Effect of shift error only on tie point coordinates.

For the X and Y coordinates, the 20 cm error in the GPS data is reflected in a translational motion of the block by about 1/3 of the error (6.6 cm) in the direction of the coordinate affected, with almost no other effects of deformation of the block (as can be seen from the fact that the standard deviation of the corrections is negligible and unchanged). This does not apply to the error in Z, where, in addition to the 1/3 shift along Z, also the Y coordinate is affected significantly (more than 25 cm). Moreover, also the standard deviation of the correction in Z increases to 12 cm, i.e. a deformation occurs.

Drift errors: As far as the simulation of drift errors is concerned, on the basis of the previous results, just an incremental error from 0.09 to 0.30 m on one coordinate at a time were considered for the lateral strip only. The results show the same behaviour of the previous shift error simulations: errors in GPS Z coordinate result in large errors in Z and Y on the ground. As previously, to highlight the effect of the drift errors only, differences on ground coordinates were referred to the block with random errors only (see Table 2.6.6).

Error value	Drift DX 20 cm		Drift DY 20 cm		Drift DZ 20 cm	
	Mean (m)	σ (m)	Mean (m)	σ (m)	Mean (m)	σ (m)
DX	-0.065	0.022	-0.001	0.013	-0.006	0.001
DY	0.000	0.033	-0.065	0.021	-0.247	0.024
DZ	0.006	0.012	0.005	0.007	-0.063	0.124

Table 2.6.6 – Effect of drift error only on tie point coordinates.

The error in the GPS data is reflected in a translational motion of the block in the direction of the coordinate concerned for about 1/3 of the average drift error (6.6 cm) with no other effects of deformation of the block (as can be seen from the fact that the standard deviation of the corrections is negligible and unchanged). This does not apply to the error in Z, where, in addition to the 1/3 shift along Z, also the Y coordinate is affected significantly (more than 25 cm). Moreover, also the standard deviation of the correction in Z increases to 12 cm, i.e. a deformation occurs.

3. EMPIRICAL ACCURACY TEST OF UAV PHOTOGRAMMETRY

Specifically, the aim of the work is to determine the accuracy of different georeferencing techniques:

- Using GCP, in order to estimate the influence of different GCP configurations on the accuracy of block orientation;
- Using GPS-on board, to assess the performance of RTK GPS acquisition mode.

In this Paragraph, two empirical studies on the potentiality of UAS photogrammetry are presented, which have been performed at the Campus of Parma University with the realization of a test-field surveyed by two flights and the experimental flight using a drone RTK-equipped at the rock glacier of Gran Sommetta.

3.1 Campus

The photogrammetric survey was realized on the basis of traditional aerial photogrammetry rules in order to check that at least the same level of accuracy can be obtained with UAS-platforms. The reference accuracy in planning the survey was mapping at 1:1000 map scale, where a tolerance (2σ) of 40 cm for horizontal and vertical components is foreseen. The 500×500 m² area covered part of the Campus of Parma University, for a total of about 23000 m² and consists of parking lots, green areas, sporting facilities as well as buildings of various heights (from 6 to 35 m). Two different case studies are presented: the first, implementing a 140 m height flight (Italian regulations limit to 150 m the maximum flight altitude for UAS commercial systems) with a GSD of 4 cm, spanning the whole area; the second, with a 70 m altitude (2 cm GSD), limited to a 5000 m² region where most buildings are located.

The employed drone is a Falcon 8 octocopter, produced by the German company AscTec equipped with a compact Sony NEX with a resolution of 14.2 Mpixel and a fixed focal length of 16.3 mm. The Falcon flew with a pre-planned flight whose strips run parallel to the shorter side of the areas. In order to avoid holes and guarantee an overabundant stereoscopic coverage, the longitudinal overlap was fixed to 80% and the side one to 40%. The GCPs, as traditional photogrammetric survey guidelines prescribe, are located on the border of the area of interest, at least one every three 60% overlap stereo-models (i.e. one GCP every five images). Points at ground level were surveyed with GPS receivers Leica 1230 and Leica SR500 in static mode, instead points on rooftop corners or markers on building roofs were surveyed with a Topcon IS203 total station. As a result, there were 28 GCPs for the flight at 140 m, and 20 for the flight at 70

m. To check the DSM accuracy, points were measured on terrain break lines and on parking lots, pavements and fields, roughly on a grid with a spacing of 4-5 m. Overall 3585 points distributed all over the Campus study area (1340 in the area covered by the 70 m flight) were measured with GPS “stop and go”, occupying each point from 2 to 10 seconds.

In this article, only the 140 m flight will be discussed for brevity reason. The analysis for the flight 140 was performed with Agisoft PhotoScan considering different bundle block configurations:

- Using only 9 GCPs distributed on the ground along the border and one in the centre of the area (Figure 3.1.1).
- Using all 28 GCPs distributed on the ground.
- Using all 28 GCPs distributed on the ground and 7 GCPs on the buildings from 25 to 32 meters high.

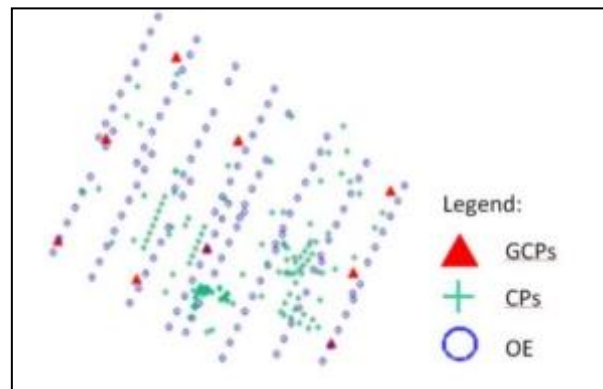


Figure 3.1.1 – Distribution of 9 GCPs for the block orientation in the a) version.

The goal is to study the restitution accuracy according to the distribution and number of GCPs in the BBA, to find out whether less GCPs might be used, reducing overall surveying costs and get a confirmation of the simulations results of Chapter 4.

The accuracy for each configuration was evaluated comparing the coordinates of CPs that have been estimated in the photogrammetric bundle adjustments with those measured with total station and GPS. The RMSE (Root Mean Square Error) of the differences was calculated for each GCP configuration, considering the whole CP dataset or collecting separated statistics of those on buildings and on the ground. The statistics are summarized in Table 3.1.1 with the number of CPs used.

The a) configuration shows the highest RMSE for Z coordinates both of CPs on buildings as well as those on the ground.

In case b) the inclusion of more GCPs improves of ca. 4 cm the accuracy of Z coordinates.

The c) is the most complete scenario, including all GCPs on the ground and also 7 on the highest buildings (ca. 30 meters). There is a further increase of Z accuracy; it is worth noting that the improvement is mainly related to CPs on buildings, while the accuracy of CPs on the ground remains basically the same of case b). This suggests that constraining GCPs on buildings improves the solution, obtaining height accuracy values of the same order regardless of the point height. Anyway, the small GSD and, likely, the image quality not so clearly inferior to professional-grade cameras, allow to achieve better than expected accuracies even in case a). It should be mentioned, however, that CP were collimated in more than two images, so an accuracy better than the normal case is foreseen.

Therefore, on the basis of discrepancies at CP, the solution using only 9 well distributed GCP is still adequate for cartographic update purposes at this scale.

Flight 140 - RMSE on the CPs

Block version	All CPs				CPs on buildings				CPs on the ground			
	N. CP	DX	DY	DZ	N. CP	DX	DY	DZ	N. CP	DX	DY	DZ
		(cm)	(cm)	(cm)		(cm)	(cm)	(cm)		(cm)	(cm)	(cm)
a) 9 GCP	127	5.6	4.6	9.2	34	7.4	4.6	9.4	93	5.1	4.7	9.1
b) 28 GCP	108	4.8	4.8	5.2	34	5.5	4.3	6.4	74	4.5	4.9	4.5
c) 28+7GCP	101	4.6	4.7	4.5	27	5.1	4.1	5.3	74	4.4	4.9	4.3

Table 3.1.1 – Flight 140: coordinates difference value in the three configuration of UAS block on all CPs, on buildings and on the ground.

Three 3D models have been produced; the first two from the 140 m flight oriented first with 28 GCP and then with 9 GCP only; the third from the 70 m flight oriented with 20 GCP. Some problems, partly related to the sudden change in image scale and partly to the quite complex roof structure, showed up on high-rise buildings roofs.

Ground surface classification	N. CP	DSM 140m Flight 28 GCPs		DSM 140m Flight 9 GCPs	
		Mean _{DZ} (m)	RMSE _{DZ} (m)	Mean _{DZ} (m)	RMSE _{DZ} (m)
Details	72	0.049	0.081	-0.047	0.073
CPs on buildings	7	0.032	0.074	-0.055	0.084
Grass fields	1242	0.073	0.086	0.029	0.079
Embankment	61	0.089	0.147	0.073	0.132
Paved areas	2056	0.019	0.077	-0.057	0.084
Total	3438	0.040	0.081	-0.023	0.056

Table 3.1.2 – Differences in elevation between the DSM 140 (version block with 28 GCPs and 9 GCPs) and CPs.

The validation was performed comparing the models with the GPS (on fields and paved surfaces) and total station (on buildings) survey data. The models were imported in ArcGis as raster, setting an interpolation resolution of 20 cm, a compromise between maintaining the details obtained with the GSD of UAS survey and the memory size of the model.

The results are summarized in Table 3.1.2 for the 140 m flight. As a general remark the model accuracy is not much influenced by the surface type, though one would expect the grass to be more difficult than paved surfaces; indeed at the time of the flight (December 2013) the grass cover is not as thick and dense as in springtime. The only noticeable difference is on the embankments where residuals are larger, perhaps due to the smoothing of the 20 cm grid size.

3.2 Gran Sometta

As mentioned in the results of the GPS-assisted Aerial triangulation simulations, the GPS receiver quality has to be geodetic and the photogrammetric block must have high forward and side overlaps. For all these reasons, the experimental flight was carried by means the eBee RTK an UAS equipped with a double frequency RTK receiver. The images were acquired with forward overlap of 85% and a sidelap of 80% at a relative flying height of 140 m with a GSD of 4 cm. The on board camera is a Sony Cyber-shot DSC-WX220 of 18 MPixel of resolution, focal length of 4.45 mm, image frame 6 × 5 mm and pixel size of 1.22 micrometres. The number of images acquired and used in the bundle block adjustment is 280.

The eBee RTK technology is based on the ground control station sending corrections in real time to the on board receiver, in order to correct image geotags in flight. In the Sometta survey, the ground control station received the corrections from a GPS master station set on a known position near the glacier.

Furthermore, 13 signalized GCPs distributed on the edges of the rock glacier were measured with a GNSS receiver GEOMAX Zenith 20 Series in RTK mode. The expected precisions in XY coordinates are 1-2 cm and 2-3 cm in Z. these points were used

as check points to verify the restitution accuracy of the RTK-oriented block.

The bundle block adjustment of the UAS survey was performed with the commercial software Agisoft PhotoScan. Using the same tie points, three different block adjustment were performed:

- with observed camera Projection Centres (PC) from the RTK GPS measurements, using all or just half of the GPS camera stations;
- with all the available GCP.

The accuracy of GPS-assisted triangulation was evaluated comparing the coordinates of CPs estimated in the photogrammetric bundle adjustments with those measured with GPS. The RMSE of the differences is reported in Table 3.2.1.

12 CP	DX (m)	DY (m)	DZ (m)
Mean	-0.005	0.006	-0.038
St. Dev.	0.040	0.031	0.061
RMSE	0.040	0.031	0.072

Table 3.2.1 – Statistics of the errors (discrepancies) at the 12 CP for the block georeferenced with all GPS-determined camera stations.

Though the number of CP available is limited (and therefore so is the confidence on the outcome significance), the RMSE obtained is in the order of a few cm, with elevations less accurate than horizontal coordinates. With respect to the simulation results in Paragraph 2.5 the accuracy is perhaps lower, even accounting for the higher relative flight elevation and lower a-priori GPS precision. However, the empirical accuracy is in the order of the GSD, and practically the same as the 140 m test flight on Campus (Table 3.1.1). As far as the goal of tracking glacier motion is concerned, being the expected displacement well above a decimetre per month in summer time, georeferencing with GPS-on board seems to be a serious alternative to the repeated survey of all GCP at every campaign. Efforts to consolidate the confidence on such results and an analysis of the conditions that guarantees such accuracy should therefore be continued.

Though the check provided by the comparison of CP coordinates is an indication of the accuracy on ground of blocks oriented with GPS, it is also interesting, for the purpose of terrain displacement analysis, to check the differences between the DSM obtained from the two different block orientations. Three dense point clouds obtained by the three previously oriented blocks were also generated in PhotoScan with a grid step of 16 cm. The produced DSMs regards the whole area framed by UAS imagery; however, the comparison is of particular interest on the rock-glacier body. For the comparison, the original DSMs were interpolated as raster with cell size of 0.5 m over the whole area and over the glacier body.

Figure 3.2.1 shows the raster of Z differences between the GCP DSM and the DSM obtained with all camera positions, with a colour scale with class intervals multiples of the Std. Dev. σ of the differences. The value range is between -20 and + 26 cm and a standard deviation of 7 cm, in full agreement with the discrepancies on Check Points.

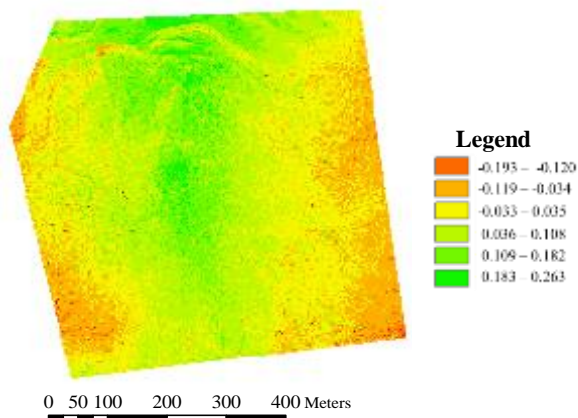


Figure 3.2.1 – Colour map at 0.5 m resolution of the differences (m) between the GCP DSM and the all GPS DSM with location of Check Points (blue triangles).

The GPS DSM is lower than the GCP DSM in the central part of the area, while it is higher at the West and East sides, with a clearly systematic behaviour (the difference surface looks correlated to the terrain topography). The reason for these systematic differences is not yet clear. In all the three block adjustments, self-calibration has been used. The comparison between the plots of the residual image errors and between the estimated IO and distortion parameters in the PhotoScan adjustment report shows that systematic residuals in the order of about half pixel occur in the central part of the image while larger ones occur on the left bottom corner. However, the pattern is pretty much the same in all cases. The IO parameters show only quite small variations (K1 and K2 values being an exception) between the GPS and the GCP adjustments.

CONCLUSIONS

Starting from the last decade, there was a dramatic increase in the use of Unmanned Aircraft Systems (UASs) in Photogrammetry and Remote Sensing (PaRS) for applications such as environmental monitoring, cultural heritage, surveillance and many other.

However, specific guidelines for UAS survey flights have not yet been established and investigations are still needed to assess the accuracies that such imagery can reach for metric purposes. Many software packages for UAV photogrammetry exist today, born either in CV or in a photogrammetric environment. This difference in background means that the output documentation is different and that differences exist in the product accuracy and completeness. This suggests that a benchmark for testing UAV software packages in different applications should be established and that some standard on processing reports should be promoted.

Being the UAV world a quite articulated one, relationships between accuracy on ground and parameters such as image scale, side and forward overlap, GCP distribution are hard to optimize as in aerial blocks with analogue cameras. On this regard, a methodological study has been carried out with Monte-Carlo simulations on georeferencing UAV blocks with GCP and GPS on board. The results show that UAV blocks, with respect to aerial photogrammetric cameras, have to compensate with higher overlaps the lower quality of the sensor and of the navigation system. This grants a greater rigidity against random error unfavourable accumulation if multi-image matching is used; moreover, a reduced number of GCP is necessary to control the BBA. Furthermore, the general acceptance in practice of large side overlaps and the transition to multi image matching in Dense Matching seem to close the gap between adjustment methods

including GCP in the BBA and CV methods based on a two-step procedure and to a gain of uniformity of restitution precision over the whole block. The accuracy potential of UAS photogrammetry both for very large scale mapping as well as, perhaps more interestingly, for periodic monitoring of decimetre-level displacements in environmental applications is certainly large.

It must be noticed, however, that empirical tests on Parma University Campus as well as on the Gran Sommetta rock glacier, where DSMs produced from the same block but adjusted with a different control (number of GCP or GPS-determined camera station) show systematic discrepancies larger than the expected accuracy. This points out that other (non-random) unmodelled error sources might be present in UAS block and that quality checks should be well focused.

As far as error sources are concerned, inaccurate interior orientation data (including lens distortion) are likely to be the first that should be examined. Their effect should be identified with additional empirical and simulated tests, which are even more important now that promising results are coming from GPS-assisted blocks, where it is well known that IO residual errors are passed to ground coordinates rather than being adsorbed by EO parameters. Results on using pre-calibration or self-calibration or a mix of the two is not yet clear-cut.

As far as quality checks are concerned, even a fair number of CP might not be enough for such systematic differences being noticed or clearly highlighted; therefore, a sensitivity analysis on the effect on the DSM of changes in exterior orientation and interior orientation should be performed.

Getting rid of Ground Control Points by using GPS-Assisted Aerial Triangulation or even Direct Georeferencing is probably currently the real hot topic for a fair range of applications of UAS photogrammetry. The GPS accuracy requirements and their vulnerability to gross errors have also been investigated with Monte Carlo simulations. The research outcomes indicate that expected performance is very good but that L1/L2 receivers are necessary for a reliable operational system. Specifically, due to high overlaps, the covariance propagation from the receiver to the ground is quite favourable and the solution accuracies are comparable with those obtained with georeferencing with GCP. Furthermore, thanks to the high multiplicity, the recognition of gross errors, which also affect a significant portion of the block, is possible. The results of an empirical test with GPS on board described in Section 3.2, though of limited significance due to the small number of CP, suggest that the same accuracy level can be reached on the ground and that this is true for the DSM generation. In other words, the technology seems indeed matured to an operational level. More testing is however needed to consolidate the confidence on such results and study the conditions that guarantees such accuracy.

For their performance, UAVs have already conquered a prominent position in the field of photogrammetry. When georeferencing using GPS in RTK mode will have achieved a sufficient degree of reliability, perhaps making use of the permanent stations networks, their role is certainly destined to grow even more.

ACKNOWLEDGEMENTS (OPTIONAL)

I want to express my gratitude to my supervisor Gianfranco Forlani. From the beginning, he supported me in the work with inspiration and brilliance.

REFERENCES

Baiocchi, V., Dominici, D., & Mormile, M. (2013). UAV application in post-seismic environment. In: *ISPRS – International Archives of the Photogrammetry, Remote Sensing and Spatial Information Sciences, Vol. XL-1 W2*, pp. 21-25.

- Bendea, H., Boccardo, P., Dequal, S., Giulio Tonolo, F., Marechino, D., & Piras, M. (2008). Low cost UAV for post-disaster assessment. In: *ISPRS-The International Archives of the Photogrammetry, Remote Sensing and Spatial Information Sciences, Vol. XXXVII (Part B8)*, 1373-1379.
- Barazzetti, L., Scaioni, M., & Remondino, F. (2010). Orientation and 3D modelling from markerless terrestrial images: combining accuracy with automation. In: *The Photogrammetric Record, Vol. 25(132)*, pp. 356-381.
- Cramer, M., Stallmann, D., & Haala, N. (2000). Direct georeferencing using GPS/inertial exterior orientations for photogrammetric applications. In: *International Archives of Photogrammetry and Remote Sensing, Amsterdam, The Netherlands, Vol. XXXIII, Part B3/1*, pp. 198-205.
- Dall'Asta, E., Delaloye, R., Diotri, F., Forlani, G., Fornari, M., Morra di Cella, U., Pogliotti, P., Roncella, R., & Santise, M. (2015a). Use of UAS in a high mountain landscape: the case of Gran Sommetta rock glacier (Ao). In: *ISPRS – International Archives Photogrammetry, Remote Sensing and Spatial Information Sciences., Vol. XL-3/W3*, pp. 391-397, doi:10.5194/isprsarchives-XL-3-W3-391-2015, 2015.
- Dall'Asta, E., Thoeni, K., Santise, M., Forlani, G., Giacomini, A., & Roncella, R. (2015b). Network Design and Quality Checks in Automatic Orientation of Close-Range Photogrammetric Blocks. In: *Sensors, 15(4)*, 7985-8008.
- d'Oleire-Oltmanns, S., Marzloff, I., Peter, K. D., & Ries, J. B. (2012). Unmanned Aerial Vehicle (UAV) for monitoring soil erosion in Morocco. *Remote Sensing, 4(11)*, pp. 3390-3416.
- Forlani, G., 1986. Sperimentazione del nuovo programma CALGE dell'ITM. In: *Bollettino SIFET, Vol. 2*, pp. 63-72.
- Forlani, G., & Pinto, L. (1994, August). Experiences of combined block adjustment with GPS data. In: *Spatial Information from Digital Photogrammetry and Computer Vision: ISPRS Commission III Symposium*, pp. 219-226. International Society for Optics and Photonics.
- Forlani, G., & Pinto, L. (2007, May). GPS-assisted adjustment of terrestrial blocks. In: *Proceeding of the 5th International Symposium on Mobile Mapping Technology (MMT'07). Padova, (on CD-ROM). ISSN*, pp. 1682-1777.
- Forlani, G., Pinto, L., Roncella, R., & Pagliari, D. (2014). Terrestrial photogrammetry without ground control points. *Earth Science Informatics, Vol 7(2)*, 71-81.
- Friess, P. (1986). A Simulation Study on the Improvement of Aerial Triangulation by Navigation Data, *ISPRS Comm. III Symposium, Rovaniemi*, pp. 269-283.
- Gini, R., Passoni, D., Pinto, L., & Sona, G. (2012). Aerial images from an UAV system: 3d modeling and tree species classification in a park area. In: *International Archives of the Photogrammetry, Remote Sensing and Spatial Information Sciences, Vol. XXXIX/B1*, pp. 361-366.
- Granshaw, S. I. (1980). Bundle adjustment methods in engineering photogrammetry. In: *The Photogrammetric Record, Vol. 10(56)*, 181-207.
- Gurtner, W., RINEX: The receiver independent exchange Format version 2, 1997.
- James, M. R., & Robson, S. (2014). Mitigating systematic error in topographic models derived from UAV and ground-based image networks. In: *Earth Surface Processes and Landforms, Vol. 39(10)*, pp. 1413-1420.
- Kraus, K. (1993). *Photogrammetry: V. 1, Fundamentals and Standard Processes*. Ferdinand Dummlers Verlag.
- Laliberte, A. S., Herrick, J. E., Rango, A., & Winters, C. (2010). Acquisition, orthorectification, and object-based classification of unmanned aerial vehicle (UAV) imagery for rangeland monitoring. In: *Photogrammetric Engineering & Remote Sensing, Vol. 76(6)*, pp. 661-672.
- Lucieer, A., de Jong, S., & Turner, D. (2013). Mapping landslide displacements using Structure from Motion (SfM) and image correlation of multi-temporal UAV photography. In: *Progress in Physical Geography, Vol. 38(1)*, pp 97-116.
- Nocerino, E., Menna, F., & Remondino, F. (2014). Accuracy of typical photogrammetric networks in cultural heritage 3D modeling projects. In: *ISPRS-International Archives of the Photogrammetry, Remote Sensing and Spatial Information Sciences, Vol. XL-5*, pp. 465-472.
- Papo, H. B. (1985). Extended free net adjustment constraints. In: *Bulletin géodésique, Vol. 59(4)*, pp. 378-390.
- Rosnell, T., & Honkavaara, E. (2012). Point cloud generation from aerial image data acquired by a quadcopter type micro unmanned aerial vehicle and a digital still camera. In: *Sensors, Vol. 12(1)*, pp. 453-480.
- Remondino, F., Barazzetti, L., Nex, F., Scaioni, M., Sarazzi, D., (2011). UAV photogrammetry for mapping and 3D modelling — current status and future perspectives. In: *ISPRS – International Archives of Photogrammetry, Remote Sensing and Spatial Information Sciences, Vol. XXXVIII-1/C22*, pp. 25–31.
- Rinaudo, F., Chiabrando, F., Lingua, A. M., & Spanò, A. T. (2012). Archaeological site monitoring: UAV photogrammetry can be an answer. In: *ISPRS-International Archives of the Photogrammetry, Remote Sensing and Spatial Information Sciences, Vol. XXXIX-B5*, pp. 583-588.
- Santise, M., Fornari, M., Forlani, G., & Roncella, R. (2014). Evaluation of DEM generation accuracy from UAS imagery. In: *ISPRS-International Archives of the Photogrammetry, Remote Sensing and Spatial Information Sciences, Vol. XL-5*, pp. 529-536.
- Santise, M.; 2016. UAS photogrammetric blocks: accuracy, georeferencing and control. PhD thesis, University of Parma, Parma, January 2016.
- Sturm, P., Ramalingam, S., Tardif, J. P., Gasparini, S., & Barreto, J. (2011). Camera models and fundamental concepts used in geometric computer vision. In: *Foundations and Trends® in Computer Graphics and Vision, Vol. 6(1–2)*, pp. 1-183.
- Van Der Vegt, J. W. (1989). GPS Test Flight Flevoland. In: *Proceedings of the 42nd Photogrammetric Week*, Stuttgart University, 11-16. Sept. 1989, pp. 285-298.
- Wu, J., & Zhou, G. (2006, July). High-resolution planimetric mapping from UAV video for quick-response to natural disaster. *Geoscience and Remote Sensing Symposium, 2006. IGARSS 2006. IEEE International Conference on (pp. 3333-3336)*. IEEE.

CONTRIBUTION OF GEOMATIC MODELS TO STRUCTURAL ENGINEERING

Anna Spangher

Dipartimento Politecnico di Ingegneria e Architettura, Università degli Studi di Udine,
via delle Scienze, 206 - 33100 Udine, tel. 0432 558719, e-mail: anna.spangher@gmail.com

KEY WORDS: Laser scanning, 3D Modelling, Cultural Heritage, Structural Analysis, Level of Detail, Finite Element Method

ABSTRACT:

The main purpose of this research can be summarized with the sentence “*which could be the possible contribution of geomatic models to Structural Engineering*”. It results in fact that, beside mechanical and constitutive characteristic of an object, the knowledge of its geometry is as well necessary for a correct approach to its structural analysis. However, contrary to what it could be expected, most of geometric models used for structural analysis are exceedingly simplified, since are often developed starting from plants and sections poor of details obtained from direct survey. This simplification, even if acceptable for the largest part of modern constructions, characterized by regularity and symmetry, is not indicated for buildings and objects belonging to cultural heritage, which present much more complex geometries. For this kind of objects it is possible to operate through geomatic surveying, obtaining realistic 3D models that reproduce geometry in high fidelity. These techniques are nowadays used in many fields, but are not so frequently applied in structural analysis. Probably, this lack of connection between the two disciplines is due to the fact that as much Geomatics seeks precision as much Structural Analysis tries to simplify. The goal of this research is therefore attempting to find a meeting point between models realized through Geomatics and that ones used for Structural Analysis. Therefore, the challenge will consist in finding the correct Level of Detail of models, in order to represent faithfully the object, without losing important information, but also in a way that could be adaptable for Structural Analysis purposes. The work is developed in a first theoretical and general part, a central part developed on cases of study and, finally, in a summarizing part where all the results are compared and analysed. Three different sizes of objects were modelled and structurally analysed, by finite element method software. Through this procedure was verified that, if opportunely processed, geomatic models allow obtaining more accurate results than simplified ones.

1. INTRODUCTION

The disciplines of surveying have improved over time, in step with technological development, from simple methods, based on direct measurements, to the image-based ones, which exploit principles analogous to descriptive geometry. The technologies recently introduced, and collected into the term “Geomatics”, allow surveying, with remarkable accuracy, and subsequently representing, all kinds of three-dimensional objects. Among the wide panorama of the existing surveying techniques, this study focuses on the use of Terrestrial Laser Scanner (TLS) and Close Range Laser Scanner (CRLS) (except for a single particular case), as later specified, without dealing with Photogrammetry, which represents the other contactless surveying technique most used in the field of cultural heritage. Whatever of these technologies has been used, the result consists in a dense point cloud that, opportunely processed, allows obtaining a very detailed 3D model. These models are largely used in the most various disciplines like archaeology, arts and architecture, virtual reality, urban planning, seismology and so on, and often are specifically requested, especially in projects regarding cultural heritage, and its possible restoration or preservation. It wonders therefore why these models are not used also for Structural Analysis, since they are formerly available, and why structural designers prefer to model by themselves a new 3D model, simpler and much less detailed than the geomatic one. The reason of such a choice must be sought in the fact that geomatic 3D models cannot be used directly into Structural Analysis software and need instead further elaborations. In this last decade the interest on the connection between Geomatics and Structural Analysis has improved but, so far, proper structural analysis on surveyed 3D models have not been so frequent. One of the most studied examples, also because of the unrestricted use of its model, is the Michelangelo’s David

model of the Stanford University, which was analysed, among others, by Lolli (2010), Pascale, Bastianini, & Carli (2011) and Intact Solutions, LLC (2009). As logical, the largest part of the published works on this argument relates to the most famous arts object, since it is natural that the major effort for saving and preserving is done on these masterpieces. In this context, it is worth willing to mention the studies held on the Bronzes of Riace statues by De Canio (2012) and on the Tullio Lombardo’s statue of Adam, preserved in the Metropolitan Museum of Art in New York (USA) (Riccardelli, Soutanian, Morris, Becker, Wheeler, & Street, 2014), as well as one of the less famous statue of the Greek philosopher Socrates, in “*Seismic performance assessment and base-isolated floor protection of statues exhibited in museum halls*” by Sorace & Terenzi (2015). Referring to architecture various researches have been held both on architectural details, like the works of Chiabrando, Donadio, Spanò, & Sammartano (2015) on archaeological arches, of Cannella (2015) on the structure of a column, of Bertolini Cestari, Chiabrando, Invernizzi, Marzi, & Spanò (2013) on the vault of the Hall of Honour of the Valentino’s Castle in Torino and of Sternberg (2006) on the vaults of the Meldorf (Germany) Cathedral; both on entire structures like the analysis of the Venetian Villa Giovanelli near Padova by Guarnieri, Pirotti, Pontin, & Vettore (2006), the Church of Villamorón (Spain) (San José, Fernández Martín, Pérez Moneo, Finat, & Martínez Rubio, 2007), the Cathedral of Modena by (Castagnetti, Bertacchini, Capra, & Dubbini, 2012) and the “Torre del Mangia” in Siena (Italy) (Pieraccini, Dei, Betti, Bartoli, Tucci, & Guardini, 2014). While researches held on structural analysis of statues involves the same 3D geomatic models, architecture examples mostly refers to simplified models, obtained from the point clouds, or, otherwise, on singular part of the structure. The most complete study on the Structural Analysis of an entire structure, starting from a proper 3D geomatic model, is

represented by the analysis of the Mastio tower of the Fortress in San Felice sul Panaro (Modena, Italy) held by Castellazzi, D'Altri, Bitelli, Selvaggi, & Lambertini (2015), which applies a FEM Analysis starting directly from the TLS surveying. The main goal of this research is therefore to find a simple method for using geomatic models also for Structural Analysis purposes. In order to define the best way to obtain this scope, three sizes of structural elements, along with their surveying and modeling issues, will be examined. In particular, statues will represent small objects, an arch the medium ones and a building the large ones. Second goal will be to obtain models that can be “much more possible directly” analysed by structural software: from the topological point of view this possibility is guaranteed only with closed 3D solid models. All the procedures for transforming surface models to solid ones were thus analysed and used. Following challenge will consist in finding the correct *Level of Detail* (LoD) of the models, otherwise the number of elements or polygons that describe the object, in order to represent faithfully the object, without losing important information, but also in a way that could be adapt for structural purposes. The LoD will be defined both in geometrical (no. polygons) and in structural (no. ashlars – finite elements) way. Final goal is the performing of the Structural Analysis on so built models and the interpretation of the obtained results. Besides the models achieved by means of Geomatics, also simplified and hypothetical models were created, in order to investigate the existing differences from the geometrical, and consequently structural point of view.

2. 3D RECORDING FOR CULTURAL HERITAGE

2.1 Documenting cultural heritage

The importance of documenting and recording data, referred to cultural and natural heritage, is well internationally recognized and has been argument of discussions and researches since the theory of restoration and conservation began to take hold. By the way, the topic interest of this research is focused only on the aspects related to geometry of the objects and their recording, carried out with the most modern techniques offered by Geomatics. Beside the level of technology acquired, surveying always had close synergy with archaeology, architecture and all those disciplines related to the study and preservation of cultural heritage. Therefore, as techniques got more advanced, also rose an increasing inventive on documenting and preserving heritage digitally. The continuous development of new sensors, data capture methodologies, and multi-resolution 3D representations, and the improvement of existing ones, can contribute significantly to the 3D documentation, conservation, and digital presentation of heritages and to the growth of the research in this field (Remondino & Rizzi, 2010).

Over decades, international organizations and agencies have passed resolutions concerning the obligation for protection, conservation and restoration of monuments. Among them, the documents in which need for documentation comes to light are:

- Athens Convention of 1931;
- Hague Convention of 1954;
- Chart of Venice of 1964;
- Italian Chart of Restoration of 1972.

Since lately new technologies supplanted traditional recording methodologies, it became increasingly important to create a standardization of the “recording strategies”. This held to the definition of two distinct documents:

- ICOMOS Principles for the Recording of Monuments, Groups of Buildings and Sites of 1996;
- UNESCO Chart on the Preservation of the Digital Heritage of 2003.

2.2 3D surveying in cultural heritage

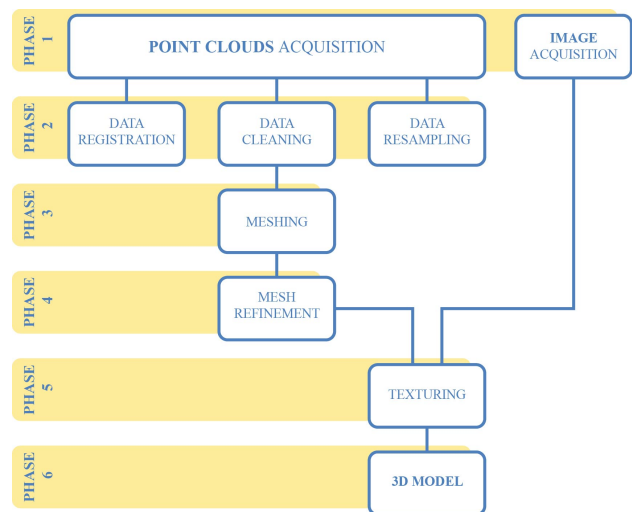
In the field of Cultural Heritage, according to UNESCO (1972), the geometric documentation can be defined as “*the action of acquiring, processing, representing and registering the data necessary for the determination of the position, shape and size of a monument within a three-dimensional (3D) space and at a given moment in time*”. That is, such documentation records the present state of a heritage element, providing the basis for the study of its past (Georgopoulos & Charalambos, 2004).

The surveying for cultural heritage has specific features, which, beyond the unquestionable value and “charm” often offered by the recorded objects, make it very interesting and, at the same time, difficult to describe with conventional schemes and standardized methodologies. Every situation is often a “special case”, and it is not uncommon that the surveying of an object is a sort of challenge for the operator, forcing him to integrate, with his own experience and sometimes with his own imagination, the lack of suitable tools in situations or environments that were highly unusual and difficult. Therefore, virtually all the “geo-topo-cartographic modern tools” can be adopted in the field of cultural heritage, but certainly some are more suited to solve the problems mentioned above (Bitelli, 2002).

On this regard, as already mentioned in *Introduction*, this research focuses on the use of Laser Scanning technologies, since considered the most adaptable for this purpose. Laser scanning surveying will generate *point clouds* as result, which will have to be later opportunely processed to obtain 3D models. Therefore the surveyed data present some common characteristics (Bonora & Tucci, 2012):

1. Data are always digital;
2. Data are 3D;
3. At the moment of acquisition, data are undifferentiated;
4. Time required for their on-site acquisition is very short but the subsequent processing carried out to meet various needs will require pretty long time;
5. Surveying is always carried out without touching the object;
6. Objects are sampled at high resolution, concept directly linked to the concept of Level of Detail (LoD);
7. Geometric data are often associated to information on texture coming from photographic images.

In order to proceed with the 3D modelling a standard pipeline (*Scheme 1*) for data processing was settled, with all the phases needed to transform a 3D point cloud into a 3D solid model, useful and adaptable to Structural Analysis software.



Scheme 1. Flow-chart of TLS data processing.

3. STRUCTURAL ANALYSIS OF MONUMENTS AND HISTORICAL CONSTRUCTIONS

The structural analysis of historical buildings in masonry, and especially of buildings of monumental character, requires attentions and precautions that are beyond the calculation approaches traditionally applied for the study of the new structures, since models and calculation methods normally employed for ordinary buildings can not be uncritically used. Moreover, to add uncertainty about methods of analysis, and interpretation of the structural behaviour, it is also to be considered the fact that, very often, it is very difficult to identify clearly the nowadays static scheme of a building that has been modified during centuries (Betti, Orlando, & Spinelli, 2015). Congruently to this concept standards and laws that rule these subject are definitely more flexible and opened to experimentation than the ones governing concrete or steel structures. The most important rules for structural analysis of masonry buildings in Italy are therefore:

- the “Technical Standards for Construction” issued by the Ministerial Decree 14th January, 2008, from now NCT 2008;
- the “Guidelines for the evaluation and reduction of seismic risk of the cultural heritage” as amended by the Ministry of Heritage and Culture, as licensed by Superior Council of Public Works, from now simply Guidelines.

According to the Guidelines and to the NCT 2008 for improving the resistance of the buildings to seismic events it is necessary to adopt the following procedure:

1. achieving an adequate knowledge of the structure, through the *path of knowledge*;
2. adopting one or more mechanical models of the structure, or of its parts;
3. defining a reference level of seismic safety;
4. evaluating the rated life in the state of fact;
5. designing the seismic intervention;
6. evaluating the rated life in the state of the project;
7. adopting appropriate rules of detail in the implementation of interventions.

While points 2. to 7. of the procedure refer only to tasks of the structural designer, point 1., which is prodromal to all the following ones, is strictly connected with the work of surveyor and 3D modeller, whom contribute could influence structural designer in choosing safety parameters. Standards define in fact three different levels of knowledge of the structure (LC1, LC2 and LC3) upon which depend the confidence factor F_C , as defined in (1), to be applied to seismic coefficients.

$$F_C = 1 + \sum_{k=1}^4 F_{Ck} \quad (1)$$

where coefficients F_{Ck} are defined in *Table 1*.

The higher will be the level of knowledge of the structure, the lower will result this coefficient, and therefore the lower the margin of uncertainty in structural calculation (*Table 2*).

In these regulatory steps, the value of the geometric survey, in relationship to other kind of investigations, can be weight according to the Council of Public Works: if the graphical representation of crack patterns and deformation is not produced, the confidence factor worse 5%, roughly as if a partial knowledge of the construction phases and interpretation of the structural behaviour or only limited investigation of the mechanical parameters of materials (Visintini & Spangher, 2013).

Geometric survey	Geometric survey complete.	$F_{C1} = 0$
	Geometric survey complete, with graphic reconstruction of cracks and displacements.	$F_{C1} = 0,05$
Historical phases of the building and characteristic of the construction	Hypothetical reconstruction of the construction phases based on a limited material survey and documental analysis.	$F_{C2} = 0,12$
	Partial reconstruction of the construction phases based on: a) limited material survey and documental analysis and a complete structural history of the building; b) complete material survey and documental analysis.	$F_{C2} = 0,06$
	Complete reconstruction of the construction phases based on a complete material survey and documental analysis and a complete structural history of the building.	$F_{C2} = 0$
Mechanical properties of materials	Mechanical properties derived from available documentation.	$F_{C3} = 0,12$
	Limited set of test and survey of materials.	$F_{C3} = 0,06$
	Complete set of test and survey of materials.	$F_{C3} = 0$
Ground and foundations	Limited set of test and survey on ground and foundations, in absence of documentation.	$F_{C4} = 0,06$
	Limited set of test and survey on ground and foundations, with limited documentation.	$F_{C4} = 0,03$
	Complete set of test and survey on ground and foundations.	$F_{C4} = 0$

Table 1. Definition of the confidence factors

Level of knowledge	Geometry	Building details	Materials properties	Analysis method	F_C
LC1	Surveying of walls, vaults, horizontal structures, and stairs. Definition of loads on each constructive element. Surveying of cracks and displacement.	Limited in situ test and survey	Limited in situ test and survey	Limited in situ test and survey	1,35
LC2		Complete in situ test and survey	Extended in situ test and survey		1,20
LC3			Complete in situ test and survey		1,00

Table 2. Correlation between Level of knowledge and F_C

As it concerns Structural Analysis of statues or small objects the most complete referring document is instead represented by the “*Guidelines for the Safeguard of Cultural Heritage against Natural Risk*” where there is a specific section, the third, dedicated to museum goods. From its analysis it clearly comes to light that in order to fully analyse the aspects that involve structurally a small-size object it is necessary to know:

- the position of its centre of gravity and its geometry;
- the condition relating to its connections with the boundary (leant, fixed, suspended...);
- the conditions of the resistance of the material composing the object;
- the damages or cracks suffered;
- the forces that might impact on the object.

4. CASES OF STUDY

4.1 Small size objects

Two cases of study were considered in this first part of the research, according to two different kind of procedure for acquiring data and according to the different kind of analysis held, as described in following chapter 5 and 6.

The first example is the statue of Emperor Claudio (*Figure 1a*) preserved in the National Archaeological Museum of Aquileia and dating, presumably, to the first century AD, whose sculptor is unknown. The statue, deeply injured, has the typical position of the “*adlocutio*”, which is the act by which a speaker addresses his audience starting the speech, and not a real salute. Emperor Augustus was the first one represented on this act and all the following emperors were, from that time, so symbolized, since the *adlocutio* was interpreted as an act of divine. The statue of Emperor Claudio had probably the right arm, actually missing, lifted upwards and the left one flexed holding the garment or something else. The right arm was probably attached to the body of the statue with a pin, of which remains the

footprint, while the right side was an integral part of the sculpture. The statuary complex is 201,3 cm tall and is set on a concrete pedestal of 70 x 70 h 35 cm. The estimated weight of the statue is set about 5,2 q, whereas a specific weight of the marble equal to 2370 kg/m³. As introduced, the state of preservation is modest: the statue in fact, besides being mutilated, has several fractures, some of which are grouted. In addition the entire surface has dark spots spread, as evidence of the action of a past fire. The presence of these fractures made this statue interesting for the study proposed in this research.

The second case of study is the statue of St. John the Baptist (*Figure 1b*), also known as St. John the Child Martelli, whose attribution is uncertain and still much debated among art historians, who are partly inclined to consider Donatello as the sole executor, partly instead prefer the hypothesis that Desiderio da Settignano is the author, as a student of the first, or, at last, was also supposed for a collaborative work between the two artists. The statue is currently conserved in the Bargello Museum of Florence from 1913, since its donation from the Martelli family, which commissioned it for sure to Donatello presumably in between 1455 and 1460 as reported in “The lives of the most excellent painters, sculptors and architects” by Vasari (1568). The statue, realized in marble, even if in full-figure, was probably set on a pedestal against a wall. Since it was always conserved in closed places, it has a perfect state of preservation, only the gilding decayed because of the time. The object has all the typical characteristic listed in the “*Guidelines for the Safeguard of Cultural Heritage against Natural Risk*” and therefore it is perfect for testing.

4.2 Medium size objects

Bollani Arch (*Figure 1c*), erected in 1556 and credited to Palladio, located at the foot of the monumental uphill leading to the Castle of Udine, on the left side of the Venetian Lodge of St. John is the medium size object used as case of study for medium size objects. The single “fornice” semi-circular arch structure is made, on the front side, of piacentina stone, and, on the backside of masonry. The backside is characterized by a particular curvature, very difficult to survey with direct methods. On the top stands the winged lion of St. Marc, as symbol of the Venetian domain. The structure is 8,24 m high and 7,74 m wide and, for the conformation of the segments, it is presumed that had been realized according to the measurements of the foot of Udine, corresponding to about 34,05 cm, and its multiple (Frangipane, 2007). This monument is geometrically simple and was therefore really suitable for a comparison between the geomatic model behaviour and the geometric one and also for underlining the differences between models realized by direct survey and a geomatic model.

4.3 Large size objects

The last case of study is represented by the Baptistery of the Basilica of Aquileia (*Figure 1d*), which dates back his origins to the fourth century. The complex of the Basilica, as it appears nowadays, is the result of several extensions and reconstructions implemented over the centuries and, taking exception to the most recent “Mosaic hall”, the present structure is basically the same of the one consecrated in 1031 by Patriarch Popone. The Baptistery is connected to the Basilica through the so-called “Church of Pagans”, a medieval hall, ending with an open porch and through an opening on its South part, it is as well attached to the already cited “Mosaic Hall”. The structure is also called “Cromatian Baptistery”, since its first construction is attributed at the time when Cromazio was Bishop of the diocese (from 387/388 to 407/408), even if the exact date remains doubtful

(Tavano, 1972). As the rest of the structure also the Baptistery changed shape and use over the centuries: now it appears as an octagonal form inscribed in a pseudo-square shape, with dimensions variable between 16 and 18 meters. The Baptistery is currently about 11 meters high but was probably much higher in past times. It was realized in masonry in a time frame some centuries long and therefore it appears enough regular in some parts and rough in others, with stones and bricks mixed in an unordered form. Beside the historical and cultural importance of the building, the reason that pushed the interest in its studying is due to the fact that its geometry is easily reproducible also into FEA Software, making the results of the research verifiable.



Figure 1. a) Statue of Emperor Claudio – b) Statue of St. John the Baptist – c) Bollani Arch – d) Baptistery of Aquileia.

5. FROM POINT CLOUDS TO 3D SOLID MODELLING AND STRUCTURAL ANALYSIS PROCESS

5.1 Point clouds acquisition

The acquisition of point clouds – *phase 1 of Scheme 1* – was realized, for all cases, through laser scanning surveying, except for the top part of the Baptistery, which was hard to reach through the available instrument and therefore was surveyed by photogrammetry, with the aid of an extensible tripod. Among the considered cases, the one of the Statue of St. John Baptist, cannot be directly compared to the others, because of the different scanning system used, (CRLS), which through a singular scan, with a handled device, allows to obtain directly the whole mesh surface. In the following *Table 3* are reported the instruments used for each survey, the number of scans realized, the number of points acquired and the step angle used for each scan, while for photogrammetric survey are reported the number of stations and the number of images acquired.

Object	Instrument used	Scans (no.)	Points acquired (No.)	Step Angle (°)
Statue of St. John Baptist	ModelMaker MMDx/MMC Handheld	1	-	-
Statue of Emperor Claudio	TLS Faro Focus 3D S120	9	9.997.224	0,044
Bollani Arch	TLS Riegl Z390i	3	3.395.200	0,120
Baptistery of Aquileia	Int. TLS Riegl Z390i	9	3.219.815	0,120
	Ext. TLS Riegl Z400	16	23.751.491	0,120
	Ext. Canon EOS6D	(4) (77)	7.937.044	-
Total			34.908.350	

Table 3. Characteristic of four cases surveying.

From the analysis of these data it results rather evident that statues are the most complex objects to survey since in need of a number of scans comparable to the ones of a building. This is due both to the presence of many occluded parts and geometry concavities, impossible to survey with only a frontal and a backside scans, but also because the Level of Detail (LoD) needed to describe such kind of objects has to be very high. On the other hand buildings have a more regular shape and need a lower LoD, therefore a lower number of scans is needed as long as each side of the building is achieved with a minimum overlapping. Referring to the Baptistery were necessary 9 scans and each one was realized placing the instrument in front of each façade. Differently, the interior part was more elaborate and challenging to survey because of the presence of decorations, of the hexagonal baptismal font, of the six columns and recesses, therefore 16 scans were necessary in order to cover the entire interior surface. Finally, the case of Bollani Arch resulted the simplest and only 3 scans were sufficient to acquire all the surface of the object with a good LoD.

5.2 Data registration, cleaning and resampling

Phase 2 of Scheme 1 refers to Data Elaboration: starting from Registration and, once obtained a unique point cloud representing the surveyed object, proceeding with Data Cleaning and Resampling, in order to obtain a point cloud easily manageable with meshing algorithms. Taking exception for St. John Baptist statue, whose scans rendered directly a surface, it was necessary to register all the data. In order to achieve this result it was necessary, for each object, to place a certain number of targets all over the surfaces to acquire. For the case of the Statue, because of the many scans acquired, and therefore because of the extremely high overlapping, it was not necessary to place a lot of targets. The building case instead needed a lot of targets, for a total amount of 70 on the exterior part and 17 in the interior. Furthermore, in order to proceed with the global registration of all the exterior and interior scans it was necessary to achieve also a topographic network of ten vertexes, surveying with a EDM total station all the placed targets and also other 43 natural points, identified on corners, edges or evident protrusions. The Arch instead, being simpler, as said in the previous paragraph, needed only 14 targets.

Object	Topographic surveying	No. and typology target used	Natural points or features	Registration Residual (mm)	Final registration Residual (mm)
Statue of Emperor Claudio	No	6 spherical targets (Ø14,5 cm) 18 checkerboards (10 x 10)	yes	3,2	1,8
Bollani Arch	No	14 cylindrical targets Ø10 cm	yes	8,0	3,3
Baptistery of Aquileia	Int.	17 targets 2 cm x 2 cm	yes	-	15,4
	Ext.	15 cylindrical targets Ø10 cm	no	-	
	Ext.	55 disk Ø5 cm	-	-	

Table 4. Registration of data reporting targets used and residuals.

Referring to registration of scans, beside the ones of the Baptistery, which were registered thanks to topography, the other two models were, at first, registered with the software in use with the instrument, respectively Scene© ver.4.8.4 for Faro and RiSCAN for Riegl, and refined through the well known ICP method. In Table 4 are summarized data on number and typologies of targets used, on the necessity to implement the laser scanning surveying with a topographical one or with the use of natural points, and main results of registration of data. As it is possible to deduce from the analysis the final registration residual grows with the dimension of the object: as logical, an error of 3 mm dimension is influencing on a small size object, but is totally not perceptible on a large size object like a whole building. Data Cleaning and Resampling are operations respectively necessary for eliminating incorrect points, due to noise of data and outlier points, and in order to arrange points on a grid, since density of points clouds is very different depending on the distance of the scan station from the object and according to the different instruments used and their characteristic settings. These operations involve that the number of points significantly decrease but point clouds result more lighter and suitable for modeling, as it is possible to see in Figure 2, for the example of the Arch Bollani, where also the points not useful for the Structural Analysis were eliminated.

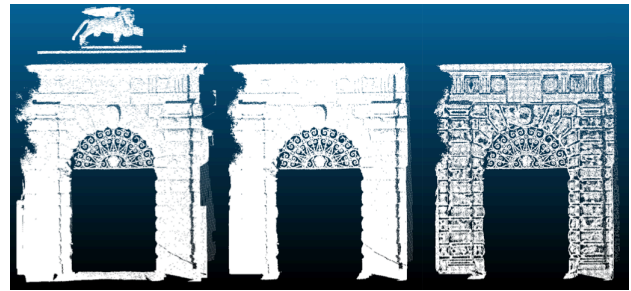


Figure 2. Arch Bollani original point cloud, point cloud after cleaning and after resampling on a 3 cm grid.

5.3 Meshing, mesh refinement and 3D solid modelling

As already specified, beside the case of the Statue of St. John, where surface is the direct result of the surveying and where software computes meshing automatically, for all the other cases it was necessary to use different algorithms in order to obtain surface models from point clouds. This procedure is called meshing and corresponds to Phase 3 of Scheme 1. The preferred algorithm for computing surfaces was Poisson Surface Reconstruction proposed by Kazhdan, Bolitho, & Hoppe (2006), of Johns Hopkins University (Figure 3). This algorithm takes into account all the points at one time without resorting to a partition space, greatly reducing surface noise, maintaining a high LoD, and it is very adaptable to the case of closed surfaces. This algorithm is implemented in all the three meshing software used that are MeshLab ver.1.3.3 (Visual Computing Lab - ISTI - CNR, 2014), CloudCompare ver. 2.6.0 (Girardeau-Montaut, 2015) and Geomagic Wrap ver. 2014 (3DSystem, 2014).

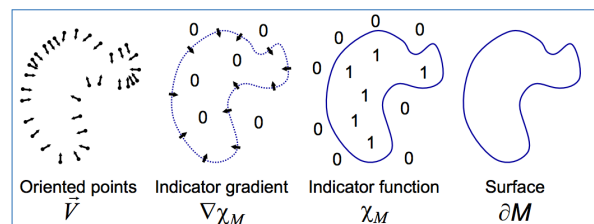


Figure 3. Intuitive illustration of Poisson reconstruction in 2D

As it is possible to see in the following *Table 5*, the average area of the triangles composing each mesh grows with the size of the objects, while the number of triangles necessary for describing the objects decreases. In the case of small size objects the surface of triangles is approximately millimetric: the Statue of St. John Baptist has an extraordinary high LoD, surely excessive for a structural analysis, while the Statue of Emperor Claudio has a low LoD, which is good enough for structural analysis, but not sufficient for any use like 3D reprinting or virtual reality. In the case of medium size objects a centimetric surface of triangles is sufficient for a good LoD of the object and even excessive for a structural analysis. Finally, as it refers to large size objects, the dimension of triangles is decimetric: as in the previous case this dimension offers a more than satisfactory geometrical LoD.

Object	No. triangles	Average surface of triangles (mm ²)	
Statue of St. John Baptist	5.178.132	0,40	
Statue of Emperor Claudio	1.595.466	3,72	
Bollani Arch	1.197.598	258	
Baptistry of Aquileia	Int.	592.936	1.489
	Ext.	497.812	1.233
	Total	1.090.748	

Table 5. Surface models obtained.

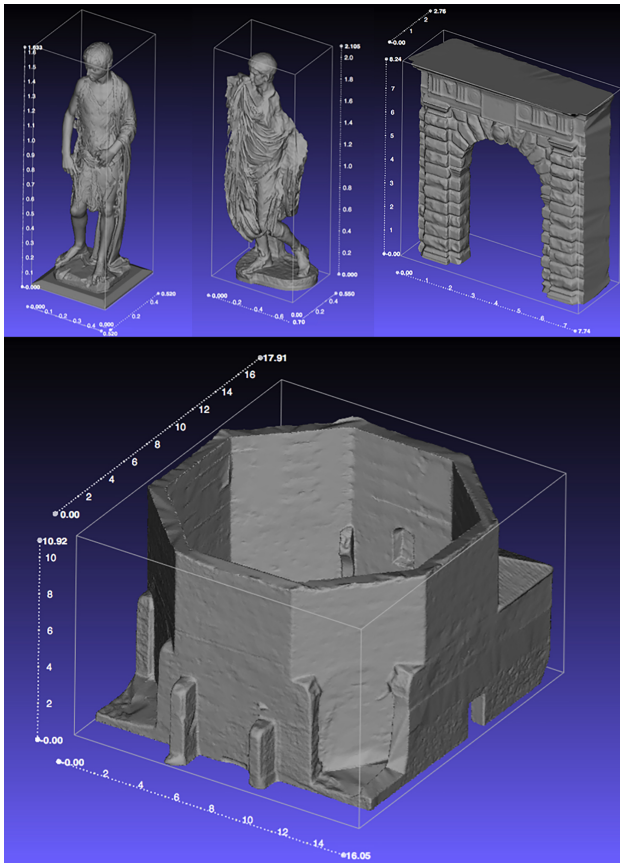


Figure 4. The four objects represented in their quoted bounding box. From the top left the Statue of St. John Baptist, the Statue of Emperor Claudio, the Bollani Arch and on the Bottom the Baptistry.

Surfaces obtained through meshing operations involve different kinds of problems like isolated vertexes, dangling edges, singular edges and vertexes, non-manifolds edges and triangles, orientation inconsistencies, surface gaps and holes and self-intersections that need to be corrected (Attene, Campen & Kobbelt, 2013). Operations that allow eliminating those

incongruences belong to the *Phase 4* of *Scheme 1* and are collected into the definition of Mesh Refinement. So defined models (*Figure 4*) resulted hypothetically structurally analysable, and therefore directly importable in Finite Element Analysis software, since:

- they are 3D solid models;
- they have no incongruences.

Otherwise, taking exception for the Statue of Emperor Claudio, where starting geometrical LoD was low, the number of triangles composing the models resulted excessive for the computing capability of the software and therefore it was necessary to provide with a further simplification of the meshes.

5.4 Alternative models

Other models of the four testing objects were realized, throughout research, following three different principles, with different purposes:

- building of hypothetical models, derived from the original one in order to verify the possible structural contribute of determinate parts of the artefacts or the different behaviour in different physical conditions;
- realization of models with simplified methods, starting from measures derived by direct surveying: these models could be assimilated to the ones realized directly within the FEA software. Subsequently was held a comparison of the behaviour of the simplified model with the geomatic one;
- realization of models with decreasing LoD, starting from 3D solid models with maximum LoD, in order to find the correct equilibrium among the necessity to represent correctly the objects and the need of simplified models for computational analysis in FEA software.

First case was applied to the study of the statue of Emperor Claudio, where beside the original model were realized two other ones (*Figure 5*): the first without the back support and the second one as a virtual restoration of the statue, supposing its original shape. In this way it was possible to define which is the load held by the back support and also the behaviour of the statue in its original configuration and to suppose why it broke.



Figure 5. In the middle the model of the statue of Emperor Claudio. On the left the model virtually restored and on the right the model lacking of the back support.

The realization of simplified models relates to medium and large size objects (*Figure 6*). The simplified model of Bollani Arch was realized within the FEM software Lisa Finite Element Analysis 8.0.0™ (LisaFEA) (Sonnenhof Holdings, 2013) using the simple ashlar there available, starting from the measures derived from direct surveying. The simplified model of the Baptistry was instead realized with Sketchup© 2015 Tecnobit S.r.l., starting from the measure of existing planimetry, integrated with some measure of direct surveying for height, since it was a lacking data.

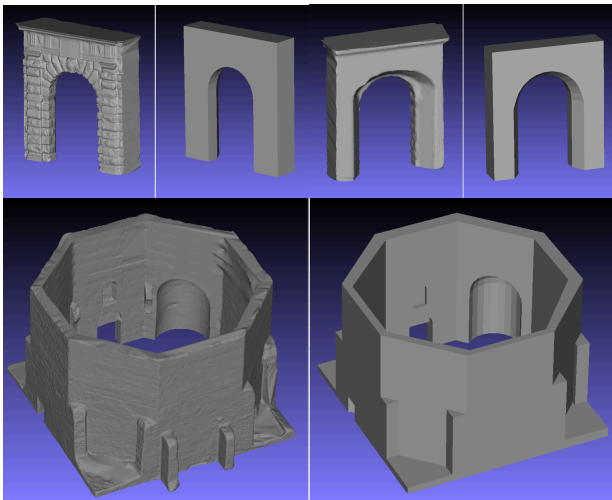


Figure 6. The arch in its original model and in the simplified one. The Baptistery in its original model and in the simplified one.

Finally last case refers to models realized starting from the original 3D solid models decreasing the LoD downstream simplified through processes of decimation (Figure 7).

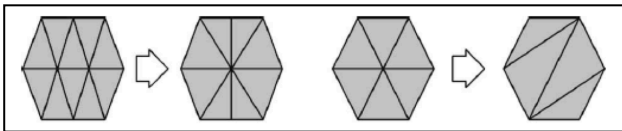


Figure 7 - Simplification of the mesh through decimation

This procedure was applied as well to the statue of St. John Baptist, to the model of the Arch and to the Baptistery. For the model of the statue St. John Baptist the decimation was taken to an extreme of 97%, by virtue of the elevated starting LoD, still conserving a good geometrical representation and maintaining the position of barycentre and centre of the mass. In fact, applying this reduction to the geometry of models, they still appeared realistic and results of the consequent structural analysis very close to the ones obtained on the original ones. As it is possible to see in Table 6 differences between volume and surface before and after decimation appear really limited and as at it refer to barycentre and centre of the mass, which are the most important for calculation, the difference is millimetric.

		Original model	Simplified model	Differences
Volume		0,066013 m ³	0,065988 m ³	0,000025 m ³
Surface		2,065576 m ²	2,005458 m ²	0,060118 m ²
Mesh barycentre	X	0,030579 m	0,030665 m	-0,000086 m
	Y	0,660129 m	0,663272 m	-0,003143 m
	Z	-0,020131 m	-0,020457 m	0,000326 m
Centre of the mass	X	0,034721 m	0,034693 m	0,000028 m
	Y	0,722907 m	0,722269 m	0,000638 m
	Z	-0,021406 m	-0,021405 m	-0,000001 m

Table 6. Values of surface and volume and coordinates of Mesh barycentre and centre of the mass of St. John Baptist model before and after decimation.

5.5 Structural Analysis

The software for Structural Analysis mostly used in the research is a Rhinoceros (McNeel, 2014) plug-in, Scan-and-Solve™ ver.1.6 (Intact Solutions, 2014), which allows analysing directly the surface models obtained without any re-meshing tasks. In fact it adopts a completely different principle, if compared to other software, based on the idea to create separate geometric and physical representation of the model to analyse and to combine them only when it results necessary. This methodology offers the opportunity to use native geometry of the objects and

therefore the pre-processing phase of structural 3D modeling is unnecessary, with a great saving of time and also with the advantage of preserving from errors due to interpretation of geometry and modeling (Freytag, Shapiro, & Tsukanov, 2011). Some models were also tested with the software Lisa Finite Element Analysis 8.0.0™ (LisaFEA)(Sonnenhof Holdings, 2013), which allows the modeling of structure through mono-bi-tri-dimensional elements and once assumed the right loads and constraints proceed with the analysis solving the model with the FEM.

In order to proceed with the FEA analysis for each model was therefore necessary to define:

- materials;
- restraints;
- forces acting;
- structural LoD.

Referring to the first topic of the list, of course, the characteristics of the materials used, for each object, were different, and are reported in Table 7. The most resistant structures are the statues, that are monolithic pieces of marble, while the less resistant is represented by the Baptistery, which is a composite material.

Object	Description	Density (kg/m ³)	Elastic modulus (Pa)	Poisson Ratio	Default failure Criterion	Ultimate tensile Strength (Pa)	Ultimate compressive strength (Pa)
Statue of St. John Baptist	Marble Low density	2370	6,00x10 ¹⁰	0,25	Coulomb Mohr	7,00x10 ⁶	6,89x10 ⁷
Statue of Emperor Claudio	Marble Low density	2370	6,00x10 ¹⁰	0,25	Coulomb Mohr	7,00x10 ⁶	6,89x10 ⁷
Bollani Arch	Brick Stone Composite	2700	2,70x10 ⁹	0,25	Coulomb Mohr	1,72x10 ⁶	7,00x10 ⁶
Baptistery of Aquileia	2Leaves folded masonry	1900	8,70x10 ⁸	0,20	Coulomb Mohr	1,05x10 ⁵	1,40x10 ⁶

Table 7. Material properties for all the models.

Referring to restraints, in all cases were adopted fixed ends at the base of the objects. This is clearly a simplification that does not keep in consideration, especially for the arch and for the Baptistery, the ground elasticity, and the behaviour of foundation. These parameters are anyway another subject argument and would need also further survey or information to be developed, therefore, for testing results on the 3D models obtained, the supposed restraints can be considered acceptable. For the case of the arch and the Baptistery (Figure 8), further restraints were also assumed in correspondence with the presence of other buildings, adopting links in this case.

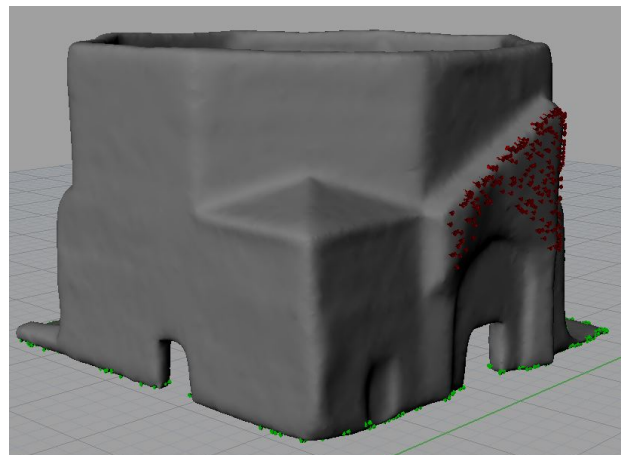


Figure 8. Restraints applied on the Baptistery. In green are represented the ground fixed ends and in red the links.

As it regards the forces acting on the objects, in all the cases, except for the statue of St. John Baptist, were considered only gravity loads. In the case of St. John Baptist statue, it was

supposed also a horizontal force acting on the barycentre, in a minimum value corresponding to the start of an oscillatory movement, in order to verify if the collapsing could be caused by over stresses or over turning (Figure 9).

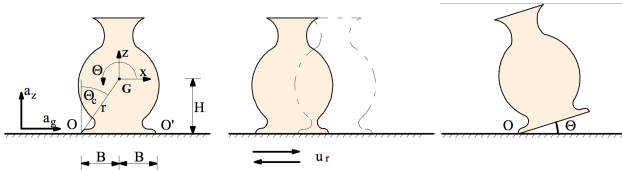


Figure 9. Applied forces on the Statue of St. John the Baptist.

As it concerns the structural LoD several models were tested, in order to verify which is the most suitable structural LoD preserving the correctness of results without having an excessive computational need. Models were tested with a different number of elementary cubes, representing the finite elements, and it resulted that the ideal structural LoD is that one with cube dimensions as much possible similar to the medium dimensions of the minimum geometric details of the object. The ideal LoD adopted for each object is reported in Table 8.

Object	Number of cubes	Dimension of cube (mm)
Statue of St. John Baptist	10.000	22
Statue of Emperor Claudio	9.999	34
Bollani Arch	108.000	91
Baptistery of Aquileia	42.800	242

Table 8. Structural LoD adopted for each model.

Once set all the parameters above described, structural analysis was performed for all the models obtained, both originals and modified, also in order to compare results, as better described in chapter 6. Of course, referring to such different objects, as it concerns dimensions, applied loads and restraints, and even materials characteristic, it is illogical to compare values about resulting stresses and strains. In order to verify the congruence of the analysis to reality the resulting total displacement of each object is reported in Table 9, along with the height of the building and the Elastic Module of the material. In order to verify data for the Statue of St. John Baptist only the value of total displacement due to gravity load is reported. Results appear to be congruent since the object less high and more stiff is the one with a lower total displacement, while the Baptistery, which is the higher object, but with lower material capability, is the one with a greater total displacement.

Object	Height (m)	Elastic modulus (Pa)	Maximum total displacement (mm)
Statue of St. John Baptist	1,63	6,00x10 ¹⁰	0,01
Statue of Emperor Claudio	2,10	6,00x10 ¹⁰	0,03
Bollani Arch	8,24	2,70x10 ⁹	0,80
Baptistery of Aquileia	10,92	8,70x10 ⁸	1,56

Table 9. Total displacement for each model, with Elastic modulus adopted and height of the objects.

6. COMPARISON OF RESULTS

As it concern the structural analysis of the model of the Statue of Emperor Claudio the most interesting aspect is for sure connected with the examination of the stress values reached in the ankles, which are the weakest parts of the monument (bottom part of Figure 10). In order to analyse completely the stress path endured, as already specified, three models were realized and compared: in this way it was possible to understand the importance of the back support and also how cracks had origin. In the virtually restored model it is evident that the weight is more elevated and therefore displacement will be evident starting right above the barycentre (left of Figure 10). As long as the statue was placed in its original recess and found sustain in it, there were no cracks, but as the statue got removed from there it probably suffered from the lacking of support,

reaching the limit value and cracking on the ankles. The importance of the back support is also underlined by the study executed virtually removing it. As it is possible to see in the last group of Figure 10, displacement grows quickly and starts just above ankles that are deeply injured and over stressed.

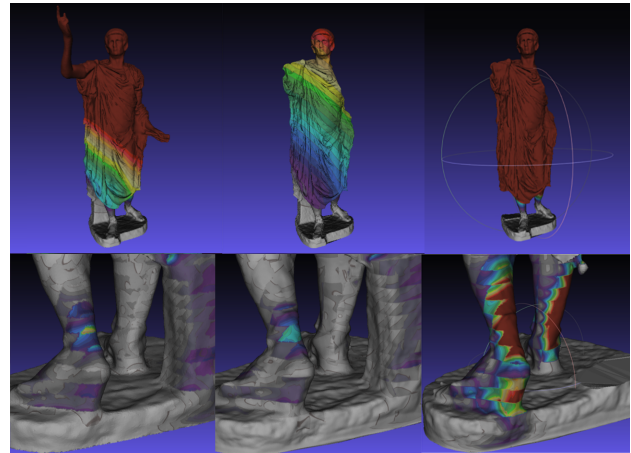


Figure 9. Displacement in the three models of the statue of Emperor Claudio. Mohr's failure criterion applied to ankles of the models.

In the case of the model of the Statue of St. John the Baptist, that did not present any kind of cracks or problem, as before specified, the analysis was held in two cases: supposing the mere gravity load acting and supposing also an addicted horizontal force. Results are reported in Figure 11, where it is evident that the statue in case of gravity load is perfectly steady while, in case of a horizontal force acting (as defined in paragraph 5.5) the collapsing of the object will be due to over stress (Figure 12), since the resistance criterion is exceeded for a value of force inferior than the one needed for overturning.

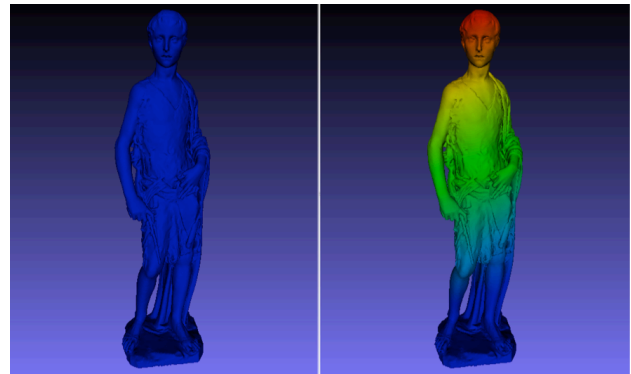


Figure 11. Total displacement trend from value 0 (blue) to 0,005 mm (red) - on the left first load condition and on the right second one.

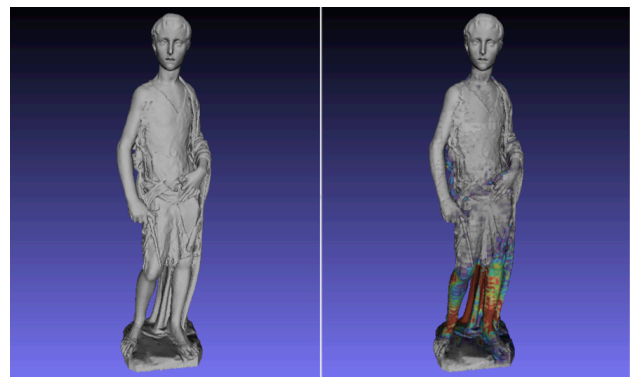


Figure 12. Verification of Coulomb-Mohr Criterion trend, from value 0 (blue) to 1 (red) - on the left the first load condition and on the right the second one.

Referring to the case of Bollani Arch the analysis focused on the estimation of displacement while varying both geometrical and structural LoD. Therefore, starting from the original DSM of the arch, made of 998.000 triangles and applying the decimation filter, by setting the maintenance of edges and curvature, and fixing the percentage of decreasing of the triangles, different models were obtained, built respectively by 500.000, 200.000, 100.000, 50.000, 20.000 and 10.000 triangles. Obviously, the greater is the number of triangles shaping the mesh, the higher will be the correspondence to reality (Figure 13).

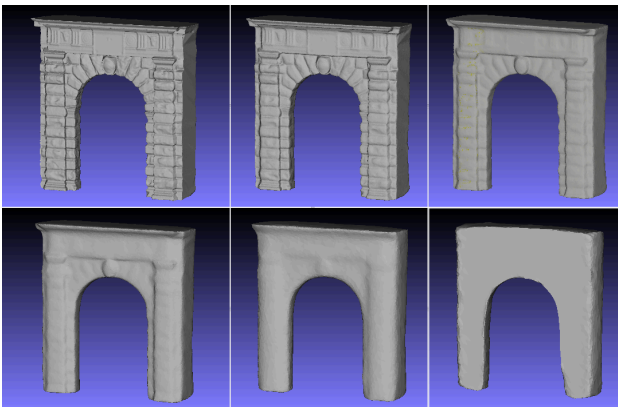


Figure 13. The model of the arch simplified starting from 500.000 triangles and arriving to 10.000 triangles.

Besides the different geometric LoD of the model, it was consider also the “structural LoD”, which is determined by the number of finite elements used in the discretization for the analysis, and for each different geometrical LoD model obtained were realized 6 different structural LoD model with 500.000, 402.000, 304.000, 206.000, 108.000 and 99.000 cubes. The results of this analysis are shown in the Figure 16, in the following page, where are reported the data of Total Displacement for each model. The trend of the displacement is represented on the DSM with a colour scale that varies from the minimum value of 0 mm (in blue) to the indicative maximum value of 1 mm (in red); obviously, the displacement is zero at the base, bound to fixed end, and increases as ascending up to reach even 1,40 mm for the structure with the lower geometrical LoD. It appears that for a decimation of the surface up to 90% in number of triangles (model 100.000), the geometry of the model is still maintained in its form and the various architectural features are rather well defined. A lower definition involves a fast decay towards geometries that hardly are representative of the object: in particular, if in the models 50.000 and 20.000 are still identified the main components of the structure, like the key of the arch and the upper moulding, are lost instead the definition of the segments. In the simplest model these differences are totally absorbed and the surface is completely smooth. In contrast, as regards the different LoD for structural modeling, having to do with an object that presents almost regular geometric peculiarity that is contained in the 10 cm approximately, the results are really similar once exceeded 108.000 the cubes for analysis. The global analysis of the results obtained leads to the assessment that the general trend of the results becomes more or less constant on a decimated model with no more than 10% and comparable to the size of the cube geometric characteristics of the object surveyed. Finally, referring to the last example of the Baptistery, the analysis was held considering the two examples of Figure 6 and comparing the results obtained. The analysis was assumed adopting the same parameters for materials, restraints and forces applied for both the models, focusing on Total Displacement.

Considering that Total Displacement represents the absolute value of the result of the linear combination of all the displacement that the structure withstands in the three principal directions, and namely the two horizontal displacements and the vertical displacement, as it is possible to see in Figure 14 the major contribute of the displacement is given by the lowering long Z-axis. In the case of the simple model the maximum value obtained is 1,22 mm and is located on the top of the vault of the aps, while, for the case of the DSM model the maximum value, corresponds to 1,56 mm, and is located exactly in the same place. In this case, the maximum value is higher about 28% than the previous case, and also the trend of values converges more quickly to the maximum value of the displacement. As logical the movement of the basis of the building is null, since a fixed end have been placed there, an the displacements results anyway close to 0 since the only load considered is that one given from the proper weight of the structure.

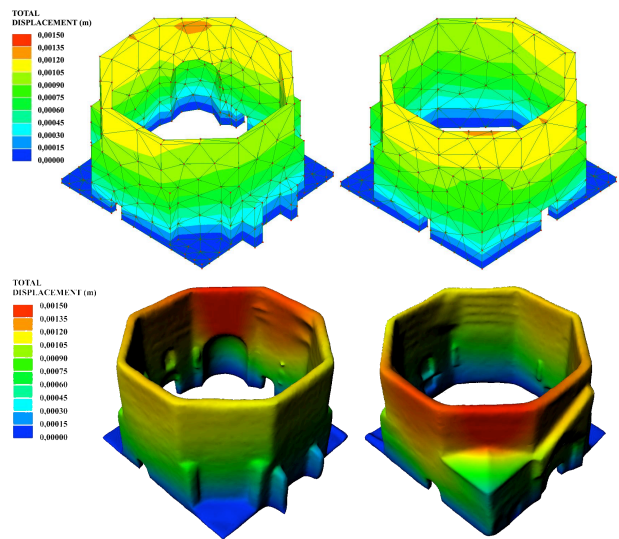


Figure 14. On the top: trend of the total displacement computed from the analysis held with Lisa FEA on the simplified model. Trend of the total displacement computed from the analysis held with Scan-and-Solve on the DSM model.

Analysing the results referred to the failure criteria emerge that the Maximum value of Danger Level exceeds the limit values defined. This “failure” value is reached in correspondence with the attachment of the roof of the Church of Pagans to the Baptistery, signed with the red colour in Figure 15. Since no cracking or yielding signs are present on the structure, it is reasonable to think that a drift of the values, only in that small area, is due to the existence of some sharpen edge or some kind of singularity, which results is a bad refinement of the calculation and consequently an uncorrected result. Therefore, except this single area of the structure the all construction is verified and never exceed the failure values.

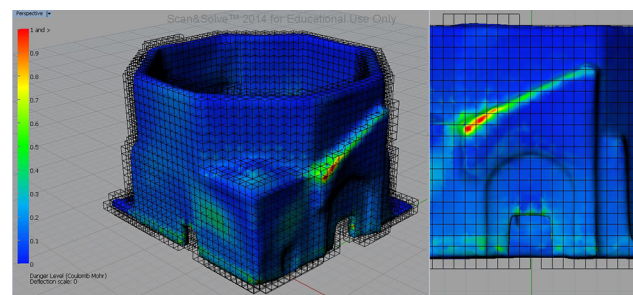


Figure 15. The attachment of the Church of Pagans to the Baptistery, values exceeding the resistance criteria.

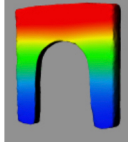
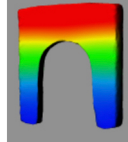
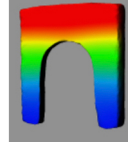
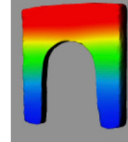
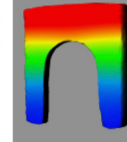
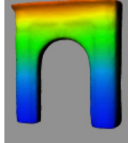
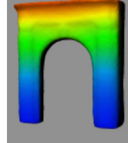
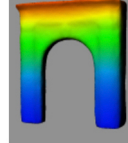
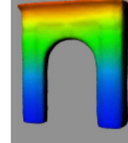
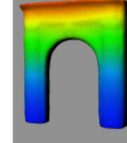
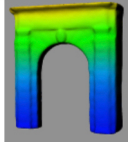
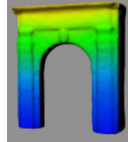
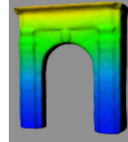
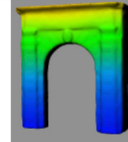
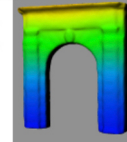
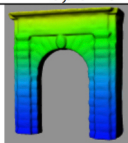
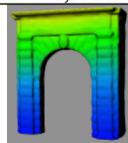
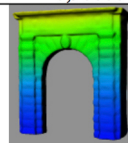
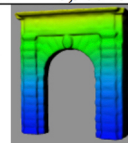
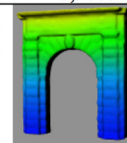
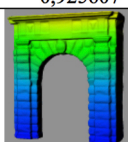
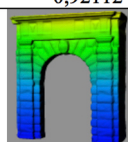
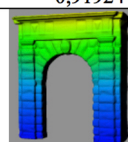
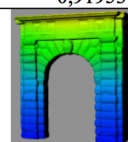
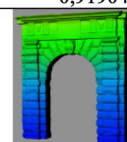
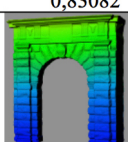
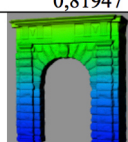
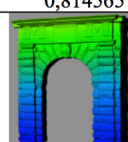
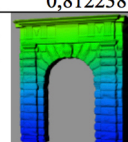
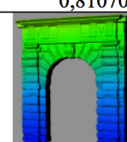
		STRUCTURAL LEVEL OF DETAIL						1 mm 0 mm					
		10.000	108.000	206.000	304.000	402.000	500.000						
GEOMETRICAL LEVEL OF DETAIL	10.000 Model	cube dimension [mm]	198	84	67	59	53	49	1 mm 0 mm				
		n° of cubes	13x38x42	29X87X97	37x108x121	42x124x138	46x136x152	49x147x164					
		max displacement [mm]	1,38372	1,40311	1,40695	1,40831	1,40974	1,41028					
		Volume	53,919 m ³										
		Surface	120,615 m ²										
		Not corrected Weight	107.838 kg										
	cube dimension [mm]	207	88							70	61	55	51
	n° of cubes	15x37x41	33x86x94							41x108x118	46x123x135	51x135x148	55x146x160
	max displacement [mm]	1,03784	1,04638	1,04813	1,04887	1,04932	1,04931						
	Volume	61,2713 m ³											
	Surface	131,15 m ²											
	Not corrected Weight	122.543 kg											
	cube dimension [mm]	210						89		71	62	56	52
	n° of cubes	15x37x40						34x87x94		43x108x117	49x124x134	53x136x147	58x147x159
	max displacement [mm]	0,945622	0,95540	0,95686	0,95752	0,95798	0,95832						
	Volume	63,7928 m ³											
	Surface	138,885 m ²											
	Not corrected Weight	127.586 kg											
	cube dimension [mm]	212						90		71	62	57	53
	n° of cubes	16x38x40						35x87x93		44x109x116	50x124x133	55x137x146	59x147x158
	max displacement [mm]	0,90229	0,90627	0,90666	0,90748	0,90755	0,90748						
	Volume	64,8658 m ³											
	Surface	144,299 m ²											
	Not corrected Weight	129.732 kg											
cube dimension [mm]	214	90						72	63	57	53		
n° of cubes	16x38x40	36x87x93						44x109x116	51x125x132	56x137x146	60x148x157		
max displacement [mm]	0,925607	0,92112	0,91924	0,91953	0,91904	0,91921							
Volume	65,7164 m ³												
Surface	151,425 m ²												
Not corrected Weight	131.433 kg												
cube dimension [mm]	216						91	72	63	57	53		
n° of cubes	16x38x40						36x88x92	45x110x115	52x126x132	57x139x145	61x149x157		
max displacement [mm]	0,83082	0,81947	0,814565	0,812238	0,81070	0,80993							
Volume	66,0589 m ³												
Surface	157,98 m ²												
Not corrected Weight	132.118 kg												

Figure 16. Models with different geometric and structural Level of Detail. Starting from the top the lowest geometrical LoD, 10.000 triangles, comparable to a model realized inside a FEM software throughout ashlar, in the bottom the highest geometrical LoD, 500.000 triangles, very similar to the original DSM mesh. The structural LoD is figured increasing from left to right from 10.000 cubes to 500.000 cubes. Results of Total Displacement are figured in a scale from 0 mm (blue), set in correspondence of the base of the arch, to values that reach or exceed 1 mm (red).

7. CONCLUSIONS

In this research path I tried to combine and implement my knowledge in Geomatics and apply it to a fundamental discipline of Engineering, and namely Structural Analysis.

As introduced, the purpose was to verify if the 3D geometric models, obtained through Geomatics, could find use, not only in the traditional fields of artistic and architectural studies, but also for Structural purposes. It results in fact that, currently, the largest part of geometric data, available from a geomatic surveying, are not considered and 3D structural models are built upon few measures, available also from a direct surveying. This implies that, often, many peculiarities of the analysed objects are not correctly weighted and in order to make up for the lack of knowledge stringent safety factors are adopted.

The answer to the research effort done is for surely positive, since the advocated meeting point, between models realized through Geomatics and that ones used for Structural Analysis, was finally found.

In order to investigate all the typical cases the research dealt with three different typologies of objects, small, medium and large size, testing a common procedure for obtaining a 3D model, adaptable for Structural Analysis software. All the objects were surveyed by means of laser scanners and the sequence of data acquisition, data processing, meshing and meshing refinement, preparatory for achieving the 3D model, were thoroughly described.

From the carried out analyses on the cases of study it is certainly to take into account the following remarks:

- 3D models obtained with Geomatics have generally a very high geometric LoD and are realized for different purposes than structural analysis (3D printing, virtual navigation ...);
- 3D models obtained with the Geomatics must be therefore adapted and transformed before Structural Analysis;
- as it concerns smaller size items the use of Geomatic models is, by now, the only one that is able to guarantee a proper degree of evaluation of the geometry of the object;
- as it concerns the medium and large size objects the method used in this research appears to be convenient for the general object while results necessary for the specific analysis of detailed, otherwise difficult to achieve.

At the end the following goals were therefore reached through this research:

- a "standard" procedure was defined for the creation of 3D solid models of objects belonging to cultural heritage, through a pipeline of operations, in depth described in chapter 5 and summarized in *Scheme 1*;
- 3D solid models derived from Geomatics and suitable for structural analysis were obtained;
- further hypothetical 3D models were realized, useful to speculate on structural behaviour due to previous or different configurations;
- the LoD necessary for a faithful representation of the objects, and appropriate Structural purposes, was defined, testing different LoD configurations, both geometrical and structural;
- Structural Analysis was performed on the obtained models (realistic and hypothetical) and the results were studied and valued;
- Structural Analysis results were compared to the ones obtained from the study of simpler geometrical models obtained through direct survey or through modelling realized with FEM software design tools.

Concluding, it can be assumed that the correctness, the accuracy and the precision of geomatic surveying are necessary, and not excessive, in the study of structural behaviour of building and artefacts belonging to cultural heritage.

Some open questions on the current state of the research, and also some possibility or further development, are related to:

- the possibility to introduce different materials on the models, since, so far, only homogeneous objects were considered – this problem was not resolved, but could be implemented through the use of other software and through the collaboration with more specialized researcher of Structural Analysis;
- the opportunity to provide with a modelling of structures with a higher control on constraints conditions and on mechanical behaviour – as in the previous case also this problematic could find a solution creating a link with Structural engineers;
- the chance to provide with a texturing of the objects, in order to acquire, also from images, further information useful for the structural analysis, like the presence of cracks or the framework and the disposition of materials.

I strongly believe that all the models realized for documenting and data recording of cultural heritage could be used also for structural purposes, without throwing away precious data: maybe it is only necessary for Geomatics to promote the obtainable output and make it suitable for Structural Engineering inputs. What I have done is just a small step towards this goal.

ACKNOWLEDGEMENTS

First, and foremost I have to, and, at the same time, I want to, express my gratitude to professor Domenico Visintini. Beside being my tutor, he represented a guide and, at the same time, he has been able to raise my interest for Geomatics and its research, involving me in many activity and making me part of a team. During these three years I had the opportunity, as well, to meet many people that contributed to make my knowledge growing, sharing their experiences and drawing me inspiration to new questions. I want to thank therefore all the staff of the Geomatics Laboratory for Conservation and Communication of Cultural Heritage of the University of Florence, for the many times they hosted me, and the staff of the Department of Civil, Chemical, Environmental and Materials Engineering of the University of Bologna, for the contribution in the study of the Aquileia Baptistery. I reserve a special thank also to the staff of Scan-and-Solve, and especially to Vadim Shapiro and Michael Freytag, for the licence of the software, for the interest in my research and for answering constantly to all my questions and doubts.

REFERENCES

- 3DSystem. (2014). Geomagic. Based on <http://www.geomagic.com/it>
- Attene, M., Campen, M., & Kobbelt, L. (2013). *Polygon mesh repairing: An application perspective*. Journal ACM Computing Survey , 45 (15).
- Bertolini Cestari, C., Chiabrando, F., Invernizzi, S., Marzi, T., & Spanò, A. (2013). *Terrestrial Laser Scanning and settled techniques: a support to detect pathologies and safety conditions of timber structures*. Advanced Materials Research , 778, p. 350-357.
- Betti, M., Orlando, M., & Spinelli, P. (2015). *La Rocca Strozzi a Campi Bisenzio: Analisi strutturali e proposte di interventi di consolidamento e miglioramento sismico*. Bollettino Ingegneri (5), 3-24.

- Bitelli, G. (2002). *Moderne tecniche e strumentazioni per il rilievo dei beni culturali*. Atti 6a Conferenza Nazionale ASITA. IX-XXIV. Perugia: ASITA.
- Bonora, V., & Tucci, G. (2012). *New technologies for cultural heritage documentation and conservation: the role of Geomatics*. Iconoarch - I Architectural and Technology International Congress, (p. 444-451). Konya.
- Cannella, M. (2015, 1 8-14). *Digital Unwrapping and visualization of complex architectural surfaces for the documentation and the restoration*. DisegnareCon (8).
- Castagnetti, C., Bertacchini, E., Capra, A., & Dubbini, M. (2012). *Terrestrial laser scanning for preserving cultural heritage: analysis of geometric anomalies for ancient structures*. Proceedings of the FIG Working Week.
- Castellazzi, G., D'Altri, A. M., Bitelli, G., Selvaggi, I., & Lambertini, A. (2015). Castellazzi, G., D'Altri, A. M., Bitelli, G., Selvaggi, I., & Lambertini, A. (2015). *From laser scanning to finite element analysis of complex buildings by using a semi-automatic procedure*. Sensors, 20, 2. Sensors (20), p. 2-20.
- Chiabrando, F., Donadio, E., Spanò, A., & Sammartano, G. (2015). *La tecnologia laser scanning per la valutazione statica delle strutture storiche*. XIX Conferenza Nazionale ASITA , (p. 253-261).
- De Canio, G. (2012). *Marble devices for the Base isolation of the two Bronzes of Riace: a proposal for the David of Michelangelo*. The 15th World Conference on Earthquake Engineering. Lisboa, Portugal.
- Frangipane, A. (2007, 1). *Natural stone portals of the town of Udine (Italy): their design, construction and materials between the 15th and 20th centuries*. Geological Society London Special Publication (27), p. 33-42.
- Freytag, M., Shapiro, V., & Tsukanov, I. (2011, April 16). *Finite element analysis in situ*. Finite element in Analysis and Design , p. 957-969.
- Georgopoulos, A., & Charalambos, I. (2004). *Photogrammetric and Surveying Methods for the Geometric Recording of Archaeological Monuments*. FIG WORKING WEEK - Workshop - Archaeological Surveys. Athens: FIG.
- Girardeau-Montaut, D. (2015). CloudCompare. Based on <http://www.cloudcompare.org/>
- Guarnieri, A., Pirotti, F., Pontin, M., & Vettore, A. (2006). *3D Surveying for structural analysis applications*. 3rd IAG/ 12th FIG Symposium. Baden.
- ICOMOS. (2015). ICOMOS - International Council of Monuments and Sites. Consulted on November 28, 2015 da www.icomos.org: <http://www.icomos.org/>
- Intact Solutions, Inc. (2014). Scan-and-Solve for Rhino. Based on <http://www.scan-and-solve.com/>
- Intact Solutions, LLC. (2009). *Scan&Solve: FEA without meshing - White paper*.
- Kazhdan, M., Bolitho, M., & Hoppe, H. (2006). *Poisson Surface Reconstruction*. Eurographics Symposium on Geometry Processing (p. 61-70). Aire-la-Ville: Dieter W. Fellner, Werner Hansmann, Werner Purgathofer, François Sillion Series Editors.
- Linee Guida per la valutazione e riduzione del rischio sismico del patrimonio culturale, prot. n. 92* (Consiglio Superiore dei Lavori Pubblici luglio 23, 2010).
- Lolli, A. (2010). *Monitoraggio per la diagnostica strutturale del David di Michelangelo*. University of Bologna, Italy.
- Norme tecniche per le costruzioni* (Decreto Ministeriale gennaio 14, 2008).
- Pascale, G., Bastianini, F., & Carli, R. (2011). *Monitoring marble cracking in the David by Michelangelo*. (11), 21-24.
- Pieraccini, M., Dei, D., Betti, M., Bartoli, G., Tucci, G., & Guardini, N. (2014). *Dynamic identification of historic masonry towers through an expeditious and no-contact approach: Application to the "Torre del Mangia" in Siena (Italy)*. Journal of Cultural Heritage (15.3), p. 275-284.
- Remondino, F., & Rizzi, A. (2010, September). *Reality-based 3D documentation of natural and cultural heritage sites—techniques, problems, and examples*. APPLIED GEOMATICS , 85-100.
- Riccardelli, C., Soultanian, J., Morris, M., Becker, L., Wheeler, G., & Street, R. (2014). *The Treatment of Tullio Lombardo's Adam: A New Approach to the Conservation of Monumental Marble Sculpture*. Metropolitan Museum Journal (49).
- Robert McNeel & Associates. (2014). Rhinoceros. Based on <https://www.rhino3d.com/it/>
- San José, J. I., Fernández MartIn, J. J., Pérez Moneo, J. D., Finat, J., & Martínez Rubio, J. (2007). Evaluation of structural damages from 3D Laser Scans. XXI CIPA International Symposium: Anticipating the Future of the Cultural. Athens.
- Sonnenhof Holdings. (2013). Lisa FEA. Based on <http://lisafea.com/>
- Sorace, S., & Terenzi, G. (2015). *Seismic performance assessment and base-isolated floor protection of statues exhibited in museum halls*. Bull Earthquake Eng , 1873-1892.
- Sternberg, H. (2006). *Deformation measurements at historical buildings with the help of three-dimensional recording methods and two-dimensional surface evaluations*. 3rd IAG/12th FIG Symposium. Baden.
- Tavano, S. (1972). *Aquileia cristiana*. Antichità Altoadriatiche (3).
- UNESCO. (1972). *Photogrammetry applied to the survey of Historic Monuments, of Sites and to Archaeology*. UNESCO Editions.
- Vasari, G. (1568). *Le vite de' più eccellenti pittori, scultori e architettori*. (M. Marini, A cura di) Roma, Italia: Newton Compton editori s.r.l.
- Visintini, D., & Spangher, A. (2013). *Rilevamento laser scanning, modello della superficie (DSM) e modello per il metodo agli elementi finiti (FEM) di una struttura*. Atti 17a Conferenza Nazionale ASITA (p. 1287-1294). Riva del Garda: ASITA.
- Visual Computing Lab - ISTI CNR. (2014, April 02). Based on Meshlab: <http://meshlab.sourceforge.net/>



AUTEc

Associazione **U**niversitari di **T**opografia **e** **C**artografia

Sezione Tematica 3 GIS e Remote Sensing

*

*Thematic Section 3
GIS and Remote Sensing*

SPATIAL DATA UNCERTAINTY SOURCES IN THE FOREST RESEARCH CONTEXT

Vanina Fissore

DISAFA – University of Torino, L. go Paolo braccini 2, 10095, Grugliasco (TO), Italy; vaninafissore@unito.it.

KEY WORDS: data quality, data metric accuracy, vertical error, LiDAR, LiDAR derived CHM, forestry.

ABSTRACT:

This dissertation focuses on spatial data metric uncertainty sources in the forest research context, with particular focus on data quality and metric accuracy as conditioning factor for results reliability. Three different applications nowadays largely addressed in the forest context were considered for this purpose. Particularly, data uncertainty management was considered within the specific research context of *treeline* mapping; assessment of how spatial data quality, with particular attention on metric accuracy, is considered and managed in *treeline* vertical position or shift identification, is given. Subsequent two applications are instead focused on LiDAR-derived data uncertainty; LiDAR-derived CHM (*Canopy Height Model*) is nowadays widely adopted by forest planners in support to forest inventories. Within the first application an uncertainty estimation method for the quality evaluation of a LiDAR-derived CHM is proposed and applied to a sample area in South Western European Alps (Piemonte region, Italy). In the second one, limits and potentialities in forest characterization (i.e. the estimation of attributes associated to forest structural properties such as tree height and diameter) by using a CHM derived from a low density LiDAR point cloud, were explored; particular attention was paid on the quantification of estimations uncertainty. Results underlined that spatial data and geomatic techniques are powerful tools that require professionalism and specific skills to achieve appropriate results. Moreover, it is clear that appropriate ecological results are dependent on spatial data management, but their reliability relies on the way metadata are interpreted and reported.

1. INTRODUCTION

1.1 Geomatic in the forest research context

In the last decades, the forest research context commonly adopted geomatic techniques and spatially georeferenced data in support to traditional field-based sampling methods, for studying and characterizing forests (e.g. tree density, tree height, tree diameter, etc...). Remote sensing technologies such as satellite and aerial acquisitions, provide profuse open access data with several different characteristics of temporal/spatial resolutions and accuracy values, making them suitable for different applications at landscape, forest stand, areal (with reference to field sample plots) and tree levels.

1.2 Importance of spatial data quality: data metric uncertainty

Data quality is a key component of any spatial data (Zandbergen P. A., 2008]. Improper data management, or lack of metadata, potentially leads to errors that may compromise reliability of results. Preserving data quality is an essential step to guarantee appropriate results. It follows that errors have to be known and their occurrence possibly predicted in order to reduce as much as possible their effect on results (Gomasasca M. A., 2009]. Data quality mainly depends on data metric uncertainty (or accuracy) (Zandbergen P. A., 2008]. While dealing with geographic positioning of features, this latter is defined by a positional accuracy value, including horizontal and vertical positions, with respect to horizontal and vertical datum. Thus, it is possible to separately consider horizontal (σ_x) and vertical (σ_z) accuracy (Gomasasca M. A., 2009]. Horizontal accuracy defines the error limit range in respect to horizontal datum, while vertical accuracy defines the error limit range respect the vertical one. As regard to vertical accuracy, its value is the principal criterion that specifies the quality of height data (ASPRS, 2015] such as DTM (*Digital Terrain Models*) and CHM (*Canopy Height Models*), often adopted in forestry

applications. Many users are unaware about the importance of the quality of height data and about their influence in derived calculations (Aguilar et al., 2009]. In fact, when working with data obtained by computations from others, source data define the uncertainty of derived ones. This process of error transference from source data to derived data is called *uncertainty propagation* (Cheung C.-K., 2000]. The CHM can be used to explain this process since it is obtained by matrix difference from a DSM (*Digital Surface Model*) and a DTM. The DTM represents the ground, while the DSM represents objects above the ground and, consequently, CHM represents trees/objects height value. Because of uncertainty propagation effect, CHM accuracy directly depends on the one of both DTM and DSM. This kind of accuracy is the “expected” one, that depends on the nature of the source data used to get the final one, and it can be defined as “*a-priori*” accuracy. On the other hand, every data can be affected by errors independent from the source data; in the specific case of CHM, errors can be negative height values and they can be investigated through apposite computations. This second kind of accuracy can be defined as “*a-posteriori*” accuracy. Anything that negatively affects accuracy defines the data error. Maintaining data accuracy and eliminating errors are essential prerequisites to avoid error-affected results (Gomasasca M. A., 2009].

1.3 Aim of the thesis

This thesis focuses on spatial data uncertainty sources, and on their effect on data quality, in the forest research context. Particularly, the research deals with three different topics of current relevance in the forest context where spatial data quality is essential for results reliability. First addressed topic (Paragraph 2) is aimed at assessing how spatial data, with particular attention on its metric accuracy, are considered and managed by scientific community in *treeline* vertical position or shift identification. In fact, in the debate over global warming, *treeline* position is considered an important ecological indicator of climate change.

Due to the current relevance and increasingly frequent adoption of LiDAR technology in forestry application (e.g classification of forest stands and individual trees, forest attributes such as tree heights and diameters, etc...), second and third applications (i.e. Paragraphs 3 and 4) particularly focuses on LiDAR-derived data uncertainty sources investigation. Specifically, the second one (Paragraph 3) is directed to estimate the quality of a LiDAR-derived CHM. Although aerial LiDAR-derived CHM is nowadays used to identify tree height variability, quite often users do not take into account internal limits and anomalies caused by raw data (point cloud) processing (i.e. vertical errors) that may affect CHM quality, generating potentially erroneous results in their applications. For this reason, the research proposes the users an auto-consistent procedure for a fast evaluation of CHM accuracy they are going to adopt over their study areas, through an indirect method based on assessment of internal anomalies affecting CHM data. Third topic (Paragraph 4) is instead aimed at quantifying uncertainty of LiDAR-based estimations of trees heights and diameters by using a low density LiDAR point cloud, in order to define its reliability in respect to ground data. In this way, this part of the thesis focused on the comparison between forest estimations from a LiDAR-derived CHM and the same obtained by ground data collection.

2. DATA UNCERTAINTY SOURCES IN TREELINE MAPPING

2.1 Introduction

In the debate over global warming, treeline position is considered an important ecological indicator of climate change and, in the last decades, analysis of upward treeline shifts is often based on various spatial data processed by geomatic techniques. Reliability of achieved treeline measures is a mandatory step, in order to support significant ecological conclusions. This study is specifically aimed at exploring if there are evident recurring limitations or methodological errors in published papers on treeline detection, by mean of spatial data and geomatics techniques, that may be limiting the reliability of the results. Specifically, first objective is to evaluate the extent that published papers reported the information needed to evaluate primary data quality with respect to measured treeline shifts; in other words, how often is reliability of mapping demonstrated. The second objective was addressed by listing and formalizing the main sources of uncertainty related to treeline mapping and suggesting possible approaches to fill the gap.

2.2 Materials and Methods

2.2.1. Dataset: We selected scientific papers for review using CAB direct and Scopus research databases spanning that last 35 years (1980-2015). We identified 31 papers considered appropriate for the study since they used a geomatic approach and were focused on treeline spatial dynamics. Selected papers focused on both approaches to treeline position (9 works) and shift (22 works) mapping.

2.2.2 Analysis: Analysis was aimed at evaluating the perceived awareness of primary data accuracy in the published papers and how accuracy was managed in subsequent computations. First, we investigated if and how metadata of spatial data were reported in the analyzed papers. Specifically, we looked for information about coordinate reference system name, geometric resolution (pixel size), nominal map scale. Additional information that we looked for was the reference scale the authors intended for their work. We also considered if, where present, geometric resolution

was “*directly*” reported or if it was “*indirectly*” deductible from data type. Additionally, if both nominal map scale and reference scale were known, we tested their consistency; this is essential information needed to assess the suitability of datasets with respect to the reference scale of the study, i.e. reliability of results. We also counted the papers that reported DTM vertical accuracy, either *directly* or *indirectly*. For indirect determination, accuracy was not explicitly reported in paper, but could be deduced if DTM source is known. An additional assessment focused on recurrence of studies dealing with treeline mapping at a single time ($h(t1)$) or in time (shifts, $\Delta h=h(t2)-h(t1)$). Second, analysis focused on vertical uncertainty of treeline mapping and developed an operational approach that can be easily adopted for its local estimation. Uncertainty depends on horizontal accuracy (σ_{xy}) of primary data used for treeline mapping, on slope, and on DTM vertical accuracy. DTM affects treeline position accuracy directly in the following ways: if treeline mapping is performed at a single time, and σ_{xy} is assumed as null, its vertical uncertainty can be retained equal to the one affecting DTM (σ_z), that strictly depends on DTM type. DTM can affect treeline vertical position accuracy *indirectly* through the effect of horizontal treeline mapping error (depending on primary data quality). It is known that in steep mountainous regions, a small horizontal shift results in a not negligible vertical shift. This effect can be modeled by Eq. 2.1.

$$\varepsilon_z = \sigma_{xy} \cdot \tan(v) \tag{2.1}$$

where ε_z is the estimated height error related to slope effect, v the local slope (degree), and σ_{xy} is the horizontal accuracy of the data used to map treeline position (satellite/aerial imagery or maps). In the best case scenario, ε_z can be assumed to be equal to the nominal horizontal accuracy of the image/map used to map treeline. As a result, local treeline vertical position uncertainty (σ_T) can be estimated according to Eq. 2.2.

$$\sigma_T = \varepsilon_z + \sigma_z \tag{2.2}$$

If mapping involves treeline shift over time (Δh) then DTM error must be propagated along the difference, according to the Variance Propagation Law (Bevington and Robinson, 2002). A first approximated estimation of shift uncertainty ($\sigma_{\Delta h}$) can be obtained as reported in Eq. 2.3.

$$\sigma_{\Delta h} = \sqrt{2} \cdot \sigma_T \tag{2.3}$$

No treeline shift that is less than $\sigma_{\Delta h}$ can be considered significant. Shifts greater than $\sigma_{\Delta h}$ are considered reliable measures and must be reported as $\Delta h \pm \sigma_{\Delta h}$.

To further explore the importance of this type of error, we considered some of the mostly used DTMs, including satellite-derived, aerial-derived, LiDAR-derived data. For satellite-derived DTMs, we considered: a) SRTM (*Shuttle Radar Topography Mission*), having an absolute height accuracy = 16 m; relative height accuracy = 10 m (Jet propulsion Laboratory – California Institute of Technology – Nasa]; geometric resolution = 1” (about 90 m) and b) ASTER GDEM (*Advance Spaceborne Thermal Emission and Reflection Radiometer - Global Digital Elevation Map*) having an absolute height accuracy = 20 meters at 95% confidence (ASTER GDEM Validation Team, ASTER Global DEM Validation Summary Report]; geometric resolution = 30 m.

We modeled ε_z to demonstrate when it reaches non-negligible values, by considering the most common nominal map scales (1:1,000; 1:2,000; 1:10,000; 1:25,000; 1:50,000;

1:100,000; 1:1,000,000) and arbitrarily changing slope value. Resulting ϵ_z values were then compared with different DTMs vertical accuracies (ALS DTM, 0.15 m; photogrammetric DTM, 5 m; SRTM, 16 m).

Finally, to further demonstrate the impact of DTMs *indirect* error (ϵ_z) in an operational context, we simulated the vertical error distribution for the entire alpine region of Northern Italy (about 51,900 km²). Vertical error was estimated by assuming that *treeline* mapping was achieved by interpreting primary spatial data having a 1:100,000 nominal map scale (Landsat TM imagery). Error classes were defined by considering vertical accuracy of ALS DTMs ($\sigma_z = 0.15$ m, error class $\sigma_z < 0.50$ m), photogrammetric DTMs ($\sigma_z = 5$ m, error class $5 \text{ m} < \sigma_z < 16 \text{ m}$), and SRTM data ($\sigma_z = 16$ m, error class $\sigma_z > 16$ m).

2.3 Results

Analysis found that the reference system was correctly defined only in eight papers; in these cases both projection (e.g. UTM zone 32) and Datum (e.g. WGS84) were reported. Conversely, 23 papers had incomplete information (commonly DATUM name is missing). Moreover, only five papers explicitly reported the reference scale intended by authors for the study. For those that did not report this, it was impossible to verify if spatial data quality was consistent with reference scale. For horizontal accuracy analysis, only 20 papers reported *direct* information (σ_{xy}). Nine studies included nominal scale of maps, permitting to indirectly estimate horizontal accuracy. No information was given in two papers. Twenty-five studies made use of a DTM for mapping treeline vertical position. Of these, 12 did not report DTM type, while 12 papers did not declared DTM vertical accuracy and, finally, only one reported DTM type and relative vertical accuracy. Five papers dealt with treeline mapping at a single time ($h(t_i)$), while 13 considered treeline shift in time (Δh).

According to the above mentioned criteria only eleven of the reviewed works measuring treeline position and shifts provided sufficient information about primary spatial data, and thus were able to demonstrate reliability of measurements. For the remaining papers nothing can be said since σ_z and/or σ_{xy} were not reported.

The importance of ϵ_z was modeled and mapped using (Eq. 2.1). The simulation was run using different values of σ_{xy} corresponding to different nominal map scales (1:1,000; 1:2,000; 1:10,000; 1:25,000; 1:50,000; 1:100,000; 1:1,000,000) and based on international standards. To point out the influence of satellite imagery GSD (*Ground Sample Distance*) on final vertical accuracy, Figure 2.1 reports the name of some well known satellite missions (that can be easily related to a correspondent map scale). Red and blue horizontal lines define the photogrammetric ($\sigma_z = 5$ m) and SRTM ($\sigma_z = 16$ m) DTMs vertical accuracy, respectively.

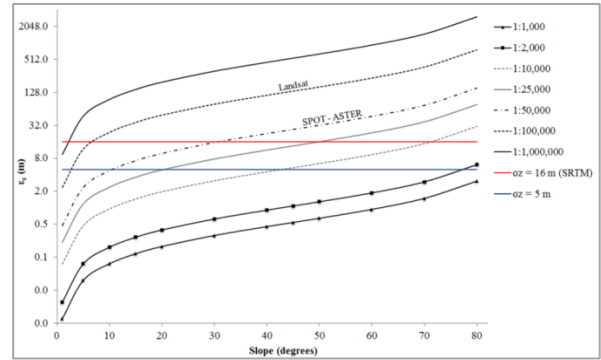


Figure 2.1 - Vertical error resulting from the combined effect of terrain slope and horizontal accuracy (theoretical) of data used for treeline mapping. Different nominal map scale values are considered; the red line represents SRTM DTM accuracy ($\sigma_z = 16$ m); the blue line represents a typical value of accuracy for a DTM obtained through aerial photogrammetry ($\sigma_z = 5$ m). Y axis is logarithmic (base 2).

For areas having slope angles higher than 8-10 degrees, the vertical error caused by slope tends to be significant respect to the adopted DTM accuracy ($\epsilon_z > \sigma_z$). For DTM having higher accuracy (e.g. ALS DTMs), lower slope angles have to be considered.

A test site was then selected to model ϵ_z and to explore where it is significant in a real landscape. The test area used was the northern Italy, where the Alps can be assumed as representative of an extreme mountainous context where *treeline* can be mapped. In the test area, height values ranged between 0 and about 4800 m a.s.l. A map of ϵ_z related to a 1:100,000 nominal map scale, was generated using SRTM DTM (Fig. 2.2). Error classes were defined according to the used data sources: ALS DTM ($\sigma_z < 0.5$ m), photogrammetric DTM ($5 \text{ m} < \sigma_z < 16 \text{ m}$), and satellite SRTM ($\sigma_z > 16$ m).

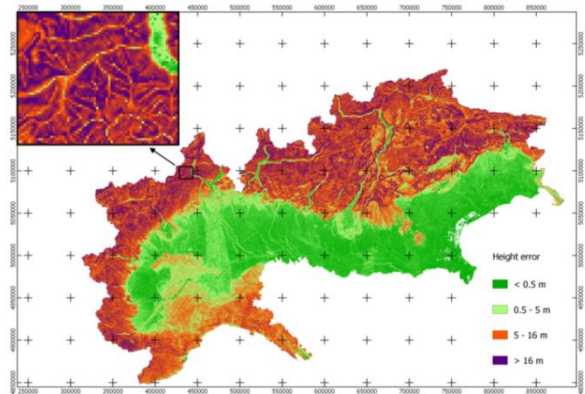


Figure 2.2 - Map of the vertical error contribution related to horizontal uncertainty of primary data used to map treeline position. The simulation used to produce the map considered a horizontal accuracy of 25 m corresponding to a nominal map scale of 1:100,000. Total local vertical error (potential) can be obtained summing this contribution to that of the DTM used for treeline height measurement (not considered in the simulation).

The cumulative histogram of ϵ_z occurring in the height range 1500 - 2500 m a.s.l., was calculated (Fig. 2.3).

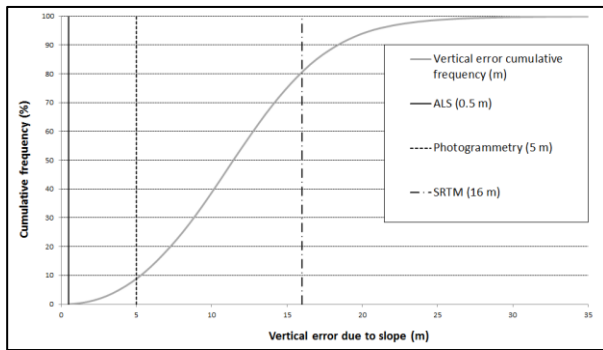


Figure 2.3 - Cumulative frequency of vertical error (related to the above simulation) affecting areas located in the height range 1500 – 2500 m a.s.l., where treeline generally is found.

According to the simulation, if Landsat imagery (compliant with a 1:100,000 nominal scale map) is used in combination with SRTM DTM, in about the 20.0% of the area a significant ε_z value can be observed.

2.4 Discussion and Conclusion

Achieved results showed that spatial data and geomatic techniques are essential in mapping treeline ecotones spatial dynamics. Moreover, the study pointed out gaps in data processing, mainly as related to uncertainty, and underscored a generally poor awareness about the effect of primary spatial data quality on uncertainty of final measurements.

This work found some “weaknesses” affecting various studies. Concerning the use of GNSS technology (specifications about survey strategy and accuracy, and instrument type often incomplete), horizontal accuracy information (generally missing or incomplete), data reference system specification (often lacking), geometric resolution of images or DTMs (not reported), nominal map scale and related horizontal accuracy (not reported). As such, no evaluation of the consistency of the processed data with respect to the expected reference scale is possible, making the evaluation of measures reliability impossible. Moreover, slope value has been demonstrated to be a key factor in treeline mapping since treeline location generally occurs in regions with steep slope. Its effect on treeline determination is not negligible, especially when using medium resolution/scale primary spatial data (Fig. 2.2).

Another DTM *indirect* effect that can further degrade treeline horizontal position is relief displacement affecting objects overlaying terrain. The simplified approach we presented above, actually, neglects this effect that generally occurs during aerial or satellite orthoimages interpretation/classification. In fact, digital orthoimages are mainly generated using DTMs and not DSMs; this determines that the top of rising objects standing over the earth’s surface (trees, houses, etc.) are shifted respect to their real position. Shift depends on object height, terrain shape and geometry of acquisition. Ordinary orthoprojection processing does not remove this discrepancy. In other words, the joint effect of acquisition geometry with terrain slope generates a further non negligible uncertainty factor in treeline mapping, that normally relies on tree canopy detection, that, for this reason, is horizontally displaced from its real position.

3. UNCERTAINTY SOURCES OF AERIAL LiDAR-DERIVED CHM: A METHOD FOR A FAST AND AUTO-CONSISTENT QUALITY EVALUATION.

3.1 Introduction

LiDAR derived datasets are frequently open access data made available from institutional subjects and not, and mainly provided “ready to use” for customers. Even if LiDAR raw data are characterized by high accuracy, they require a pre-processing step to be used. At this point some uncontrolled artifacts (i.e. vertical errors) may occur, especially when processing means point cloud gridding (Aguilar et al., 2010). For this reason users should always consider the possibility of testing by their own the quality of the data they are going to use. In this way, this application was specifically aimed at developing a possible approach for estimating CHM vertical accuracy without any ground survey. CHM is here intended as obtained by matrix difference from a DSM and DTM that were supplied already gridded. This represents the most common format that public institutions make their data available for users. This work suggests a fast way for users to quantify and map, over their study area, CHM uncertainty without any focus on the way gridding of the original LiDAR point cloud was achieved. Dependence of CHM uncertainty from topography was also explored and modeled. Finally, the effects of CHM uncertainty in forest applications are pointed out.

3.2 Materials and Methods

3.2.1 LiDAR dataset: The LiDAR dataset of Piemonte Region released for free in a gridded format (DTM and DSM) was adopted. LiDAR dataset was acquired during the so called ICE aerial-photogrammetric survey (2009 - 2011) and it covers the entire regional territory. DTM and DSM were pre-processed by suppliers from the original LiDAR point clouds by filtering and regularization, resulting in a geometric resolution of 5 m. The reference technical report provided by Piemonte Region (Regione Piemonte 2012) concerning DTM quality check states that “data control is assessed as positive if no more than 5% of ΔQ differences results (in absolute value) higher than 0.60 m value; moreover, for areas declared as “reduced accuracy”, i.e. mountainous forested areas, threshold value is set to 1.44 m”. Since this reference values can be considered equal to the double of DSM/DTM precision (tolerance), we assumed tolerance as statistical measure of CHM uncertainty (errors).

It is important to note that the regional cartographic department states that the DSM dataset is “not explicitly tested” because it is an intermediate product in the generation of DTM. Since no specification is given we assumed for DSM tolerance the same as the DTM one. All data were delivered in the UTM 32N WGS84 reference frame. DTM tile size matches the one of the correspondent 1:10,000 section of the Regional Technical Map (CTR).

LiDAR point clouds were acquired by LEICA ALS50-II sensor (Leica Geosystems, 2006). Nominal point density is about 0.5-1 pt/m². A land cover map of “Forests and other territory covers” (FTC) was also obtained from the regional database (<http://www.SistemaPiemonte.it/montagnaeforeste/SIFOR>) in vector format. The FTC reference frame is the UTM WGS-84 zone 32N, and the nominal scale is 1:10000.

3.2.2 Study area: In order to guarantee a representative selection of the entire regional framework, sample areas used for this study were extracted from the three regional landscape contexts (lowland, hill, mountain). Ninety-six tiles

were totally selected: 24 tiles representing the lowland context, 37 tile for the hill one and 35 for the mountain context (Fig. 3.1).

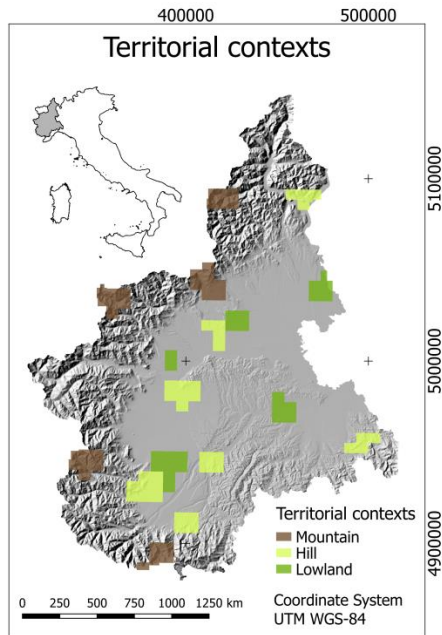


Figure 3.1. Sample DTM/DSM tiles distribution over Piemonte Region area: green = lowland, yellow = hill and brown = mountain tiles.

3.2.3 Analysis: analysis was first directed to estimate CHM errors. It is important to point out that the only errors this approach is able to recognize are the ones related to negative values of CHM. In fact CHM expected value, at whatever position, has necessarily to be positive or zero. Therefore, CHM negative values have necessarily to be interpreted as indirect estimation of local CHM error. Since tolerance (double of precision) was assumed as statistical measure of CHM uncertainty statistics summarizing occurrences of CHM negative values, is hereafter called “*a-posteriori*” CHM tolerance (τ_{CHM}). Nevertheless, according to tolerance values of DTM (τ_{DTM}) and DSM (τ_{DSM}) it is also possible to get an estimation of the “expected” CHM tolerance (hereafter called “*a-priori*” tolerance, $\hat{\tau}_{CHM}$). This can be done applying the Variance Propagation Law (VPL, Bevington and Robinson, 2002] to Eq. 3.1:

$$CHM(x, y) = DSM(x, y) - DTM(x, y) \quad (3.1)$$

Assuming that $\tau_{DTM} = \tau_{DSM}$, then

$$\hat{\tau}_{CHM} = \sqrt{2}\tau_{DTM} \quad (3.2)$$

According to DTM and DSM metadata, $\hat{\tau}_{CHM}$ results 0.83 m in the best case ($\tau_{DTM} = \tau_{DSM} = 0.60$ m) and 2.03 m in the worst case, e.g. mountain and forested areas, where $\tau_{DTM} = \tau_{DSM} = 1.44$ m. We assumed 0.83 ($\hat{\tau}_{CHM}$, “best” tolerance) and 2.03 m (ϑ_{CHM} , “worst” tolerance) as reference values to compare CHM *a-posteriori* tolerance.

Since no direct validation dataset was available, we assumed some statistics concerning CHM negative values exceeding the expected tolerance reference value, as a proxy of CHM uncertainty. For each of the 96 selected tiles covering the above mentioned municipalities, CHM was calculated from the correspondent gridded DTM and DSM; negative CHM values (Δ^-) were found and the following statistics computed:

$$p1 = \frac{N_{\Delta^-}}{N_{im}} \cdot 100 \quad (3.3)$$

where N_{im} is the total number of tile pixels and N_{Δ^-} is the number of CHM pixels with values lower than 0. This statistic is intended to define the occurrence of CHM errors (just the negative part of population) over images.

$$p2 = \frac{N_{\Delta^-}^{\hat{\tau}_{CHM}}}{N_{\Delta^-}} \cdot 100 \quad (3.4)$$

where $N_{\Delta^-}^{\hat{\tau}_{CHM}}$ is the number of CHM pixels with $\Delta^- < -\hat{\tau}_{CHM}$;

$$p3 = \frac{N_{\Delta^-}^{\vartheta_{CHM}}}{N_{\Delta^-}} \cdot 100 \quad (3.5)$$

where $N_{\Delta^-}^{\vartheta_{CHM}}$ is the number of CHM pixels with $\Delta^- < -\vartheta_{CHM}$.

$P2$ and $p3$ define the percentages of CHM pixels (for each tested tile) where CHM error exceeds the expected tolerance thresholds. Reference statistical population in this case is N_{Δ^-} (i.e. all CHM negative values).

Second analysis was performed to investigate if any relationship between CHM errors and landscape morphometry was present. The relationship between potential CHM error and terrain slope was also modeled. At this point, a geostatistical analysis was also performed through variograms to improve interpretation of spatial pattern of errors.

By using the model defined at the previous step a map of the local potential vertical error affecting CHM for the whole Piemonte Region to map was obtained. Finally, focus was made on potential consequences CHM error can produce in forested areas by using the FTC map.

All computations and statistics were run and managed by SAGA GIS and IDL (*Interactive Data Language*) programming tools.

3.3 Results

Results showed that the percentage of negative CHM values significantly different from zero was not negligible, especially in mountain areas (Tab. 3.1).

Landscape contexts	$p1$	$p2$	$p3$
Lowland	0.63	13.58	1.32
Matching tiles			
Hill	0.29	13.21	3.58
Mountain	4.41	30.41	9.30

Table 3.1 – CHM error occurrences ($p1, p2, p3$) calculated for the tested tiles. Reported values are obtained averaging $p1, p2, p3$ statistics of tiles belonging to the same landscape context (lowlands, hill and mountain).

Slope was found to strongly condition errors, showing increasing error values with slope in both hill and mountain contexts. Figure 3.2 reports histograms showing CHM errors distribution in slope classes ((a) = hill, I = mountain]; scatterplots and fitted models relating $|m|$ and $|M|$ with slope ((b) = hill, (f) = mountain]; scatterplots relating observations and estimations given by model respectively for $|m|$ and $|M|$ ((c, d) = hill, (g, h) = mountain].

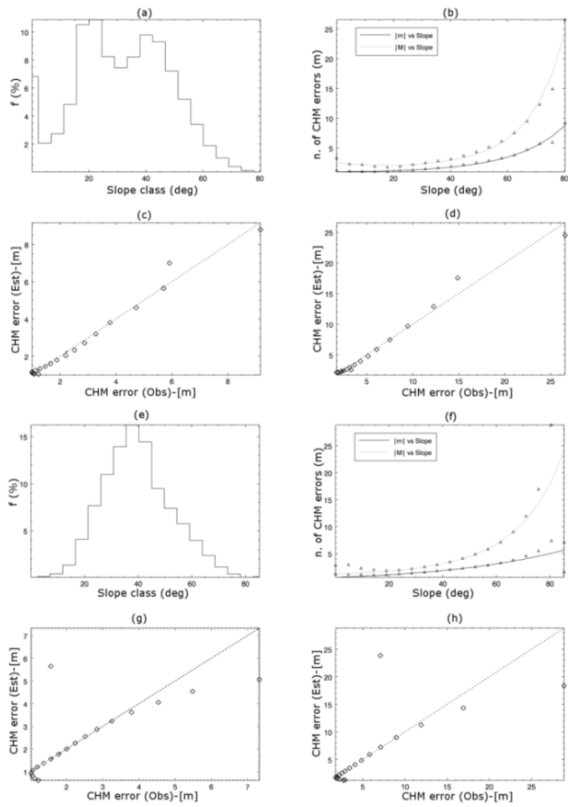


Figure 3.2

The further investigation concerned CHM error spatial autocorrelation, i.e. the effect of position on CHM errors. The variogram and the surface variogram techniques were applied to the sample tile previously used for error distribution analysis (Fig. 3.3, Fig. 3.4).

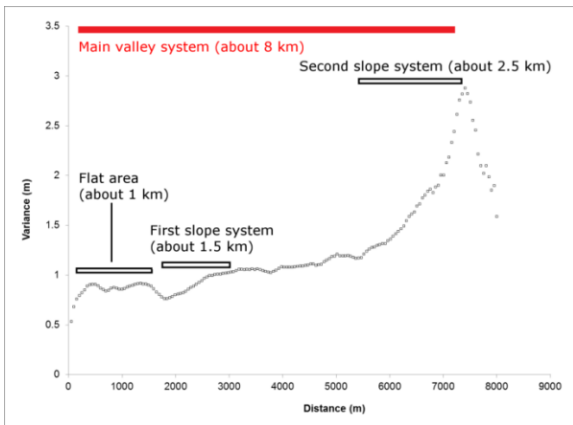


Figure 3.3 – Variogram of CHM errors (not directional) for 190130 tile. Point distribution suggests that CHM error is spatially auto-correlated, i.e. area morphology is a conditioning factor. Distance range where spatial auto-correlation persists (up to about 8 km) is consistent with the length of the main valley system. Within this distance, small holes can be related to local slope size).

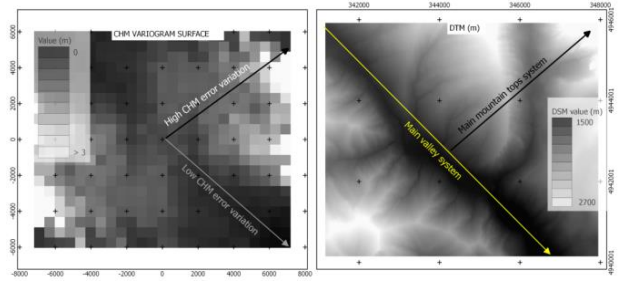


Figure 3.4 (left) Surface variogram and (right) corresponding DTM section. If left and right images are compared it can be deduced that CHM error variance is weak where area is flat and it starts increasing when slopes becomes steepest.

Once CHM errors dependence from terrain slope was confirmed and modeled, the CHM potential error map obtained for the whole regional context clearly highlighted that significant |M| error values (> 3 m) only occurred where hill or mountain was present (Fig. 3.5).

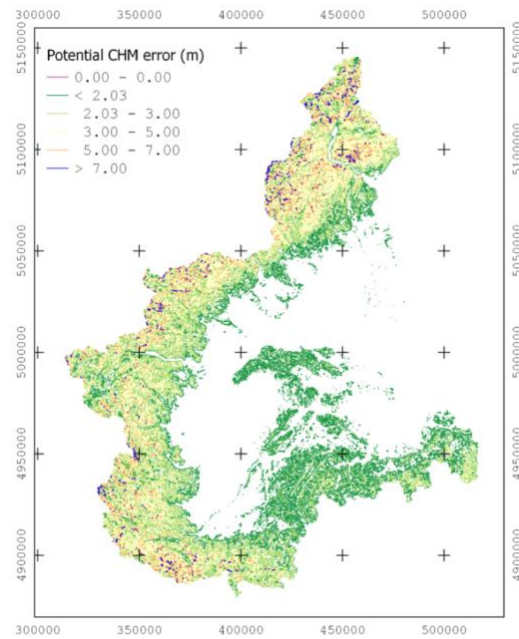


Figure 3.5 – Potential CHM |M| error distribution in Piemonte

CHM error (m)	Area (%)	
	m	M
< 0.83	51	0
0.83 – 1.66	40	65
1.66 – 2.03	5	14
2.03 – 3.00	2.6	16
3.00 – 4.00	0.4	4
4.00 – 6.00	1	0.8
> 6.00	0	0.2

Table 3.5 – CHM errors distribution in regional area. Percentage of regional area falling in the considered CHM error (|m| and |M|) classes.

CHM potential error was finally related to forested areas. The available FTC vector map was used considering Polygon zonal statistics (mean and standard deviation of $|m|$ and $|M|$) were calculated for 12 classes of forest categories including main forest Types of Piemonte Region. Figure 3.6 reports mean and standard deviation values of $|m|$ and $|M|$ for tested forest classes. These last were ordered according to the class slope mean value (from lowest to higher).

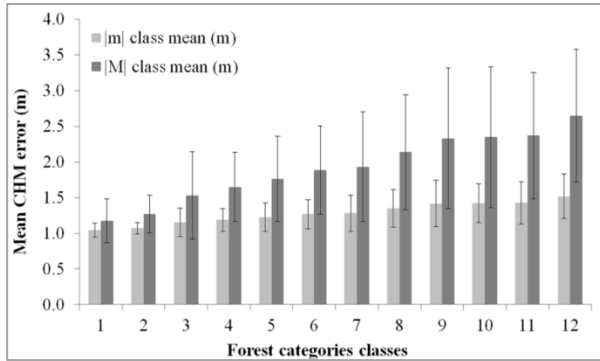


Figure 3.6 - Forest classes mean values of $|m|$ and $|M|$ and correspondent standard deviation (STD). Classes were ordered according to their mean slope value (lowest to the higher); classes are the following: 1 = Riparian willow and poplar forest, 2 = Black Locust forest, 3 = Sessile oak, Oak-Hornbeam and Turkey oak forests, 4 = Downy oak and Hop-Hornbeam forests, 5 = Chestnut forest, 6 = Conifer tree plantation, 7 = Mesophilous mixed broad-leaves forest, 8 = Scots pine, Mountain pine and Cluster pine forests, 9 = Mixed broad-leaves pioneer forest and shrub forest, 10 = Beech forest, 11 = Larch and Arolla pine forest, 12 = Silver fir and Spruce forests.

3.4 Discussion and Conclusion

The local potential CHM error was estimated and its strictly dependency from terrain morphometry, particularly from slope, demonstrated. CHM potential error over the whole Piemonte Region was estimated and locally mapped. Table 3.5 showed that both mean and maximum potential CHM errors were surprisingly lowly occurring: in 51 % of regional territory $|m|$ value is lower than the declared “best” tolerance of the tested dataset (0.83 m); in about 80 % of regional territory $|M|$ value is lower than the expected “worst” tolerance (2.03 m). Only in 20 % of the regional context, corresponding to highest mountain areas, CHM uncertainty is not negligible (2.33 - 2.55 m).

CHM potential error occurrence in the forested areas of Piemonte Region was also tested. The analysis showed that $|m|$, assumed as the average potential committable CHM error, is almost forest class independent in terms of both class mean value and standard deviation (1.10 – 1.45 m). Differently, if $|M|$ is considered as indicator of the most unfavorable situation (highest CHM potential error), it can be noted that both class mean and standard deviation of forest classes increases while slope rises. When operating with specific forest classes, the values we proposed may be assumed as reference estimates for the potential class CHM error. It is worth to remind that reported class values actually depend on the prevailing morphometry (slope values) of the areas where the considered forest class can be found and not on forest species.

4 UNCERTAINTY SOURCES IN FOREST PARAMETERS ESTIMATION FROM A LOW DENSITY LIDAR POINT CLOUD.

4.1 Introduction

In forest characterization, LiDAR data is frequently used to provide tree heights particularly where no data from the ground have been collected, and thus to characterize the whole forest stand. Tree heights are obtained from direct point cloud elaboration or from the CHM (*Canopy Height Model*), which represents tree heights. Obtained height values are successively used to estimate forest structural parameters through estimation models at species level or mixed-species level (VanderSchaaf C. L., 2012). Consequently, it is of fundamental importance to quantify the uncertainty of LiDAR-derived estimations, in order to define its quality as predictor of ground data. In this way, this last application was aimed at exploring limits and potentialities of low density LiDAR point clouds derived data in forest characterization, with particular focus on the quantification of uncertainty of LiDAR-derived estimations. Since open access remotely sensed datasets provided by public institutions, thus potentially the most immediately usable, often are low point density and low/medium geometric resolution (Jakubowski M.K. et al., 2012), for this work the low density LiDAR point cloud of Minnesota (USA) (0.5-1 return/m²) and a medium resolution Landsat 8 OLI (*Operational Land Imager*) image were chosen. An integrated approach of data (LiDAR and satellite) was adopted in order to achieve complete information about analyzed forest stand: from the processing of a low density LiDAR point cloud tree crowns can be identified but no information about vegetation types is instead achievable; conversely, multispectral satellite data can easily discriminate vegetation types based on their spectral signatures.

4.2 Materials and Methods

4.2.1 Dataset: Ground data (tree diameter values, tree density and species types) were collected during a ground survey in year 2013 within 230 semi-permanent forest inventory plots of 16 m radius. LiDAR raw data were downloaded without access constraints from the Minnesota Geospatial Information Office website (MnGeo) (<http://www.mngeo.state.mn.us>) for the Central Lakes Region. LiDAR acquisition was collected over the Itasca county in April 2012. LiDAR data were provided in the UTM NAD83 Zone 15N coordinate system. Vertical and horizontal accuracy values are, respectively, 0.5 m and 1.15 m at 95 percent confidence level. Flight overlap is 25%. ALS60, ALS70 and Optech ALTM Gemini systems were used for data acquisitions..

A NIR (*Near Infrared*) Landsat 8 OLI (*Operational Land Imager*) image acquired on 2013-11-10 was freely downloaded already at-ground-reflectance calibrated from EarthExplorer distribution system (<http://www.earthexplorer.usgs.gov>) and successively adopted to classify the CEF vegetation composition at areal level with reference to ground sample plots.

4.2.2 Study area: The study site is the west part of the Cutfoot Sioux Experimental Forest (CEF) within the Chippewa National Forest in north-central Minnesota (Itasca county, USA) and occupies 507 ha of the total surface (1,255 ha). This area is dominated by *Pinus resinosa* Ait. mainly originating after one of 6 major fire events occurred between 1864 and 1918 (Adams et al., 2004), with varying amounts of Jack pine (*Pinus banksiana* Lamb.) and Eastern white pine

(*Pinus strobus* L.). Paper birch (*Betula papyrifera* Marsh.) and Quaking aspen (*Populus tremuloides* Michx.) are common components of the pine-dominated stands and in some places are the most dominant species (Experimental Forests of the Northern Research Station, U.S. Forest Service, 2008].

4.2.3 Analysis: By using ground data collected within 230 sample plots we derived individual tree heights (H, m) by species-specific ipsometric curves ($H = f(D)$), tree density (n/ha) and plots mean diameter (D, cm). The Landsat 8 OLI image was classified by *Minimum Distance* algorithm in order to separate broadleaves from conifers. Reference spectral signatures for algorithm training were deduced from plots' prevalent vegetation composition. Classification was used as the base for the application of correct ipsometric curves (calibrated on the national Minnesota dataset) for diameter estimation from LiDAR derived height values. LiDAR data processing with LASTools provided a DTM and the correspondent DSM with 1 m of geometric resolution. Subsequently the correspondent CHM was derived. Successively, by investigation of *local maxima* on the CHM, considering the whole CEF, points which likely represents individual trees of the dominant layer of the forest were identified. By crossing their positions with the obtained classification each point was labeled as "broadleaves" or "conifer" and, consequently, the correspondent ipsometric function for diameter ($D = f(H)$) estimation applied. Once the strong underestimation of values by LiDAR in tree counting (probably only trees of dominant layer were identified) was found, a tree level comparison was excluded. Diameter and height values, from ground and LiDAR, were then averaged at plot level and compared. A strong inconsistency between estimations was found and, consequently, an investigation analysis of inconsistency sources was accomplished; sources of inconsistencies were first searched in tree density differences between ground and LiDAR-derived data, and, second, in the presence of an eventual systematic error (i.e. *bias*) affecting the LiDAR point cloud. The *bias* was found and modeled, and its relation with flight acquisition geometric parameters investigated through geostatistic techniques. Finally, particular importance was given to LiDAR-derived estimates reliability; uncertainty of LiDAR-derived estimations, with particular focus on height and diameter since they are key attributes in many forest parameters computation, was quantified by computing the MAE (*Mean Absolute Error*, $MAE = \frac{1}{n} \sum_{i=1}^n |f_i - y_i|$) on ground and LiDAR-derived height and diameter errors (i.e. differences).

4.3 Results

The plot level comparison shows that average H and D from LiDAR are overestimated respect the correspondent ground values, while tree density is underestimated. Obtained MAE values resulted of 7.22 m for H, of 0.21 m for D and of 294 trees/ha for tree density. Given the strong inconsistency between ground and LiDAR-derived forest parameters, we proceeded to compare, through *P-P plots*, normalized statistic distributions of H and D (Figure 4.1). Differences between distributions are evident.

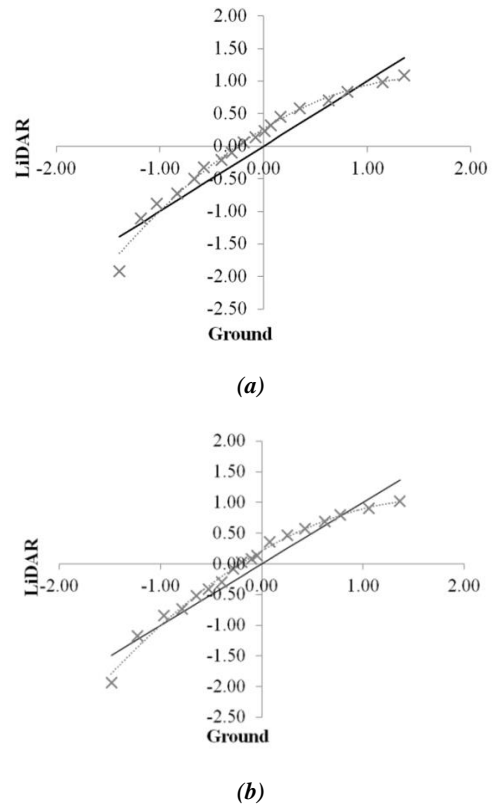
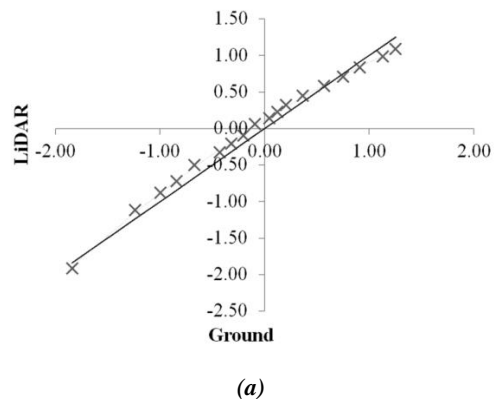


Figure 4.1 – P-P plots of (a) H and (b) D normalized distributions (grey dotted lines).

Given the strong inconsistency between ground and LiDAR-derived distributions, we supposed the existence of anomalies conditioning the datasets. We first explored tree density underestimation as possible reason of inconsistency. In order to verify this hypothesis, equaled tree density values within plots from LiDAR and ground data were considered, and new mean values for H and D from ground were obtained. Through this method, we assumed to consider only trees of dominant layers.

Lower MAE values were achieved: 4.0 m for H and 0.19 m for D. Relative *P-P plots* were again generated. Lower deviations from the comparison line were achieved, indicating an improvement in height distribution trend. No significant change was instead observed for diameter plot.



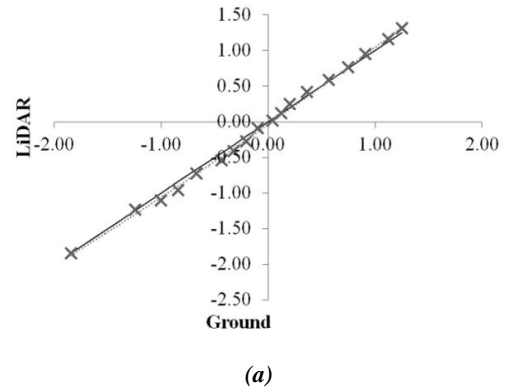
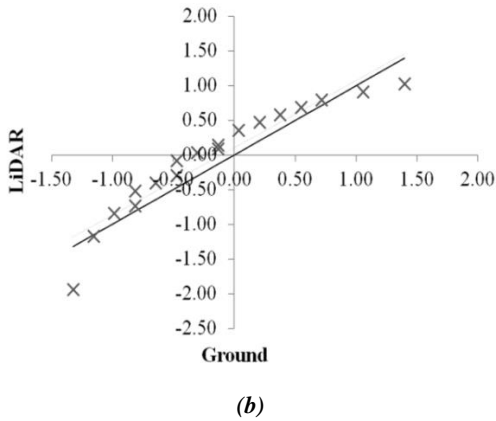


Figure 4.2 – P-P Plots of normalized (a) H and (b) of D distributions (grey dotted line) after tree equaling. Improvement in height distributions similarity is evident.

After proving tree density as a conditioning factor for ground and LiDAR data inconsistency, and since respective data distributions were still affected by differences, we also investigated the presence of a possible *bias* affecting the original LiDAR point cloud. In the attempt of modeling the possible *bias*, correlation between height estimation error and LiDAR-derived plots height values was tested. Obtained determination coefficient (R^2) between trends resulted equal to 0.6512 (i.e. $R = 0.80$), endorsing the hypothesis of a systematic error (*bias*) affecting the LiDAR point cloud. A logarithmic regression model (Eq. 4.1) proved to be well fitting *bias* modeling.

$$\theta = 15.37 \ln H_{\mu}^L - 44.981 \quad (4.1)$$

Bias modeling of Eq. 4.10 was tested as “corrective model” for original tree height values adjustment. In this context, θ represents the “correction” to be applied to H_t^L to remove the effect of systematic error, as in Eq. 4.2:

$$\hat{H}_t^L = H_t^L - \theta \quad (4.2)$$

where \hat{H}_t^L is the “corrected” tree height value from LiDAR, H_t^L is the “biased” value and θ is the correction to remove the effect of error, where H_{μ}^L of Eq. 10 is replaced by H_t^L values.

Eq. 4.1 and Eq. 4.2 were applied on all trees detected on CHM within the whole CEF and new “corrected” \hat{H}_t^L values were obtained.

The MAE was again computed on differences between new H values and lower value equal to 1.32 m was obtained. Due to the improved similarity with ground-based tree heights, \hat{H}_t^L values were successively used to recompute plots “corrected” D values; the MAE computed on diameter differences decreased from 0.19 m to 0.08 m. Since improved MAE values were obtained, *P-P plots* (Fig. 4.3) were again achieved.

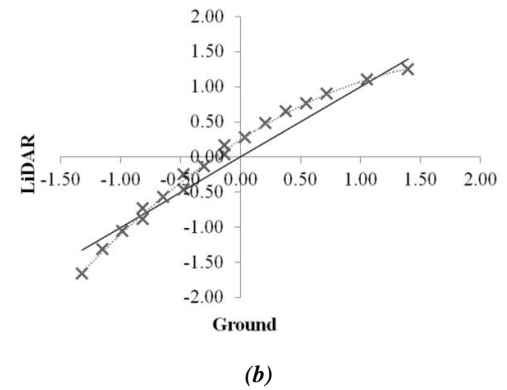
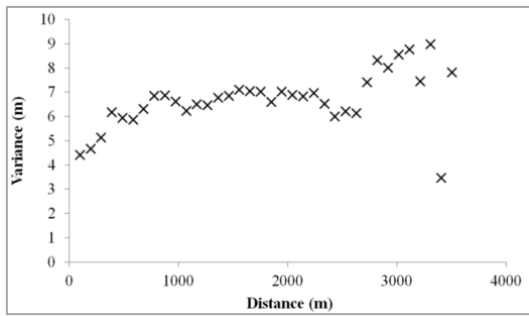


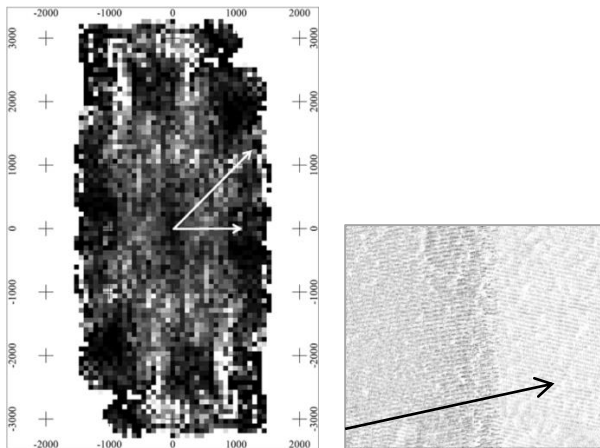
Figure 4.3 - P-P Plots of normalized (a) H, and (b) of D distributions (grey dotted line) after tree density equaling and LiDAR height “correction”.

A further improvement of similarity for height distributions (a), demonstrates that a strong influence of modelled systematic error on LiDAR-derived data was present and was responsible for biased values of forest parameters. Deviations from the comparison line instead still characterize diameter plot (b), indicating the persistence of differences between ground and LiDAR distributions.

After proving the existence of a *bias* affecting the LiDAR point cloud, we looked for its source considering flight acquisition geometry. Investigation concerned the spatial autocorrelation of height error (i.e. the effect of position on errors), intended as ΔH between ground and LiDAR-derived CHM caused by the *bias*. The variogram and surface variogram techniques were applied on plots ΔH before the application of the “corrective” model. Figure 4.4 shows obtained variograms.



(a)



(b)

(c)

Figure 4.4 – (a) Variogram of ΔH . Point distribution suggests that height errors are spatially auto-correlated, i.e. some geometric features are conditioning factors; (b) Surface variogram of ΔH . Height error variations gradually increase from the strip's center toward the side edge with perpendicular direction respect the flight one's following a NE-SW direction (white arrows). (c) Overlapping zone above strips. Scanning lines direction above overlapping strips is NE-SW, as suggested by the surface variogram.

Variogram (Fig. 4.4a) shows that height errors are spatially auto-correlated. Particularly, variance increases from 0 to 800/900 m distance, suggesting that for this distance some geometric features are involved and condition height errors. A new increase of variance is present from 900 m to 1600 m distance, and then autocorrelation persists in the successive distance range (about 1600-2200 m). A decay of autocorrelation is registered for higher distances. Indication given by variogram was better explored by generating a surface variogram (b), where direction of variation was taken into account.

Surface variogram showed that ΔH variations are present (see white arrows) and persist along NE-SW direction. The size of these variable zones in the variogram and the direction of prevailing changes, if compared with point cloud acquisition geometry (scanning geometry on overlapping strips) (c), indicated a geometric acquisition dependent scheme of height errors. In fact, ΔH variance was found to gradually increase from the strip's center toward the side edge with perpendicular direction respect the flight one's and along direction of scanning angle lines (NE-SW) above overlapping zones. On the contrary, more homogeneous variations occurred where no flight overlapping is present.

4.4 Discussion and Conclusion

A strong inconsistency was initially found between ground and LiDAR-derived data distributions. A general overestimation from LiDAR-derived data was observed and computed MAE values on estimation error were surprisingly high: 7.22 m for H, 0.21 m for D.; underestimation instead characterized tree density from LiDAR-derived CHM, with a MAE of 294.7 trees less than ground density. Inconsistency between LiDAR-derived estimations and ground data was first explained by different tree densities. By equaling of these lasts through the removal of dominated layers considered in ground data collection, MAE values on height and diameter errors slightly decreased: 4.0 m for H (reduction of 3.22 m), 0.19 m for D (reduction of 0.02 m). Still present discrepancies provided the opportunity to investigate the presence of a *bias* affecting the LiDAR point cloud. The presence of a systematic error in LiDAR data was proved, the *bias* was modeled and a “correction model” to remove the error effect from height values at tree level, formulated. In this way MAE values further decreased reaching 1.32 m for H (reduction of 5.9 m), 0.08 m for D (reduction of 0.13 m). Through geostatistic instruments the relationship between modeled *bias* and geometric parameters of acquisition was demonstrated, providing a further endorsement that flight acquisition geometry (i.e. scanning geometries on overlapping strips as scanning line direction, scan angle) is a conditioning factor of errors in LiDAR point clouds.

Different results were instead achieved for diameter estimations. In fact, original inconsistency between trees positions from ground and from LiDAR-derived CHM did not allowed to recognize species within plots from CHM and, consequently, to apply species-specific models for diameter estimation to identified trees. We were only able to develop an estimation model considering prevalent vegetation composition within plots. Inevitably, more coarse results about diameter estimations from LiDAR-derived CHM were achieved. Considering obtained results, as regard to the specific low point density LiDAR dataset, we can conclude that achieved height estimations at plot level, after *bias* removal, can be retained reliable predictors of ground based one's and consequently adopted for the estimate of derivable forest parameters. Conversely, for diameter estimation a higher point density is probably needed for a successful comparison of individual trees positions, with consequent identification of species and application of species-specific models for diameter estimation, and to achieve finer results.

5. GENERAL CONCLUSIONS

The present thesis dealt with spatial data uncertainty sources in the forest research context, with particular focus on data quality and metric accuracy as conditioning factor for results reliability. This work underlined that spatial data and geomatic techniques are powerful tools that require professionalism and specific skills to achieve appropriate results. Moreover, it is clear that appropriate ecological results are dependent on spatial data management, but their reliability relies on the way metadata are interpreted and reported. For these reasons, every measurement should always be qualified, indicating metadata and data quality information.

Considering that reliable ecological results are dependent on correct management of spatial data and metadata, the following suggestions (minimum requirements) are here provided:

- a) the coordinate reference system has to be rigorously defined in terms of datum, projection type, zone (eventually) for all spatial data;
- b) geometric resolution of images, raster digital maps, and DTM has to be explicitly reported; if maps are supplied in a vector format the nominal map scale needs to be reported. However, direct reporting of vertical and horizontal accuracy of data is always better;
- c) consistency of primary spatial data scale with respect to reference scale of the study has to be demonstrated by comparing theoretical accuracy of reference scale with the one potentially affecting primary spatial data; this has to be managed along the workflow, taking care to be aware of eventual error propagation;
- d) if optical multispectral satellite/aerial imagery are used, all information about spectral and radiometric features of the available bands needs to be clearly stated;
- e) if scanned aerial images (or native digital ones) are used, the following minimal information has to be supplied: airplane flight height, camera focal length, base of the acquisition (if stereo-pairs are considered), sensor/film size and, for scanned paper prints, scan quality information (dots per inch, dpi);
- f) if GNSS technology is used, receiver model type needs to be reported, together with survey accuracy and differential correction strategy (if involved);
- g) every final measurement should have a reported value and related uncertainty to make eventual users aware of limitations about the information.

Considering these minimum requirements can minimize uncertainty of results while maximizing reliability of spatial measurements.

The quality of a gridded LiDAR-derived CHM was evaluated in Paragraph 3 through the development of an indirect method based on assessment of internal anomalies, e.g. negative height values. According to achieved results, we can assert that the analyzed Piemonte Region gridded LiDAR dataset can be used to generate a CHM whose quality is generally consistent with the declared tolerance values ($|m| = 0.83$ m and $|M| = 2.03$ m). This fact makes it valuable for many forest applications being consistent with ordinary ground survey. Moreover, this study supplied the users an easy tool (the model relating CHM error and slope) to estimate by their own the potential CHM error they are going to adopt over their study areas. They certainly have to proceed under more cautionary conditions in their computations while studying mountainous forested territory where steeper conditions may decrease the vertical accuracy declared for the original LiDAR acquisition, and consequently increase vertical errors. Finally, the research identified the Piemonte Region gridded LiDAR datasets as a valuable tool for forestry applications and can be potentially used in an effective way for the most of them.

The last application (Paragraph 4) explored limits and potentialities of a low density LiDAR point cloud in forest characterization at tree and plot -level. Main emphasis was set on uncertainty sources potentially conditioning forest parameters estimation and on the quantification of related metric uncertainties. This research proved that the adopted LiDAR dataset was affected by a systematic error dependent from flight acquisition geometry, in the specific case from scanning geometries on overlapping strips. In order to assess its effect on data quality and reliability, the systematic error affecting the adopted LiDAR point cloud was modeled. In this way, a simple and fast method to model the identified *bias* was described and biased LiDAR-derived CHM values were “corrected” at tree level. Specifically, the developed method for *bias* modeling involves the following phases: a) modelling of *bias* by testing the correlation between height

errors and height from LiDAR-derived CHM; b) identification of the best fitting regression model for *bias* trend modeling; c) adoption of *bias* model for the “correction” of LiDAR-derived height estimations at tree level, by the removal of *bias* from tree height value; d) detection of *bias* source in flight acquisition geometric parameters, through investigation of spatial autocorrelation of height errors (i.e. differences between ground and LiDAR-based estimations) by variogram technique and of direction of height errors variation by surface variogram technique.

On the whole, the study provides an easy tool for LiDAR data users to a) test reliability of estimations from LiDAR-derived data, b) check the presence of potential systematic errors affecting LiDAR point clouds, c) correct biased LiDAR-derived height values and, finally, d) investigate the source of error. Moreover, this study underlined that every LiDAR dataset is potentially affected by errors that need to be modeled, and demonstrated their effect on results reliability.

Concluding, this thesis underlined which are the main uncertainty sources of digital spatial data commonly adopted in forest applications and highlighted their not-negligible effects on results. The work demonstrated that appropriate knowledge about geomatic techniques and spatial data quality are necessary prerequisites to achieve reliable results. Since reliable results are dependent on spatial data quality, users should always consider and investigate the possibility of errors occurrence negatively affecting quality of data and of them propagation along computation in order to minimize errors effect on results. Preserving data quality is an essential step to guarantee appropriate results, and thus to produce good quality scientific research.

6. REFERENCES

- Adams, M.B., Loughry, L., Plaughter, L., 2004. Experimental forests and ranges of the USDA Forest Service. In. USDA For. Serv. Gen. Tech. Rep. NE-321, 178p;
- Aguilar F. J., Mills J. P., Delgado J., Aguilar M. A., Negreiros J. G., 2010. Modelling vertical error in LiDAR-derived digital elevation models. *Journal of Photogrammetry and Remote Sensing* 65: 103-110;
- Andersen H.E., Reutebuch S.E., McGaughey R.J., 2006. A rigorous assessment of tree height measurements obtained using airborne lidar and conventional field methods. *Canadian Journal of Remote Sensing*, 32 (5): 355-366. DOI: <http://dx.doi.org/10.5589/m06-030>;
- ASPRS, 2015. Positional Accuracy Standards for Digital Geospatial Data, *Photogrammetric Engineering & Remote Sensing*, 81(3): A1-A26, DOI: 10.14358/PERS.81.3.A1-A26;
- ASTER GDEM Validation Team (2009) ASTER Global DEM Validation Summary Report;
- Cheung C.-K., 2000. PhD Thesis Reliability of spatial data and its analysis in GIS, Pao Yue-kong Library, The Hong Kong Polytechnic University, Hung Hom,
- Gomarasca M. A., 2004. *Elementi di Geomatica*. Edizioni AIT Firenze, pp. 650;
- Jet propulsion Laboratory – California Institute of Technology – Nasa;
- Leica ALS50-II Airborne Laser Scanner Product Specification Leica Geosystems AG, (2006) Heerbrugg, Switzerland;

- Regione Piemonte, 2012. Produzione di supporti topografici per la pianificazione a livello locale nella Regione Piemonte (IT), Relazione MDE Blocco 03;
- VanderSchaaf C. L., 2012. Mixed-Effects Height-Diameter Models for Commercially and Ecologically Important Conifers in Minnesota. *Northern Journal of Applied Forestry* 29:1;
- DOI: <http://dx.doi.org/10.1016/j.rse.2004.02.001>;
- Zandbergen P. A., 2008. Positional Accuracy of Spatial Data: Non-Normal Distributions and a Critique of the National Standard for Spatial Data Accuracy, *Transaction in GIS*, 12 (1): 103–130. DOI: 10.1111/j.1467-9671.2008.01088.x.

SPATIAL ONTOLOGIES FOR ARCHITECTURAL HERITAGE

F. Noardo ^{a,*}

^a Politecnico di Torino, c.so Duca degli Abruzzi, 24, Torino, Italy – francesca.noardo@polito.it

KEY WORDS: Cartography, 3D digital map, Semantics, Ontologies, CityGML, Interoperability, Architectural Heritage, 3D GIS

ABSTRACT:

A new generation of digital maps is today possible, and is the essential base to make smart cities an actual reality. The management and representation of the cartographic data by means of harmonized and unambiguous structures is an urgent necessity for cartographic disciplines and actors. An advanced form of geographical information systems has to be employed, as recommended by the European and international standards. The cited standards (mainly INSPIRE Directive and OGC documents) propose open languages, metadata formats and complex but comprehensive data models to be used, pursuing the objective of internationally harmonized maps. However, it is not so simple to use them, because of the lack of some intermediate (hardware and software) structures permitting to manage the so-formatted data in a user-friendly, rapid and useful way. Another kind of danger, that could worry, in particular, the Cultural Heritage operators, could be the excessive flattening of the data to a generic system unable to represent the local peculiarities. For this last issue, in this study an application domain extension to an existing standard to manage 3D urban data, the OGC CityGML, was proposed, in order to make that system flexible enough to include Architectural Heritage data in the future advanced digital maps and information systems. The extension and a prototype testing it is described in the paper, together with some practical solutions for dealing with the available tools for managing such kind of data.

1. INTRODUCTION

The great challenge of cartographic disciplines from recent years is the translation of existing national and regional cartographic products to make them harmonized and compliant with the proposed international standards. Some data standards are available as both open languages and data formats to manage the data and data structures (ontologies and data models) useful to realize such kind of maps. However, some problems to the actual employment of them persist.

First, the near inexistence of suitable, affirmed and user-friendly tools to manage such kind of data. This is a strong drawback for the systems to be applied by the national and subnational mapping agencies (until the small municipality office level). Another problem is the existence of local peculiarities of the represented cities, which risk to be lost in a flattering international standard data model. This is particularly important in some historical context, such as the European cities, which are rich in historical sites, structures, and monuments.

In this study, a system was realized in order to manage the architectural heritage items by using an extended standard data model, permitting to include such data in wider contexts, so that they can be analysed by means of automatic tools. Moreover, some elements giving flexibility to the model were introduced, for including a high-level of detail in the representation of the architectures, so that the advantages of analysing wider series of data (also having small dimensions and very detailed geometry) in a unique environment and reference system can be exploited. New advanced analysis and information sharing systems are permitted by advanced informatics technologies, but the condition is the structuring of the data in interoperable explicit and formal (that is, machine-readable) formats.

A unique framework is therefore needed in order to make the conceptualizations structuring the data, and, consequently, the data themselves, unambiguous. A solution to this is the use of ontologies (Guarino et al., 2009; Laurini, 2015) for reducing the

risk of misinterpretation and possible consequent damages or loss of information (Guizzardi, 2005). In addition, the definition of an explicit and shared data model permits the production and sharing of open data, with the connected advantages (Janssen et al., 2012). Such known and explicit structures permit the realization of advanced analysis and enhanced queries: some artificial intelligence mechanisms can be exploited for extracting new knowledge. In fact, besides being object to the usual queries, the datasets can be considered for inferring new knowledge, both using simple deductive mechanisms, and applying some more complex procedures performing also inductive or abductive reasoning. The structured datasets can also be the base for effective data mining, which is a current issue for geographical information management (Miller, Han, 2009). The difference from a simple database query is that users may not know what information or patterns they are seeking in advance (Worboys, Duckham, 2004).

The application of such technologies permit the achievement of an advanced form of 3D Geographical Information System (3D GIS).

The same interoperability is the base of the ideas of international standards, Semantic Web, and Smart City (Barnaghi et al., 2012; Chourabi et al., 2012; Schaffers et al., 2011). It is for making these ideas a reality, that such ontologies and standards have to be employed for managing and sharing the cartographic data at all levels of detail, including the architectural one. In addition, the cultural aspects (including the monument knowledge and promotion) are an important pillar of the smart cities concept, to be integrated in their substructures.

This study aims are intended in this direction. A part of this study was already published in (Noardo, 2016).

1.1 Existing standards, ontologies and vocabularies

The world of a new cartography, intended as spatial knowledge management and geographical intelligence, is developing tools

* Corresponding author

for the realization of an effective “geoweb” (Laurini, 2014). The results of such work are expressed in the directives of some national and international institutions dealing with cartography or environmental entities management. For example, the INSPIRE (INfrastructure for Spatial InfoRmation in Europe) European Directive is developed by the European Parliament and the Council of 14th March 2007 (Directive 2007/2/EC) (<http://inspire.ec.europa.eu/>). Equally, some international industry standards are being developed by consortiums of major stakeholders and actors of the sector, becoming the base for interoperability and open data. In this framework, the OGC (Open Geospatial Consortium) (www.opengeospatial.org/) standards (including the model for urban data CityGML) are conceived.

The OGC CityGML (<http://www.opengeospatial.org/standards/citygml>) is an open data model, available in form of an application schema (XSD) for GML files. Its goals are the representation, storage and exchange of 3D urban objects information. Its semantic definition can be input to manage the semantics of the data by means of the tools offered by artificial intelligence and informatics.

Some further examples can be found in the opposite direction, that is, the effort of the world of semantic thematic data to include geographic information. For this reason, GeoSPARQL (<http://www.opengeospatial.org/standards/geosparql>) is developed by OGC as an extension of the W3C (World Wide Web Consortium) (www.w3.org) SPARQL (SPARQL Protocol and RDF Query Language) (<http://www.w3.org/TR/rdf-sparql-query/>), which is the designed language to query RDF-structured data. It is considered for the inclusion of spatial data in RDF-OWL information.

These languages represent the crucial technology for the application of the open-data and interoperability theories. Among these, some markup languages allow to write content and provide information about which role the content plays using a both human and machine-readable format. In particular, XML (eXtensible Markup Language) (www.w3.org/XML/) is a metalanguage for markup: it provides a uniform framework, and tools for the interchange of data and metadata among applications. This is why XML is the base of most of languages born to structure open and application-independent data and exchange them through various applications or through the web. Some of the relevant XML – based languages are, for example, RDF (Resource Description Framework) (www.w3.org/RDF/), permitting the management of semantic data (by means of a triple mechanism), OGC GML (Geographic Markup Language) (www.opengeospatial.org/standards/gml) to archive geographical objects, COLLADA (Collaborative Design Activity) (<https://it.wikipedia.org/wiki/COLLADA>), which is an interchange format for 3D models, and so on. The structure of the XML-based files is defined in equally XML-based formats, such as simple XML Schema Definition (XSD), which is the one used to structure GML data, or extended ones such as RDFS (RDF Schema) - OWL (Ontology Web Language) (www.w3.org/2004/OWL/).

An example of geographic issues managed on the web using the described technologies is GeoNames (<http://www.geonames.org/>), which is a database including toponyms gazetteers and information related to the included named places.

In the Cultural Heritage documentation field, database interoperability and information retrieval have always been crucial aims (<http://www.icomos.org/en/charters-and-texts>). A correct interpretation is only permitted if the data are unambiguous and contextualized with meta-information.

The CIDOC (International Committee for Documentation) conceptual reference model (CRM), developed by the Committee of the ICOM (International Council of Monuments) is considered the core ontology for Cultural Heritage (Doerr et al., 2007). It uses RDF-OWL for the management of thematic data. It became standard ISO 21127.

A further existing database exploiting the described theories and technologies consists in a set of vocabularies developed by the Getty Institute (<http://vocab.getty.edu/>). These are oriented to structure Cultural Heritage related terms and items, and are divided in four vocabularies: the Art and Architecture Thesaurus (AAT), the Thesaurus of Geographic Names (TGN), the Union List of Artist Names (ULAN) and the Cultural Objects Name Authority (CONA). The AAT hierarchically structures the terms linked to the description of the works of art and architectures. The Getty TGN, differently from GeoNames, includes also historical denominations in its items. The ULAN contains the names and synthetic information about the cultural heritage authors; and finally, the CONA describes the different denominations of a cultural item over the time. In them, the spatial component is not present, but they can be the reference for the denomination of parts which unequivocally have a spatial connotation (e.g. all the architectural parts or toponyms), or for related information (such as authors or object names).

Recently some effort has been done also towards the inclusion of some geographical information in cultural heritage descriptions. Some localization data is tried to be included in semantic structures. For example, the Getty project ARCHES (<http://archesproject.org>; Myers et al., 2013), based on CIDOC-CRM structure, integrates some WebGIS function; the CRMgeo project (Doerr et al., 2013) includes spatio-temporal representation potentiality in CIDOC-CRM.

However, these geographic references are often bi-dimensional and have a little defined geometry (points, lines or approximate polygons), since the aim is not the analysis and reading of the artefact geometry, but its localization for a territorial reading. Recently, another extension to the CIDOC CRM was realized: the CRMB. It is expressly realized for the documentation of standing buildings (Ronzino et al., 2015). However, the gap in this research could be found in the lack of management of complex 3D models in connection with other parts of the city and the landscape, which is a topic treated by CityGML.

For the particular needs of architectural heritage information management, 2D (often small-scale) data are not sufficient. 3D dense data have to be exploited with higher levels of detail (high measurements and georeferencing accuracies) and complex semantic definition (object-oriented structures) (Laurini, 1992).

The availability of the 3D dense models is a reached aim of survey and geomatics discipline (Chiabrandò, Spanò, 2013). However, the potentiality of management, analysis and editing, typical of traditional GIS (Geographical Information Systems), are at the present moment reduced for this kind of data. The development of new software structure or user interfaces are needed, based on either adapted or new theoretical frameworks (Brahim et al., 2015; Solovyov, 2012), which again permit the usability of the systems in a real effective way.

A final note on the use of historical building information models (HBIM): these and the IFC standard, employed to structure the so-managed data, are not chosen as a solution for this study, since the necessity of an often too rigid parametric modelling of the surfaces could cause the loss of some information in the geometry of such irregular and unique buildings, as monuments are. Moreover, the georeferencing tools have reduced performances compared to the GIS systems, and, consequently, the contextualization of the monument in its urban or landscape environment suffers. Therefore, even if in the future probably the

field of BIM (born to project new buildings) will meet GML models, at present it's too rigid for describing Cultural Heritage buildings, which need more flexibility.

1.2 Proposal Aims

In this research, a solution to the need of a data model for architectural heritage 3D high-level-of-detail data is proposed, by modelling an extension of the existing structure OGC CityGML by means of its ADE (application domain extension) procedure.

CityGML was chosen as a base since it is a standardized model already dealing with buildings in their double dimensions: as a part of the city and the landscape, and as a higher-detailed 3D object (even if in the practice, such very highly-detailed models almost do not exist yet). It is important to consider this double nature also in architectural heritage emergences, because they are often both meaningful to the definition of the cultural values of the considered buildings. Moreover, CityGML includes the possibility to have multi-scale representations. The improvement of digital cartographic products by the integration of the monument in wider maps of the city, or the landscape, permits to perform strategic analysis of various aspects of the urban life: an intelligent viability, tourism and cultural itineraries, education, safety and security issues, development dynamics of the city, further economical considerations. Moreover, the monument can also be studied in a broader context, offering to the art and architecture historians and to the architecture scientists a powerful knowledge base.

CityGML is shared as a data model, already in a potentially implementation-ready format. The UML (Unified Modelling Language) diagrams are published in the OGC encoding standard (OGC, 2012). They are already in an advanced phase of the data modelling process, since the database design details are specified as in a logic-level model (e.g. an object-oriented approach is envisaged and types of data and code-lists are defined). Moreover, the XSD files are shared and available for the direct use in implementation. However, for its generality in representing urban models, including a comprehensive list of attributes and aspects, independently from the specific study and performed application, it can be considered an ontology (Métral et al., 2009; Kolbe et al., 2008). It aims at representing a common frame for urban 3D maps data.

Therefore, for extending CityGML including structures for the management of spatial data complexity of architecture and monuments, some preliminary general reflections are reported, which can be valid as ontological-level thinking. Nevertheless, the extension is then realized in accordance with the formats and structures used in CityGML (implementation-oriented), to be coherent with the extended model and for permitting the test also in the implementation.

However, some considerations and necessities of the representation remain at present unimplemented, about more evolved constrains to be imposed to the model. It will be object of future work.

The second part deals with the procedure followed for the implementation of the model extension. The method proposed by OGC best practice is followed as a starting point; however, some manual intervention is necessary in order to really realize an effective implementation.

In the end, a prototype is realized, taking in consideration the processing phases to be followed (from the processing of the 3D model to its semantic visualization).

2. CITYGML CHADE (CULTURAL HERITAGE APPLICATION DOMAIN EXTENSION)

OGC CityGML data model can be extended in order to model further aspects linked to specific application domains. The so-composed extensions use specific characteristics and procedures of CityGML, being defined as ADE (Application Domain Extension). Some official ADEs exist (<http://www.citygmlwiki.org/index.php/CityGML-ADEs>). They regard especially some urban-scale themes (for example, the noise ADE exists, or the inclusive routing one). Some of these are instead specific on buildings, for example GeoBIM integrates some classes derived from IFC standard (Industry Foundation Classes)

(https://en.wikipedia.org/wiki/Industry_Foundation_Classes), which is used in BIM (Building Information Modelling) (De Laat, Van Berlo, 2011).

A further research was performed for the extension of CityGML model in order to include some information about the CH (cultural heritage) nature of the building and some surface characteristics, such as the deterioration (Costamagna, Spanò, 2013). However, it could not permit to specify a sufficient geometric complexity and granularity of the represented surfaces, following the irregularities, uniqueness and richness of information for architectural heritage buildings. In the model proposed in this study, the characteristics of the surface geometric complexity are considered. Moreover, some attention is drawn to the traceability of the stored information, in order to include in the data the elements useful to technicians for interpreting the stored information and evaluating the degree of fuzziness of the data.

In Figure 1 the CityGML Cultural Heritage Application Domain Extension (CHADE) for the building module of CityGML is summarized. It is then analysed in detail in the following subsection. The extension has been developed and will be tested on the building module; anyway, once its validity will be proved, its concepts and classes can be applied also to the other CityGML modules.

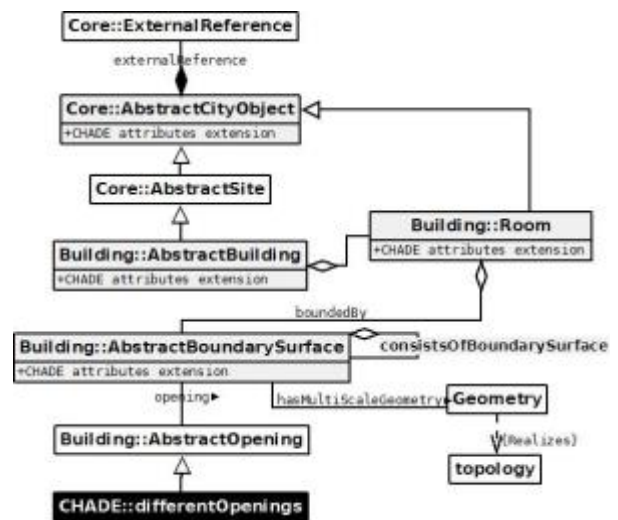


Figure 1. Synthesis of the CityGML CHADE in UML diagram. In white the CityGML classes, in grey (black for the whole class) the CHADE extensions and the inserted relations.

2.1 The CHADE Components: Research of Granularity, Flexibility and Traceability

Starting from the general scale to the detailed particular, the first problem was to include in the object description some attributes useful for the identification of the monument and some related information (e.g. if a CH declaration exists, what are the related documents, who are the owners and what is the preservation authority). Some of these attributes have been borrowed from previous researches (Costamagna, Spanò, 2013), and extend the Core class “AbstractCityObject”.

An interesting possibility offered by CityGML is the use of the “ExternalReference” class, already foreseen by the standard model, which permits to relate the model to further databases managing data about the same object. For example, considering the management of the Versailles castle, the reference can be realized to the instance having ID:700000350 of the Getty Institute CONA vocabulary, describing it (<http://www.getty.edu/cona/CONAFullSubject.aspx?subid=700000350>).

The second issue is the extension of the attribute list for the “AbstractBuilding” class. In particular, its function and its denomination. Both these values are complex when regarding a historical item, since both can change over the time, and must rest archived as historic series of data for being a reference for researches and element for understanding the history of the building. For this reason, in the implementation phase, for both a DataType is included. A DataType is the format of particular entities included in the model, and correspond to some complex attributes form composed by a series of further attributes. This permits to store inside the same attribute, besides the proper value, also the reference time, the source of that information, and whatever useful information that could enrich the data.

The BLDG Function data type includes at first the function name (at present in English, specific future works with historians could evaluate if eventually considering different languages in order not to lose meaning local nuances). The reference to the URI of the Getty Institute vocabulary AAT (Art and Architecture Thesaurus) follows, which includes the terms linked to the buildings function as subclasses of “single built works by function”. The last two attributes are present almost everywhere in the detailed added data types, because they are of critical importance for historic data connotation. The time attribute is defined as a time object defined in the same GML general schema. A further possibility is its definition as a TM_Object (time object) as stated in ISO TC211 ISO 19108:2006 Temporal Schema; however, some incompatibilities among some ISO TC211 definitions and GML requirements persist (https://en.wikipedia.org/wiki/Geography_Markup_Language).

Anyway, both schemas have issues for detailing the time considered, as a date, as a period, with different degrees of fuzziness and with the possibility to establish a sort of topology for temporal data, in a temporal reference system. It is of obvious importance for managing historical data. The second attribute is “Source”, which is detailed, in turn, in a data type, including metadata, reference to the source, codes for its identification and retrieval and the same attribute “time”.

In similar way, the attributes of the class “Room” are extended, adding “RoomClass”, “RoomFunction” and “RoomUsage”, all with references to the Getty AAT vocabulary URI. The “RoomUsage” attribute, which can change over the time, is detailed in a dedicated data type.

The, may be, more interesting part of the model is the extension of the CityGML class “AbstractBoundarySurface”. In the original model it has no attributes, and can be specialized as belonging to the main categories for classifying the parts of a building (e.g.

FloorSurface, RoofSurface, CeilingSurface, WallSurface, etc.). The change of this class aims at a major flexibility in the description of the parts of the historical and artistic buildings, which are stratified and articulated and even small portions can have different meanings. With “portions” also “fiat parts” (without “bona fide”, that is well defined, boundaries) are intended. Therefore, a recursive mereological “part of” relation is added from AbstractBoundarySurface to the same AbstractBoundarySurface. This make it possible to articulate the surfaces in hierarchical, semantically clear, multi-scale and possibly topologically related parts. Several attributes are added and defined following the already explained criteria.

Among these, the “LevelOfSpecialization” (LOS) attribute deserves a particular explication. The 3D models are usually considered for their metric accuracy, which are mainly due to the production methods and measurement systems. This characteristic is stored in GML models as a LOD (Level of Detail) characterizing each geometry. Even if it implies some consequence on the level of semantic definition, it is mainly linked to the possibilities of geometric representation offered by the available data, and thus to the accuracy and data density. The Level of Specialization, is added in order to manage the definition of parts and subparts which can be recognizable on the same model (with homogeneous accuracy and LOD) but need to be separately specified because of the different meanings they assume if considered in the whole or as a singular part (Figure 2).



Figure 2. Examples of consecutive LOS (increasing from left to right) specified on parts of a homogeneous-LOD 3D model. The colors represent the parts in which the object is divided in semantically-homogeneous parts.

A further extension of this class regards the associated geometric levels of detail: since CityGML aim is a cartographic representation, the envisaged levels of details are not high enough to be used for small architectonic details. The CityGML Levels Of Detail are conceived to manage data from a urban or regional scale (approximately 1:25000) to a higher level of detail, useful to represent some building characteristics. However, being CityGML oriented to an urban representation, the maximum detail that can be included in the model, for being meaningful to the representation and consistent with the other levels, is approximately 1:500 (Fan, Meng, 2009). Some more detailed representation can be achieved using textures on the surfaces, permitting to add some details usually present in higher representation scales. For including architectural heritage in the urban representation, it is though necessary to reach further levels of detail, because also smaller parts should be geometrically represented, without losing their complexity. Therefore, two more LODs are added, a LOD5, for approximately 1:200 or 1:100 scale and a LOD6 for bigger ones. The associated geometry class must be defined as a “Geometric complex::GM_CompositeSurface”, since it is structured and hierarchical, in the same way as the boundary surfaces must be also semantically defined. Moreover, it has to be related to a “Topological Complex::TP_Complex”, deriving from the “Topology” part of the standard ISO TC211 – ISO 19107:2003

Spatial Schema or the GML specification (they should be harmonized for the same issues regarding the time objects). This last described part is complex to be used within the current software, and requests some more efforts. A proposal of the topological relations to be included in the model is represented in Figure 3.

OGC has processed some topological and mereo-topological structure for helping to correctly store the data, but they are already oriented to linked open data formats, without regarding GML (<http://ows10.usersmarts.com/ows10/ontologies/>).



Figure 3. Schema of Egenhofer Topological Relations to be included in the model and verified. Some exception can exist (for example, a pillar can be considered only for one half as a component of a bay, admitted that they belong to the same classification), these must be so analyzed in order to confirm or not the validity of this model. The same kind of considerations can be made also for less detailed geometries, for example regarding the objects located on the national boundaries, or, for example, some city wall. Egenhofer relations are considered even if they deal with 2D geometry, because an only reference surface is considered, although being a 3D surface.

2.2 Implementation Issues

Ontologies exploit object-oriented structures and methods, which are unusual in current and known GIS management systems: some of the most spread ones (PostgreSQL-PostGIS, ArcGIS Geodatabase tool, Oracle) implement object-relational schemas, which are hybrid systems including some constructs of object-oriented databases, but not the whole potentiality. Some studies about the development of some semantic GIS have been performed, beginning in the mid-1990s (Mennis, 2003; Fonseca et al., 2002). In these studies, an object-oriented approach was used as an effective solution for expressing and storing the data meanings (Scholl, Voisard, 1992). In this way, even more powerful systems could be built with significant data interoperability and a reduction of any potential ambiguity. Anyway, at present moment few similar systems are available, preferring to use SQL-based implementations (Belussi et al., 2011). This is due to the necessity to adapt the exigencies to the available platforms and software systems and to the necessity to change the storing methods to permit the production and management of computationally heavy files. In the next years probably the object-oriented GIS will be developed again or, some different interface from the GIS we know will be improved to include spatial analysis and query functionalities.

The described model has been implemented using the method defined as best practice by OGC (Van den Brink et al., 2014). UML schemas are modified, which use stereotypes defined by a GML UML profile, so that their meaning can be understood by the machine and the performed transformation can be coherent and correct. In particular, for building the system, the proprietary commercial software Sparx Systems – Enterprise Architect is used. Contrary to the indications of using open source software for managing public (and open) data, it is recommended also in some official documents (for example for the management of INSPIRE schemas, or in the OGC practices). The software permits to import existing models (in this case, obviously CityGML building module and some general schemas such as

GML are used; also ISO 19108 for temporal objects and ISO 19107 for spatial issues could be considered). The classes, selected and imported in the new extension model, maintain all their characteristics and relations with the other parts of the model they belong to. This is crucial for not creating an isolated new model, but for being inserted in a complex existing framework.

From this basis, new classes can be added, the attributes can be defined and new relations can be established.

In particular, following the OGC best practice, for extending an existing class with further attributes, a subclass having the same name of the class to be extended and stereotype “ADElement” should be created. The specialization relation is marked with stereotype “ADE”. For adding a new class, a simple subclass having stereotype “featureType” must be added (Van den Brink et al., 2012).

The so-formed model (Figure 4) can then be exported in different formats, including XSD for being used as a GML application schema.

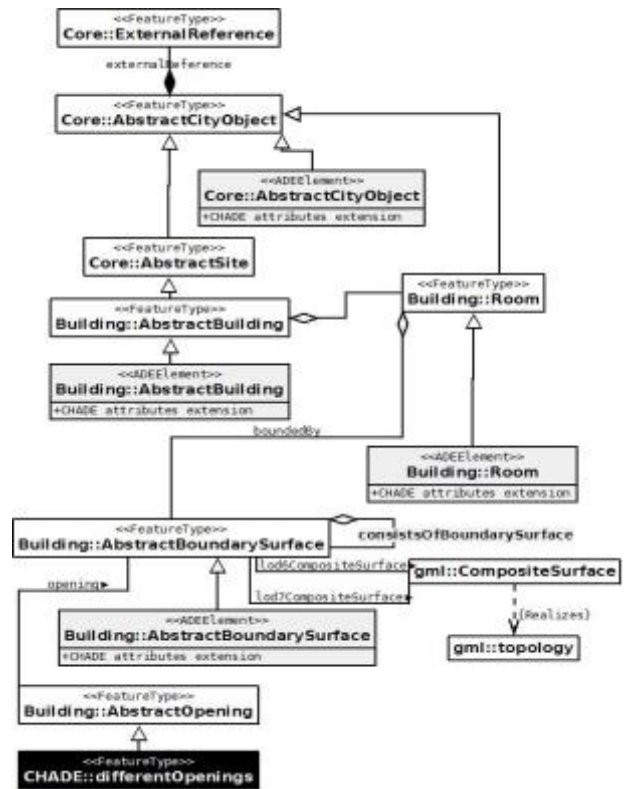


Figure 4. Synthesis of the UML model modified for extending CityGML – Building module in the CHADE, following the OGC best practice indication (Van den Brink et al., 2012).

Other interesting formats are OWL, ArcGIS workspace and similar. From the XSD file also SQL (Simple Query Language) relational or object-relational database schemas could be generated. The transformation can be directly performed by the software, exporting the model in SQL format, to be used for generating an SQL database. However, the translation is not so immediate, since the codes and the data types used in the different languages vary, and it is necessary to carefully control them. A further possibility is to generate the SQL database from the XSD, by passing through different software, such as Altova XMLSpy, which permits to manage XML documents, and eventually manually adapt the data formats. However, the

passage from an object-oriented model to a relational one often cause some complexity to be lost. The analysis aims for which the ontological structures and data models were conceived are therefore undermined. For this reason it is recommended to use GML data and XSD structures, although being SQL data more easily manageable, thanks to the well-affirmed and evolved software tools to manage them.

Following the generation of the XSD for structuring complex GML data, the translation can be automatically performed from the modified UML model. The passages have to be controlled and corrected, since they need correct information or reference files describing, in the specific software-understandable language, how the transformation must be done. Some specific applications and a proper UML profile exist for this aim, but they are not always easily available and compatible in any situation. Waiting for this progress, possibly planned as future work, the resulting files of the transformation have to be manually corrected by editing the XML text following the rules for the ADEs realization.

3. PREPARING THE 3D DATA

For processing and interchanging the data about the paper case study, which is the medieval Staffarda abbey church (in the north-west of Italy) some of the previously described technologies are used. The main problems along the whole workflow are often linked to the inability of the software tools to manage some functionalities and algorithms and/or formats at the same time. For this reason, several passages in specific software are needed.

In this study, existing and available software are used, being not the implementation of new applications tools among the objectives. In particular, open source solutions are preferred, when possible, for interoperability and replicability issues. Moreover, open source software can be often modified for adapting it to the specific application, without being constrained to the existing structures.

When the schemas are ready, the dense high-level-of-detail 3D models have to be prepared. Since the managed surfaces are complex, being composed by miles (or millions) of triangles (stored in form of rings composing a multiple composite surface), it is obviously not possible to store manually the singular point coordinates, but they have to pass through a series of phases that permit their export to a GML format.

The church was surveyed with a high level of detail using integrated geomatics techniques. The lower part of the church and the interiors were acquired by means of terrestrial laser scanning technique. The obtained model was integrated with the roofs and the higher part of the church measured and modelled using images from UAV (Unmanned Aerial Vehicle) processed in digital photogrammetry and structure-from-motion software (Bastonero et al., 2014). The final model reached high accuracies, since it should be useful for being support to a preservation project. Here, the acquisition and processing phases are not described in detail. They exploit a series of techniques for georeferencing the model in a known reference system (Chiabrando et al., 2013; Dabove et al., 2014), for measuring points with various methods and variable accuracy and density (Bryan, Blake, 2000), and for processing the models to finally obtain an integrated, correct, georeferenced and optimized 3D model (Figure 5). The obtained model was further integrated for including another, even higher, level of detail, which could permit to analyze the single parts of a capital. This model was obtained by means of terrestrial images, processed with digital photogrammetry integrated with structure-from-motion technique.

It is not necessary here to describe the processes of generation of the model, but we suppose then to start the process from the already generated, georeferenced and optimized 3D model of the church.



Figure 5. Views of the 3D model (textured mesh) of the Staffarda abbey church, processed using LIDAR acquisitions integrated with photogrammetric data acquired from UAV (Unmanned Aerial Vehicle) (Bastonero et al., 2014).

The first editing phases to be performed on the models regard on the one hand the reduction of its points, caring the conservation of the original definition (Figure 6). This process can be performed using different algorithms, not always known in proprietary software. Anyway, the topic should be further analyzed in order to establish the methods and the limits of this practice.

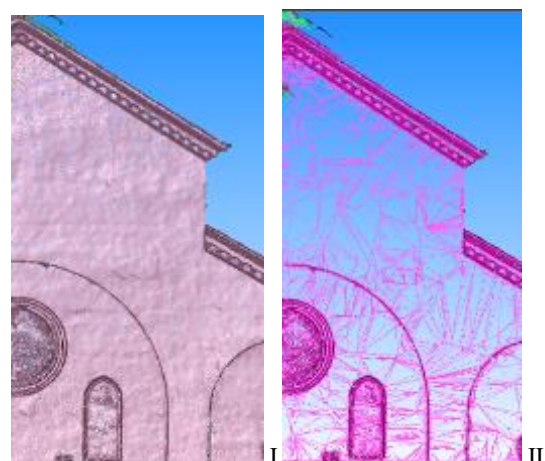


Figure 6. 3D models of the church façade before (I) and after (II) the reduction of the number of triangles composing the surface. Both models views are in wireframe modality (only the triangle edges are shown).

On the other hand, the model must be segmented, so that every part must be isolated from the others for being suitably managed

both geometrically and semantically (Figure 7). Moreover, the temporal connotation must be considered in the segmentation, since it is essential for historical objects (Donadio, Spanò, 2015). A surface can be eventually repeated if it is part of more than one instance having different LOS as attributes. Also for this issue, a quantity of techniques should be analyzed for finding the most suitable one. In this first application, each part of the model was manually segmented in a 3D modelling software (Hexagon 3D Reshaper was used, but the operations could be equally realized in open source software, such as Meshlab or Cloud Compare).



Figure 7. 3D model with texture of one segmented capital.

These phases can be performed in 3D model processing and editing software, such as Hexagon 3D Reshaper (proprietary software), which has the advantage of managing coordinates that have high values such as cartographic ones, therefore georeferenced models can be directly managed. Moreover, advanced editing tools are integrated in it.

At this point, two main alternatives are available for translating the 3D model into a CityGML-compliant format. The first one is the use of Safe Software FME (again a proprietary software), which is expressly dedicated to these operations. FME permits to map objects in different formats and schemas to some predisposed data models, implemented in the software libraries. In particular, it is conceived for filling-in CityGML databases, or INSPIRE-compliant datasets, or it is possible to translate the original data to other specific formats. However, being FME a close proprietary software, it is impossible to modify its internal libraries for including the extended schema CityGML-CHADE. For this reason, a manual editing of the resulting file is anyway necessary to adapt the data to the new schema.

The second option is the use of ESRI ArcGIS, which is equally a proprietary software, but being widely spread, its formats and procedures are often considered as de-facto standards. This last one is used in this case for this reason, even if the passage from an ESRI shapefile format, which is based on a relational model, does not give the possibility to directly specify the final structure of the data. Anyway, also the ESRI processing integrates the FME algorithms in the ArcGIS “Data Interoperability Toolbox” extension.

For using the processing integrated in ESRI ArcGIS, some more passages are necessary. The processed 3D model must be exported in COLLADA format for the following transformation. This open exchange format is not managed by some proprietary software, therefore the model must be exported in a 3D model format (such as OBJ or PLY) and reimported in further software tools able to do the exportation. For example, the open source software MeshLab can do that. The problem is that it has difficulties in managing high coordinate values, so that the whole model must be translated near the origin for this passage. The exported COLLADA files can be then reimported in ESRI

ArcGIS, as multipatch shapefiles (ESRI, 2008). Here they have to be retranslated to their original position in georeferenced coordinates, and can be exported, through the “Data Interoperability” toolbox to a generic CityGML file. The result is the inclusion of the geometry and the attributes of the single parts of models in files structured as CityGML and semantically classified as “GenericCityObjects”. The GML file (readable as XML structured text) has to be manually modified for including in the description schema the CHADE and to correctly define the semantics of each part.

In particular, the reference to the extension namespace must be added in the heading of the file, since there is no way of modifying the FME libraries (used directly or through ArcGIS toolbox) for including the extensions. Moreover, each segmented part of the multipatch is exported as a distinct object having a geometry attribute (in form of `gml:MultiSurface`), but they are not hierarchically structured and they have not a specific semantics yet (being all “GenericCityObjects”). Therefore, the hierarchy must be set and the correct labels must be applied following the CityGML file format. Moreover, all the textual attributes must be manually filled in. In this phase it is obviously considered the extended model CityGML+CHADE. Another important issue is to add suitable identifiers, in order to uniquely identify the objects for performing queries, for retrieving the information, and for realizing some connections, for which, for example, the Xlink syntax (which requires IDs for linking to specific objects) are used. It is preferable if the IDs are composed in form of URIs (Unique Resource Identifiers), following the rules used in best practices also in linked data environment [47]. In this way, the produced information could be more easily translated to linked data for the effective sharing and processing through the Semantic Web.

The Xlink syntax can also be considered and used for the establishment of mereo - topological relations among the parts. XML processing software (some used alternatives can be, for example, the proprietary software ALTOVA XMLSpy or the open source software Xpad) can validate the obtained GML file.

4. RESULTS: THE ARCHIVE IN A GRAPHICAL INTERFACE

At this point, the GML file could be shared through the web and read by several applications or interfaces for being consulted and analyzed.

In this case, an open source software was used and tested in order to read the GML archive based on CityGML CHADE. An open source software was chosen for two main reasons: first, for the already cited goals of interoperability and replicability of the procedures; secondly, because the open source software tools often permits to access the source code of the libraries they use, and possibly modify them. This is useful in order to include the CHADE schema for the correct interpretation of objects that refer to it.

The FZK software (<http://www.iai.fzk.de/www-extern/index.php?id=2315>) was used, which is one of the more developed available CityGML viewers. It includes the schemas of some versions of CityGML, and also some official CityGML ADEs (e.g. the Noise ADE). Furthermore, it has an open structure, which can be customized by adding, for example, other CityGML schemas to be used. For this research, the CHADE schema (in XSD) was added in the directory of the reference files of the software for the described data to be interpreted. This is unequivocally an advantage of the open structure of the software.

In this way the software is able to read the resulting GML archive (Figure 8).

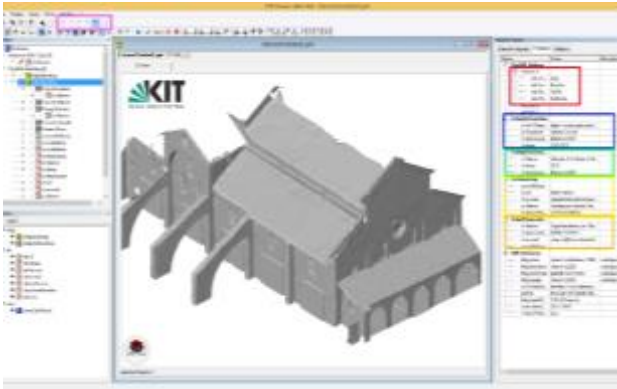


Figure 8. GML model structured using the CityGML CHADE in the FZK software interface: on the left, the objects in the model are listed, in the center the 3D model is visualized and, on the right, the properties can be read. The attributes, which are, in turn, objects themselves or data types (and are therefore composed by a set of attributes) are highlighted by the colored frames. The level of detail to be visualized can be chosen, since the data are multi-scale (in the left part of the toolbar, framed in the figure).

In the visualization platform the objects inserted in the archive can be read, including the relationships among them (Figure 9); some measurements can be directly made on the 3D model (Figure 10); and some thematic visualization can be generated similarly to GIS management software environments (Figure 11). Moreover, statistics about the data are computed.

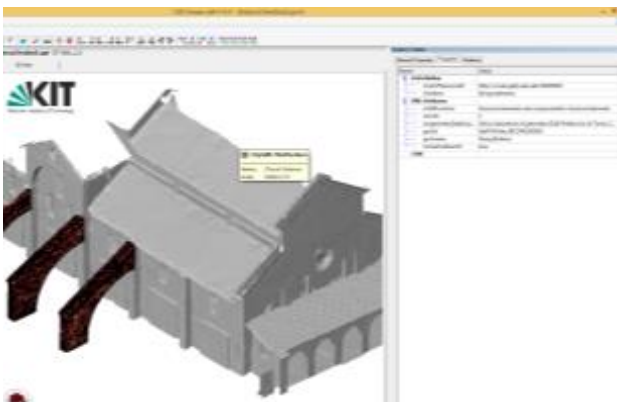


Figure 9. On the right box (“relations” window) it is possible to select and visualize related objects (geometry and thematic attributes). In the image, the result of the relation of the whole object to one of its parts (the flying buttress). They are selected in the representation and the attributes are listed in the right part.

However, the application should be developed in order to include the possibility to effectively manage some elements introduced by the extension, for example the inclusion of different addresses (referred to the building but also to the owners, the authority, etc.) gives sometimes problems in their visualization. In the same way the links inserted in the GML file for cross-referencing the objects or for inserting references to external resources (for example the Getty vocabularies) do not function in the software, because probably some changes in the reading of such components should be done.

Equally, the levels of detail that can be visualized are limited to the ones envisaged by CityGML. For including the more detailed

ones added in the CHADE, the application should be modified not only by adding the schemas but even in its tools and interface code. Also, the possible thematic visualizations are limited to some attributes of CityGML and do not consider the ones introduced by the extension. The same is for the statistics and analysis that can be performed, which are limited to some pre-set parameters and it would be interesting to enhance them. However, these limits are connected to the visualization platform, while the previously structured GML file is independent from them.

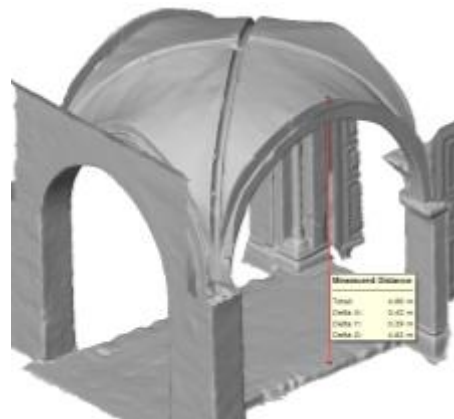
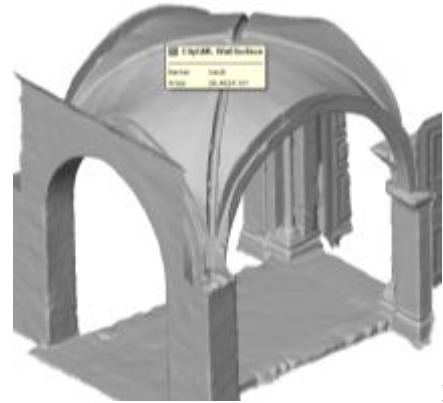


Figure 10. Example of direct measurements possibilities on the 3D model: areas (I) and distances (II). This can be extremely useful for architectural heritage researchers and operators.

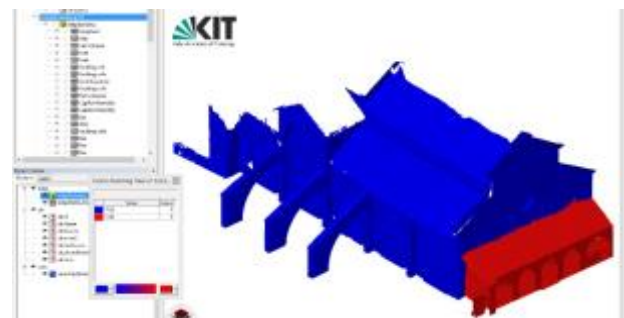


Figure 11. Example of thematic visualization (based on the attribute “year of construction”).

5. DISCUSSION AND PERSPECTIVES

Reference domain ontologies are essential for managing the information in the framework of interoperability established by the recent theories developed by informatics and communication disciplines, which are shared with the Semantic web and the world of standards.

Also cartographic (including architectural heritage) information should be effectively documented using this technology. However, there is not a suitable model for architectural heritage documentation in the urban map context. For this reason the available standards dealing with building, landscape or city representation and cultural heritage management were analyzed and taken as a starting point either for developing an architectural heritage extension or for their reciprocal integration. The OGC CityGML model was selected as best reference ontology for representing and documenting buildings. Being it the international standard for the urban digital maps information, the double sides of the problems (the inclusion of the monument in its urban context and the enrichment of the urban data with cultural issues) can be solved. The CityGML standard data model can be considered an ontology for being independent from the specific application, although many implementation details are proposed and defined in the published standard.

The multi-faceted, complex, and multi-scale 3D models needed a specific structure for being effectively managed. This goal was realized by means of an extension of the OGC CityGML model, which was proposed and tested for this aim. The important aspects and issues typical of the architectural heritage are included in the extension, both from the spatial and the thematic points of view.

Two main implementation phases should be considered: the definition of the data model extension and the filling in with the data. The first one, that is, the conceptual definition of the extension, was implemented by means of some existing tools, which are proposed in the same standards as best practice for realizing extensions. However, there are still some residual difficulties in correctly and automatically performing some passages. Therefore, the resulting products need to be manually refined by editing the generated XML file for obtaining a valid XSD. Major control and automation in the processes performances will be the aim of future improvements.

The same limits in realizing automatic processes are found in managing the 3D models, for which some complex steps are required and the passage through different software tools for preparing the data are often necessary. The generated GML file must be manually edited also in this case. This could be solved if it would be possible to modify the software tools libraries for inserting the extensions to the reference models. Little alternative exists to their use.

The use of XML language as base for writing the files is beyond doubt an advantage, since it can be read by humans and by a number of applications, which permit to read, process and edit them. Moreover, it requires basic tools (even a simple text-editor could be effective) to be managed. On the other hand, the required skills are not within everyone's reach.

In the developing of the model, some fundamental aspects are cared, such as the granularity of the information, its traceability, which is essential when dealing with historical items, the flexibility of the model, to adapt to the representation of such unique artefacts as the monuments are, and the inclusion of thematic data with eventual reference to external databases and vocabularies.

Some automated reasoning on the built knowledge is enabled by the realization of standardized datasets using reference ontologies; this is even more powerful if the information is shared and accessible on the web. Furthermore, the use of ontologies permits the interoperability of the generated urban map and an easier retrieval of the information in compliant databases, including the semantic web.

The architectural heritage research and monument preservation issues can obviously have great advantages by the use of such systems, but they can also be critical for connected topics,

important to the ("smart") city management, such as administration, tourism, risk analysis and further activities.

At present, the built archive can be used in applications similar to the known GIS, which permit the surfing of the archive, the realization of queries, the application of symbols, the measurement of the model, and so on.

The result would consist in a 3D GIS having advanced performances in terms of managed data meanings, actual 3D information management (not only 2,5D as in the common GIS) and possible analysis, exploiting artificial intelligence possibilities.

However, the present available platforms should be modified and improved in order to permit a wider range of analysis and statistics and to include enhanced visualization options.

Future work will be performed for including the real management of advanced spatial issues, such as topology and mereo-topological constraints, in the models and in the data, in order to enhance the analysis potentialities and transversal information retrieval.

A further improvement will be needed for making the connection to external reference to vocabularies effective (possibly using methods similar to the use of gazetteers for toponyms). Also the inclusion or link to further data models and ontologies will be considered: for example, the connection to the CIDOC CRM could be of primary importance.

Another critical passage will be the translation of both the model and the dataset as linked open data. This would permit an effective exploitation of the Semantic Web technologies and the connection to similar information. This translation will be a future development of this study and proposal.

Once these aspects will be solved, a further step towards the world-wide management of the architectural heritage documentation in a unique effective framework for their preservation, retrieval and analysis will be made.

6. REFERENCES

- Barnaghi, P., Wang, W., Henson, C., Taylor, K., 2012. Semantics for the Internet of Things: early progress and back to the future. In *International Journal on Semantic Web and Information Systems (IJSWIS)*. 8 (1). p.1-21.
- Bastonero, P., Donadio, E., Chiabrando, F., Spanò, A., 2014. Fusion of 3D models derived from TLS and image-based techniques for CH enhanced documentation. In *ISPRSAnnals of the photogrammetry, remote sensing and spatial information sciences.2*. p.73-80.
- Belussi, A., Liguori, F., Marca, J., Migliorini, S., Negri, M., Pelagatti, G., Visentini, P., 2011. Validation of geographical datasets against spatial constraints at conceptual level. In *UDMS 2011: 28th Urban Data Management Symposium, Delft, The Netherlands, September 28-30, 2011*. Urban Data Management Society, OTB Research Institute for the Built Environment, Delft University of Technology.
- Brahim, L., Okba, K., Laurini, R., 2015. Mathematical framework for topological relationships between ribbons and regions. In *Journal of Visual Languages & Computing*. 26. p.66-81.
- Bryan, P., Blake, B., 2000. *Metric survey specifications for English Heritage*. English Heritage.
- Chiabrando, F., Lingua, A., Piras M., 2013. Direct photogrammetry using UAV: tests and first results, In: *ISPRS International Archives of the photogrammetry, remote sensing*

- and spatial information sciences. XL-1/W2. ISSN: 2194-9034. p.81-86.
- Chiabrando, F., Spanò, A., 2013. Points clouds generation using TLS and dense-matching techniques. A test on approachable accuracies of different tools. In *ISPRS Annals Of The Photogrammetry, Remote Sensing And Spatial Information Sciences*. 5. p.67-72.
- Chourabi, H., Nam, T., Walker, S., Gil-Garcia, J. R., Mellouli, S., Nahon, K., Scholl, H. J., 2012. Understanding smart cities: An integrative framework. In *System Science (HICSS), 2012 45th Hawaii International Conference on*. IEEE. p.2289-2297.
- Costamagna, E., Spanò, A., 2013. CityGML for Architectural Heritage. In *Developments in Multidimensional Spatial Data Models*. Springer Berlin Heidelberg. p.219-237.
- Costamagna, E., Spanò, A., 2012. Semantic models for Architectural Heritage documentation. In *Lecture Notes in Computer Science*. Springer. p.241-250.
- Dabove, P., Manzano, A. M., Taglioretti, C., 2014. GNSS network products for post-processing positioning: limitations and peculiarities. In *Applied Geomatics*. 6(1). p.27-36.
- De Laat, R., Van Berlo, L., 2011 Integration of BIM and GIS: The Development of the CityGML GeoBIM Extension. In *Advances in 3D Geo-Information Sciences*. LNG&C. p.211-225.
- Doerr, M., Hiebel, G., Eide, Ø., 2013. CRMgeo: Linking the CIDOC CRM to geoSPARQL through a spatiotemporal refinement. In *Institute of Computer Science, Tech. Rep. GR70013*.
- Doerr, M., Ore, Ch.E., Stead, S., 2007. In The CIDOC Conceptual Reference Model - A New Standard for Knowledge Sharing. In *Tutorials, posters, panels and industrial contributions at the 26th International Conference on Conceptual Modeling*. ACS. 83. p.51-56.
- Donadio E. and Spanò A. (2015). Data Collection and Management for Stratigraphic Analysis of Upstanding Structures. In *Proceedings of the 1st International Conference on Geographical Information Systems Theory, Applications and Management*. ISBN 978-989-758-099-4. p.34-39. DOI: 10.5220/0005470200340039.
- ESRI, 2008. *The Multipatch Geometry Type*. ESRI White Paper. Available from: <https://www.esri.com/library/whitepapers/pdfs/multipatch-geometry-type.pdf> [Accessed on 12/11/2015].
- Fan, H. C., Meng, L. Q., 2009. Automatic derivation of different levels of detail for 3D buildings modelled by CityGML. In *24th International Cartography Conference*, Santiago, Chile, pp. 15-21.(2009)
- Fonseca, F., Egenhofer, M., Davis, C., Camara, G., 2002. Semantic granularity. In *Ontology-driven geographic information systems*. AMAI Annals of Mathematics and Artificial Intelligence, 36 (1-2). p.121-151.
- Guizzardi, G., 2005. *Ontological foundations for structural conceptual models*. CTIT, Centre for Telematics and Information Technology.
- Guarino, N., Oberle, D., Staab, S., 2009. What is an Ontology?. In *Handbook on ontologies*, Springer Berlin Heidelberg. p.1-17.
- Janssen, M., Charalabidis, Y., Zuiderwijk, A., 2012. Benefits, adoption barriers and myths of open data and open government. In *Information Systems Management*, 29(4). p.258-268.
- Kolbe, T. H., Gröger, G., Plümer, L., 2008. CityGML–3D city models and their potential for emergency response. In Zlatanova, S., Li, J. (eds.). *Geospatial information technology for emergency response*. CRC Press.
- Laurini, R., 2015. Geographic Ontologies, Gazetteers and Multilingualism. In *Future Internet*. 7(1). p.1-23.
- Laurini, R., 2014. A conceptual framework for geographic knowledge engineering. In *Journal of Visual Languages & Computing*. 25(1). p.2-19.
- Laurini, R., Thompson, D., 1992. *Fundamentals of spatial information systems*. Academic Press.
- Mennis J.L., 2003. Derivation and implementation of a semantic GIS data model informed by principles of cognition. In *Computers, Environment and Urban Systems*. 27. p.455-479.
- Métral, C., Falquet, G., Cutting-Decelle, A. F., 2009. Towards semantically enriched 3D city models: an ontology-based approach. In *Academic track of geoweb*.
- Miller, H. J., Han, J., 2009. *Geographic data mining and knowledge discovery*. CRC Press.
- Myers D., Avramides Y., Dalgity A., 2013. Changing the Heritage inventory paradigm, The ARCHES Open Source System. In *Conservation Perspectives, The GCI newsletter*. 28(2).
- Noardo, F., 2016. Architectural heritage ontology concepts and some practical issues. In *GISTAM 2016 - Proceedings of the 2nd International Conference on Geographical Information Systems Theory, Applications and Management*, pp. 168-179. Selected for publication (under revision) as: A spatial ontology for architectural heritage information, in: Grueau, G., Gustavo Rocha, J., Laurini, R., *GISTAM 2016 – Revised selected best papers*. Communication in Computer and Information Science. Springer series.
- OGC, 2012. *CityGML UML diagrams as contained in CityGML Encoding Standard Version 2.0*, OGC Doc. No. 12-019.
- Ronzino, P., Niccolucci, F., Felicetti, A., Doerr, M., 2015. CRMba a CRM extension for the documentation of standing buildings. In *International Journal on Digital Libraries*. p.1-8.
- Schaffers, H., Komninos, N., Pallot, M., Trousse, B., Nilsson, M., Oliveira, A., 2011. Smart Cities and the Future Internet: Towards Cooperation Frameworks for Open Innovation. In *Future Internet Assembly*. 6656. pp.431-446.
- Scholl, M., Voisard, A., 1992. Object-oriented database systems for geographic applications: an experiment with O2. In *Proc. Int. Workshop on Database Management Systems for Geographical Applications*. Springer.
- Solovyov, S. A., 2012. Categorical foundations of variety-based topology and topological systems. In *Fuzzy Sets and Systems*. 192. p.176-200.

- Van den Brink, L., Janssen, P., Quak, W., & Stoter, J. E. (2014). Linking spatial data: automated conversion of geo-information models and GML data to RDF. In *International Journal of Spatial Data Infrastructures Research*. 9, 2014. <http://www.getty.edu/cona/CONAFullSubject.aspx?subid=700000350> [Accessed on 15/02/2016].
- Van den Brink, L., Stoter, J. E., Zlatanova, S., 2012. Modelling an application domain extension of CityGML in UML. In *ISPRS Conference 7th International Conference on 3D Geoinformation, The International Archives on the Photogrammetry, Remote Sensing and Spatial Information Sciences*. XXXVIII-4, part C26, 16–17 May 2012, Québec, Canada. ISPRS.
- Worboys, M. F., Duckham, M., 2004. *GIS: a computing perspective*. CRC press.
- <http://inspire.ec.europa.eu/> [Accessed on 11/11/2015]
- www.opengeospatial.org/ [Accessed on 11/11/2015]
- <http://www.opengeospatial.org/standards/geosparql> [Accessed on 12/11/2015].
- www.w3.org [Accessed on 09/11/2015].
- <http://www.w3.org/TR/rdf-sparql-query/> [Accessed on 12/11/2015].
- www.w3.org/XML/ [Accessed on 09/11/2015].
- www.w3.org/RDF/ [Accessed on 10/11/2015].
- www.opengeospatial.org/standards/gml [Accessed on 12/11/2015].
- <https://it.wikipedia.org/wiki/COLLADA> [Accessed on 12/11/2015].
- www.w3.org/2004/OWL/ [Accessed on 11/11/2015].
- <https://it.wikipedia.org/wiki/COLLADA> [Accessed on 11/11/2015]
- <http://www.geonames.org/> [Accessed on 12/11/2015].
- <http://www.icomos.org/en/charters-and-texts> [Accessed on 11/11/2015].
- <http://vocab.getty.edu/> [Accessed on 12/11/2015].
- <http://archesproject.org> [Accessed on 09/11/2015].
- <http://www.opengeospatial.org/standards/citygml> [Accessed on 10/11/2015].
- https://en.wikipedia.org/wiki/Industry_Foundation_Classes [Accessed on 09/11/2015].
- <http://ows10.usersmarts.com/ows10/ontologies/> [Accessed on 11/11/2015].
- https://en.wikipedia.org/wiki/Geography_Markup_Language [Accessed on 16/11/2015].
- <http://www.citygmlwiki.org/index.php/CityGML-ADEs> [Accessed on 17/11/2015]
- https://en.wikipedia.org/wiki/Industry_Foundation_Classes [Accessed on 17/11/2015]

DIGITAL SURFACE MODEL GENERATION OVER URBAN AREAS USING HIGH RESOLUTION SATELLITE SAR IMAGERY: TOMOGRAPHIC TECHNIQUES AND APPLICATION TO 3-D CHANGE MONITORING

M. Porfiri^a

^aUniversity of Rome 'La Sapienza', DICEA, Geodesy and Geomatics Division, Via Eudossiana 18, 00184, Rome, Italy -
martina.porfiri@uniroma1.it

University of Rennes 1, IETR, Remote Sensing Group, Campus de Beaulieu-Bat 11D, 263 Av General Leclerc, 35042, Rennes, France -
martina.porfiri@univ-rennes1.fr

KEY WORDS: SAR tomography, high resolution data, TerraSAR-X, urban analysis, 3D monitoring

ABSTRACT:

One of the most important applications of SAR (Synthetic Aperture Radar) remote sensing is the generation of Digital Surface Models (DSM), that is, 3-D models of the Earth's surface. In suburban and urban areas these models are very useful for a great number of applications, that include urban planning and monitoring, safety and security issues, risk mapping, inter-visibility calculations (e.g. for the optimization telecommunication antennas location), orthoimage generation, and more. Three different 3-D imaging SAR-based techniques may be discerned: the radargrammetry, the interferometry and the tomography.

Here the attention is focused on the SAR Tomography: starting from a stack of images collected using multibaseline data performed in interferometric configuration, such a technique allows to retrieve height information forming a synthetic aperture in the elevation direction in order to achieve a substantially improved resolution.

The present PhD thesis aims to demonstrate high potentialities of tomographic techniques in 3-D change monitoring and characterization for complex and dense built-up areas using basic mono-dimensional estimators as Beamforming, Capon and MUSIC combined to very high resolution satellite SAR imagery. 2-D and 3-D analysis have been presented over the urban area of Paris using TerraSAR-X data at high resolution and Single Polarisation (SP). The present work is mainly focused on the 3-D reconstruction by very fast estimation techniques and does not take into account parsimonious signal estimators.

A global 3-D characterization over the city of Paris has been performed in order to develop a monitoring tool for the 3-D changes of single structures. Moreover, the possibility to correct the geometric distortions due to the layover (that strongly affects such kind of scenarios) and to determine the information about the number of scatterers (up to three) and the corresponding reflectivity within one resolution cell have been evaluated. Several 3-D reconstructions of single structures have been performed both in term of buildings heights and vertical reflectivity. Moreover an innovative time stability analysis of the observed scene have been carried out in order to detect the stable and unstable scatterers.

1. INTRODUCTION

Remote sensing is the science of obtaining and interpreting information from a distant point of view, using sensors that are not in physical contact with the object being observed (MicroImages, Inc., 2012). The science of remote sensing in its broadest sense includes aerial, satellite, and spacecraft observations of the surfaces and atmospheres of the planets in our solar system, though the Earth is obviously the most frequent target of study. Imagery acquired by the different sensors provides an important source of information for mapping and monitoring natural and man-made features on the land surface.

Starting from 2007 the new generation of high resolution SAR (Synthetic Aperture Radar) satellite sensors as the Italian COSMO-SkyMed, the German TerraSAR-X and the Canadian RADARSAT-2 allowed to acquire SAR images up to 1 m GSD (Ground Sample Distance) in SpotLight mode, and with different incidence angles. At the present the attention is on the recent new family of missions called Sentinels (-1 for SAR technology) and developed by the ESA (European Space Agency) specifically for the operational needs of Copernicus, the Earth observation programme headed by the European Commission in partnership with ESA and aimed to provide accurate, timely and easily accessible information to improve the management of the environment, understand and mitigate the effects of climate change and ensure civil security.

One of the most important applications of SAR remote sensing is the generation of Digital Surface Models (DSM), that is, three-dimensional (3-D) models of the Earth's surface. In modern map production, the 3-D imaging techniques have become an information source for scene analysis and understanding, for change detection, for GIS database updating, for cartographic 3-D feature extraction and reconstruction. In suburban and urban areas it is very useful for a great number of applications, that include urban planning and monitoring, safety and security issues, risk mapping, inter-visibility calculations (e.g. for the optimization telecommunication antennas location), orthoimage generation, and more. Starting from the SAR data, with respect to the requirements of data accuracy and completeness and of realization efficiency and versatility, three different 3-D imaging techniques may be discerned: radargrammetry, interferometry and tomography.

The present PhD thesis is focused on the analysis of dense and complex urban areas by means of tomographic techniques applied to high resolution satellite SAR imagery. Starting from the classical second product of this approach, that is the reflectivity two-dimensional tomograms, a global 3-D characterization has been performed in order to develop a monitoring tool for the changes of single structures. Moreover, the possibility to correct the geometric distortions due to the layover (that strongly affects such kind of scenarios) and to determine the information about the number of scatterers (up to three) and the corresponding

reflectivity within one resolution cell have been evaluated. Several 3-D reconstructions of single structures have been performed both in terms of buildings heights and vertical reflectivity. Moreover an innovative time stability analysis of the observed scene have been carried out in order to detect the stable and unstable scatterers. The processing have been performed using an adequate high resolution MultiBaseline SAR Interferometric (MB-InSAR) data acquired over Paris urban area by TerraSAR-X. The final goal is to demonstrate the high potentialities of tomographic techniques in 3-D change monitoring and characterization for built-up areas using basic mono-dimensional estimators as Beamforming, Capon and MUSIC combined to very high satellite resolution data. The present work is mainly focused on the 3-D reconstruction by very fast estimation techniques and does not take into account parsimonious signal estimators.

Starting from these purposes, in Section 2 and 3 a brief introduction of, respectively, SAR imaging principles and the tomographic focusing techniques is given, including the state-of-the-art for the urban analysis. Sections 4 and 5 describe, respectively, the 2-D and 3-D experimental results. Eventually the conclusions and perspectives are presented in section 6.

2. SAR: PRINCIPLEAS AND FEATURES

The SAR technology was developed in the 1960s in order to improve the resolution of radar images (for detailed discussions one can refer to, e.g., (Curlander and McDonough, 1991, Franceschetti and Lanari, 1999)). Thanks to its complete independence from the illumination (daylight) and weather (clouds) conditions and to the new generation satellite sensors able to operate with very high spatial and temporal resolution, nowadays SAR data became valuable tools for urban areas and man-made infrastructures analysis and monitoring.

The SAR system measures the time delay between transmission and reception of a pulse in order to determine where targets are relative to one another in the range direction. Consequently, the SAR systems are range-based. This leads to geometric distortions due to relief displacement, such as *foreshortening*, *layover*, *shadowing*, that decrease the reliability of radar imageries (Ferretti et al., 2007).

Whereas shadowing causes dark (i.e. zero signal, zero information) regions, layover leads to a superposition of different reflection components, i.e. several scattering contributions related to different scatterers at different elevation positions (e.g. the building façades or roof and the ground, see Figure 1(a)) are mixed in the same resolution cell. This causes a scattering ambiguity problem along the vertical direction that, generally, can be solved by SAR tomographic techniques. An example of the layover effect is depicted in Figure 1(b) where the well-known Tour Eiffel (image taken from (Auer et al., 2010)) is imaged 'laying down' onto the ground along the range direction (one may also note the Tower's shadow over the bottom of the figure).

3. 3-D SAR IMAGING: TOMOSAR

Due to the specific SAR geometry, SAR imaging represents a projection of the 3-D space (x, y, z) into the bi-dimensional cylindrical zero-Doppler coordinates (x, r). For each pixel of a SAR image, the scattering response consists of a sum of contributions from all scatterers at the same range, encompassing all heights. Hence information about the vertical structure is lost. To recover such information, 3-D imaging techniques are required, whose derived secondary products consists in DSM. One may discern

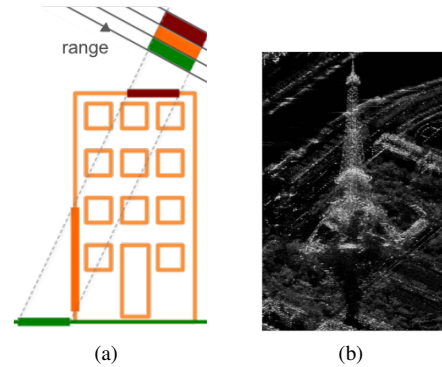


Figure 1. Layover effect for urban areas(a) and the Tour Eiffel(b)

three 3-D imaging techniques: (i) radargrammetry (Leberl, 1990, Mèric et al., 2009, Capaldo et al., 2013, Nascetti et al., n.d., Perko et al., 2011, Toutin and Chenier, 2009, Capaldo et al., 2014, Nascetti et al., 2015) and (ii) interferometry (Graham, 1974, Massonnet et al., 1993, Zebker et al., 1994, Ferretti et al., 1999, Gamba et al., 2000, Ferretti et al., 2001, Lanari et al., 2004), and (iii) tomography (Reigber and Moreira, 2000), evolution of (ii) and based on the use of more than two SAR acquisitions performed in interferometric configuration. Here the attention is focused on tomographic SAR (TomoSAR). Currently, it represents the most effective SAR technology for the monitoring of complex areas, such as, for example, urban scenarios. It is an evolution of the interferometric approach by extending one scattering phase center (Bamler and Hartl, 1998) to several scatterers by using a coherent combination of images acquired in MB-InSAR configuration and performing a 3-D imaging by the formation of an additional synthetic aperture in elevation (Reigber and Moreira, 2000, Zhu and Bamler, 2009). This technique directly retrieves the distribution of the backscattered power in the vertical direction.

TomoSAR allows also to solve the layover distortion problems, analyzing the distribution at the different heights of the backscattering energy and separating different targets inside the same pixel. Furthermore, by analysing dataset of images distributed in time, is even possible to estimate the deformation affecting each single interfering target, through the extraction of its deformation time series. TomoSAR is also a valuable technique to achieve veritable DSM of the observed scene, allowing the possibility to extract detailed 3-D models of single structures on ground (such as buildings).

3.1 State-of-the-art in urban areas

Over the years in literature several works have demonstrated the great TomoSAR potential in respect to different applications, such as forest structures retrieval (Reigber and Moreira, 2000, Tebaldini, 2010, Huang et al., 2011, Tebaldini and Rocca, 2012), ice thickness (Tebaldini and Ferro-Famil, 2013) or building heights (Zhu and Bamler, 2012, Fornaro and Serafino, 2006, Huang and Ferro-Famil, 2009) estimation, layover distortions correction, especially in complex urban areas (Budillon et al., 2011, Huang et al., 2012, Reale et al., 2011, Porfiri et al., 2015).

Built-up area analysis has been always a great challenge in particular starting from the availability of the first sensors able to provide sufficient resolution. Complex urban scenes, being rich of man-made structures, are considered as complex scenarios needed of a refined analysis as the observations are frequently affected by layover effects. In literature, the tomographic study of dense urban environment characterization has been mainly performed from two different point of view: using full polarimetric MB data acquired by airborne sensors (e.g. E-SAR) or using Single Polar-

isation (SP) MultiBaseline (MB) data acquired by satellite sensor (e.g. TerraSAR-X).

Regarding the former, in (Ferro-Famil and Pottier, 2007), (Huang and Ferro-Famil, 2009) and (Sauer et al., 2011) several demonstrations of the effectiveness of different spectral estimation methods for building height estimation and scatterers physical properties retrieval are given.

Regarding the latter, in literature different studies about the 3-D and the 4-D tomography and the layover correction have been published. In particular passing through (Zhu and Bamler, 2009, Zhu and Bamler, 2010a, Zhu and Bamler, 2012, Zhu et al., 2009, Zhu and Bamler, 2010b) one may appreciate the description of several decomposition methods and the relative comparisons presented by the authors. On the other side, several investigations about the tomographic capability to resolve layover cases, e.g. separating single and double-scattering mechanisms within imaged pixels, are performed in (Fornaro et al., 2014, Fornaro et al., 2009, Fornaro and Serafino, 2006, Fornaro et al., 2015, Reale et al., 2011).

3.2 Focusing techniques

The objective of tomographic focusing is to estimate the height profile of a medium and the corresponding set of reflectivity coefficients ($\sigma(z)$). The basic principle of SAR satellite tomographic focusing is illustrated in Figure 2. In order to achieve focusing in height direction and to generate a 3-D SAR image, the additional aperture is synthesized in the normal direction \hat{n} , perpendicular to the range (line-of-sight) \hat{r} and the azimuth \hat{x} directions. This normal direction can be projected onto the elevation direction \hat{z} or the ground range direction \hat{y} in case of, respectively, airborne or satellite systems. The former consider parallel flight tracks at different elevations; while the latter consider different, as equally spaced as possible, orbit tracks at the same elevation (Figure 2).

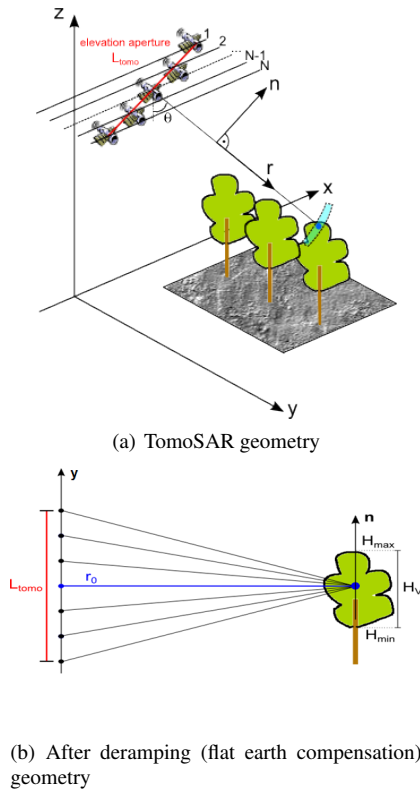


Figure 2. Tomographic SAR satellite imaging geometry

The tomographic inversion is essentially a spectral analysis problem solved applying methods ranging from classical Fourier-based to high resolution approaches. In order to perform a refined analysis of volumetric structures of the observed scenes, these techniques are applied to MB-InSAR data sets in order to localize multiple scattering contributions within a range-azimuth resolution cell and their height z_i .

Considering a resolution cell containing D backscattering contributions from scatterers located at different heights and assuming no decorrelation between the different acquisitions, the data vector measured by M SAR acquisitions, $\mathbf{y} \in \mathbb{C}^{M \times 1}$, can be formulated as follows:

$$\mathbf{y}(l) = \sum_{d=1}^D s_d \mathbf{a}(z_d) + \mathbf{n}(l) = \mathbf{A}(\mathbf{z})\mathbf{s} + \mathbf{n}(l) \quad (1)$$

where $l = 1, \dots, L$ indicates one of the L independent realizations of the signal acquisition, also called looks. The source signal vector, $\mathbf{s} = [s_1, \dots, s_D]^T$, contains the unknown complex reflection coefficient of the D scatterers, and $\mathbf{n} \in \mathbb{C}^{M \times 1}$ represents the complex additive noise, assumed to be Gaussianly distributed with zero mean and variance σ_n^2 , and to be white in time and space. The steering vector $\mathbf{a}(z)$ contains the interferometric phase information associated with a source located at the elevation position z above the reference focusing plane and is given by:

$$\mathbf{a}(z) = [1, \exp(jk_{z_2}z), \dots, \exp(jk_{z_M}z)]^T \quad (2)$$

where $k_{z_j} = \frac{4\pi}{\lambda} \frac{B_{\perp j}}{r_1 \sin\theta}$ is the two-way vertical wavenumber between the master and the j th acquisition tracks. The carrier wavelength is represented by λ , whereas θ stands for the incidence angle and r_1 is the slant range distance between the master track and the scatterer. The steering matrix $\mathbf{A}(\mathbf{z})$ consists of D steering vectors corresponding each to a backscattering source:

$$\mathbf{A}(\mathbf{z}) = [\mathbf{a}(z_1), \dots, \mathbf{a}(z_D)] \quad (3)$$

with $\mathbf{z} = [z_1, \dots, z_D]^T$, the vector of unknown source heights. The data covariance matrix \mathbf{R} can be represented as:

$$\mathbf{R} = \mathbf{A}\mathbf{R}_s\mathbf{A}^\dagger + \mathbf{R}_n \quad (4)$$

where $\mathbf{R}_s = E(\mathbf{s}\mathbf{s}^\dagger)$ is the source covariance matrix describing the correlations between the responses of the D scatterers and $\mathbf{R}_n = E(\mathbf{n}\mathbf{n}) = \sigma_n^2 \mathbf{I}_{(M \times M)}$ is the white noise covariance matrix. Considering now interferometric decorrelation between different acquisitions, the initial model in equation (1) may be reformulated as a sum of contributions from random sources (Gini and Lombardini, 2005):

$$\mathbf{y}(l) = \sum_{d=1}^D \mathbf{x}_d(l) \odot \mathbf{a}(z_d) + \mathbf{n}(l) = \sum_{d=1}^D \mathbf{y}_d(l) + \mathbf{n}(l) \quad (5)$$

where $\mathbf{x}_d \in \mathbb{C}^{M \times 1}$ is unknown and accounts for both the reflection coefficient of the d th source, s_d , and its potential variations between the interferometric acquisitions over the L realizations. Depending on the type of scatterer under observation, the source signal \mathbf{x}_d possesses varying statistical properties.

3.3 Nonparametric tomographic estimators

Generally, nonparametric spectral analysis techniques are considered as robust, since they do not require any assumptions about the statistical properties of the received signals. Accordingly, they can be used in situations with lack of information about these

properties (Stoica and Moses, 2005). These methods aim to estimate the Direction of Arrival (DOA), that is, given a spatially propagating signal, to determine its angle of arrival at the array. Their principal drawback lies in poor spectral resolution due to the high variance of the periodogram and correlogram estimates. In this section classical estimators like the Beamforming and the Capon method are presented for a MB-InSAR configuration. For tomographic purpose, the goal is to determine an estimation \hat{z} of the elevation of the scatterers under observation as the coordinates of the local maxima of an objective function with a scalar elevation argument $P(z)$:

$$\hat{\mathbf{z}} = \arg \max_{z, loc} P(z) \quad (6)$$

This objective function is given by the continuous estimate of the reflectivity, i.e. $P(z) = \hat{\sigma}(z)$.

3.3.1 Beamforming The Beamforming method has been derived for estimating DOA as mentioned in (Van Veen and Buckley, 1988, Johnson and Dudgeon, 1992). In (Homer et al., 2002), Beamforming was firstly suggested for solving the layover problem using MB-InSAR data sets. The Beamforming method for spatial frequency estimation can be derived as a Finite Impulse Response (FIR) filter (Stoica and Moses, 2005), assuming a spatially white scenario, i.e. such a signal in the array output can be considered as impinging on the array with equal power from all direction θ . The Beamforming spectrum is associated to the PSD of the received MB-InSAR data $\mathbf{y}(l)$, and its objective function is given by the continuous L -look estimate of the reflectivity:

$$P_B(z) = \hat{\sigma}_B(z) = \frac{1}{L} \sum_{l=1}^L \frac{|\mathbf{a}^\dagger(z)\mathbf{y}(l)|^2}{M^2} = \frac{\mathbf{a}^\dagger(z)\hat{\mathbf{R}}\mathbf{a}(z)}{M^2} \quad (7)$$

Nevertheless, as shown in (Stoica and Moses, 2005), if this method is consistent in the single-source case ($n = 1$), in the general case of multiple sources it leads to biased estimates for the height and reflectivity. In order to get better resolution and reduce the leakage problems, the Capon method has been proposed.

3.3.2 Capon The Capon method has been derived under the same condition of minimum interfering power as the Beamforming method, but considering the general case of nonwhite interference scenario. Contrarily to the Beamforming, the Capon filter is designed in a 'data-dependent' way aiming to steer to a certain DOA (or spatial frequency) θ and to attenuate any other signals that actually impinge on the array from a $DOA \neq \theta$. This method was applied for time series data in (Capon, 1969, Lacoss, 1971), and array signal processing (Stoica and Moses, 2005) as well as for MB-InSAR data processing (Gini and Lombardini, 2005).

In the MB-InSAR configuration, the Capon spectrum of the received data is represented by the continuous estimate of the reflectivity:

$$P_C(z) = \hat{\sigma}_C(z) = \frac{1}{\mathbf{a}^\dagger(z)\hat{\mathbf{R}}^{-1}\mathbf{a}(z)} \quad (8)$$

The elevations of scatterers \hat{z} correspond to the locations of the D local maxima of $\hat{\sigma}_C(z)$ using equation (6) and their reflectivities can be obtained directly from $\hat{\sigma}_C(\hat{\mathbf{z}})$.

3.4 Parametric tomographic estimators: MUSIC method

Parametric estimators exhibit an excellent capability to discriminate scatterers located at different elevations, assuming the number of scatterers D is a priori known. Hence, after determining the number of effective sources, i.e. model order, parametric methods can be applied to estimate the spatial frequencies of the

detected signals with an improved resolution, compared to non-parametric methods. Here the noise is assumed to be spatially white with components having identical variance and to be uncorrelated respect to the signals.

The Multiple Signal Classification (MUSIC) method (Schmidt, 1986) is a generalization of Pisarenko's harmonic retrieval method (Pisarenko, 1973), and a parametric spatial frequency estimator for signals buried in white noise. MUSIC may be considered as a subspace-based technique as it uses a partition of the eigenstructure of the covariance matrix \mathbf{R} modelled as in (4). Indeed the eigenstructure of \mathbf{R} contains complete information on the frequencies related to \hat{z} (Stoica and Moses, 2005).

MUSIC is a subspace-based single-dimension technique, whose objective function is a measure of the orthogonality between a steering vector and the noise subspace and is given by:

$$P_M(z) = \frac{1}{\mathbf{a}^\dagger(z)\hat{\mathbf{E}}_n\hat{\mathbf{E}}_n^\dagger\mathbf{a}(z)} \quad (9)$$

where $\hat{\mathbf{E}}_n$ represents the matrix of covariance eigenvectors which span the noise subspace. Once $\hat{\mathbf{z}}$, is determined by inserting equation (9) in the (6), the estimate of the complex reflectivity vector $\hat{\mathbf{s}}(l)$ can be obtained by solving a LS problem.

In (Gini and Lombardini, 2005, Stoica and Moses, 2005) a numerical analysis has been performed in order to compare the MUSIC methods with the Beamforming and Capon ones, demonstrating its effective better estimation results, even in presence of multiplicative noise. MUSIC performance quality depends mainly on the correlation between the scatterers. In fact, if they are fully correlated the source covariance matrix \mathbf{R}_s is rank deficient and the eigenvectors belonging to the signal subspace may leak into the noise subspace.

4. PROPOSED APPROACH AND INNOVATIVE ASPECTS

As mentioned, the main goal of the present thesis is to perform a global 3-D characterization and change monitoring of dense and complex urban areas. In order to achieve the aim, it has been chosen to apply tomographic SAR techniques to high resolution satellite data. In particular, the strong potentialities of the classical non- and parametric spectral estimators combined to high resolution data have been evaluated, whereas parsimonious signal estimators have not been taken into account.

The proposed approach allows to correct the geometric distortions due to the layover and to determine the information about the number of scatterers and the corresponding reflectivity within one resolution cell. The analysed Area Of Interest (AOI) represents the of Paris, characterized by mixed features, as vegetation, infrastructures, buildings, skyscrapers, etc. In this context, in the same resolution cell one may find the superposition of the information related to a dominant scatterer and one or maximum two others minor scatterers. For that, the maximum number of the effective sources N_0 within one resolution cell has been set to three. In order to detect, for each resolution cell, the number of the effective sources, the iterative Model Order Selection (MOS) technique has been applied to the selected estimation methods. Given a "quasi" ML solution for well separated sources, it is based on the following steps: for each resolution cell and for three iterative steps, starting from the first elevation value z_{loc} coming from the maxima local research performed by means of the estimation method, a test over its intensity $P(z_{loc})$ has been evaluated as followed:

$$\frac{P(z_{loc})}{P(z_{max})} > I_{threshold} \quad (10)$$

where $I_{threshold}$ is the customized threshold set for the analysed area and $P(z_{loc})$ is normalized respect to the absolute maximum intensity value $P(z_{max})$. If the test was positive, z_{loc} represented a real source and the process restarted in order to find the potential second or third source; if the test was negative, the process stopped.

Two different processing chains have been proposed depending on the selected estimation method. For non-parametric methods, i.e. Beamforming and Capon, the local maxima research has been performed following the proposed iterative MOS technique. For parametric methods, i.e. MUSIC, at first it has been determined a priori the number of the sources N_S as a little bit bigger than N_0 within one resolution cell; successively, it has been applied the proposed iterative MOS technique. An important advantage of this solution is that the artefacts are not considered, due to their low intensity values.

Moreover, an innovative idea has been proposed for the 3-D change monitoring and detection of single structures. For this aim it has been necessary to perform a 3-D tomographic focusing using of Maximum-Likelihood Ratio Test (MLRT) detectors (see subsection 6.3).

5. 2-D ANALYSIS AND RESULTS

This section is focused on the analysis of the quality of the processed data set, as well as for interferometric purpose and scatterers time stability, and on the extraction of tomographic 2-D second products, i.e. tomograms.

The analysed stack consists of 21 SP TerraSAR-X images acquired in High Resolution Spotlight mode over the urban area of Paris with a mean incidence angle of about 34.7° with a slant-range resolution of 1.2 m and an azimuth resolution of 1.1 m (the approximate image center latitude and longitude are respectively 48.846545° and 2.286024°).

In Figure 3(a) and 3(b) the spatial baseline and the spatial-temporal baseline distributions are respectively shown; the maximum elevation aperture size is about 583.5 m and the temporal baseline ranges from 24th January 2009 and 26th November 2010. It is possible to do the first considerations about the stack quality. From Figure 3(a) it is clear that the image with ID 20 represents an outlier respect to the relative spatial baselines between the other images, whose value is about 334.4 m. Moreover, in 3(b) the same image is an outlier also in term of temporal baseline, together the image with ID 21 (the last one). This leads to expect, in the successive interferometric quality analysis phase, a different behaviour in term of phase component of these two images.

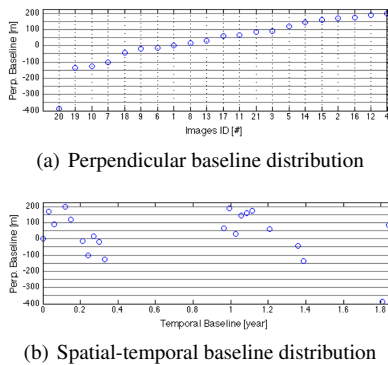


Figure 3. Baselines distributions of the 21 acquisitions

5.1 Interferometric quality and temporal stability analysis

A first step for the tomographic processing is the analysis of the interferometric quality of the data to be used. The analysis has been performed considering all the combinations of two images out of the stack, that is $\frac{N \cdot (N - 1)}{2}$ samples (with N the number of processed images). Starting from a co-registered and flattened data set, a calibration of the atmospheric phase component has been applied to the signals, treating the problem as a low-pass filtering one.

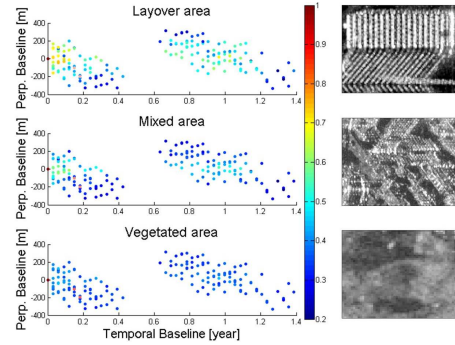


Figure 4. Spatial-temporal trend of coherence mean values (left) evaluated over different image subsets (right)

In Figure 4 (left plots) it is represented the mean coherence values evaluated respect to the spatial and temporal baselines. The interferometric coherence γ is defined by (Bamler and Hartl, 1998) as a normalized complex cross-correlation between two received signals s_1 and s_2

$$\gamma_{int} = \frac{E\{s_1 s_2^*\}}{\sqrt{E\{|s_1|^2\} E\{|s_2|^2\}}}$$
 (11)

Its phase is the expected interferometric phase ϕ_0 of the selected pixel and its magnitude is related to phase noise. Thus, the coherence measures the interferogram quality and influences the estimation of interferometric phase, since it is related to phase stability or predictability.

Several image subsets characterized by different scenes, such as layover, mixed and vegetated areas, have been cropped and showed in Figure 4 (right tiles). As expected, the highest coherence values are related to the area characterized by layover induced by a single structure (the Tour Mirabeau), whereas the lowest ones are related to the area mostly covered by vegetation. Moreover, the coherence increases especially for the layover area decreasing the spatial baselines values.

From Figure 5 one may better appreciate the globally interferometric trend over the stack. In particular, in Figure 5(a) and 5(b) the calibrated coherence maps evaluated along both the increasing temporal and absolute spatial baselines are reported. Amplitude images (principal diagonal), coherence images (upper triangular part) and flattened and calibrated interferograms (lower triangular part) computed over the entire processed stack are depicted. Both figures show the trend of the interferometric phase quality for all the combinations of two images out of the stack. As anticipated, image with ID equal to 20 results highly uncorrelated with all other images most probably because it presents both the higher spatial baseline value (about -386.7 m) and a dispersed acquisition date (see Figure 3(a) and 3(b)). On the other hand, pair images with small baselines are characterized by a higher correlation presenting better and brighter coherence images. Interferometric phase quality, and consequently tomographic elevation resolution, strongly depends on temporal and spatial baseline

characteristics. Indeed, as depicted in Figure 5(b), the global interferometric quality increases with decreasing spatial baseline values, i.e. moving from the upper-right and lower-left corners of the matrix to the principal diagonal.

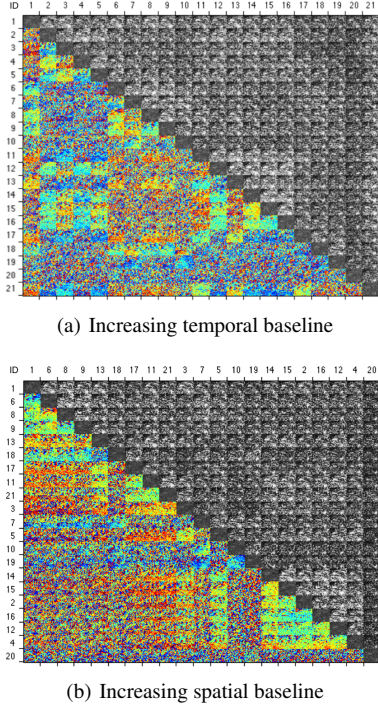


Figure 5. Calibrated coherence maps along temporal and spatial baselines

Above results highlight the high coherence level between the majority of the images within the stack, confirming the effective capabilities of TerraSAR-X high resolution data. On the basis of these preliminary analysis the two (temporally) last images have been discarded and the experimental results have been achieved processing the leftover 19 images.

In order to deeply describe the urban AOI, a time stability analysis of the signals have been carried out adapting to the SP data two statistical descriptors related to the signal stationary aspect and coherence presented in (Ferro-Famil and Pottier, 2007, Hu et al., 2013) for polarimetric SAR data based on Maximum Likelihood statistic test.

The 2-D temporal coherent stability between the $\{s_j\}_{j=1, j \neq i}^{19}$ signals has been computed accordingly to the indicator ρ_T given by

$$\rho_T = 1 - |\hat{\mathbf{R}}|^{1/N} \quad (12)$$

where $\hat{\mathbf{R}} = \mathbf{PRP}$, with $[P]_{ii} = \text{diag}(\sqrt{\mathbf{R}_{ii}^{-1}})$. Its values range from 1 (maximum correlated case) and 0 (decorrelated case). In Figure 6(a) its trend shows (and confirms) that natural environments such as the river in the upper right part of the images have low ρ_T values. On the contrary, coherent reflectors like man-made targets and buildings show the highest values of ρ_T especially over the squared lower-left roof.

The 2-D temporal incoherent stability characterization has been assessed over the data stack by testing the fluctuation of the intensities $\{I_i(x, y)\}_{j=1, j \neq i}^{19}$ of the signal computing the parameter Λ by the equation (13)

$$\Lambda(j, k) = \frac{\prod_{i=1}^N \mathbf{I}_i(j, k)^{\frac{1}{N}}}{\frac{1}{N} \sum_{i=1}^N \mathbf{I}_i(j, k)} \quad \forall(j, k) \quad (13)$$

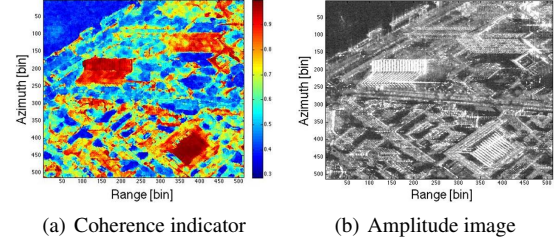


Figure 6. Coherence indicator trend over the selected subset

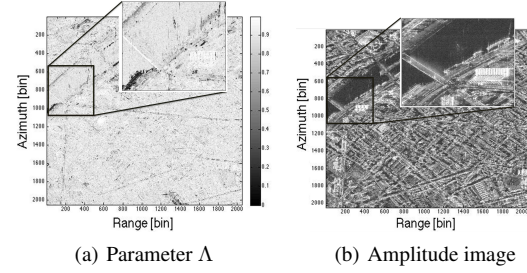


Figure 7. Image of the parameter Λ on Paris test site

where $\mathbf{I}_i(j, k)$ represents the (j, k) th element of the intensity matrix of the i th image. The relative image over all the test site is represented in Figure 7: not moving features like buildings and bridges show high Λ values, whereas boats and cars over main streets are affected by a very low stationary behaviour. These results show the capability of these indicators to provide complementary information, adapted to the case of man made environments.

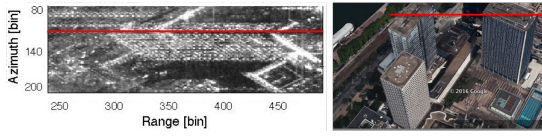
5.2 Tomograms generation

In this section SAR tomographic results have been achieved implementing and applying different mono-dimensional estimators over the selected dataset. 2-D tomograms have been generated over several azimuth profiles in order to estimate building heights and to distinguish different scatterers within the same resolution cell. Tomograms here illustrated in Figure 8 are referred to the image profile highlighted on the SAR and Google Earth images in Figure 8(a) by the red line and strongly characterized by the geometric distortions related to the layover induced by the Tour Keller. Thanks to the high quality resolution of the processed data, it is possible to distinguish, for some resolution cells, more than one intensity local maxima. These peaks are related to different scatterers due mainly to the skyscraper features and the ground as depicted in the relative scheme on the right of the tomograms. In particular from Figure 8(b) it is possible to detect two scatterers, corresponding for example to the ground and the building façade. In Figure 8(c) one may appreciate the presence of up to three scatterers within the same resolution cell due, for example, to the addition of the building roof. This represents a valuable capability of tomographic techniques that allows to obtain complete point clouds and, hence, complete DSMs.

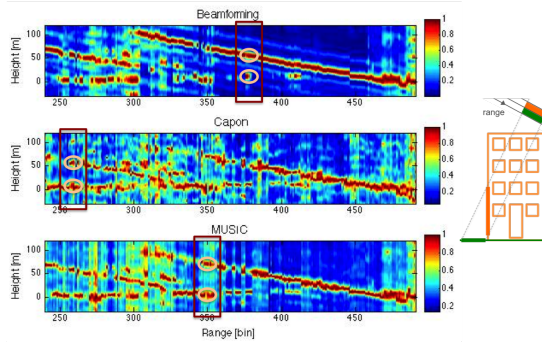
Especially for MUSIC results (bottom tomograms in Figure 8(b) and 8(c)), one may appreciate how thanks to the proposed approach, the artefacts are not taken into account as real sources, thanks to their low intensity values. Furthermore, the presence of artefacts has been strongly reduced filtering the signal by means of two masks obtained by a threshold computed on the parameter ρ and Λ , previously described. From the tomograms obtained by the MUSIC approach one may note how the hypothesis to set the number of the sources N_S equal to 4, i.e. as a little bit bigger than $N_0 = 3$, allows to achieve very good results in terms of vertical

resolution and accuracy and source detection.

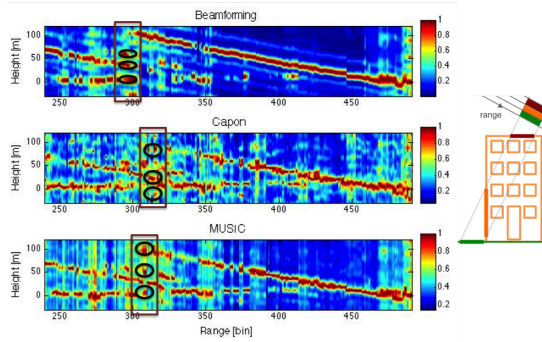
Results reported in the present section have demonstrated the



(a) Amplitude and Google Earth image of the analysed red profile



(b) Slant range normalised reflectivity tomograms: 2 detected scatterers



(c) Slant range normalised reflectivity tomograms: 3 detected scatterers

Figure 8. Tomograms generated over one layover-affected profile applying Beamforming, Capon and MUSIC spectral estimators

possibility to perform dense urban area 2-D analysis using tomographic techniques and high resolution satellite SAR data. Exploiting mono-dimensional spectral estimation models, the buildings heights estimation and the scatterers number extraction have been carried out. In this way it has been possible to resolve pixels affected by the layover distinguishing up to three scatterers within the same resolution cell.

6. 3D ANALYSIS AND RESULTS

In the present section a global 3-D characterization of dense and complex urban areas exploiting SAR tomographic techniques is presented. In this sense, several reconstructions in terms of building height, vertical reflectivity and time stability have been carried out processing an adequate set of multitemporal high resolution TerraSAR-X images in order to deeply analyse build-up areas. Starting from experimental results obtained in the previous section, here the study has been widened to urban azimuth/range tiles. The 3-D views have been reconstructed in ground range processing the results obtained considering up to three scatterers within one resolution cell and Beamforming, Capon and MUSIC approaches. The investigation have been carried out for three different intensity levels, in each of which the maximum absolute

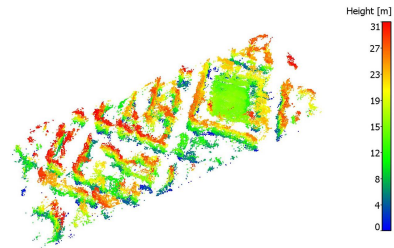
reflectivity value has been identified from the spectrum evaluated for each resolution cell within the tile.

6.1 Height map generation

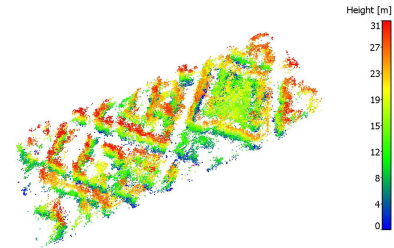
In order to operate in the 3-D field, the 2-D spectral analysis for an azimuth profile is widened to the azimuth/range resolution cells within the selected tile leading to the generation of sparse point clouds.



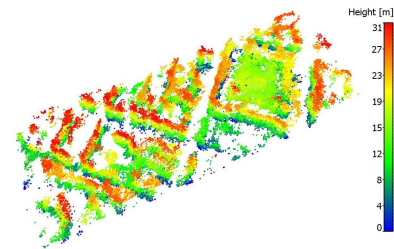
(a) 3-D map of the selected tile



(b) All detected sources: Beamforming



(c) All detected sources: Capon

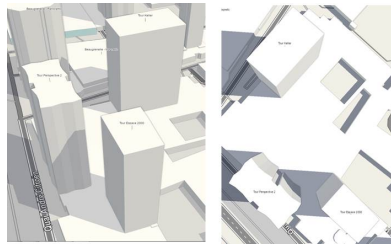


(d) All detected sources: MUSIC

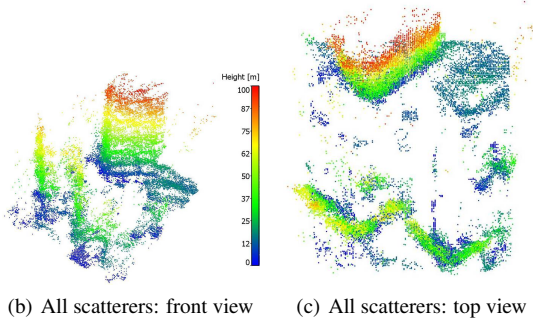
Figure 9. 3-D height maps represented in ground range over a mixed urban area considering all the detected sources

Figure 9 represents the height maps generated over the area underlined by the red lines (Figure 9(a)) and characterized by several residential buildings and a big almost squared structure defined by different features. As one may note, the height map extracted by Capon method appears to be sparser and noisier, whereas the Beamforming and the MUSIC ones show tidier point clouds. Point clouds generated using MUSIC approach are characterized by a higher rate of completeness (in particular the $\sim 4.8\%$ and $\sim 5.5\%$ more of detected points than, respectively, Beamforming and Capon methods). Comparing the 3-D views with the simplified 3-D map in the top of the figure, one may perceive the reconstruction of the main building shapes and location and the streets orientation. Especially for the big squared structure, considering all the detected sources one may recognize the

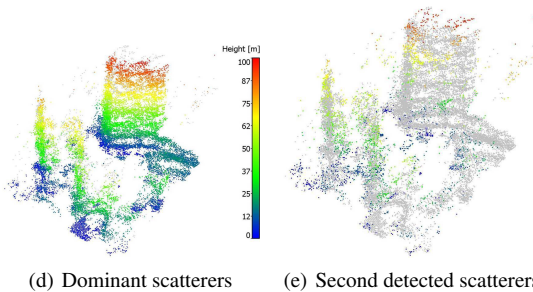
principal features, such as the external wall, the internal edifice and the external patio. It is also evident that the main information is given by the dominant scatterers, even though second sources give a contribution mainly for scatterers at lower height. It is important to underline that elevation values represented in the height map and pointed out in figure legends appear to be coherent with the one estimated from Google Earth. It has been taken into account this data due to the lack of a ground truth as e.g. one obtained by means of the LiDAR technology. The obtained products have led to focus the attention, in the following, over the ones extracted by means of the MUSIC method. The main interesting capability of TomoSAR is the layover dis-



(a) 3-D views of the Tour Keller's area



(b) All scatterers: front view (c) All scatterers: top view



(d) Dominant scatterers (e) Second detected scatterers

Figure 10. 3-D height maps of Tour Keller area represented in ground range and extracted considering several detected scatterers using MUSIC method

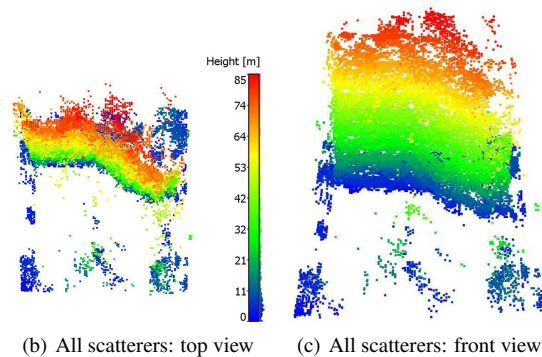
tortion correction, that is detecting and distinguishing different scatterers with different elevation imaged together in the same range/azimuth resolution cell of the SAR image. In order to demonstrate it, the Tour Keller layover imaging over the Tour Espace 2000 and the Tour Perspective 2 has been taken into account (the effect is well visible in Figure 8(a)). Figure 10(a) reports the front and top (simplified) map views that if compared with, respectively, Figure 10(b) and Figure 10(c) gives an additional confirmation of the potential of this technique combined with high resolution satellite SAR data. Focusing on the biggest skyscraper, one may perceive its shape and the location of its two façades. Moreover, it is clear that resolution cells affected by layover have been georeferenced and the information related to features below them has been partially reconstructed in the others two main buildings and the ground. It is also interesting make a comparison between Figure 10(d) and Figure 10(e) where rela-

tive detected scatterers are highlighted respect to the point cloud populated by all the estimated sources (imaged in gray). One may note how the majority of the second source (that consists in about the 13.4% of the total detected points) are related to pixels affected by the layover, that is scatterers related to a relative peak in the reflectivity spectrum.

Eventually, in order to perform the investigation of a single building reconstruction the Tour Mirabeau has been selected, thanks to its particular shape (as one may note in Figure 11(a)) and strong layover distortions. In this case the layover induced by the structure does not involve other important features but the ground. Hence several views of merely the point cloud extracted considering all the detected sources are represented. Comparing the top view in Figure 11(b) with the right one in Figure 11(a) one may note the good reconstruction of the particular shape of the two façades facing the radar signal. At the same time the frontal view depicted in Figure 11(c) show the point detection at the different height, reconstructing partially the roof of the building. Moreover pixels imaged in layover are quite geometrically corrected and georeferenced in relation to the others demonstrating the extraction of the form of the global building. Nevertheless, ground involved by the layover has been reconstructed for a very small part, showing anyway the limits of this technique.



(a) 3-D views of the Tour Mirabeau



(b) All scatterers: top view (c) All scatterers: front view

Figure 11. 3-D height maps of Tour Mirabeau represented in ground range and from different point of views and obtained using the MUSIC method

6.2 Vertical reflectivity estimation

Another important characterization of the built-up areas consists in the estimation of the vertical reflectivity information. For ground imaging, the reflectivity may be modelled as the superposition of the echoes from a large number of uncorrelated scatterers randomly dispersed through the resolution cell. Hence it is expected to be characterized by low reflectivity values. For building imaging, the reflectivity is supposed to be higher at the wall-ground interaction where typically occurs the double bounce reflection. It is important to restate that the reflectivity profile is used to estimate scattering parameters, such as the number of scatterers in a pixel, their elevations, and their reflectivity strength. Here it has been decided to focus on the analysis of the Tour Keller and Tour

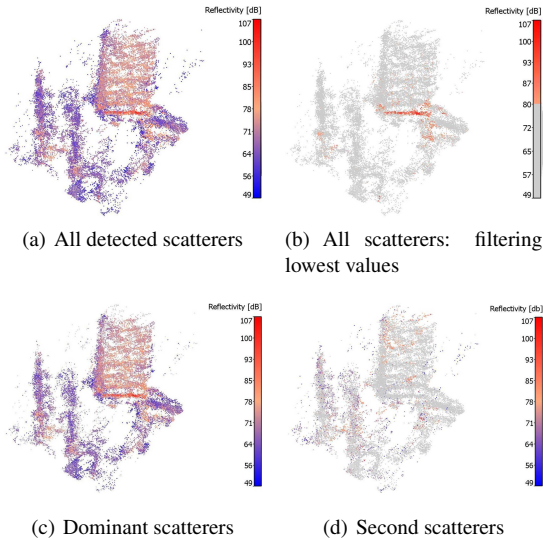


Figure 12. Tour Keller area 3-D reflectivity maps in ground range extracted considering several detected scatterers

Mirabeau areas, due to their high elevation spread. Figure 12 represents the reflectivity maps evaluated at different point detection steps for Tour Keller area. Figure 12(b) show points characterized by high reflectivity value, considering all the detected sources. It is evident that these points are located at the basis of the main buildings due to the strong double bounce reflection occurring at the wall-ground interaction. On the other side the ground, accordingly with the expectations, is characterized by lower reflectivity values (see Figure 12(a)). Moreover, from the histograms in Figure 13 one may note how the majority of the scatterers with high reflectivity values (i.e. ≤ 80 dB) have been detected at the first step, i.e. for the dominant scatterers. This is congruent with the assumptions set for the detection of the sources at the different reflectivity levels.

Regarding the Tour Mirabeau structure, Figure 14(a) and 14(b) underline the double bounce effects at the wall-ground interaction, revealed by the presence of scatterers characterized by the highest reflectivity. Moreover Figure 14(a) shows mean reflectivity values in correspondence of the roof of the building, probably related to the correlated surface scattering.

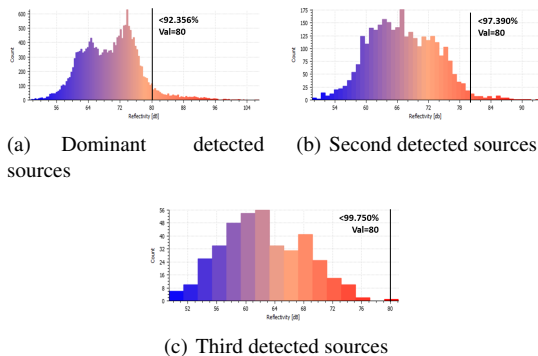


Figure 13. Tour Keller area: reflectivity histograms

6.3 Time stability analysis

The previous sections results in terms of height map extraction and vertical reflectivity estimation have been presented over different tiles. In the present section it is presented an innovative

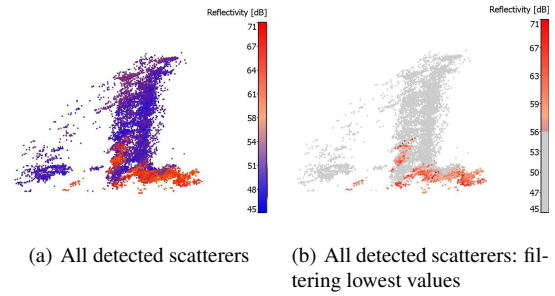


Figure 14. Reflectivity maps of the Tour Mirabeau in ground range and extracted considering all the detected scatterers

3-D time stability analysis of the observed scene, aimed to identify unstable detected scatterers and processed images from the time point of view.

The basic idea is to evaluate a set of 3-D intensities

$$I_i(x,y,z) \quad \text{with } i = 1, \dots, N_{im} \quad (14)$$

discarding for each step the current image, that means consider the signals

$$\{s_j\}_{j=1, j \neq i}^N \quad \text{with } N \text{ the image number} \quad (15)$$

of the $N - 1$ 2-D images. Since these 3-D intensity estimates have similar resolution properties, the variations with i permit to appreciate the importance of the missing image. The temporal stability at coordinates (x, y, z) can then be measured using a Modified Coefficient of Variation, CV_m , derived from the set of intensities

$$\{I_i(x,y,z)\}_{i=1}^{N_{im}} \quad (16)$$

The Coefficient of Variation is expressed as the ratio of the standard deviation σ to the mean μ . It is a statistical measure of the dispersion of data points in a data series around the mean, that is the higher the CV the greater the dispersion in the variable.

Figure 15(a) plots an extraction of the most perturbing image contributions varying the number of discarded images and the number of the unstable pixels at the different steps, i.e. discarding always one more image, is showed in Figure 15(b) from where one may note how the majority of the unstable pixels are detected at the first step. Figure 15(c) is a 3-D view of the image indices that more influence scatterers time stability at the first step (i.e. discarding one image) and as one may observe from Figure 15(d) the resulting one is image with ID 6. The trend of the estimated CV_m is showed in Figure 16(a) and the 3-D reconstruction in Figure 16(b) displays the stable and unstable scatterers in term of the estimated CV_m : unstable (orange) pixels, i.e. points with CV_m values higher than the estimated threshold, lie mostly on the main skyscraper façades. Focusing on the unstable images, in Figure 15 is represented an example of the time analysis aiming to extract the number and the indices of images that more perturb the 3-D temporally unstable scatterers.

Also the Tour Mirabeau has been taken into account in this analysis. As shown in Figure 17 the analysis performed in terms of the CV_m reveals that the greater number of the pixel is stable in the time domain. For that the IDs of the unstable images have not been computed.

7. CONCLUSIONS, FURTHER INVESTIGATIONS AND IMPROVEMENTS

The main goal of this work was to develop a global and 3-D characterization of complex and dense urban areas using tomographic

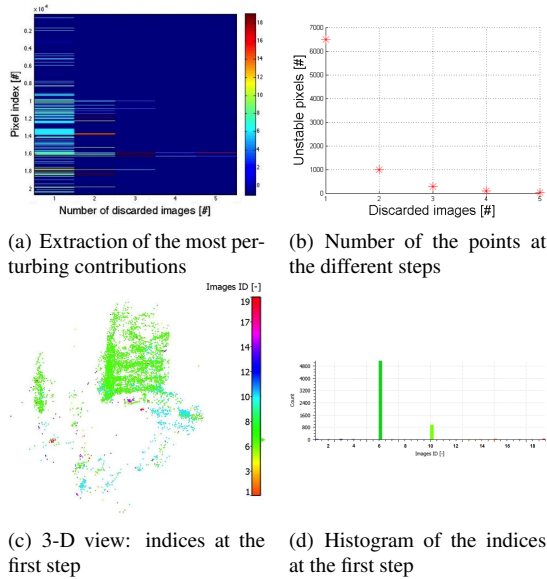


Figure 15. Tour Keller area: analysis about the unstable images

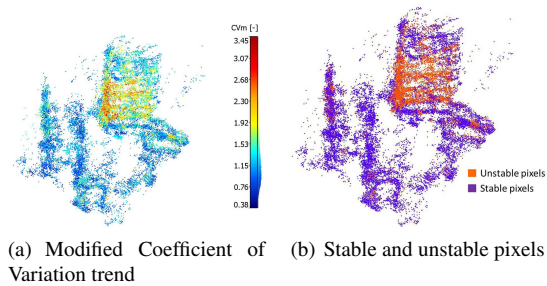


Figure 16. 3-D views of the Tour Keller's area in terms of the CVm

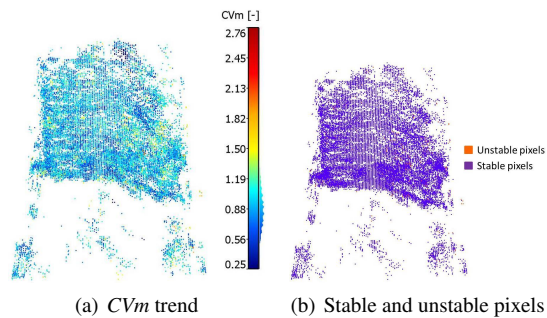


Figure 17. Tour Keller: 3-D views in terms of the CVm

techniques and high resolution satellite SAR imagery. In particular it was taken into account the classical non-parametric and parametric spectral estimation techniques such as the Beamforming, Capon and MUSIC. The approach here proposed is based on an iterative MOS technique aimed to detect for each resolution cell the number of the effective well separated sources. It has been applied to the selected estimation methods, proposing a customized "quasi" ML solution. 2-D and 3-D analysis have been presented over the urban area of Paris acquired by TerraSAR-X sensor in High Resolution SpotLight and Single Polarization mode. The present work is mainly focused on the 3-D reconstruction by very fast estimation techniques and does not take into account parsimonious signal estimators. In section 5.1 it was underlined the good quality of high reso-

lution SAR data, such as ones acquired by TerraSAR-X, both from the interferometric and time stability and coherence points of view. The analysis of the results and the coherence maps generated over the entire stack allowed to choose the adequate set of multitemporal data to be processed, discarding images considered as outlier in terms of temporal and spatial baselines. Further, in section 5.2 the extraction of 2-D tomograms over different azimuth-profile has showed the capabilities to distinguish more than one scatterer within the same resolution cell and to reconstruct the vertical building profiles. The analysis have regarded the expectation, that is the parametric MUSIC method, respect to the other non-parametric twos, revealed a better sidelobes reduction and accuracy of the estimated products.

Starting from these results the 3-D analysis has been performed in section 6 considering different tiles characterized both by mixed features (residential buildings, streets and vegetation) and single skyscrapers inducing a strong layover. The generated point clouds reveal the good reconstruction of building shape and location and a good estimation of their elevation. Indeed, façades intersection, structure features and main streets are well visible from the 3-D reconstruction. Moreover, being able to detect up to three scatterers within the same resolution cell, it has been possible not only to generate more complete point clouds, but also to solve the distortions due to the layover. This has been highlighted for the Tour Keller area, where the second detected sources are mostly related to information lying down the strong layover induced by the tallest skyscraper. The MUSIC approach allowed to detect the highest number of points, especially in the layover cases, and the Capon's results appear to be sparser and noisier respect also to the Beamforming ones.

The analysis performed in terms of vertical reflectivity estimation has led to the identification of strong intensity of the signals at the interaction wall-ground, revealing the double bounce strong reflection occurring in that area. At the same time, the ground is characterized by low reflectivity values.

The most innovative aspect of the present work is represented by the 3-D analysis of the time stability of the detected scatterers. Considering step by step all the images but the one corresponding to the relative step, a set of 3-D intensity have been generated and the stable and unstable scatterers have been distinguished and the IDs of the most perturbing contributions have been found. The study has been developed considering a modified Coefficient of Variation, respect which the more unstable pixels appeared to belong to the façades of the Tour Keller.

Eventually, it is possible to assert that processing high resolution SAR data allows to achieve a strong improvement in 3-D imaging capabilities. The 3-D reconstructions presented in the present thesis enabled to perform a global characterization of build-up areas, processing an adequate set of multitemporal high resolution SAR images. It has been demonstrated the potentialities of TomoSAR technique in distortions correction, in determining information about the number of scatterers and the corresponding reflectivity within one resolution cell and in 3-D change monitoring using basic mono-dimensional estimators as Beamforming, Capon and MUSIC.

Even though the inferred conclusions lead to good and encouraging results, there are still interesting issues which may enhance and deepen the developed processing chain. Future investigations should be directed towards improving tomographic technique robustness, refining 3-D change detection and monitoring, studying the integration with other techniques. Summarizing, as main topics one can list:

- *Considering thermal building variations.* In order to enhance the second products quality, it may be interesting to take into account the analysis of the building expansion and

contraction due to the thermal loads from exposure to changes in the ambient temperature. This kind of changes, strongly depend on the different temperatures to which the structure is subjected, may occur slowly and may impact the time stability of the detected sources

- *Improving tomographic techniques.* Spectral estimators robustness may be improved applying more sophisticated estimation techniques and a comparison with the Compressive Sensing approach may be performed in order to evaluate the main pros and cons of the two approaches
- *Processing data sets acquired at different spatial resolutions.* Certainly, the processing chain might be applied to other stack(s) representing a complex and dense urban scenarios and acquired both at high and low resolution. An interesting and challenging investigation might be handling Sentinel-1 data, characterized by 5x20m spatial resolution (in Interferometric Wide Swath) and provided by ESA for free and on-line thought the scientific data hub tool. This may lead to study the limits of tomographic techniques respect to the spatial resolution of the preprocessed data
- *Integration with the Polarimetric SAR.* Polarimetric SAR Tomography (PolTomSAR) is a well-known technique based on the combination of tomograms computed over different polarimetric channels. In this way two different scattering mechanisms could be identified: the single-bounce reflection over rough surface (e.g. ground or building roofs) and the double-bounce reflections characteristic of ground-tree trunk or dihedral-like objects. In literature the application of PolTomSAR technique to urban scenarios by means of SAR satellite data represents an innovative topic and such a technique may be used to retrieve a land cover classification, largely useful tool in different engineering civil application fields. As last goal, all final products could become a valuable tools to supply topographic information in complex environments, in particular urban areas. In this sense a TerraSAR-X proposal project has been successfully submitted and approved and a huge amount of dual polarimetric data stacks, acquired over different AOIs (as Spain, Germany and Japan), is already available to perform the tomographic and polarimetric processing chain
- *DSMs validation.* A DSMs assessment might be performed comparing the extracted DSMs with a more accurate ground truth one, e.g. obtained by means of the LiDAR technology, in order to evaluate their elevation accuracy

8. ACKNOWLEDGEMENT

I would like to acknowledge the DLR for providing TerraSAR-X data used for the present research in the frame of the project ID LAN1746

REFERENCES

- Auer, S., Hinz, S. and Bamler, R., 2010. Ray-tracing simulation techniques for understanding high-resolution sar images. *IEEE Transactions on Geoscience and Remote Sensing* 48(3 PART2), pp. 1445–1456.
- Bamler, R. and Hartl, P., 1998. Synthetic aperture radar interferometry. *Inverse Problems* 14(4), pp. r1–r54.
- Budillon, A., Evangelista, A. and Schirinzi, G., 2011. Three-dimensional sar focusing from multipass signals using compressive sampling. *IEEE Transactions on Geoscience and Remote Sensing* 49(1), pp. 488–499.
- Capaldo, P., Crespi, M., Fratarcangeli, F., Nascetti, A., Pieralice, F., Porfiri, M. and Toutin, T., 2013. DSMs generation from COSMO-SkyMed, Radarsat-2 and TerraSAR-X imagery on Beauport (Canada) test site: Evaluation and comparison of different radargrammetric approaches. Vol. 40Number 1W1, pp. 41–46.
- Capaldo, P., Fratarcangeli, F., Nascetti, A., Pieralice, F., Porfiri, M. and Crespi, M., 2014. High Resolution Radargrammetry - 3D Terrain Modeling. In: D. D. Closson (ed.), *Land Applications of Radar Remote Sensing*, InTech, chapter 6, pp. 167–190.
- Capon, J., 1969. High-Resolution Frequency-Wavenumber Spectrum Analysis. *Proceedings of the IEEE* 57(8), pp. 1408–1418.
- Curlander, J. and McDonough, R. N., 1991. *Synthetic Aperture Radar: Systems and Signal Processing*. Wiley.
- Ferretti, A., Monti-Guarnieri, A., Prati, C. and Rocca, F., 2007. InSAR Principles: Guidelines for SAR Interferometry Processing and Interpretation. ESA.
- Ferretti, A., Prati, C. and Rocca, F., 1999. Multibaseline InSAR DEM reconstruction: the wavelet approach. *IEEE Transactions on Geoscience and Remote Sensing* 37(2 I), pp. 705–715.
- Ferretti, A., Prati, C. and Rocca, F., 2001. Permanent scatterers in SAR interferometry. *IEEE Transactions on Geoscience and Remote Sensing* 39(1), pp. 8–20.
- Ferro-Famil, L. and Pottier, E., 2007. Urban area remote sensing from L-band PolSAR data using time-frequency techniques. *Urban Remote Sensing Joint Event, URS*.
- Fornaro, G. and Serafino, F., 2006. Imaging of single and double scatterers in Urban areas via SAR tomography. *IEEE Transactions on Geoscience and Remote Sensing* 44(12), pp. 3497–3505.
- Fornaro, G., Pauciullo, A., Reale, D. and Verde, S., 2014. Multilook SAR Tomography for 3-D Reconstruction and Monitoring of Single Structures Applied to COSMO-SKYMED Data. *IEEE Journal of Selected Topics in Applied Earth Observations and Remote Sensing* 7(7), pp. 2776–2785.
- Fornaro, G., Reale, D. and Serafino, F., 2009. Four-Dimensional SAR Imaging for Height Estimation and Monitoring of Single and Double Scatterers. *IEEE Transactions on Geoscience and Remote Sensing* 47(1), pp. 224–237.
- Fornaro, G., Verde, S., Reale, D. and Pauciullo, A., 2015. CAESAR: An Approach Based on Covariance Matrix Decomposition to Improve Multibaseline-Multitemporal Interferometric SAR Processing. *IEEE Transactions on Geoscience and Remote Sensing* 53(4), pp. 2050–2065.
- Franceschetti, G. and Lanari, R., 1999. *Synthetic Aperture Radar Processing*. CRC Press.
- Gamba, P., Houshmand, B. and Saccani, M., 2000. Detection and extraction of buildings from interferometric SAR data. *IEEE Transactions on Geoscience and Remote Sensing* 38(1 II), pp. 611–618.
- Gini, F. and Lombardini, F., 2005. Multibaseline cross-track SAR interferometry: A signal processing perspective. *IEEE Aerospace and Electronic Systems Magazine* 20(8 II), pp. 71–92.
- Graham, L. C., 1974. Synthetic interferometer radar for topographic mapping. *Proceedings of the IEEE* 62(6), pp. 763–768.
- Homer, J., Longstaff, I., She, Z. and Gray, D., 2002. High resolution 3-D imaging via multi-pass SAR. *IEE Proceedings: Radar, Sonar and Navigation* 149(1), pp. 45–50.

- Hu, C., Ferro-Famil, L. and Kuang, G., 2013. Ship discrimination using polarimetric SAR data and coherent time-frequency analysis. *Remote Sensing* 5(12), pp. 6899–6920.
- Huang, Y. and Ferro-Famil, L., 2009. 3-D characterization of buildings in a dense urban environment using L-band pol-insar data with irregular baselines. *International Geoscience and Remote Sensing Symposium (IGARSS)* 3, pp. III29–III32.
- Huang, Y., Ferro-Famil, L. and Lardeux, C., 2011. Polarimetric SAR tomography of tropical forests at P-Band. pp. 1373–1376.
- Huang, Y., Ferro-Famil, L. and Reigber, A., 2012. Under-foilage object imaging using sar tomography and polarimetric spectral estimators. *IEEE Transactions on Geoscience and Remote Sensing* 50(6), pp. 2213–2225.
- Johnson, D. and Dudgeon, D., 1992. *Array Signal Processing-Concepts and Techniques*. Prentice Hall, pp. 111–190.
- Lacoss, R., 1971. Data adaptive spectral analysis methods. *Geophysics*, 36, pp. 134–148.
- Lanari, R., Mora, O., Manunta, M., J.J., M., Berardino, P. and Sansosti, E., 2004. A small-baseline approach for investigating deformations on full-resolution differential SAR interferograms. *IEEE Transactions on Geoscience and Remote Sensing* 42(7), pp. 1377–1386.
- Leberl, F. W., 1990. *Radargrammetric image processing*. Norwood, MA : Artech House.
- Massonnet, D., Rossi, M., Carmona, C., Adragna, F., Peltzer, G., Feigl, K. and Rabaut, T., 1993. The displacement field of the Landers earthquake mapped by radar interferometry. *Nature* 364(6433), pp. 138–142.
- Mèric, S., Fayard, F. and Pottier, E., 2009. Radargrammetric SAR Image Processing. In: *Geoscience and Remote Sensing*, Pei-Gee Peter Ho, chapter 20, pp. 421–454.
- MicroImages, Inc., 2012. Introduction to remote sensing with TNTmips®.
- Nascetti, A., Capaldo, P., Peralice, F., Porfiri, M., Fratarcangeli, F. and Crespi, M., n.d. Springer Berlin Heidelberg, Berlin, Heidelberg, chapter Radargrammetric Digital Surface Models Generation from High Resolution Satellite SAR Imagery: Methodology and Case Studies, pp. 1–7.
- Nascetti, A., Capaldo, P., Porfiri, M., Peralice, F., Fratarcangeli, F., Benenati, L. and Crespi, M., 2015. Fast terrain modelling for hydrogeological risk mapping and emergency management: the contribution of high-resolution satellite SAR imagery. *Geomatics, Natural Hazards and Risk* 6(5-7), pp. 554–582.
- Perko, R., Raggam, H., Deutscher, J., Gutjahr, K. and Schardt, M., 2011. Forest Assessment Using High Resolution SAR Data in X-Band. *Remote Sensing* 3(4), pp. 792–815.
- Pisarenko, V. F., 1973. The Retrieval of Harmonics from a Covariance Function. *Geophysical Journal of the Royal Astronomical Society* 33(3), pp. 347–366.
- Porfiri, M., Ferro-Famil, L. and Nicolas, J.-M., 2015. Building profile reconstruction using terrasar-x data time-series and tomographic techniques. In: *Analysis of Multitemporal Remote Sensing Images (Multi-Temp)*, 2015 8th International Workshop on the, pp. 1–4.
- Reale, D., Fornaro, G., Pauciuolo, A., Zhu, X. and Bamler, R., 2011. Tomographic imaging and monitoring of buildings with very high resolution sar data. *IEEE Geoscience and Remote Sensing Letters* 8(4), pp. 661–665.
- Reigber, A. and Moreira, A., 2000. First demonstration of airborne SAR tomography using multibaseline L-band data. *IEEE Transactions on Geoscience and Remote Sensing* 38(5 I), pp. 2142–2152.
- Sauer, S., Ferro-Famil, L., Reigber, A. and Pottier, E., 2011. Three-Dimensional Imaging and Scattering Mechanism Estimation Over Urban Scenes Using Dual-Baseline Polarimetric InSAR Observations at L-Band. *IEEE Transactions on Geoscience and Remote Sensing* 49(11), pp. 4616–4629.
- Schmidt, R. O., 1986. Multiple emitter location and signal parameter estimation. *IEEE Transactions on Antennas and Propagation* AP-34(3), pp. 276–280.
- Stoica, P. and Moses, R., 2005. *Spectral Analysis of Signals*. Prentice Hall, pp. 22–37, 159–164, 263–285.
- Tebaldini, S., 2010. Single and multipolarimetric SAR tomography of forested areas: A parametric approach. *IEEE Transactions on Geoscience and Remote Sensing* 48(5), pp. 2375–2387.
- Tebaldini, S. and Ferro-Famil, L., 2013. High resolution three-dimensional imaging of a snowpack from ground-based sar data acquired at X and Ku Band. In: *Geoscience and Remote Sensing Symposium (IGARSS)*, 2013 IEEE International, pp. 77–80.
- Tebaldini, S. and Rocca, F., 2012. Multibaseline Polarimetric SAR Tomography of a Boreal Forest at P- and L-Bands. *IEEE Transactions on Geoscience and Remote Sensing* 50(1), pp. 232–246.
- Toutin, T. and Chenier, R., 2009. 3-D Radargrammetric modeling of RADARSAT-2 ultrafine mode: Preliminary results of the geometric calibration. *IEEE Geoscience and Remote Sensing Letters* 6(2), pp. 282–286.
- Van Veen, B. and Buckley, K., 1988. Beamforming: A Versatile Approach to Spatial Filtering. *IEEE ASSP Magazine* 5(2), pp. 4–24.
- Zebker, H., Rosen, P., Goldstein, R., Gabriel, A. and Werner, C., 1994. On the derivation of coseismic displacement fields using differential radar interferometry: the Landers earthquake. *Journal of Geophysical Research* 99(B10), pp. 19,617–19,634.
- Zhu, X. and Bamler, R., 2009. Very High Resolution SAR Tomography via Compressive Sensing. In: *Proc. ESA FRINGE*.
- Zhu, X. and Bamler, R., 2010a. Tomographic SAR inversion by L1-norm regularization-the compressive sensing approach. *IEEE Transactions on Geoscience and Remote Sensing* 48(10), pp. 3839–3846.
- Zhu, X. and Bamler, R., 2012. Demonstration of super-resolution for tomographic SAR imaging in urban environment. *IEEE Transactions on Geoscience and Remote Sensing* 50(8), pp. 3150–3157.
- Zhu, X. X., Adam, N., Brcic, R. and Bamler, R., 2009. Spaceborne high resolution SAR tomography: experiments in urban environment using TerraSAR-X Data. In: *Urban Remote Sensing Event, 2009 Joint*, pp. 1–8.
- Zhu, X. X. and Bamler, R., 2010b. Very High Resolution Spaceborne SAR Tomography in Urban Environment. *IEEE Transactions on Geoscience and Remote Sensing* 48(12), pp. 4296–4308.



Associazione **U**niversitari di **T**opografia **e** **C**artografia

c/o TESAF, Dipartimento Territorio e Sistemi Agro-Forestali - Università degli Studi di Padova

Viale dell'Università 16, 35020 Legnaro (PD)

Prof. Antonio Vettore tel. 049-8272688

e-mail antonio.vettore@unipd.it

con il supporto di



ISBN 978-88-905917-9-2

Giugno 2017